Searches for decays of the Standard Model Higgs boson to dielectrons and to dimuons with the ATLAS detector

Thesis submitted in accordance with the requirements of the University of Liverpool for the degree of Doctor in Philosophy by

Hanna Maria Borecka-Bielska

July 2020

Department of Physics
Oliver Lodge Laboratory
University of Liverpool

Searches for decays of the Standard Model Higgs boson to dielectrons and to dimuons with the ATLAS detector

Hanna Maria Borecka-Bielska

Abstract

Searches for the yet unobserved decays of the Standard Model Higgs boson to dielectrons and to dimuons are presented. The searches are performed using data collected by the ATLAS detector in proton-proton collisions in Run 2 of the LHC at a centre-of-mass energy of 13 TeV corresponding to an integrated luminosity of 139 fb^{-1}. The results show no evidence for either process and are in agreement with both Standard Model and background-only hypotheses within the uncertainties. The observed (expected) limit at 95% confidence level on the branching fraction for the $H \to ee$ channel is $3.6 \cdot 10^{-4}$ $(3.5 \cdot 10^{-4})$. The observed (expected) significance for the $H \to \mu\mu$ channel is 2.0σ (1.7σ) and the best fit value for the signal strength is $\mu = 1.2 \pm 0.6$. ATLAS Semiconductor Tracker radiation damage studies are also presented, including leakage current simulations using two phenomenological models and an estimation of the full depletion voltage using hit efficiency curves. The predictions of the leakage current using both models agree well with the data and can be used to estimate its further evolution until the end of Run 3. While the estimated value of the full depletion voltage is consistent with results obtained using other methods, it is higher than the predictions and requires further investigation.

Declaration

This thesis is the result of my own work, except where explicit reference is made to the work of others, and has not been submitted for another qualification to this, or any other, university. This thesis does not exceed the word limit for the respective Degree Committee.

Hanna Maria Borecka-Bielska

Acknowledgements

This PhD was the hardest thing I have ever done and it would not be possible without many kind people I met along the way.

I would like to express my extreme gratitude to my supervisor Jan Kretzschmar. It is always a pleasure to see and work with someone so dedicated to his work and who absolutely enjoys what he is doing. I want to thank him for his enormous help, which allowed me to contribute to two ATLAS papers, for his patience and for answering my numerous questions.

I am very grateful to the ATLAS Liverpool Team for offering me a PhD studentship in their group. I would like to thank Helen Hayward for supervision of my qualification task and Max Klein for providing advice whenever it was needed. I would like to thank my CERN officemate Carl Gwilliam for always finding time to answer my questions, for helping me to rehearse many important talks and, to quote him, for "staying enough out of the office so I could focus on my work".

I am very grateful to the ATLAS $H\mu\mu$ and Hee teams for entrusting me with the tasks I was working on. I would like to particularly thank Tom Neep for his help with the spurious signal study.

I would like to express my gratitude to the ATLAS SCT team for being so welcoming to me and for entrusting me with the tasks I carried out. Our friendly weekly meetings were the part of the week I looked forward to the most. I would like to thank in particular Dave Robinson for welcoming me in the team, Koichi Nagai for entrusting me with many tasks, Shigeki Hirose for many discussions about the hit efficiency study, Hide Otono for many discussions and help whenever it was needed, Kazuya Mochizuki for his help with my tasks, for explaining to me patiently everything about the SCT DAQ and DCS during

shifts and for being such a great friend in general. Most importantly, I would like to thank Taka Kondo for sharing with me his knowledge about radiation damage and for spending hours helping me. I have learned so much from him.

I could not miss here my friends whom I met at CERN and in Liverpool. I would like to thank them for the occasional distractions from work, numerous cups of coffee during the day and the beers we had in the evenings.

I am extremely grateful to my family for the financial support throughout my education. I know how much they had to sacrifice so I could move for my undergraduate studies to Cracow which allowed for my further career in physics. Finally, I would like to thank the most special person in my life, my husband Rafał. Thanks to his support, I have the courage and strength to follow my dreams.

Preface

This thesis summarises work carried out in collaboration with other members of the ATLAS experiment and focuses on parts of the research where my contributions were the most significant. I contributed to the $H \to ee$ search by estimating the background modelling systematic uncertainty. The study included implementation of the detector response parameterisation to electrons, validation and generation of the high-statistics fast simulation of the main background process, and performing fits to the generated samples to estimate the number of spurious signal events. The task was carried out under the supervision of Dr. Jan Kretzschmar and Dr. Tom Neep, and is documented in Section 7.5. My main contribution to the $H \to \mu\mu$ search was the implementation and optimisation of the recovery of final state radiation photons to improve dimuon mass resolution. The task was carried out under the supervision of Dr. Jan Kretzschmar and is presented in details in Section 8.3.

I performed the radiation damage studies documented in Chapter 4 in close collaboration with the members of the ATLAS SCT detector team. In particular, I completed the leakage current study under the supervision of Prof. Takahiko Kondo. I worked on the estimation of the full depletion voltage from hit efficiency curves in consultation with with Prof. Takahiko Kondo, Dr. Kazuya Mochizuki, Dr. Shigeki Hirose, Dr. Koichi Nagai and Dr. Hidetoshi Otono.

Contents

List of acronyms

SM	Standard Model	14
FCal	Forward Calorimeter	39
LHC	Large Hadron Collider	14
CERN	European Organisation for Nuclear Research	28
LS1	Long Shutdown 1	29
LS2	Long Shutdown 2	30
IP	interaction point	28
ID	Inner Detector	32
SCT	Semiconductor Tracker	14
TRT	Transition Radiation Tracker	38
IBL	Insertable B-Layer	35
HLT	High Level Trigger	46
L1	Level 1	46
LAr	liquid argon	39
FCal	Forward Calorimeter	39
EMEC	Electromagnetic Endcap Calorimeter	39
HEC	Hadronic Endcap Calorimeter	39
PMT	photomultiplier	42
MS	Muon Spectrometer	42
MDT	Monitored Drift Tubes	43
CSC	Cathode Strip Chambers	43
RPC	Resistive Plate Chambers	43
TGC	Thin Gap Chambers	43
JVT	Jet Vertex Tagger	100
BDT	Boosted Decision Tree	101
WP	working point	88
EM	electromagnetic	17

MC	Monte Carlo 81
ggF	gluon-gluon fusion 21
VBF	vector boson fusion 21
NNLO	next-to-next-to-leading-order 22
NLO	next-to-leading-order 104
N^{3}LO	next-to-next-to-next-to-leading-order 21
LO	leading-order 21
QCD	quantum chromodynamics 18
DY	Drell-Yan 105
FSR	final state radiation 11
ISR	initial state radiation
LH	likelihood 88
PDF	parton distribution function 59
PDG	Particle Data Group 113
QED	quantum electrodynamics 18
GRL	Good Runs List 108
ZDC	Zero Degree Calorimeter 45
HV	high voltage 32
PSB	Proton Synchrotron Booster 28
PS	Proton Synchrotron 28
SPS	Super Proton Synchrotron 28
LUCID-2	LUminosity Cherenkov Integrating Detector 31
AFP	ATLAS Forward Proton 45
ALFA	Absolute Luminosity For ATLAS 45
NIEL	Non-Ionising Energy Loss 58
PKA	Primary Knock-on Atom 58
SUC	sensor under consideration 74
LV	low voltage 64
VEV	vacuum expectation value 19
BSM	beyond the Standard Model 14
ME	matrix element 83

Chapter 1

Introduction

The Standard Model (SM) of particle physics is one of the most successful theories in the history of science. It is capable of describing a wide range of elementary interactions, and over the several decades of its development managed to predict numerous phenomena and the existence of many of the fundamental particles observed experimentally. The last observed particle of the SM is the Higgs boson, the discovery of which was one of the main goals of the ATLAS and CMS experiments at the Large Hadron Collider (LHC). After its discovery in 2012, the era of precise measurements of its properties began.

One of the interesting Higgs boson decays is an yet unobserved $H \to \mu\mu$ process as it gives a possibility to measure the Higgs coupling to second-generation fermions. Its low branching fraction and the presence of a high irreducible background make the search for this decay very challenging, therefore, it is important to optimise the analysis techniques along with adding more data. Another interesting and yet unobserved decay channel is the $H \to ee$ process. Although it is unlikely to be observed due to its even lower branching fraction, it is an important test of the SM as any signal could indicate a contribution from the beyond the Standard Model (BSM) physics.

Silicon detectors, such as the ATLAS Semiconductor Tracker (SCT), play an important role in physics analyses, as thanks to them it is possible to reconstruct the trajectories of charged particles, to reconstruct the particle momenta and to reconstruct primary and secondary vertices with a great precision. As

they are placed closest to the interaction point, they have to withstand extremely challenging conditions due to high particle fluences. It is therefore vital to monitor the effects of radiation damage to the silicon sensors in order to ensure adequate performance of the detector.

The document is organised as follows. Chapter 2 provides a short introduction to the SM, the Higgs mechanism and predictions for the SM Higgs boson production and decay. Chapter 3 gives an overview of the LHC accelerator complex and the ATLAS detector with all its components. An overview of the silicon strip detectors and the radiation damage in silicon sensors followed by a discussion of radiation damage effects observed in the ATLAS SCT detector is provided in Chapter 4. Chapter 5 discusses the steps required to model physics processes. Algorithms and selections required to reconstruct different types of objects in the ATLAS detector are discussed in Chapter 6. The search for the Higgs boson decay to dielectrons is presented in Chapter 7 and the search for the Higgs boson decay to a pair of oppositely-charged muons is presented in Chapter 8. A summary of all results is provided in Chapter 9.

Chapter 2

Theoretical background

2.1 The Standard Model of Particle Physics

The Standard Model of particle physics is a theory describing the elementary building blocks of matter and the fundamental forces between them. According to the SM, all matter (and antimatter) is composed of 12 types of fermions – particles with fractional spin number $\frac{1}{2}$ characterised by Fermi-Dirac statistics, summarised in Table 2.1. These elementary fermions are categorised in two sets of six particles – quarks and leptons, which are further divided into three generations each. Quarks are massive particles with fractional electrical charge. In each quark generation, one quark is usually referred to as an up-type quark (u, c, t) and the other as a down-type quark (d, s, b). Each lepton generation consists of a massive negatively charged lepton (e, μ, τ) and a corresponding massless[1] neutral neutrino (ν_e , ν_μ , ν_τ). First generation quarks, u and d, together with electrons (a first generation lepton) compose atoms and thus all visible matter. Second and third generation fermions are heavier and, with the exception of the neutrinos, decay into lighter particles. All fermions have their antimatter counterparts with the same mass and opposite charge.

There are three types of interactions described by the SM – electromagnetic, weak and strong – each carried by the different types of gauge bosons, spin-1 particles characterised by the Bose-Einstein statistics, summarised in Table 2.2.

[1] Although the SM was constructed assuming massless neutrinos, it is known today that the neutrino masses are small but non-zero, which allows for neutrino oscillations discovered in the late 1990s and early 2000s. [1]

	Leptons			Quarks		
		q	m [GeV]		q	m [GeV]
First	$\boldsymbol{e^-}$	-1	0.0005	**u**	$+2/3$	0.0022
Generation	$\boldsymbol{\nu_e}$	0	$< 1.1 \cdot 10^{-9}$	**d**	$-1/3$	0.0047
Second	$\boldsymbol{\mu^-}$	-1	0.106	**c**	$+2/3$	1.27
Generation	$\boldsymbol{\nu_\mu}$	0	$< 0.19 \cdot 10^{-6}$	**s**	$-1/3$	0.093
Third	$\boldsymbol{\tau^-}$	-1	1.777	**t**	$+2/3$	172.76
Generation	$\boldsymbol{\nu_\tau}$	0	$< 18.2 \cdot 10^{-6}$	**b**	$-1/3$	4.18

Table 2.1: Elementary fermions of the Standard Model and their properties in terms of electric charge q and mass m [2].

The electromagnetic (EM) interactions are a result of unification of two forces – electric and magnetic. They occur between all electrically charged fermions and are carried by photons – massless neutral particles travelling with the speed of light, giving these interactions an infinite range. The weak interactions occur between all types of particles and are mediated by three heavy gauge bosons – the charged W^+ and W^- bosons, and the neutral Z boson. Due to the high mass of the weak bosons, the range of the weak force is relatively short.

The strong force is the strongest of the fundamental forces (hence the name). Unlike the other forces in the SM, its strength grows at small energies or large distances, leading to the confinement of quarks and gluons to bound states (hadrons) and the non-observation of free quarks or gluons. On the other hand the strong force becomes weaker at short distances or high energies, a phenomenon termed asymptotic freedom.

The interactions in the SM are mathematically described as arising from local gauge symmetries. The electromagnetic and weak interactions are built on the conserved hypercharge Y and the weak isospin of left-handed fermions with the

symmetry groups $U(1)_Y \times SU(2)_L$. The strong force is described by the theory of quantum chromodynamics (QCD), which builds on the $SU(3)_C$ symmetry related to the colour charges of quarks and gluons.

The fourth type of interaction – gravity – is not described by the Standard Model. Due to its low strength and long range it is significant at macroscopic scale, but not at the fundamental-particle scale. The inability to include gravity in the SM is considered one of its biggest limitations, along with its failure to describe the matter-antimatter asymmetry in the Universe.

Interaction type	Gauge boson	Mass [GeV]
Electromagnetic	photon (γ)	0
Weak	$W^{\pm}, Z$	80.379, 91.1876 [2]
Strong	8 gluons (g)	0

Table 2.2: Fundamental interactions and the corresponding gauge bosons.

2.2 Electroweak symmetry breaking

Weak interactions were first introduced in the 1930s to explain the mechanism of radioactive beta decay. Since this type of interactions has a short range, it was postulated that the mediator – a charged W boson – should be a massive particle. However, a model for the weak interactions that would be similar to quantum electrodynamics (QED) could not account for the W boson mass, as gauge invariance required the bosons to be massless. A solution to this problem came in 1964 from the works of Brout, Englert and Higgs [3, 4], who proposed that masses are not initially a part of the model, but rather arise through spontaneous symmetry breaking. In the SM, this is implemented through a complex scalar field ϕ, defined as:

$$\phi = \begin{pmatrix} \phi^+ \\ \phi^0 \end{pmatrix}, \tag{2.1}$$

which allowed massive particles to exist. The doublet can be written in terms of scalar fields as:

$$\phi^+ = \frac{\phi_1 + i\phi_2}{\sqrt{2}}, \phi^0 = \frac{\phi_3 + i\phi_4}{\sqrt{2}}. \tag{2.2}$$

The Lagrangian of this field can be written in the form:

$$\mathcal{L} = (D_\mu \phi)^\dagger (D^\mu \phi) - V(\phi), \tag{2.3}$$

where $V(\phi)$ is the Higgs potential defined as:

$$V(\phi) = \mu^2(\phi^\dagger \phi) + \lambda(\phi^\dagger \phi)^2, \tag{2.4}$$

and D_μ is the covariant derivative:

$$D_\mu = \partial_\mu + i\frac{g}{2}\boldsymbol{\sigma} \cdot \boldsymbol{W_\mu} + i\frac{g'}{2} Y B_\mu. \tag{2.5}$$

This specific construction with the gauge fields B_μ and $W_\mu^{(j)}$ for the $U(1)_Y$ and $SU(2)_L$ symmetries ensures the local gauge invariance of the Lagrangian. The μ (mass parameter) and λ (self-coupling parameter) are free parameters. If $\mu^2 > 0$ and $\lambda > 0$, the Higgs potential has one minimum at $\phi_0^2 = 0$. However, in the case where $\mu^2 < 0$ and $\lambda > 0$, $V(\phi^\dagger \phi)$ has an infinite number of minima for non-zero values of ϕ and a spontaneous symmetry breaking occurs (Figure 2.1). The minima can be found by requiring:

$$\frac{dV(\phi^\dagger \phi)}{d(\phi^\dagger \phi)} = 0 \Rightarrow \mu^2 + 2\lambda(\phi^\dagger \phi) = 0. \tag{2.6}$$

This leads to:

$$\phi^\dagger \phi = \frac{-\mu^2}{2\lambda} = \frac{v^2}{2}, \tag{2.7}$$

where v is referred to as the vacuum expectation value (VEV). In terms of the real fields, the above-mentioned equation can be written as:

$$\frac{1}{2}\left(\phi_1^2 + \phi_2^2 + \phi_3^2 + \phi_4^2\right) = \frac{v^2}{2}. \tag{2.8}$$

If only one value from the minima is chosen, the electroweak symmetry is broken. In order to keep the photon massless, the field ϕ_3 is chosen to be non-zero. In this case, the doublet can be written as:

$$\langle \phi \rangle_0 = \frac{1}{\sqrt{2}} \begin{pmatrix} 0 \\ v \end{pmatrix}. \tag{2.9}$$

The expansion around the minimum when $\phi_3 = v + H$ is:

$$\phi' = \frac{1}{\sqrt{2}} \begin{pmatrix} 0 \\ v + H \end{pmatrix} \tag{2.10}$$

and introduces a scalar Higgs field H which manifests itself as a new scalar boson.

The weak interactions were later unified with the electromagnetic in a theory developed by Glashow, Salam and Weinberg [5–7], predicting the existence of another massive particle – the neutral Z boson. The theoretical predictions were proven correct in the early 1980s with the direct observation of both massive electroweak force carriers by the UA1 and UA2 experiments at CERN [8–11]. The discovery of the Higgs boson had to wait another 30 years; it was announced by the ATLAS and CMS experiments in 2012 [12, 13].

By evaluating the Lagrangian given by Equation 2.3, one can obtain the mass terms for the photon, $W^{\pm}$ and Z bosons:

$$M_\gamma = 0, \tag{2.11}$$

$$M_W = \frac{1}{2} g v, \tag{2.12}$$

$$M_Z = \frac{1}{2}\left(g^2 + g'^2\right)^{1/2} v = \frac{1}{2}\frac{gv}{\cos\theta_w}, \tag{2.13}$$

where $\cos\theta_w = \frac{M_W}{M_Z}$ and θ_w is the Weinberg angle.

The fermion masses are introduced through Yukawa couplings. The lagrangian for a lepton doublet can be written in the form:

$$\mathcal{L} = -g_f \left(\overline{\nu}_l \; \overline{l}\right)_L \phi' l_R, \tag{2.14}$$

where $\left(\overline{\nu}_l \; \overline{l}\right)_L$ is the $SU(2)_L$ doublet and ϕ' is defined in Equation 2.10. The mass terms of spin-1/2 particles can be written in the form:

$$m_f = g_f \frac{v}{\sqrt{2}}, \tag{2.15}$$

where g_f is the Yukawa coupling of the fermions to the Higgs field and the VEV equals 246 GeV.

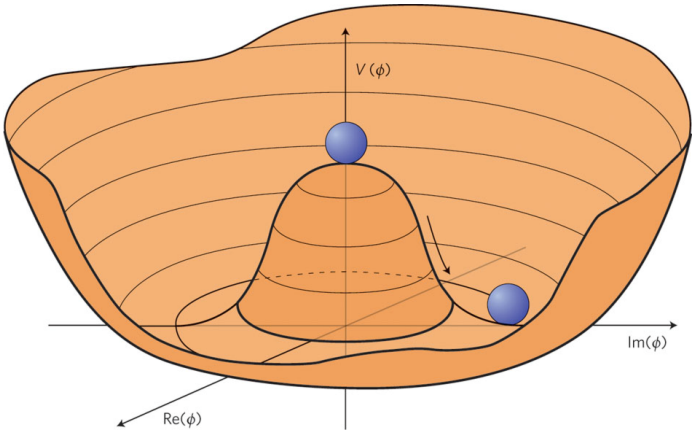

Figure 2.1: An effective potential $V(\phi^\dagger\phi)$ in the form of a "Mexican hat", which leads to the spontaneous symmetry breaking, where the ground state occupies a randomly chosen point among the infinite number of possible minima (symbolised by the lower blue ball) [14].

2.3 Higgs boson production in pp collisions

The Higgs boson can be produced in pp collisions via several processes. The dominant channel is gluon-gluon fusion (ggF). The corresponding leading-order (LO) Feynman diagram is presented in Figure 2.2a. As the Higgs boson does not couple to massless gluons, the process occurs via a virtual loop. The loop is dominated by the top quark due to its high mass and therefore large Yukawa coupling, as presented in Equation 2.15. A smaller contribution comes from a bottom quark, which accounts for roughly 5%. The corresponding cross-section has been calculated to a high precision at next-to-next-to-next-to-leading-order (N^3LO) and for the Higgs boson with a mass of 125 GeV at the LHC with a pp collision energy of 13 TeV it is [15]:

$$\sigma_{\text{ggF}} = 48.58 \text{ pb} \, {}^{+2.22 \text{ pb}}_{-3.27 \text{ pb}} \, (\text{QCD}) \pm 1.56 \text{ pb} \, (\text{PDF} + \alpha_S). \tag{2.16}$$

The second-largest contribution to the cross-section for Higgs boson production corresponds to the vector boson fusion (VBF) process presented in Figure 2.2b. The Higgs boson is produced as a result of two scattering quarks exchanging vector bosons (either Z or W) which interact. This process provides a test of electroweak symmetry breaking, as a direct coupling to a vector boson can be

measured. The current best theoretical value for the cross-section for the VBF process is calculated at next-to-next-to-leading-order (NNLO):

$$\sigma_{\mathrm{VBF}} = 3.92 \text{ pb } {}^{+0.02 \text{ pb}}_{-0.008 \text{ pb}} \text{ (QCD)} \pm 0.074 \text{ pb (PDF} + \alpha_S). \tag{2.17}$$

Although the cross-section for the VBF process constitutes only 8% of the ggF cross-section, it provides a distinctive final-state signature that often has lower backgrounds than the ggF process.

Smaller contributions to Higgs boson production come from associated production with a W or Z boson (Figure 2.3) or with $t\bar{t}$ or $b\bar{b}$ pair (Figures 2.4). A summary of Higgs production cross-sections calculated for the pp collision energy of 13 TeV is presented in Table 2.3.

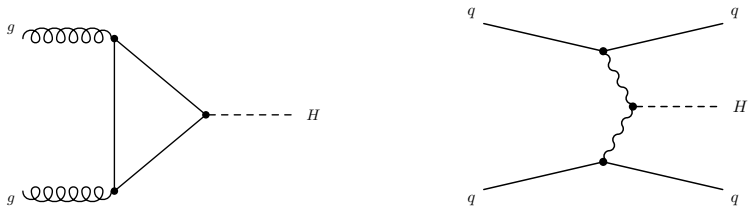

(a) (b)

Figure 2.2: Leading order Feynman diagrams for the ggF (a) and VBF (b) Higgs boson production processes [16].

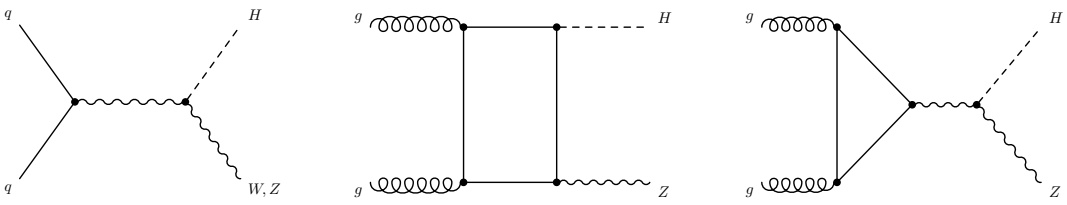

(a) (b) (c)

Figure 2.3: Leading order (a) and one-loop (b,c) Feynman diagrams for the associated production of a Higgs boson with a W or Z boson [16].

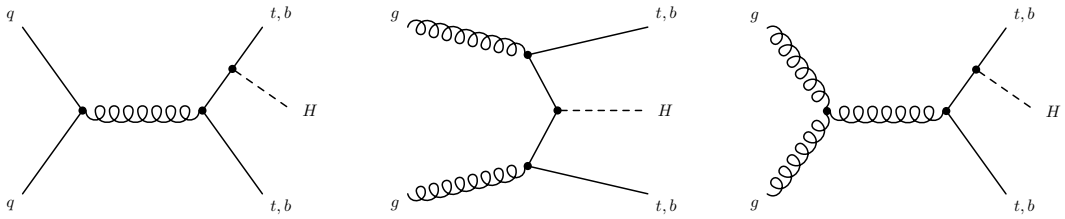

(a) (b) (c)

Figure 2.4: Leading order Feynman diagrams for the associated production of a Higgs boson with a $t\bar{t}$ or $b\bar{b}$ pair [16].

Production channel	Cross-section [pb]
ggF	48.58
VBF	3.92
WH	1.37
ZH	0.88
$ggZH$	0.88
$t\bar{t}H$	0.51
$b\bar{b}H$	0.49

Table 2.3: Production cross-sections for 13 TeV in pp collisions at the LHC [15].

2.4 Higgs boson decays

Within the SM, the Higgs boson's branching ratios to different fermions and bosons can be calculated from its mass, as presented in Figure 2.5. The highest branching ratio for a Higgs boson with a mass of around 125 GeV is for the $H \to b\bar{b}$ channel. The experimental observation of this decay is however very challenging due to the high background of $b\bar{b}$ pairs produced in other QCD processes and this is the reason that it has only been observed recently, with the Higgs boson produced in the VH process [17, 18]. The decay into a pair of oppositely charged W bosons has the second highest branching ratio and was observed in the leptonic final states [19, 20]. It is characterised by relatively large backgrounds and poor mass resolution, but provides a clean final-state signature and much higher cross-section than the cleanest channels.

The $H \to ZZ^*$ process (also already observed [21, 22]) has a relatively high branching ratio, however the requirement of further decay of the Z bosons into two charged leptons each leads to a lower rate. It is the cleanest Higgs boson decay process and provides an excellent signal-to-background ratio and mass resolution. The decay of H to diphotons was already observed [23] thanks to the good diphoton invariant mass resolution, which leads to a narrow peak on top of a continuous background. The decay into $\tau^+\tau^-$ pairs is challenging due to the relatively poor tau reconstruction efficiency compared to muons and electrons, and a large background [24, 25]. The discovery of the Higgs boson in the ATLAS and CMS experiments [12, 13] was made through the combination of the $H \to \gamma\gamma$, $H \to ZZ^* \to 4l$ and $H \to WW^* \to l\nu l\nu$ channels.

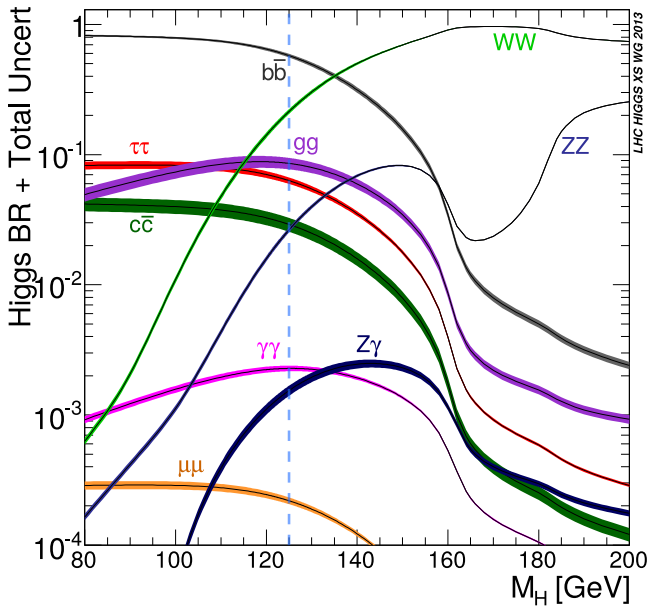

Figure 2.5: Standard Model Higgs boson decay branching ratio as a function of its mass for different decay processes [15]. The vertical dashed blue line indicates the mass of the discovered Higgs boson.

A summary of the cross-section times branching fraction values of the accessible Higgs boson decay channels corresponding to the different Higgs boson production processes measured in ATLAS is presented in Figure 2.6. It can be observed that all results are consistent with the SM prediction within the uncertainties.

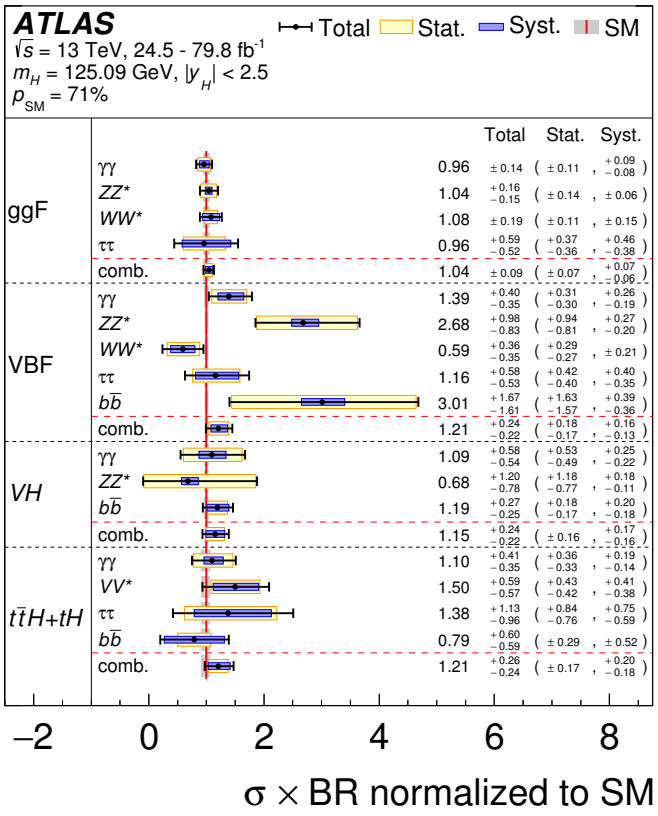

Figure 2.6: Cross-section times branching fraction normalised to the corresponding SM predictions for the Higgs boson decay channel: $\gamma\gamma$, ZZ^*, WW^*, $\tau\tau$, in different Higgs boson production processes, ggF, VBF, VH, $t\bar{t}H$+tH, as measured in the ATLAS experiment [26]. The yellow rectangles represent the statistical uncertainty and the blue rectangles the systematic uncertainty. The error bars show a combination of the two. The red vertical line represents the SM prediction.

Only couplings to bosons and third-generation fermions have been measured so far. The couplings to second-generation fermions could be measured in decays to charm or strange quark pairs and to dimuons. However, the small mass of the strange quarks and the inability to identify jets originating from s-quark makes this channel impossible to observe. Also, despite the high branching fraction for $H \to c\bar{c}$, searches for this decay are very challenging due to the large QCD background and ambiguous distinction between c- and b-jet [27]. Therefore, the decay to dimuons is the most promising channel to first observe the Higgs boson coupling to a second-generation fermion. It is characterised

by the simple final-state signature of two muons, which leads to a well reconstructed narrow resonance as a result of a good dimuon mass resolution. However, the very low branching ratio of $2.17 \cdot 10^{-4}$ [15] and the large irreducible backgrounds are an experimental challenge [28, 29]. A search for the yet unobserved $H \to \mu\mu$ decay is particularly interesting since any deviation from expectations in the observed rates could be a sign of physics BSM [30].

The $H \to ee$ process is characterised by a very low branching fraction in the SM to which no currently operating experiment is sensitive. Despite that, searching for this decay is an important test of the SM and any evidence of this process could indicate contributions from BSM physics.

A combination of the Higgs boson couplings to different fermions and gauge bosons measured by the ATLAS experiment and compared to the SM prediction is presented in Figure 2.7. It can be observed that all currently available results are consistent with the SM prediction within the uncertainties. The Higgs boson coupling to muons presented here is based on a preliminary result using 139 fb^{-1} of ATLAS data [31]. It is clearly visible that this coupling is measured with a limited precision.

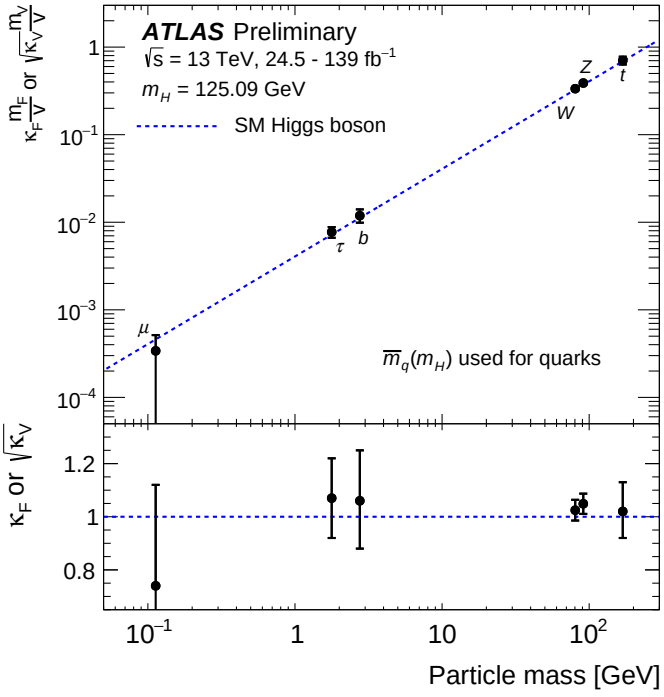

Figure 2.7: Reduced coupling strength modifiers to fermions $(\kappa_F \frac{m_F}{v})$ and gauge bosons $(\sqrt{\kappa_V}\frac{m_V}{v})$ for the VEV of 246 GeV as a function of particle mass [32]. The values are obtained assuming no BSM contributions to the Higgs boson decays. The dashed blue line represents the SM prediction. The lower panel shows the ratios of the obtained values to their corresponding SM predictions.

Chapter 3

LHC and the ATLAS detector

3.1 The CERN accelerator complex and the LHC machine

The world's highest energy particle accelerator – the LHC [33] – started its operation in 2009 at the European Organisation for Nuclear Research (CERN). This 27 km long ring placed 45–170 m underground is the last stage of the CERN accelerator complex, where the highest-energy particle collisions take place. The acceleration process starts with a bottle of compressed hydrogen gas from which hydrogen atoms are released in packets. Electrons are separated from the hydrogen atoms by applying a pulsating electric field. The protons are then injected into the first accelerator, the Linac 2 where they are accelerated to an energy of 50 MeV and then injected into the Proton Synchrotron Booster (PSB). Here, the proton packet is divided into four packets circulating in separate rings. A pulsating electric field increases the velocity of the circulating beams and electromagnets bend their trajectories. The acceleration in the PSB stops when the protons achieve an energy of 1.4 GeV and then are injected into the Proton Synchrotron (PS). Here, protons are accelerated to 25 GeV and after that they are injected into the Super Proton Synchrotron (SPS), where they are accelerated to an energy of 450 GeV before the final injection to the LHC. The proton packets are fed into two beam pipes of the LHC ring, which are kept at ultra-high vacuum. One beam circulates in the clockwise and the other in the anti-clockwise direction. The proton beams are accelerated to the energy of 6.5 TeV to be then crossed in four interaction points (IPs), where

four large experiments, ATLAS, CMS, LHCb and ALICE, are located and the collisions take place. The CERN accelerator complex and location of the four experiments on the LHC ring are presented in Figure 3.1. Along all different accelerators a wide range of electromagnets is used to focus, bend, squeeze and keep the protons on their trajectories.

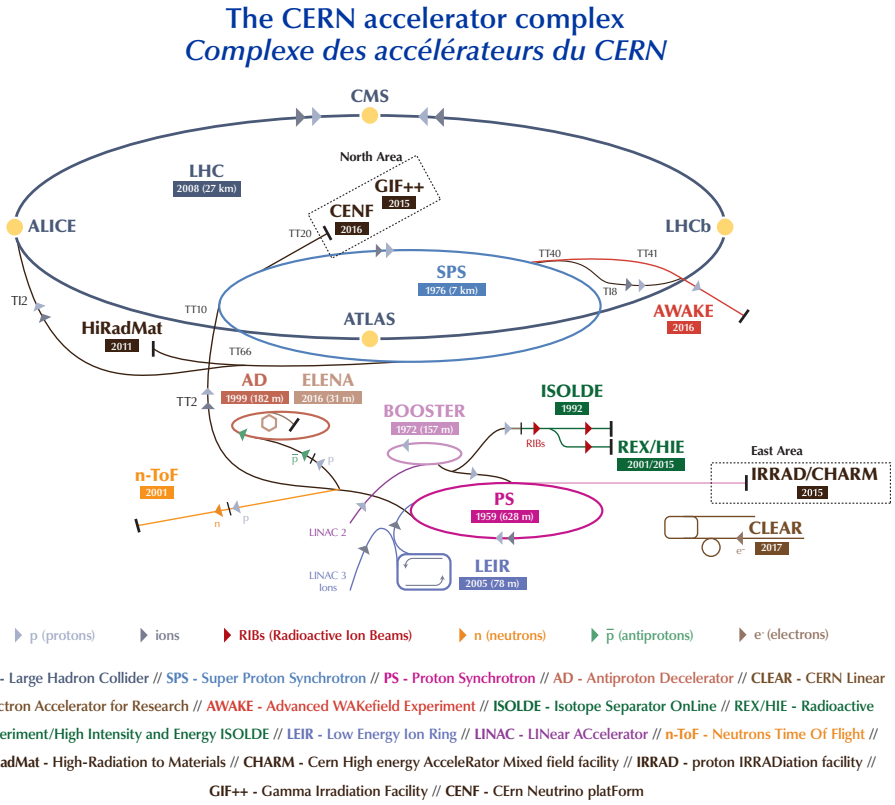

Figure 3.1: CERN accelerator complex and the location of the four big experiments at the LHC [34].

In 2010 and 2011 the proton beams were collided at a centre-of-mass energy of 7 TeV and in 2012 with 8 TeV. These three years correspond to a period of operation called Run 1, which was followed by Long Shutdown 1 (LS1) in 2013 and 2014. The LHC resumed its operation in 2015 with the start of Run 2, which lasted until the end of 2018. During this time the proton beams were collided at a centre-of-mass energy of 13 TeV, which is close to the design value of 14 TeV. Typically, at the end of each operation year the LHC collides heavy-ion beams (Pb-Pb, p-Pb or Xe-Xe) which makes possible performing

studies of quark-gluon plasma. After the end of the Run-2 operation, the Long Shutdown 2 (LS2) period started during which the LHC machine and experiments undergo upgrades in preparation for Run 3 which starts in 2022.

3.2 Luminosity

The number of events of interest produced in a beam-crossing point of a circular collider can be expressed as:

$$N_{\text{event}} = L^{\text{int}}\sigma, \tag{3.1}$$

where σ is the cross-section for the process of interest and $L^{\text{int}} = \int L dt$ is the integrated luminosity. The machine instantaneous luminosity depends on the beam properties and for a Gaussian beam distribution can be calculated as [33]:

$$L = \frac{N_b^2 n_b f_{rev} \gamma_r}{4\pi\epsilon_n \beta^*} F, \tag{3.2}$$

where N_b and n_b denote the number of particles per bunch and number of bunches respectively, f_{rev} is the revolution frequency, γ_r is the relativistic gamma factor, ϵ_n is the normalised transverse beam emittance and β^* is the beta function at the collision point. The term F is the geometric luminosity reduction factor due to the crossing angle at the IP, defined as:

$$F = \left(1 + \frac{\theta_c \sigma_z}{2\sigma^*}\right)^{-1/2}, \tag{3.3}$$

where θ_c is the full crossing angle at the IP, σ_z is the RMS bunch length and σ^* is the transverse RMS beam size at the IP. The instantaneous luminosity defined in Equation 3.2 is given in $\text{m}^{-2}\text{s}^{-1}$. Typically, when discussing the luminosity of a specific dataset a cumulative (integrated) luminosity in a given period of time is quoted and its value is provided in the units of barn b with appropriate prefix, where 1 barn corresponds to 10^{-28} m^2. Figure 3.2 presents the integrated luminosity during the Run-2 data-taking period, showing both the luminosity delivered by the LHC and that recorded by the ATLAS detector. Integrated luminosity after data quality selection ("good for physics") is also

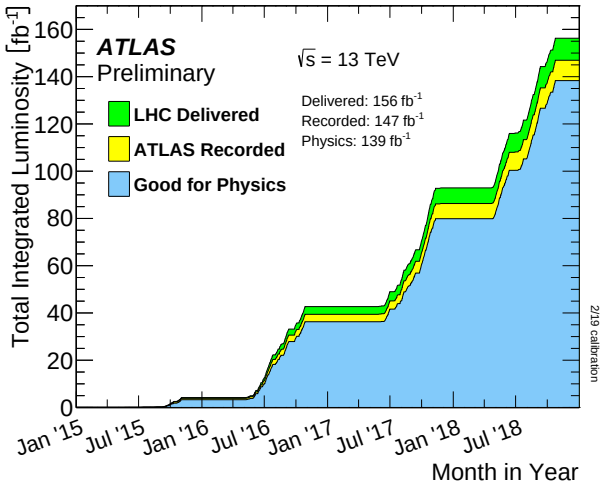

Figure 3.2: Integrated luminosity as a function of time presented for the Run-2 data-taking period [35]. The green histogram represents the cumulative luminosity provided by the LHC, whereas the yellow histogram represents the cumulative luminosity recorded by the ATLAS detector. The integrated luminosity recorded by the ATLAS detector for events passing all data quality criteria is presented in the blue histogram.

presented. The two searches presented in this document are performed using the full Run-2 dataset satisfying the data quality criteria and corresponding to an integrated luminosity of 139 fb^{-1}.

Accurate determination of the luminosity is essential as the corresponding uncertainty is usually among the largest uncertainties in cross-section measurements. The luminosity for a single bunch crossing can be expressed in terms of the visible average number of interactions μ_{vis} and the visible pp inelastic cross-section σ_{vis}:

$$L_b = \frac{\mu_{vis} f_{rev}}{\sigma_{vis}} \tag{3.4}$$

The visible average number of interactions is measured using the LUminosity Cherenkov Integrating Detector (LUCID-2). The visible cross-section is found by combining Equation 3.4 and the luminosity expressed in terms of beam parameters:

$$L_b = \frac{N_1 N_2 f_{rev}}{2\pi \Sigma_x \Sigma_y}, \tag{3.5}$$

where N_1 and N_2 represent the number of protons in each bunch of the pair crossing in the IP, and Σ_x and Σ_y are convolved beam sizes in x and y direction, respectively. The beam sizes are extracted from data collected in special runs, the so-called van der Meer scans [36], in which the two opposite beams are being slowly displaced against each other in the vertical and horizontal direction. As LUCID-2 measurements of the μ_{vis} combined with calibration from the van der Meer scan may lead to different than the actual values of the luminosity due to different conditions (different pile-up or bunch train running), dedicated methods are used to correct for them. The corrections are provided using luminosity measurements extracted from track counting in the Inner Detector (ID) or from current drawn from the high voltage (HV) power supply for calorimeter. The luminosity uncertainty of the combined Run-2 dataset is 1.7% [37].

Figure 3.3 presents an average number of interactions per crossing in ATLAS detector during Run 2. The mean values presented in the legend are obtained as the means of the Poisson distributions of the number of interactions per crossing for each bunch. The average pile-up in Run 2 was 34.

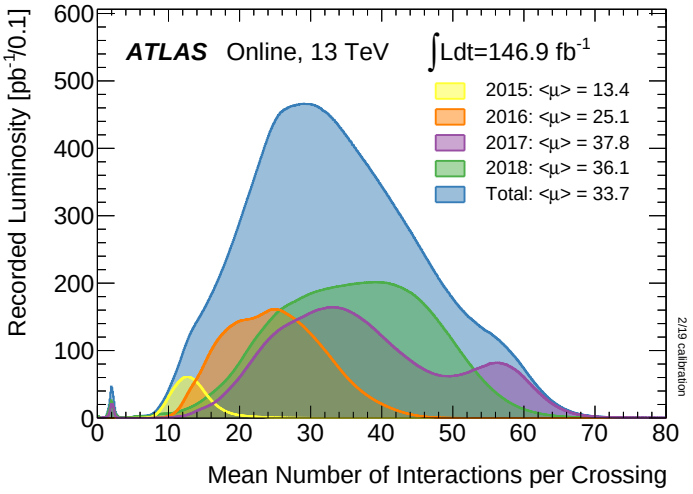

Figure 3.3: The mean number of interactions per bunch crossing in pp collisions at the centre-of-mass energy of 13 TeV during Run-2 operation [35].

3.3 The ATLAS detector

ATLAS is one of the two general-purpose detectors at the LHC. The physics programme of the experiment covers a wide range of topics including studies of the Higgs mechanism, searches for supersymmetry, measurements with top quarks, electroweak bosons and many others. The detector is 46 m long, 25 m high and 25 m wide. It consists of inner tracking detectors, two types of magnets, EM and hadronic calorimeters, and muon spectrometers. A cut-away view of the ATLAS detector is presented in Figure 3.4. ATLAS uses a right-handed coordinate system with its origin at the nominal IP in the centre of the detector and the z-axis along the beam pipe. The x-axis points from the IP to the centre of the LHC ring, and the y-axis points upwards. Cylindrical coordinates (r, ϕ) are used in the transverse plane, ϕ being the azimuthal angle around the z-axis. The pseudorapidity is defined in terms of the polar angle θ as $\eta = -\ln\tan(\theta/2)$. The angular distance is measured in units of $\Delta R \equiv \sqrt{(\Delta\eta)^2 + (\Delta\phi)^2}$.

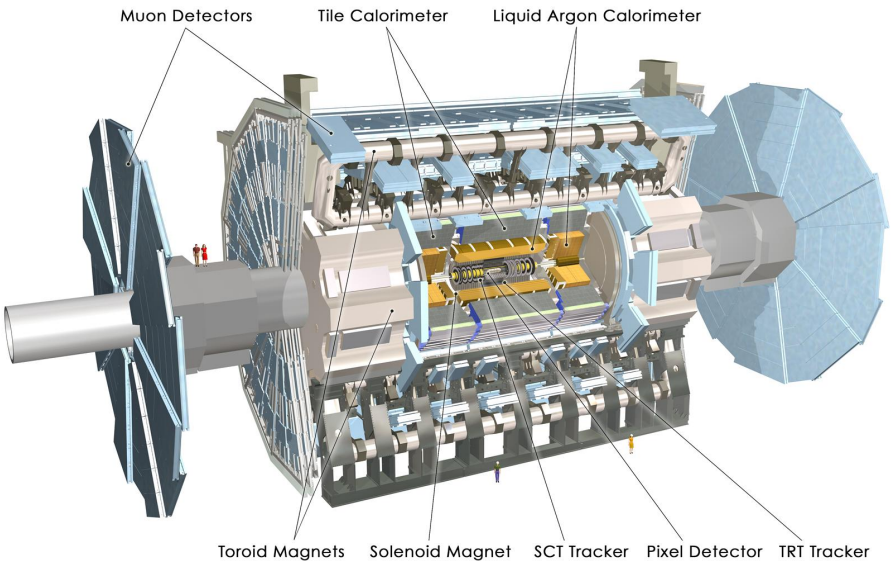

Figure 3.4: Cut-away view of the ATLAS detector indicating the location of each sub-system [38].

3.4 Inner Detector

The inner tracking system, also called the ID, provides high precision measurements of track momenta, impact parameters, and interaction vertex positions. It comprises three types of detectors: silicon pixels, silicon microstrips and a straw-tube detector. Figure 3.5 presents the layout of the Inner Detector. The ID is immersed in a 2 T axial magnetic field provided by a superconducting solenoid magnet. The magnet is located between the ID and a barrel EM calorimeter with which it shares a vacuum vessel.

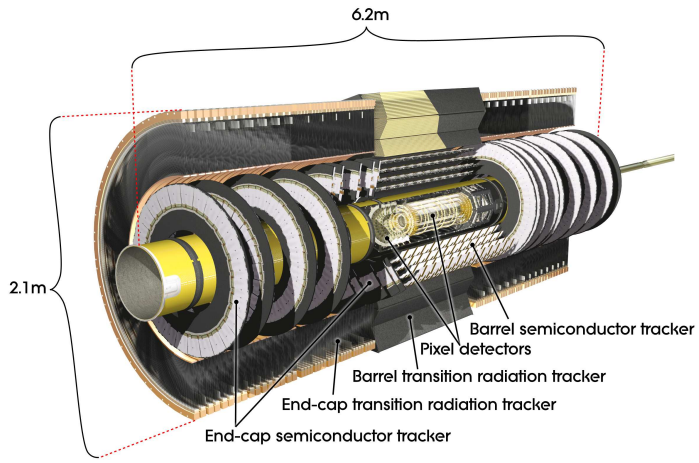

Figure 3.5: A schematic view of the ATLAS Inner Detector [38].

3.4.1 Pixel detector

Both pixel and strip detectors utilise the same method of detecting particles. When a charged particle traverses the sensitive area of a module, it ionises the detector material atoms creating electron-hole pairs. These charge pairs then drift in an electric field towards electrodes, where the charge is collected and passed on to front-end electronics.

The innermost part of the ID – the Pixel Detector – is arranged in three cylinders in the barrel region and three disks on each side in the endcap region. Both the pixel barrel and the endcaps are covered with similar modules with a typical pixel size of 50×400 μm^2. The precision of a position measurement is 10 μm $(R-\phi), 115$ μm (z) in the barrel and 10 μm $(R-\phi), 155$ μm (R)

in the endcaps. During LS1, the beam pipe was replaced by a beam pipe of a smaller radius (3.3 cm) and a fourth layer of pixels, the Insertable B-Layer (IBL), was inserted in between the first pixel layer and the new beam pipe. The IBL is a matrix of 50×250 μm^2 pixels with two types of silicon sensors, planar and 3D. It is particularly important in localising primary and secondary vertices from decays of long-lived particles like b-hadrons. The full pixel detector provides a measurement of particle trajectories with $|\eta|$ up to 2.5 and provides a measurement of four space-points per track.

3.4.2 Semiconductor Tracker

The ATLAS SCT is a silicon microstrip detector. It is the second innermost detector and covers a radial distance between 299 and 560 mm from the beam and an $|\eta|$ range up to 2.5 similarly to the Pixel detector. It consists of 4088 modules arranged in four concentric layers in the barrel region and two endcaps with nine disks each. The SCT typically provides eight strip measurements per track, giving four space-points and provides a position measurement accuracy of 17 μm in $(R-\phi)$ and 580 μm in the z and R direction. Figure 3.6 presents a schematic view of one quadrant of the SCT detector with all its components.

All SCT barrel modules are of the same type. The modules consist of four rectangular sensors. Two sensors are daisy-chained together and an identical pair is glued back-to-back with a stereo angle of 40 mrad. The modules are organised in a way that the strips are roughly parallel to the beam axis. The strip pitch size is 80 μm. A picture and a schematic view of the barrel modules are presented in Figure 3.7. The endcap modules have trapezoidal shape and are glued back-to-back with a stereo angle of 40 mrad. Unlike the barrel modules, they come in different types corresponding to three different endcap rings: inner, middle and outer. The outer and middle ring modules consist of two sensors per side and the inner ring module consist of only one. The strips are organised in the radial direction with an average pitch size of 80 μm. A picture and a schematic view of the three types of endcap modules are presented in Figure 3.8.

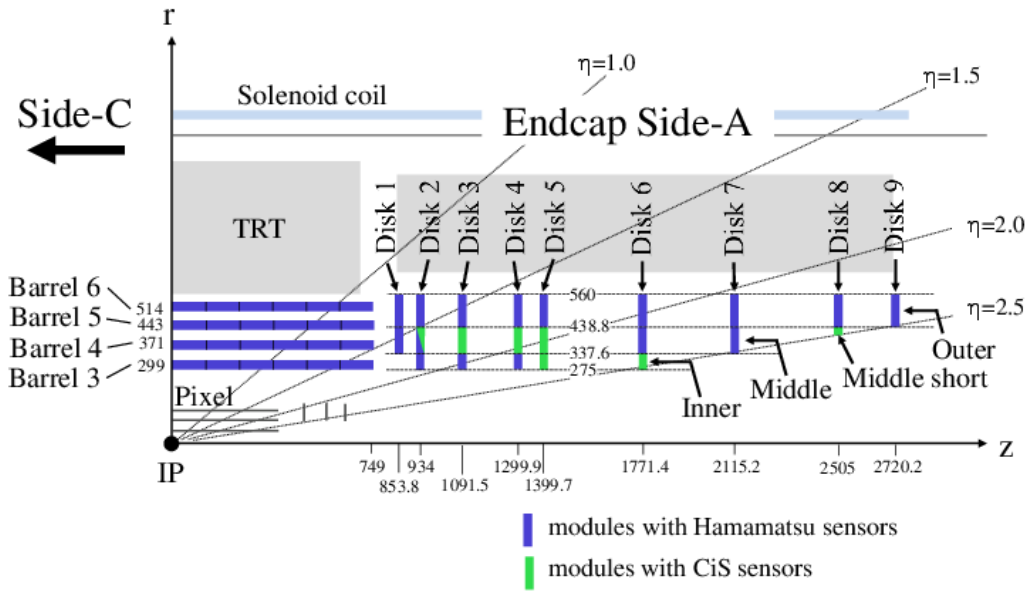

Figure 3.6: A schematic view of one quadrant of the SCT detector [39]. The four barrel layers are numbered starting from 3 to 6 and endcap disks are numbered from 1 to 9. Each side of the barrel layer consists of modules arranged in the η direction starting from $\eta_{\text{index}} = 1$ up to 6. In the endcaps, the modules are also numbered according to the η_{index} with 0 corresponding to the outer, 1 to the middle and 2 to the inner ring. The number of modules in the ϕ direction depends on the layer and is not visible here. Modules with sensors provided by different manufacturers are marked with different colours with the blue colour corresponding to Hamamatsu Photonics and the green to CiS.

The SCT sensors have a uniform thickness of 285 μm with n-type bulk and p-type implants. The sensors were provided by two manufacturers, Hamamatsu Photonics and CiS, with the vast majority produced by Hamamatsu (all barrel and 90 % of endcap modules). The sensors are typically made of wafers with $< 111 >$ crystal orientation, however, there is a small number (around 90) of sensors with $< 100 >$ crystal orientation.

Both the Pixel detector and the SCT have to be kept at low temperatures in order to reduce the radiation damage effects. The cooling is provided by a bi-phase evaporative cooling system [40] based on compressors and a distribution system to the cooling staves using C_3F_8 fluid. The cooling temperatures on

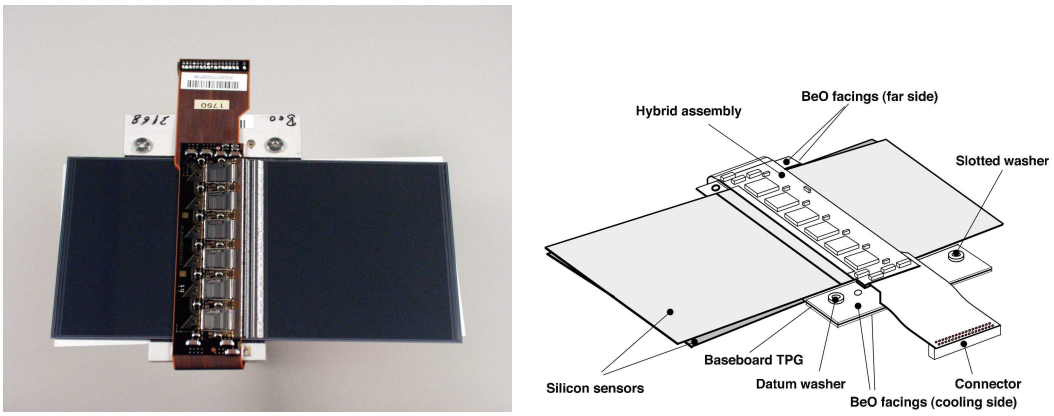

(a) (b)

Figure 3.7: Picture (a) and a schematic view (b) of the SCT barrel module [38]

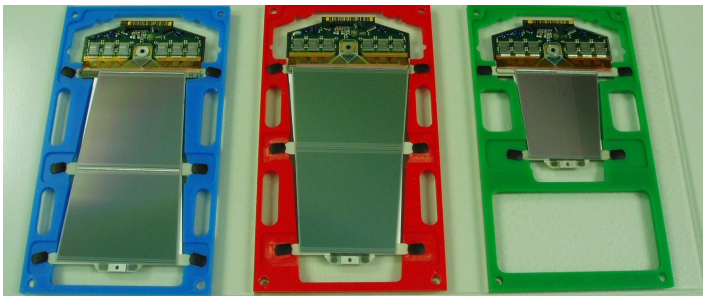

(a)

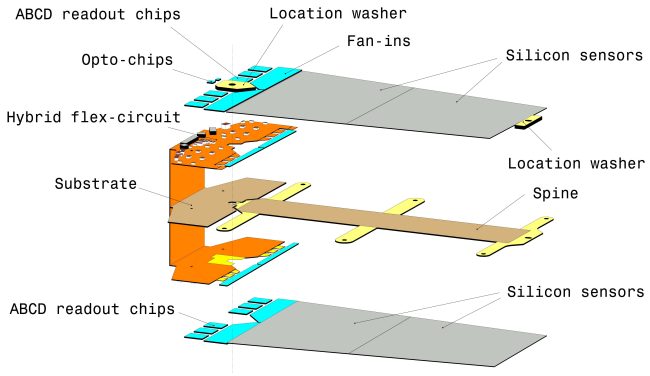

(b)

Figure 3.8: A picture of the three types of the SCT endcap modules (from left to right: outer, inner and middle ring module) and a schematic view of the middle-ring module (b) [38].

the staves are typically set to -20°C for barrel layers 3, 4 and 5 and to -14.3°C for the endcap disks. The outermost SCT barrel layer, layer 6, requires setting higher temperature of -10°C as it is close to the Transition Radiation Tracker (TRT) detector, which must be operated at room temperature to avoid mechanical stress. The temperatures set on the staves are lower than the actual operation temperatures due to thermal impedance between the mechanical structures and the cooling channels. Since September 2018 a thermosiphon [41] is operating as the main cooling system and the compressor system is kept as a backup. Thanks to the thermosiphon it is possible to achieve even lower operation temperatures to further limit the increasing radiation damage in the silicon sensors.

3.4.3 Transition Radiation Tracker

The Transition Radiation Tracker is the outermost sub-detector in the ID volume. It is a straw tube detector, which covers radially the distance between 563 and 1066 mm and $|\eta| < 2$. It consists of straw tubes made of kapton with a diameter of 4 mm. The inner surface of each straw is coated with aluminium set at a 1.5 kV potential and serves as a cathode. In the middle of each tube, there is a gold-plated tungsten wire with a diameter of 31 μm set at a ground potential serving as an anode. The straw tubes in the barrel region have a length of around 1.5 m and are organised in parallel to the beam axis. In the endcap region, 0.4 m long straw tubes are placed perpendicularly to the beam axis. The tubes are filled with a gas mixture of 70% Xe + 27% CO_2 + 3% O_2. The particle detection is based on ionisation of the gas atoms and each straw tube with a wire inside works like a proportional counter. The TRT typically provides over 30 hit measurements per track and measures the tracks with a resolution of 130 μm.

Apart from the detection of ionising particles, the TRT plays an important role in electron identification thanks to transition radiation detection. When a particle passes through a material made of two media with different dielectric or magnetic properties it produces photons highly collimated along its

trajectory. In order to allow the production of transition radiation inside the TRT volume, special radiators are placed in between the straw tubes. In the barrel they are in the form of thin fibres and in the endcap in the form of thin foils. The amount of the transition radiation produced is proportional to the relativistic factor γ which is important in particle identification. When a particle traversing the detector produces transition radiation, the TRT front-end electronics detect two signals passing different thresholds, one expected for a minimum ionising particle and another, much higher signal, expected for X-rays from the transition radiation. The main gas in the TRT gas mixture, xenon, is good for such purposes due to its short absorption length. Due to many gas leaks, which started already in Run 1, the TRT in Run 2 was partially operated with an Argon-based gas mixture to reduce the costs.

3.5 Calorimeter system

Precision measurement of photons, electrons, hadrons, as well as missing transverse energy is provided by the calorimeter system. It consists of liquid argon (LAr) detectors and scintillator tiles (Tile calorimeter), which form two electromagnetic components, three hadronic components and the Forward Calorimeter (FCal). The full system covering the $|\eta|$ range up to 4.9 is presented in Figure 3.9. Both the LAr and Tile are sampling calorimeters, which means that both consist of alternating layers of absorber, where the showers develop, and active medium, where the signal is recorded.

3.5.1 Liquid Argon calorimeters

All calorimeters with liquid argon as an active medium are placed within three separate cryostats to keep the argon in the liquid phase: one holding the electromagnetic barrel calorimeter and one for each endcap, holding the electromagnetic and hadronic endcap calorimeters (Electromagnetic Endcap Calorimeter (EMEC), Hadronic Endcap Calorimeter (HEC)), as well as the FCal.

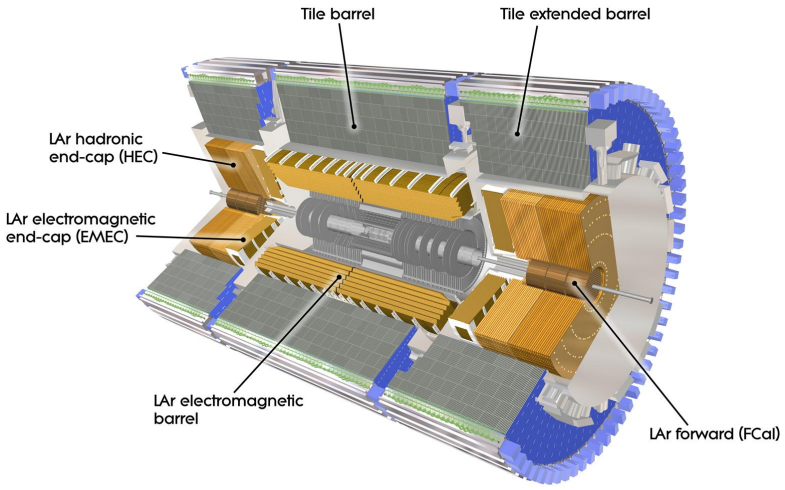

Figure 3.9: ATLAS calorimeter system [38].

The LAr electromagnetic calorimeter consists of two half-barrels with a 4 mm gap between them covering a range of $|\eta| < 1.475$, and two wheels per each endcap, covering a range of $1.375 < |\eta| < 3.2$. Its modules with lead absorbers have an accordion shape as presented in Figure 3.10, which provides full coverage in the ϕ direction and improves the readout time. The barrel modules comprise three layers which differ in granularity, with the first one being the most finely segmented in the η direction to provide good electron and photon identification. The second and third layers with lower granularity contain almost the whole developed shower and limit leakage of the shower to the next sub-detectors. The thickness of the barrel part varies between 22 and 30 radiation lengths (X_0) for $|\eta| < 0.8$ and between 24 and 33 X_0 for $0.8 < |\eta| < 1.3$. The thickness of the EMEC varies between 24 and 38 X_0 in the $|\eta|$ region between 1.475 and 2.5, and between 26 and 36 X_0 for $2.5 < |\eta| < 3.2$. In front of the EM calorimeter in the region $|\eta| < 1.8$ there is an additional instrumented layer of liquid argon, a pre-sampler, which provides measurement of the energy lost by photons and electrons upstream of the main calorimeter.

The LAr hadronic calorimeter occupies the range of $1.5 < |\eta| < 3.2$ and consists of two wheels in each endcap with an outer radius of 2.03 m, the front and rear wheel. Both wheels consist of 32 trapezoidal modules placed

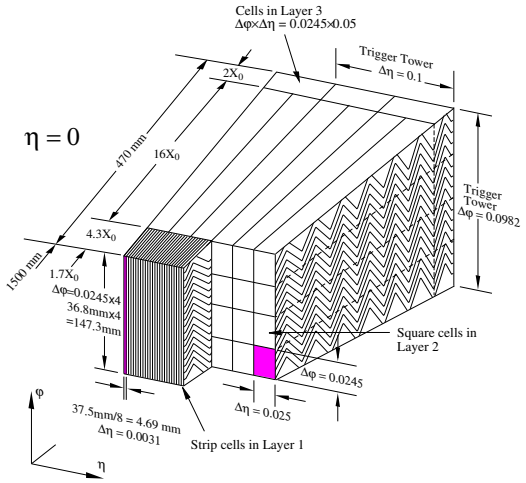

Figure 3.10: A schematic view of the barrel module of the liquid argon electromagnetic calorimeter [38].

radially, which differ between the wheels in thickness and the number of copper absorber plates (24 25 mm-thick plates in the front wheel and 16 50 mm-thick plates in the rear wheel) and hence differ in the sampling fractions. The total thickness of the HEC corresponds to 10λ.

The LAr Forward Calorimeter is placed 5 m away from the IP and covers the very forward region of $3.1 < |\eta| < 4.9$. It consists of three layers with the first one (closest to the IP), FCal1, dedicated to electromagnetic calorimetry and the latter two, FCal2 and FCal3, responsible for hadronic calorimetry. FCal1 uses copper as the absorber whereas FCal2 and FCal3 use tungsten. Each module consists of a set of cylindrical electrodes placed parallel to the beam axis with the anode in the form of a rod and a tube as the cathode with a very small gap between them filled with liquid argon. The total thickness of the three layers amounts to 10 interaction lengths.

3.5.2 Tile calorimeter

The Tile calorimeter is a sampling detector with steel as the absorber and scintillating tiles as the active medium. It consists of two main parts: the central barrel covering $|\eta| < 1.0$ and the extended barrels occupying a range of $0.8 < |\eta| < 1.7$. They are divided into three layers differing in thickness,

which correspond to 1.5, 4.1 and 1.8 λ (1.5, 2.6, 3.3 λ) in the central (extended) barrel giving a total thickness of 7.4 interaction lengths. The barrels are segmented azimuthally into 64 wedge-shaped modules. A schematic view of a Tile calorimeter module is presented in Figure 3.11. Each side of the scintillating tile is read out by one photomultiplier (PMT) and signals from both sides of the same tile form a cell.

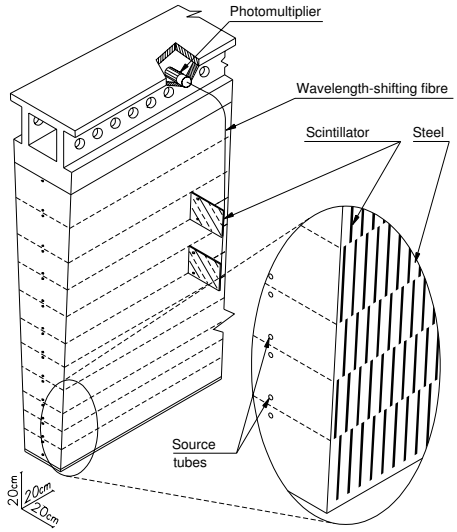

Figure 3.11: A schematic view of one module from the Tile calorimeter [38].

3.6 Muon detector

The Muon Spectrometer (MS) forms the outermost part of the ATLAS detector and provides a precise measurement of the momentum and trajectory of muons, which are the only particles not absorbed by the calorimeters apart from undetectable neutrinos. It contains chambers for precision measurements and for triggering. Trajectories of muons traversing the detector are bent using three toroidal magnet systems. In the barrel region ($|\eta| < 1.4$) the magnetic field is produced by a large barrel toroid with the bending power on average of $\int Bdl = 2.5$ Tm. In the range of $1.6 < |\eta| < 2.7$ the magnetic field is provided by the endcap toroids and the bending power is up to 6 Tm. In the transition region ($1.4 < |\eta| < 1.6$), the resulting magnetic field is a combination of the fields provided by the barrel and endcap magnets and is characterised by a lower value of $\int Bdl$. Each toroidal magnet consists of eight coils placed sym-

metrically and radially around the beam pipe. In the barrel region each coil is housed in its own cryostat, whereas the endcap coils are located in one large cryostat per side. The layout of the magnet system is presented in Figure 3.12.

Precision measurement of muon momenta is provided by two types of chambers, Monitored Drift Tubes (MDT) and Cathode Strip Chambers (CSC). MDT are gaseous chambers, which consist of drift tubes filled with $Ar/CO_2/H_2O$ gas serving as cathodes, and tungsten-rhenium wires as anodes. They are organised in three layers in the barrel and each endcap, and cover the pseudorapidity range of $|\eta| < 2.7$. The inner endcap layer in the range of $|\eta| > 2$ is covered by a quadruplet of CSC which perform well in the higher radiation environment. The CSC are multiwire proportional chambers filled with an Ar/CO_2 gas mixture with radially oriented wires and segmented strip cathodes. A separate muon trigger system is formed using the Resistive Plate Chambers (RPC) and Thin Gap Chambers (TGC). RPC are electrode-plate detectors made of two parallel plastic laminate plates separated by insulating spacers and filled with $C_2H_2F_4/\mathrm{Iso} - C_4H_{10}/SF_6$ gas. They are organised in three doublet layers in the barrel region ($|\eta| < 1.05$). The endcap region is covered by the TGC forming one triplet layer followed by two doublet layers in pseudorapidity range of $1.0 < |\eta| < 2.4$. TGC, similarly to CSC, are multiwire proportional chambers, however the wire-to-cathode distance is smaller than the distance between the wires and they are filled with a gas mixture of $CO_2/\mathrm{n} - \mathrm{pentane}$.

A schematic view of the muon spectrometer layout presenting the location of the muon chambers is shown in Figure 3.13 and the position and time resolutions for each chamber type are presented in Table 3.1.

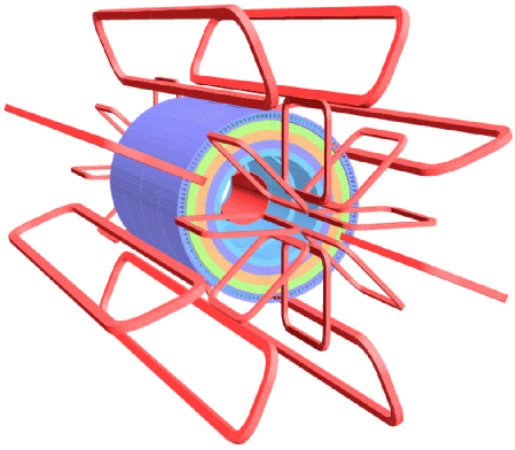

Figure 3.12: Layout of the ATLAS magnets [38]. The toroid windings are shown in red. The coloured structure represents the Tile calorimeter steel.

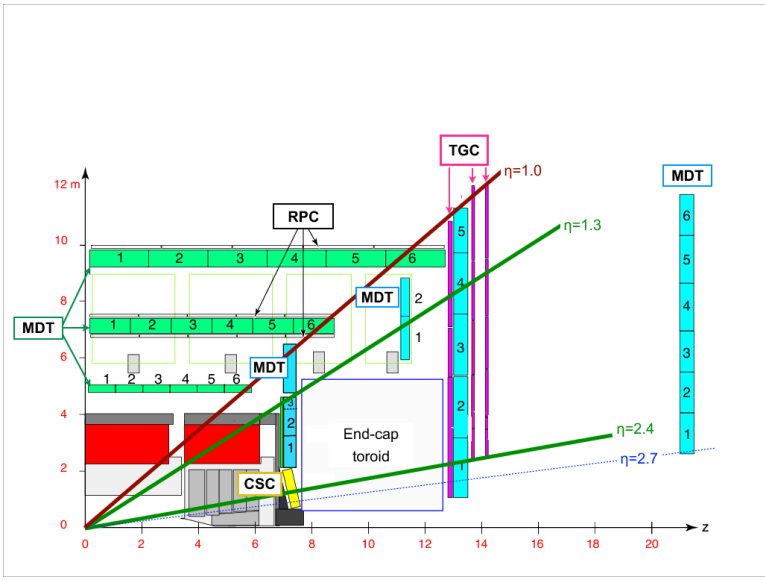

Figure 3.13: A schematic view of one quadrant of the muon system [38].

Chamber type	Position resolution		Time resolution
	R/z	ϕ	
MDT	35 μm (z)	-	-
CSC	40 μm (R)	5 mm	7 ns
RPC	10 mm (z)	10 mm	1.5 ns
TGC	2–6 mm (R)	3–7 mm	4 ns

Table 3.1: Position and time resolutions for each type of muon chambers.

3.7 Forward detectors

There are four systems placed in the forward region on each side of the ATLAS detector. They are dedicated to the luminosity measurement or studies of proton elastic scattering.

The LUCID-2 [42] consists of two symmetric systems located 17 m away from the interaction point on opposite sides of the ATLAS detector. It is a system dedicated to measurement and monitoring of the luminosity. Each side consists of 16 PMTs organised in four groups and using quartz windows as Cherenkov medium. Additionally, there are four quartz fibre bundles also acting as Cherenkov media, which are read out by four PMTs located 1.5 m away in a lower radiation region. The luminosity measurement is performed using two algorithms implemented in the custom-made electronics.

The Zero Degree Calorimeter (ZDC) [43] is located at ± 140 m from the interaction point at almost zero degrees to the beam pipe. The ZDC is mostly used during heavy-ion collisions to detect neutral particles in the very forward region. Each side consists of one electromagnetic (29 X_0) and three hadronic (1.14 λ) calorimeters located inside the neutral beam absorber. The modules are sampling calorimeters with tungsten plates as absorbers and layers of quartz strips to produce Cherenkov radiation read out by PMTs.

The ATLAS Forward Proton (AFP) [44] and Absolute Luminosity For ATLAS (ALFA) detectors [45] are in the forward region and focus on the measurement of the elastic proton scattering at very small angles. They are located at ± 210 and ± 240 m, respectively. Both detectors are built using Roman Pot technology, which means that they are kept in their own vacuum space with the possibility to move them closer to or farther away from the beam. Each AFP system consists of two stations, near and far, kept in separate vacuum spaces. In the near station there are four modules of silicon pixels tilted at 14° for the trajectory measurement. In the far section, there are again the same four modules of silicon pixels, but followed by the Time of Flight detector.

Each system of the ALFA detector has two pairs of Roman Pots, one above and one below the beam. It is divided into two parts, the main detector and the overlap detector. The main detector consists of 20 layers of scintillating fibres organised in two planes, whereas the overlap detector consists of three layers of the same scintillating fibres but arranged in a different plane. The detector read out is performed using PMTs. Data-taking for measurement of the total cross-section for proton elastic scattering using ALFA is done during runs with special beam optics and very low pile-up.

The location of the forward detectors with respect to the main ATLAS detector is presented in Figure 3.14.

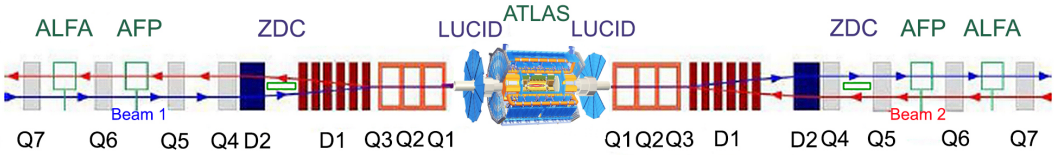

Figure 3.14: Location of the ATLAS forward detectors [46].

3.8 Trigger system

The large interaction rates in the ATLAS detector require an efficient system to select interesting events already during the data taking by requiring certain trigger conditions. The ATLAS trigger [47] is a two-level system consisting of a hardware Level 1 (L1) followed by a software-based High Level Trigger (HLT). The L1 decision whether to keep an event for further processing is formed by the Central Trigger Processor (CTP) which combines the information delivered by the L1Muon, L1Calo and L1Topo subsystems. L1Calo and L1Muon use data from calorimeters and muon trigger detectors respectively to build trigger objects with approximately measured energy and $\eta - \phi$ location. The information can be further extended by the L1Topo processor providing multi-object topological variables such as invariant mass or angular separation. The hardware trigger stage reduces the event rate from around 40 MHz to at most 100 kHz with a latency of 2 μs. Its decision is sent to the Read-Out Drivers

(ROD) which format and buffer the data close to the detectors. Upon negative decision, the data are discarded and upon a positive one, the full event data are sent to the Read-Out System (ROS), which further buffers them until the HLT decision is made. HLT processing is based on Regions of Interest (RoI) – $\eta - \phi$ regions around each object passing the L1 trigger selection. Fast event reconstruction is performed on a dedicated computing farm with software algorithms similar to those used in offline reconstruction, however, using only partial event data received from the ROS and corresponding to the RoI. The event rate is further reduced at this stage to around 1 kHz and the selected events are stored for offline analysis with a bandwidth of around 1 GB/s. Figure 3.15 presents the data flow in the ATLAS trigger and data acquisition system.

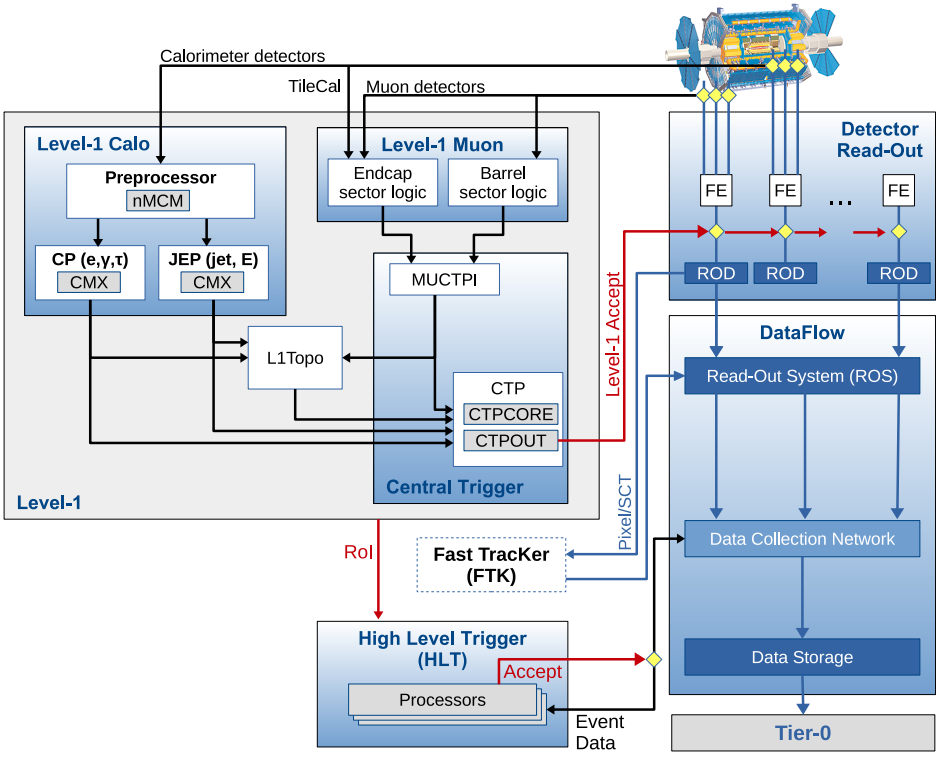

Figure 3.15: A diagram presenting the data flow in the ATLAS trigger and data acquisition system [48].

Chapter 4

Radiation damage in ATLAS Semiconductor Tracker

Silicon semiconductor detectors are characterised by very good spatial resolutions of around 10 μm, excellent time resolutions of the order of 10 ns, high density, enabling building very thin sensors (the typical width of a silicon sensor is around 300 μm) and good tolerance to radiation doses. Thanks to these characteristics, silicon detectors are widely used in high energy physics experiments to measure charged particle trajectories to reconstruct their momenta, to reconstruct primary and secondary vertices with a high resolution and to identify photon conversion vertices. In ATLAS there are two tracking detectors with silicon sensors: the Pixel detector and the SCT. This chapter focuses on the ATLAS SCT detector (the general description of the SCT detector is provided in Subsection 3.4.2) and in particular the effects of the radiation damage in its silicon sensors observed during and after its operation in Run 2.

4.1 Principles of semiconductor detectors

Resistivity is an important property of materials used in electric circuits as it describes how the material allows or resists electric current flow. It is given in the units of Ωm. According to its value (or according to conductivity which is the inverse of the resistivity) one can classify materials into three groups: insulators, conductors (also referred to as metals) and semiconductors, as presented in Figure 4.1. Similar distinctions can be made based on band theory. According to the band theory, there are some energies in an atom that electrons are

allowed or forbidden to take. In a single isolated atom, electrons can occupy only discrete levels of energy called orbitals. In a solid material consisting of many atoms ($> 10^{20}$) the number of orbitals is so large that the differences in the energy between these energy levels is very small and therefore they are characterised by continuous energy bands rather than discrete energy levels. The energy bands are filled by electrons starting from the lowest energies. The valence band is the last fully or partially filled band. The band above that is the conduction band, which is important for the conduction process in a material. In between the valence and the conduction band there is a band gap, i.e. energy region in which electrons are not allowed. This is graphically presented for different types of materials in Figure 4.2.

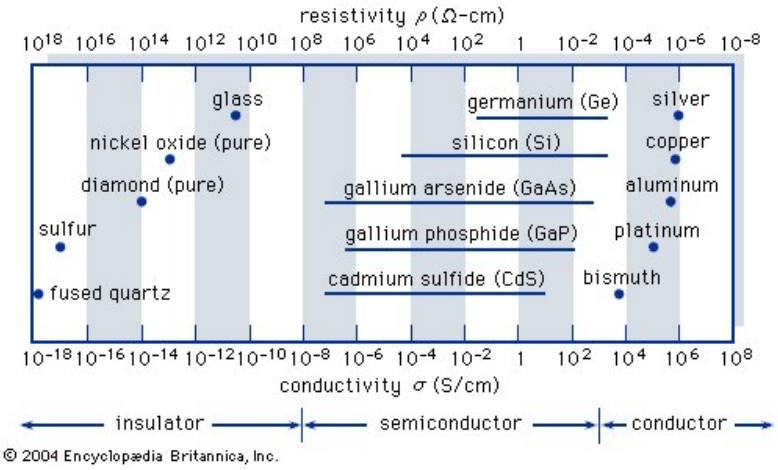

Figure 4.1: Classification of materials according to resistivity and conductivity [49].

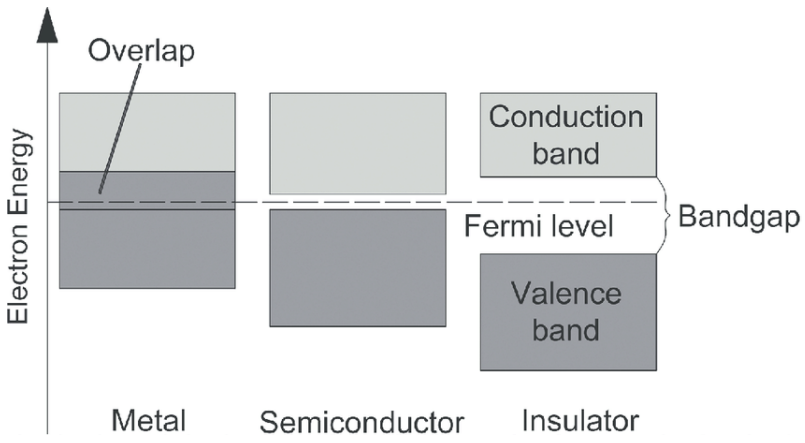

Figure 4.2: Band diagrams corresponding to different types of materials [50].

Insulators are materials with very low or zero number of free electrons leading to no current flow even when a high electrical voltage is applied. They are characterised by high resistivity of an order of millions of Ωm and large band gaps. Example insulators are fused quartz, PVC plastics or rubber.

Conductors are characterised by a high number of free electrons which means they let current flow very easily. The resistivity of conductors is typically of the order of $\mu\Omega$m. The valence bands and conduction bands overlap. Materials like copper and aluminium are very good conductors and therefore are widely used in electric cables.

The resistivity range between insulators and conductors is occupied by materials classified as semiconductors as their properties make them neither good insulators nor good conductors. In semiconductor materials, the valence and conduction bands do not overlap, however, the band gap is small and the thermal excitation of an electron could move it to the conduction band.

Silicon is the most widely used semiconductor material in electronic circuits. It has four electrons in its valence orbit which form covalent bonds with neighbouring atoms. This leaves pure silicon without any free electrons. A schematic view of the crystal lattice of pure (intrinsic) silicon is presented in Figure 4.3. For silicon the band gap is $E_g = 1.12$ eV. The intrinsic silicon acts more like an insulator due to the lack of free electrons. However, it is possible to change its properties to improve conductivity by adding impurities to the silicon lattice in a process called doping. This means that some silicon atoms in the lattice are exchanged with atoms of elements from different groups in the periodic table. Depending on which group atom is added, there are two types of extrinsic semiconductors (semiconductors with added impurities): n-type and p-type.

Silicon of n-type is created when a fraction of silicon atoms is replaced by atoms with five outer electrons. Atoms that satisfy these requirements and can be used to create n-type silicon are phosphorus, arsenic or antimony. An example silicon crystal lattice with impurities added in the form of phosphorus atoms is

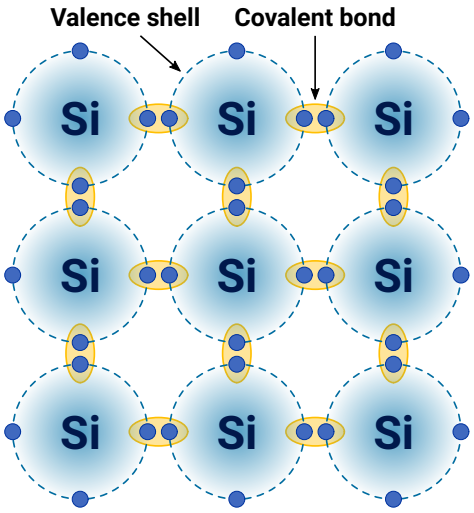

Figure 4.3: A schematic view of the crystal lattice of pure silicon. Only valence bands are presented for simplicity.

shown in Figure 4.4a. As presented four electrons in phosphorus valence orbit form covalent bonds with neighbouring silicon atoms leaving one free electron. A dopant atom that when added to the silicon lattice forms an n-type material is called a donor.

Silicon of p-type is formed when atoms with three outer electrons are added to the silicon lattice. Example dopants in this case are gallium or boron as presented in Figure 4.4b. The three valence electrons of the boron atom form covalent bonds with silicon atoms leaving a hole in the lattice which effectively is a positive charge. A dopant atom that when added to the silicon lattice forms a p-type material is called an acceptor.

In the ATLAS SCT sensors, p-type strips are implanted in a high-resistivity n-type bulk material.

4.1.1 The p-n junction

When p-type and n-type semiconductors are fused together they form a p-n junction. At first electrons from the n-type silicon or holes from the p-type silicon diffuse across the junction forming a net charge in a previously charge-neutral material. The net charge on both sides leads to electric field build

up to the point when an equilibrium is reached and no net charge movement occurs. In the region near the interface of the two silicon blocks as a result of the electric field, there are no mobile charges. This region is called the depletion region or space-charge region. A schematic view of the p-n junction along with graphs of the charge density, electric field and voltage across the depletion region is presented in Figure 4.5. The width of the depletion region differs in the two semiconductors as a result of different doping concentrations.

4.1.2 Width of the depletion region

A few assumptions are needed in order to calculate the width of the depletion region:

- the non-zero electric field is present only within the depletion region,
- there are no free charge carriers in the depletion region,
- the junction is abrupt,
- all dopants are ionised.

As known from Gauss's law, the relation between an electric field $\vec{E}$ and electric charge density can be written in differential form as:

$$\nabla \cdot \vec{E} = \frac{\rho}{\epsilon}, \tag{4.1}$$

where ρ is the charge density and $\epsilon = \epsilon_0 \epsilon_s$ with ϵ_0 being the vacuum permittivity and ϵ_s being the relative permittivity of the material. In one dimension, this formula can be written as:

$$\frac{dE}{dx} = \frac{\rho}{\epsilon}, \tag{4.2}$$

which can be rearranged to find E:

$$E = \int dE = \int \frac{\rho}{\epsilon} dx. \tag{4.3}$$

The charge density on each side of the junction can be expressed in terms of dopant concentrations N_A (acceptors) and N_D (donors) as:

$$\rho = \begin{cases} -qN_A & \text{for } -x_p \leq x \leq 0 \\ qN_D & \text{for } 0 \leq x \leq x_n \end{cases}. \tag{4.4}$$

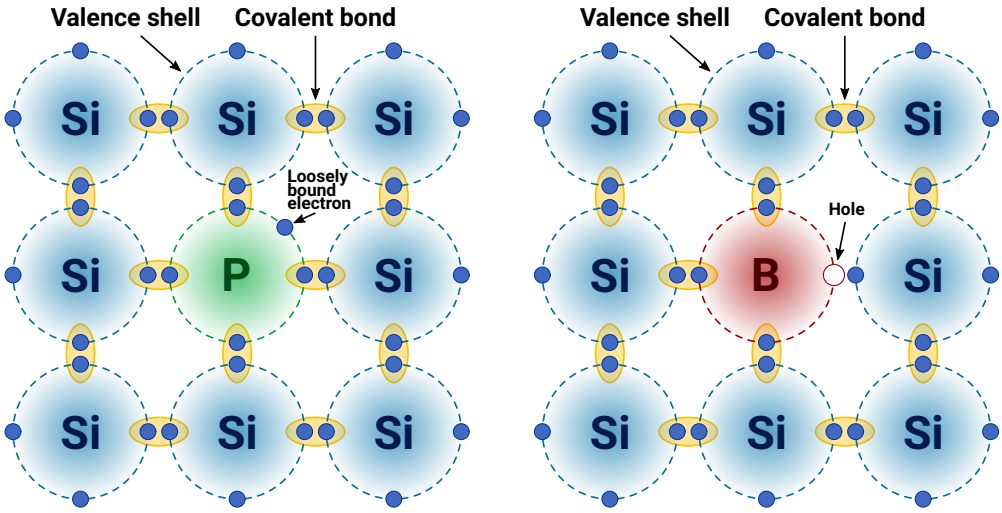

(a) n-type (b) p-type

Figure 4.4: A schematic view of the silicon crystal lattice after adding impurities of type indicated in sub-figure captions. Only valence bands are presented for simplicity.

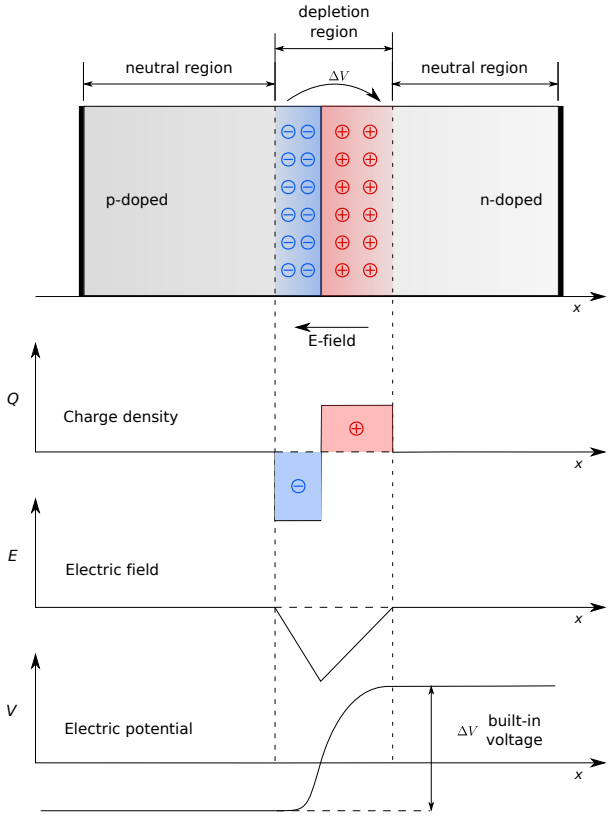

Figure 4.5: Schematic view of a p-n junction as well as distributions of the charge density, electric field and electric potential along the depletion region [51].

Taking into account the assumption that the electric field should equal zero at the boundaries of the depletion region, the formula for the electric field can be written as:

$$E = \begin{cases} -\frac{qN_A}{\epsilon}x - \frac{qN_A}{\epsilon}x_p & \text{for } -x_p \leq x \leq 0 \\ \frac{qN_D}{\epsilon}x - \frac{qN_D}{\epsilon}x_n & \text{for } 0 \leq x \leq x_n \end{cases}. \tag{4.5}$$

The electric field and voltage are related by:

$$E = -\nabla V = -\frac{dV}{dx}, \tag{4.6}$$

hence the voltage can be expressed as:

$$V = \begin{cases} \frac{qN_A}{2\epsilon}(x + x_p)^2 & \text{for } -x_p \leq x \leq 0 \\ \frac{qN_D}{\epsilon}\left(x_n - \frac{x}{2}\right)x + \frac{qN_A}{2\epsilon}x_p^2 & \text{for } 0 \leq x \leq x_n \end{cases}. \tag{4.7}$$

Here, the assumption is made that $V_p(x = 0) = V_n(x = 0)$ and since we are only interested in the voltage difference $V_p(x = -x_p)$ can be arbitrarily set to 0. The maximum voltage is at $x = x_n$. It can be written as:

$$V_{\max} = V_n(x = x_n) = \frac{q}{2\epsilon}\left(N_D x_n^2 + N_A x_p^2\right) \tag{4.8}$$

and it is typically called the built-in voltage, denoted by V_{bi}. Equation 4.8 can be further manipulated using the relation

$$N_D x_n = N_A x_p, \tag{4.9}$$

and x_p and x_n are found to be:

$$x_p = \left(\frac{2\epsilon V_{\text{bi}}}{q}\frac{N_D}{N_A(N_A + N_D)}\right)^{1/2}, \tag{4.10}$$

$$x_n = \left(\frac{2\epsilon V_{\text{bi}}}{q}\frac{N_A}{N_D(N_A + N_D)}\right)^{1/2}. \tag{4.11}$$

The total width of the depletion region is the sum of x_p and x_n and after manipulation can be written as:

$$W = \sqrt{\frac{2\epsilon V_{\text{bi}}}{q}\left(\frac{1}{N_A} + \frac{1}{N_D}\right)}. \tag{4.12}$$

4.1.3 Forward and reverse biasing of the p-n junction

In an unbiased p-n junction, the built-in potential prevents the majority carriers moving to the other side of the junction. By applying an external biasing voltage, one can reduce or enlarge the potential difference to enable or prevent even more majority charge migration. A voltage source can be connected to the p-n junction in two ways. If the positive terminal of the voltage source is connected to the p-type region and negative terminal to the n-type region the junction is forward biased. In the opposite case the junction is reverse biased. This connection affects significantly the depletion region.

In case of the forward bias connection, the external electric field is in the opposite direction to the built-in electric field and hence decreases the barrier that the majority carriers must overcome to get to the other side of the junction. This leads to a decrease of the depletion region width as the electrons from the n-type region are attracted towards the positive terminal of the voltage source and holes from the p-type region are attracted to the negative terminal of the battery. As a result a current will flow across the junction.

On the other hand, if the external electric field is in the same direction as the built-in electric field then the potential difference in the junction increases. The majority carriers are then pushed away from the depletion region effectively leading to its increase. In each region, however, a number of thermally generated minority charge carriers is present (in the n-type region these are holes and in the p-type region these are electrons). These minority charge carriers can easily cross the depletion region (polarity of the reverse bias potential does not oppose movement of the holes from n-type region and electrons from p-type region) giving rise to a small current called the saturation current I_s.

Silicon sensors are typically operated with a reverse bias voltage. This ensures a large depletion region leading to a higher number of charge-carrier pairs being produced and therefore a higher signal. It also provides a high electric field across the depletion region which is important as it ensures that the electron-

hole pairs created along the path of incident particles are separated before they can recombine.

4.1.4 Effective doping concentration and full depletion voltage

If an external reverse-bias voltage is applied to the p-n junction, the total width of the depletion region can be expressed as:

$$W = \sqrt{\frac{2\epsilon V}{q}\left(\frac{1}{N_A} + \frac{1}{N_D}\right)}, \tag{4.13}$$

where $V = V_{\text{bi}} + V_{\text{ext}}$. If one side of the junction is heavily doped and one side is lightly doped, taking into account the relation from Equation 4.9, the depletion region extends mostly in the lightly depleted region. In the SCT sensors the p-type strips are heavily doped (which is denoted by p^+) leading to essentially the whole depletion region extending in the n-type bulk. The width of the depletion region for the p^+-n junction can be written as:

$$W = \sqrt{\frac{2\epsilon}{qN_D}V}. \tag{4.14}$$

It is impossible to produce either n-type silicon with only donor atoms or p-type silicon with only acceptor atoms. Impurities are always present, although for n-type silicon $N_D >> N_A$ and for p-type $N_A >> N_D$. In this case, the width of the depletion region presented in Equation 4.14 can be expressed in terms of an effective doping concentration, defined for n-type bulk as:

$$N_{\text{eff}} = N_D - N_A. \tag{4.15}$$

The width can therefore be written as:

$$W = \sqrt{\frac{2\epsilon}{q\,|N_{\text{eff}}|}V}. \tag{4.16}$$

If the depletion region extends across the whole bulk material ($W = d$, where d is the maximum thickness of the junction) then the sensor is fully depleted and the corresponding full depletion voltage can be expressed as:

$$V_{\mathrm{FD}} = \frac{qd^2}{2\epsilon} \left| N_{\mathrm{eff}} \right| . \tag{4.17}$$

The initial values of the full depletion voltage are 64.8±9.5 V and 84.5±19.7 V for the SCT sensors manufactured by Hamamatsu and CiS, respectively [52].

4.1.5 Leakage current

As already discussed, if the p-n junction is reverse biased there is a small current flowing through the depletion region caused by the migration of minority charge carriers. This saturation current is a leakage current. The transfer of minority carriers is, however, not the only mechanism that contributes to the overall leakage current in the silicon detector and in fact, this contribution is very small. High electric fields close to the edge of the depletion region or surface impurities (related to, for example, humidity or fabrication processes) lead to a surface current. This contribution is not easy to quantify, however, it is not expected to be significant. The major contribution to the overall leakage current is related to thermal generation of charge carrier pairs in the depletion region giving rise to a generation current I_{g}. The generation current is a result of the presence of deep impurity levels in the band gap (generation centres) which increase the probability of thermal excitations of electrons in the valence band. The generation current at a constant temperature depends on the depletion region width and therefore on the applied voltage:

$$I_{\mathrm{g}} \propto W \propto \sqrt{V} \tag{4.18}$$

up to the point where the sensor is fully depleted and I_{g} reaches a plateau. It also depends on a charge carrier life time τ_{g}:

$$I_{\mathrm{g}} \propto \frac{1}{\tau_{\mathrm{g}}}, \tag{4.19}$$

which is inversely proportional to the density of generation centres, making the generation current proportional to the generation centre density. The value of I_g strongly depends on the temperature, hence it is important to cool the device to limit the increase of leakage current. The cooling system for the SCT detector (and Pixel detector) is discussed in Subsection 3.4.2.

4.2 Radiation damage

The *pp* collisions at the centre of the ATLAS detector produce thousands of energetic particles in each bunch crossing that interact further with the beam pipe, services and detectors to produce even more secondary particles. The location of the silicon detectors close to the IP means they have to operate in severe conditions. Understanding and correct modelling of radiation-inducted effects is essential to ensure good performance of the detector during data taking.

Radiation-induced effects can be classified as surface and bulk damage. The surface damage is expected to be less important for the operation of the SCT detector and therefore is not covered here. More information about surface defects in silicon detectors can be found in Ref. [53].

Bulk damage is related to changes in the silicon lattice due to the interactions of the incident particles with silicon atom nuclei, referred to as Non-Ionising Energy Loss (NIEL). A displacement of the silicon atom from a lattice is possible only if a sufficient energy is transmitted. Typically, an energy of at least 25 eV is required and such a dislocated atom is called a Primary Knock-on Atom (PKA). An empty site in a lattice is called a vacancy, whereas an atom out of a lattice site is called an interstitial and these two form a Frenkel pair. An interstitial and a vacancy can recombine leading to no observed damage. It is also possible that the PKA leads to the displacement of other atoms in a small area of the silicon lattice if its energy is sufficient. Such regions with many displaced atoms are referred to as clusters.

Typically, the radiation damage caused by charged and neutral particles of different energy is expressed in terms of 1 MeV neutron equivalent fluence Φ, given in the units of cm^{-2} for easier comparison. A conversion of delivered pp luminosity to Φ requires a conversion factor which can be obtained by propagating inelastic pp interactions generated with PYTHIA8 [54] with the MSTW2008LO parton distribution function (PDF) set [55] and the A3 set of tune parameters [56] through the ATLAS detector material using the particle transport code FLUKA [57, 58]. A simulation of the fluence in one quadrant of the ATLAS ID corresponding to 1 fb^{-1} of pp collisions at 13 TeV is presented in Figure 4.6.

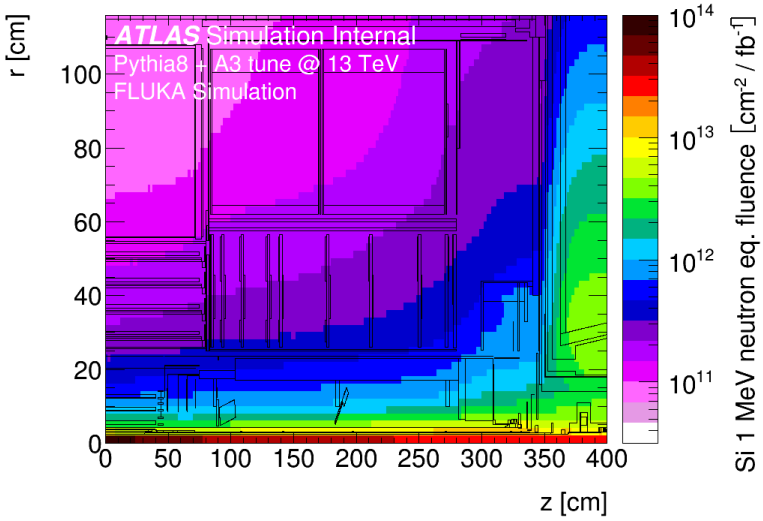

Figure 4.6: 1 MeV n-eq fluence normalised to $1\mathrm{fb}^{-1}$ in one quadrant of the ATLAS ID. The fluence is obtained with the FLUKA simulation for pp collisions at $\sqrt{s} =$ 13 TeV [59].

The bulk damage has three main implications: increase of the leakage current; changes in the effective doping concentration; and charge trapping, which are described in more detail below.

4.2.1 Increase of the leakage current

Generation centres that are produced in the band gap due to irradiation of silicon lead to an increase of the leakage current as they increase the probability

of thermal excitation of valence electrons to the conduction band. The increase of the leakage current ΔI in a depleted volume v is proportional to the fluence:

$$\frac{\Delta I}{v} = \alpha\Phi \tag{4.20}$$

with the factor α being the current-related radiation damage rate. After the irradiation is finished, the radiation-induced current decreases, which is known as a leakage current annealing. The annealing behaviour is parameterised differently in the two models discussed in this chapter, hence it is described separately in Section 4.3.

4.2.2 Changes in the effective doping concentration

Exposure to high fluences significantly affects the effective doping concentration and therefore the full depletion voltage. At first following the irradiation of n-type silicon sensors the effective doping concentration decreases. This is due to the removal of donors leading to a decrease of N_D, and the creation of acceptor defects, leading to an increase of the N_A term in Equation 4.15. This process continues and at a point where the concentration of donors and acceptors is the same, $N_{\text{eff}} = 0$. The sensor acts then as if it is intrinsic. The number of p-type defects as well as a donor removal, however, still progresses which means that N_A term starts to dominate and the bulk material becomes effectively p-type. The depletion from now onwards grows from the backplane side. The point corresponding to $N_D = N_A$ is referred to as the type inversion point.

The evolution of the effective doping concentration described above is related to three mechanisms that take place during irradiation. The change in N_{eff} can be expressed as:

$$\Delta N_{\text{eff}}\left(\Phi, t(T)\right) = N_a\left(\Phi, t(T)\right) + N_c\left(\Phi\right) + N_y\left(\Phi, t(T)\right). \tag{4.21}$$

The $N_a\left(\Phi, t(T)\right)$ term represents the short-term annealing which leads to a decrease of effective doping concentration in type-inverted silicon. As it decreases the full depletion voltage, this type of annealing is also referred to as

beneficial annealing. The stable damage denoted by $N_c(\Phi)$ depends only on the fluence and therefore is constant with time. The $N_y(\Phi, t(T))$ term describes anti-annealing or reverse annealing which leads to an increase of the effective doping concentration in a type-inverted material.

4.2.3 Charge trapping

The radiation-induced defects present in the silicon lattice not only change the effective doping concentration and increase the leakage current, but also act as traps for charges drifting to electrodes, decreasing the overall signal height. This can be mitigated by providing a higher reverse bias voltage to the sensors (overdepleting the sensors), assuming that there is enough margin for the HV changes. The electric field across the depletion zone is then high enough to sweep drifting charges towards electrodes before they are trapped.

4.3 Radiation damage models of leakage current

Radiation damage in silicon sensors is still not well understood. It is, however, necessary to determine how best to operate the detector. Two phenomenological models can be used to track and predict evolution of the leakage current, the Sheffield model [60] and the Hamburg model [61]. Both models are used to study the leakage current in the SCT sensors and their more detailed description is provided below.

4.3.1 The Sheffield Model

The annealing of the leakage current after a short-term irradiation can be parameterised by a set of exponential functions:

$$g(t) = \sum_{k}^{n} A_k \exp\left(\frac{-t}{\tau_k}\right), \tag{4.22}$$

where the sum of all amplitudes A_k equals 1 and τ_k are time constants corresponding to different defects. This formula, however, does not consider the

fact that the annealing starts already during irradiation. To account for this effect, the annealing parameterisation is modified as follows:

$$g(t_{\mathrm{ir}}, t') = \sum_{k}^{n} A_k \frac{\tau_k}{t_{\mathrm{ir}}} \left[1 - \exp\left(-\frac{t_{\mathrm{ir}}}{\tau_k}\right)\right] \exp\left(-\frac{t'}{\tau_k}\right), \tag{4.23}$$

where t_{ir} is the irradiation time and t' is the annealing time. To introduce the temperature dependence of the leakage current, the time axis is scaled using the Arrhenius formula:

$$\Theta_A\left(T\right) = \exp\left[-\frac{E_I}{k_B}\left(\frac{1}{T} - \frac{1}{T_{\mathrm{ref}}}\right)\right], \tag{4.24}$$

where $E_I = (1.09 \pm 0.14)$ eV [62] is the activation energy, k_B is the Boltzmann constant and T_{ref} is the reference temperature of 293.15 K. Including the Arrhenius relation the annealing term can be written as:

$$g_{n,i}\left(t\right) = \sum_{k=1}^{5} \left\{ A_k \frac{\tau_k}{\Theta_A(T_i)t_i} \left[1 - \exp\left(\frac{-\Theta_A(T_i)t_i}{\tau_k}\right)\right] \exp\left(-\frac{1}{\tau_k} \sum_{j=i+1}^{n} \Theta_A(T_j)t_j\right)\right\} \tag{4.25}$$

and the leakage current in a depleted volume can be expressed as:

$$\frac{I_n}{v} = \alpha \sum_{i=1}^{n} g_{n,i} \delta\Phi_i, \tag{4.26}$$

with $\alpha = (7.00 \pm 0.20) \cdot 10^{-18}$ A/cm, which is the recalculated value of the current-related damage constant given in Ref. [60] at -7°C due to the increase of the temperature-dependent band gap to $E_g = 1.21$ eV [63]. The sum is over contributions to the overall leakage current from different irradiation periods. The values of time constants and amplitudes used to model the annealing behaviour of the leakage current are presented in Table 4.1.

4.3.2 The Hamburg Model

In the Hamburg model, the short-term annealing is also parameterised by an exponential function. To additionally include the effects of long-term annealing, found to follow a logarithmic function, the current-related damage constant from Equation 4.20 is expressed as:

$$\alpha(t) = \alpha_I \exp\left(\frac{-t}{\tau_I}\right) + \alpha_0^* - \beta \ln(\frac{\Theta_A(T)t}{t_0}), \tag{4.27}$$

k	τ_k [min]	A_k
1	$(1.2 \pm 0.2) \cdot 10^6$	0.42 ± 0.11
2	$(4.1 \pm 0.6) \cdot 10^4$	0.10 ± 0.01
3	$(3.7 \pm 0.3) \cdot 10^3$	0.23 ± 0.02
4	124 ± 25	0.21 ± 0.02
5	8 ± 5	0.04 ± 0.03

Table 4.1: Values of the time constants τ_k and amplitudes A_k used in the annealing term of the prediction for the leakage current in the Sheffield Model [62].

where $t_0 = 1$ min. The α_I parameter describing the short-term annealing is found to be $(1.23 \pm 0.06) \cdot 10^{-17}$ A/cm. Parameter τ_I is temperature-dependent and can be found from the following relation:

$$\frac{1}{\tau_I} = k_{0I} \exp\left(-\frac{E_I}{k_B T}\right), \tag{4.28}$$

where $k_{0I} = 1.2^{+5.3}_{-1.0} \cdot 10^{13}$ s^{-1} and $E_I = (1.11 \pm 0.05)$ eV. The parameters describing the long-term annealing α_0^* and β equal $7.07 \cdot 10^{-17}$ A/cm and $3.29 \cdot 10^{-18}$ A/cm, respectively. The temperature dependence in the logarithmic term is added by scaling the time axis using:

$$\Theta_A(T) = \exp\left[-\frac{E_I^*}{k_B}\left(\frac{1}{T} - \frac{1}{T_{\text{ref}}}\right)\right], \tag{4.29}$$

with $T_{\text{ref}} = 294.15$ K and $E_I^* = (1.30 \pm 0.14)$ eV.

4.4 SCT leakage current

The leakage current data used for comparisons with model predictions are obtained by normalising the measured module HV current to 0°C using the temperature-scaling formula:

$$I_{\text{norm}} = I_{\text{meas}} \left(\frac{T_{\text{norm}}}{T_{\text{meas}}}\right)^2 \exp\left[-\frac{E_g}{2k_B}\left(\frac{1}{T_{\text{norm}}} - \frac{1}{T_{\text{meas}}}\right)\right]. \tag{4.30}$$

Here, I_{norm} is the normalised leakage current, I_{meas} is the HV current measured at temperature T_{meas}, and T_{norm} is the normalisation temperature, which in

this case is 0°C (273.15 K). Parameter E_g is the effective generation energy of (1.214 ± 0.014) eV [63]. The normalised current is then divided by the volume of the sensitive part of the module. The inputs to leakage current models are: the times of irradiation (or times in between irradiations), temperature measurements and fluences.

Leakage current simulations are presented for three modules located in different layers of the SCT detector:

- barrel 3 with $\eta_{\text{index}} = 1$ and $\phi_{\text{index}} = 21$,
- barrel 6 with $\eta_{\text{index}} = 1$ and $\phi_{\text{index}} = 21$,
- disk 9 in endcap A with $\eta_{\text{index}} = 0$ and $\phi_{\text{index}} = 1$.

This particular choice of modules is motivated by the η-dependence of the fluence (barrel 3 is the most irradiated barrel layer and disk 9 is in the highest fluence region, as can be seen in Figure 4.6) and temperature (barrel 6 has to be operated at higher temperature, as mentioned in Subsection 3.4.2).

For each of the modules, fluence factors are different and therefore fluence is calculated separately. Graphs presenting the integrated luminosity delivered by the LHC and the integrated 1 MeV n-eq fluences calculated using fluence factors obtained from FLUKA simulations are presented in Figures 4.7, 4.8 and 4.9 for barrel 3, barrel 6 and disk 9 modules, respectively. As expected, fluence is highest in the disk 9 module and lowest in the barrel 6 module. Distributions of parameters affecting leakage current simulations are also presented for each considered module and they are shown in Figure 4.10 for the barrel 3 module, Figure 4.11 for the barrel 6 module and Figure 4.12 for the disk 9 module. The low voltage (LV) flag with value of 1 indicates that the module is powered and the temperature used in the simulation is taken from measurement from the sensor hybrid (T_S). If the flag is 0, the modules are not powered and their temperature is close to the temperature measured at the end of cooling stave, denoted by T_C. The presented HV current values before normalisation to 0°C

correspond to HV set to 150 V. The reverse bias voltage applied to the sensors is also shown for completeness.

Presented in Figures 4.13, 4.14 and 4.15 are the Hamburg and Sheffield model leakage current predictions overlaid with the leakage current data for modules in barrel 3, barrel 6 and disk 9, respectively. The shaded areas represent the 1σ systematic uncertainty of the predictions, which includes the effects of model parameter variations, a 2°C temperature measurement uncertainty and a 3.7% uncertainty on the fluence factors. It can be appreciated that both models agree well with the data although Hamburg model shows slightly better agreement for barrel 6 and disk 9 modules, but the data points for barrel 3 module are always higher than the prediction. The Sheffield model slightly overestimates the leakage current in the disk 9 module. In general, the ratios between data and prediction of both models lie within a 1σ range. As expected, the smallest leakage current corresponds to the least irradiated barrel 6 module. The distributions show also a few important features. As expected, at the times when there is no beam, the leakage current annealing behaviour is visible. At the end of each year, when there is a technical stop and the detector is kept at room temperature, the leakage current drops significantly. At the time corresponding to the end of LS1, it becomes almost flat and the exposure to high fluences in Run 2 leads to more rapid changes.

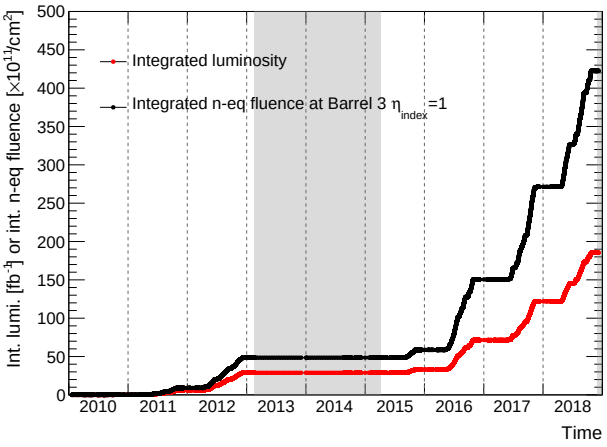

Figure 4.7: Integrated luminosity (red points) and integrated 1 MeV n-eq fluence (black points) corresponding to the module in barrel 3 with $\eta_{\text{index}} = 1$ and $\phi_{\text{index}} = 21$ between the beginning of 2010 and the end of 2018. The fluence conversion factors corresponding to different collision energies are obtained from FLUKA simulations. The grey shaded areas represent the LS1 and LS2 (LS2 is almost invisible as the shutdown started close to the end of 2018).

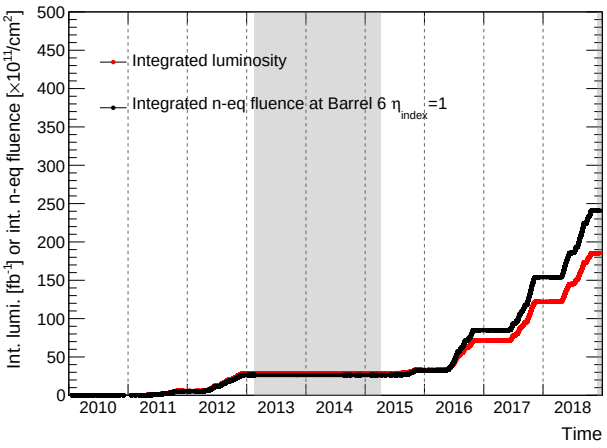

Figure 4.8: Integrated luminosity (red points) and integrated 1 MeV n-eq fluence (black points) corresponding to the module in barrel 6 with $\eta_{\text{index}} = 1$ and $\phi_{\text{index}} = 21$ between the beginning of 2010 and the end of 2018. The fluence conversion factors corresponding to different collision energies are obtained from FLUKA simulations. The grey shaded areas represent the LS1 and LS2 (LS2 is almost invisible as the shutdown started close to the end of 2018).

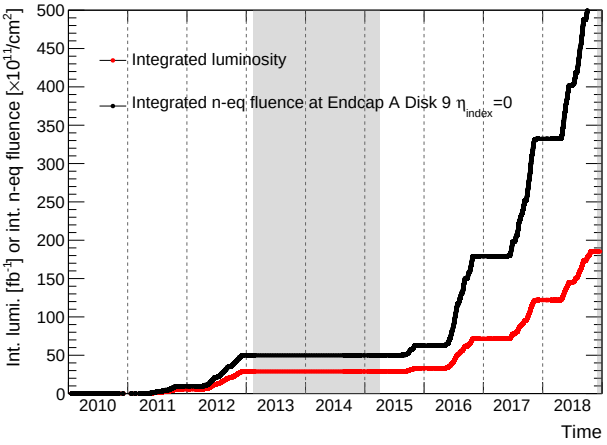

Figure 4.9: Integrated luminosity (red points) and integrated 1 MeV n-eq fluence (black points) corresponding to the module in disk 9 in endcap A with $\eta_{\text{index}} = 0$ and $\phi_{\text{index}} = 1$ between the beginning of 2010 and the end of 2018. The fluence conversion factors corresponding to different collision energies are obtained from FLUKA simulations. The grey shaded areas represent the LS1 and LS2 (LS2 is almost invisible as the shutdown started close to the end of 2018).

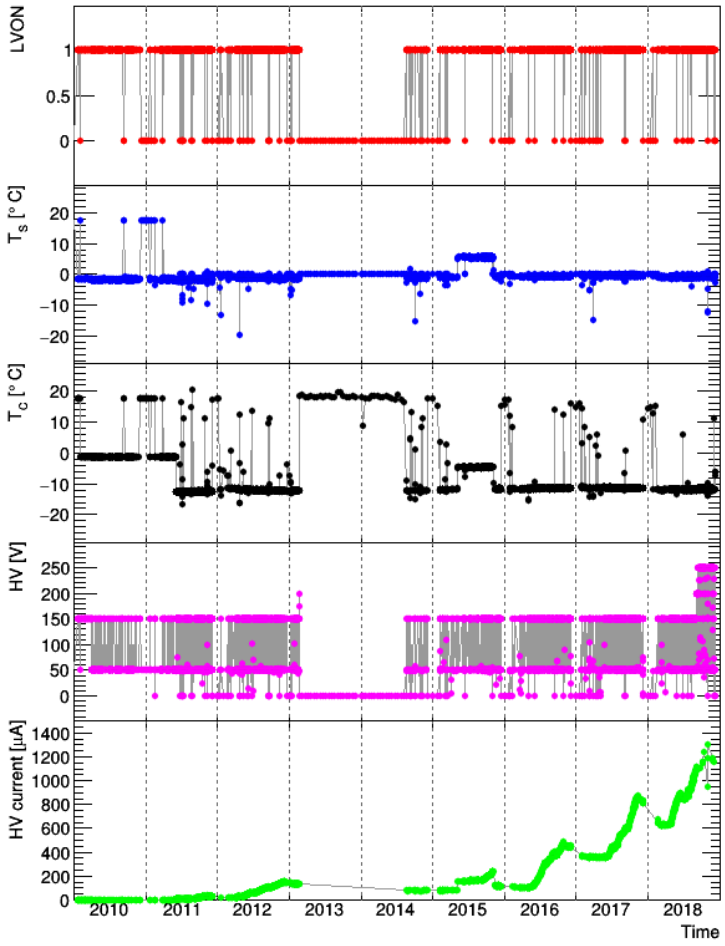

Figure 4.10: Parameters affecting the leakage current simulation corresponding to the module in barrel 3 with $\eta_{\text{index}} = 1$ and $\phi_{\text{index}} = 21$: LV flag (LVON), temperature reading from the module hybrid T_S, temperature set in the cooling system T_C, and HV applied to the module. The measured HV current in the lower panel after scaling to 0°C is used for comparison with model predictions.

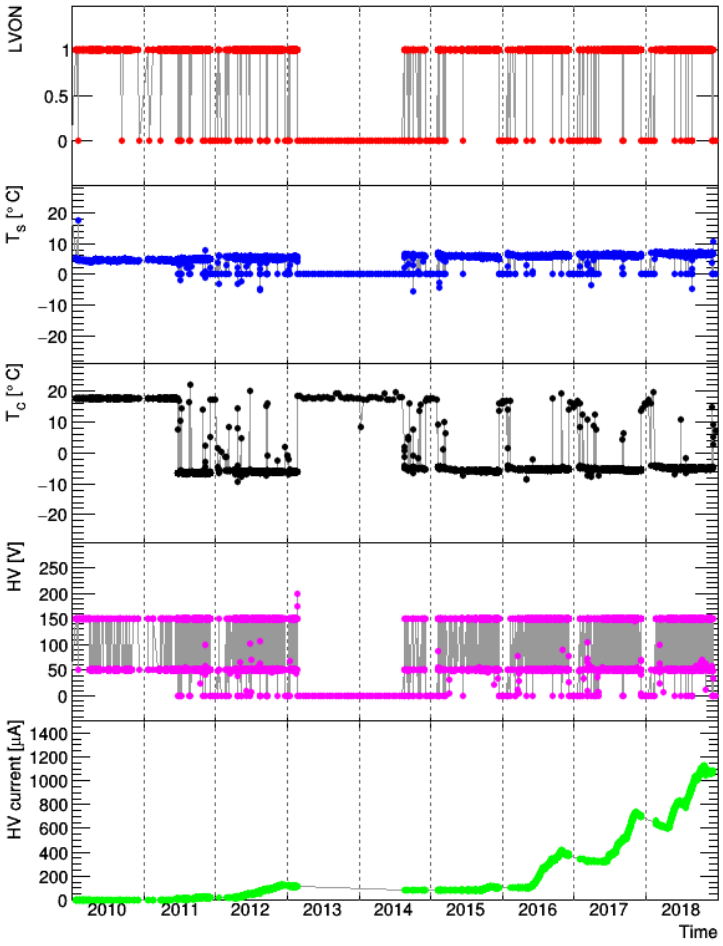

Figure 4.11: Parameters affecting the leakage current simulation corresponding to the module in barrel 6 with $\eta_{\text{index}} = 1$ and $\phi_{\text{index}} = 21$: LV flag (LVON), temperature reading from the module hybrid T_S, temperature set in the cooling system T_C, and HV applied to the module. The measured HV current in the lower panel after scaling to 0°C is used for comparison with model predictions.

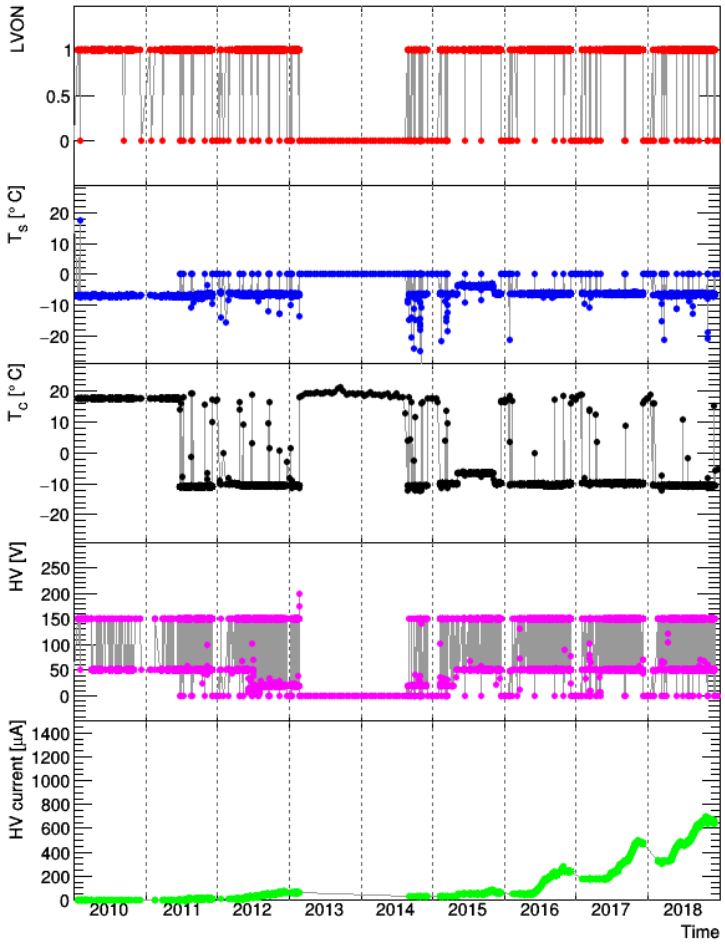

Figure 4.12: Parameters affecting the leakage current simulation corresponding to the module in disk 9 in endcap A with $\eta_{\text{index}} = 0$ and $\phi_{\text{index}} = 1$: LV flag (LVON), temperature reading from the module hybrid T_S, temperature set in the cooling system T_C, and HV applied to the module. The measured HV current in the lower panel after scaling to 0°C is used for comparison with model predictions.

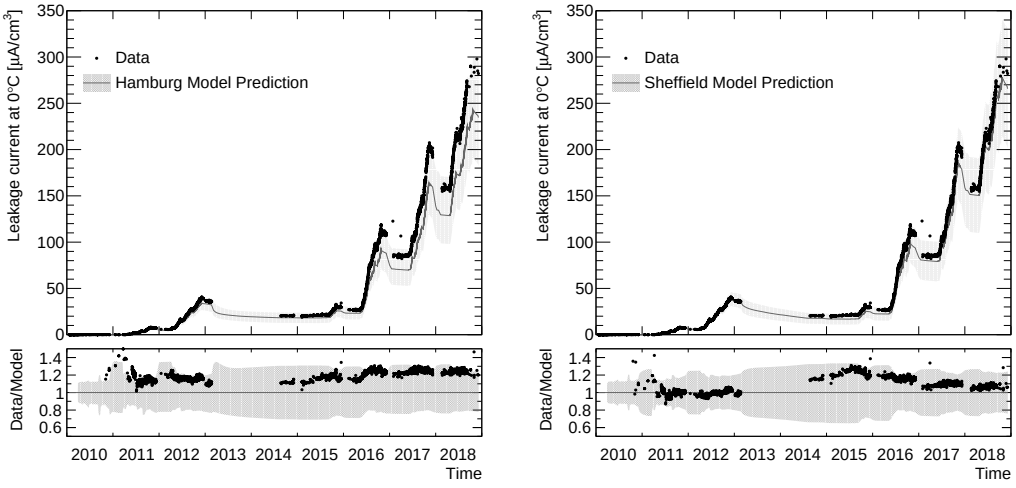

(a) Hamburg Model (b) Sheffield Model

Figure 4.13: The upper panels present the leakage current in a depleted volume in the SCT barrel 3 module with $\eta_{\text{index}} = 1$ and $\phi_{\text{index}} = 21$ between the beginning of 2010 and the end of 2018. The data points represent the measured HV current normalised to 0°C and the solid grey line represents the prediction obtained with model indicated in the sub-figure caption. The lower panels present the data-to-model prediction ratio. The grey shaded areas in both panels represent the systematic error band including the effects of model parameter variations, a 2°C temperature measurement uncertainty and a 3.7% uncertainty on the fluence factors.

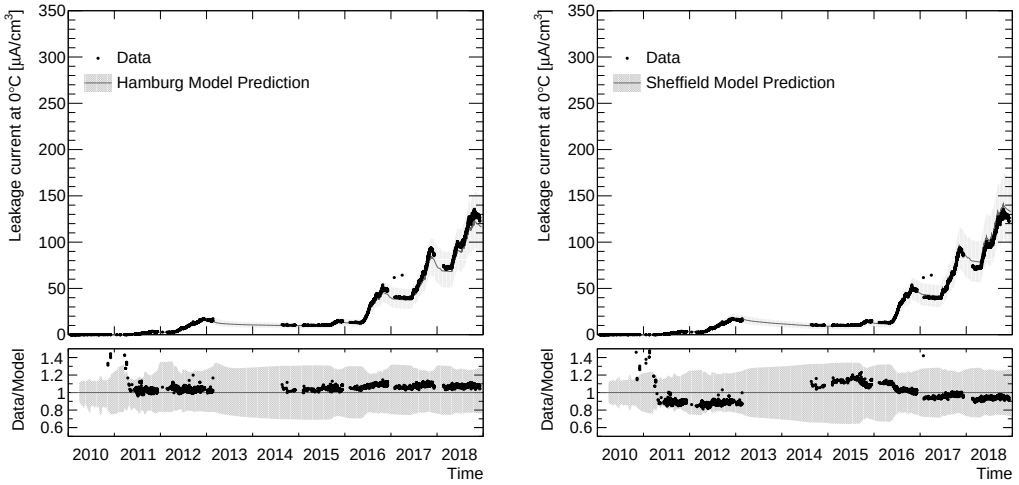

(a) Hamburg Model (b) Sheffield Model

Figure 4.14: The upper panels present the leakage current in a depleted volume in the SCT barrel 6 module with $\eta_{\text{index}} = 1$ and $\phi_{\text{index}} = 21$ between the beginning of 2010 and the end of 2018. The data points represent the measured HV current normalised to 0°C and the solid grey line represents the prediction obtained with model indicated in the sub-figure caption. The lower panels present the data-to-model prediction ratio. The grey shaded areas in both panels represent the systematic error band including the effects of model parameter variations, a 2°C temperature measurement uncertainty and a 3.7% uncertainty on the fluence factors.

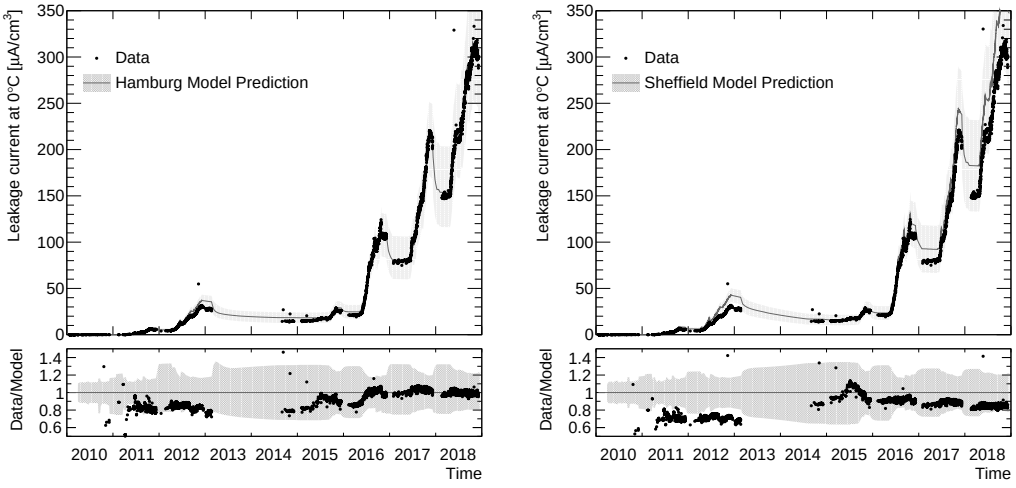

(a) Hamburg Model (b) Sheffield Model

Figure 4.15: The upper panels present the leakage current in a depleted volume in the SCT endcap A disk 9 module with $\eta_{\text{index}} = 0$ and $\phi_{\text{index}} = 1$ between the beginning of 2010 and the end of 2018. The data points represent the measured HV current normalised to 0°C and the solid grey line represents the prediction obtained with model indicated in the sub-figure caption. The lower panels present the data-to-model prediction ratio. The grey shaded areas in both panels represent the systematic error band including the effects of model parameter variations, a 2°C temperature measurement uncertainty and a 3.7% uncertainty on the fluence factors.

4.5 SCT hit efficiency

Special scans, where the reverse bias voltage applied to the SCT sensors is varied, are performed at different times during ATLAS data-taking period. Thanks to these HV scans, the effects of radiation damage on the full depletion voltage can be monitored by looking at the dependence of quantities like cluster width, noise or hit efficiency on the applied HV. As changing the HV affects the detector performance, the HV scans are performed occasionally and typically over layers with the highest expected irradiation like barrel 3 or disk 6 in both endcaps. The estimation of the full depletion voltage based on the hit efficiency is presented in this section.

The hit efficiency is defined as:

$$\varepsilon = \frac{N_{\text{clusters}}}{N_{\text{clusters}} + N_{\text{holes}}}, \tag{4.31}$$

where N_{clusters} and N_{holes} are the number of clusters and holes associated with a track, respectively. A hole is created when no hit is observed although it is expected. The tracks used in the hit efficiency calculation must be well reconstructed therefore they must pass certain criteria. As pile-up can lead to reconstruction of fake tracks, only events with number of tracks $N_{\text{tracks}} < 500$ are considered. Each track is required to have reconstructed $p_{\text{T}} > 1$ GeV, transverse impact parameter $|d_0| < 10$ mm, incident angle (the angle between the track and the normal to the module surface) $|\phi_{\text{inc}}| < 40°$ and a reasonable quality of the track fit by imposing a requirement of $\chi^2/N_{\text{dof}} < 3$. The number of SCT hits excluding the sensor under consideration (SUC) is required to be at least 6 and the number of hits in silicon sensors (in both Pixel and SCT detectors) excluding the SUC is required to be at least 7. The number of holes in the silicon sensors excluding the SUC is required to be at most 1. Additionally, no holes in all pixel layers are allowed and at least one hit in the two innermost pixel layers is required. Clusters not already assigned to a track but within 0.2 mm distance around it are included in the N_{clusters} and excluded from the N_{holes} term to avoid bias. The track selection criteria are

summarised in Table 4.2.

Quantity	Requirement
N_{tracks}	< 500
p_{T}	> 1 GeV
$\lvert d_0 \rvert$	< 10 mm
$\lvert \phi_{\text{inc}} \rvert$	$< 40°$
χ^2/N_{dof}	3
$N_{\text{hits}}^{\text{SCT}}$ (excluding SUC)	≥ 6
N_{hits}^{Si} (excluding SUC)	≥ 7
N_{holes}^{Si} (excluding SUC)	≤ 1
$N_{\text{holes}}^{\text{Pixel}}$	0
$N_{\text{hits}}^{\text{Pixel}}$ in 2 innermost layers	≥ 1
D_{cut}	0.2 mm

Table 4.2: Track selection criteria for hit efficiency calculation.

All graphs presented in this section show results using data for the first bunch crossing to avoid bias coming from preceding bunches and the values on both side-0 and side-1 of a given layer are averaged unless otherwise stated. The HV in the graphs represents the reverse bias voltage set on a power supply and is higher than the actual HV on the sensor due to voltage drop over the resistance on the hybrids.

Figure 4.16 presents an η-dependence of the hit efficiency shown for different HV points for barrel 3 using data from the HV scan performed in September 2018 (two months before the end of pp collisions in Run 2). The clear η-dependence is a result of the lower incident angle of a traversing particle in the central region (lower η_{index}) leading to less charge carriers produced in the sensitive area and therefore lower hit efficiency. This is most pronounced when lower HV is applied. No significant difference is observed between the efficiency for positive and negative η_{index}, thus the remaining plots for the

barrel 3 show the averaged efficiency curves for the corresponding negative and positive η_{index}. Modules with crystal orientation $< 100 >$ (15 in barrel 3, 0 in disk 6 of both endcaps) are excluded from the efficiency calculation as they may show a slightly different behaviour.

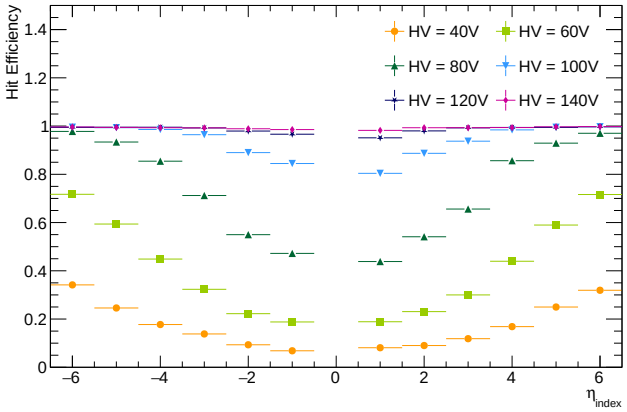

Figure 4.16: Hit efficiency for barrel 3 modules with different η_{index} measured using data collected in the HV scan performed during pp collisions at $\sqrt{s} = 13$ TeV in September 2018. Different coloured points correspond to different values of the HV set on a power supply. Only statistical uncertainties are included in the error bars. Modules with crystal orientation $< 100 >$ are excluded from the efficiency calculation.

Due to the η-dependence observed in Figure 4.16, the efficiency curves are presented separately for modules with different η-indices. Figure 4.17 presents the efficiency curves for barrel 3 when the hit efficiency is calculated separately taking into account only the first bunch crossing and all bunches. The effect of preceding bunches is visible and leads to a small drop in the observed efficiency even with nominal HV. Figure 4.18 presents the efficiency curves separately for side-0 and side-1. It can be observed that there is no difference between the two, hence it is correct to take the average of both sides. The V_{FD} estimated from the point where efficiency starts to drop is around 110-120 V.

Similar efficiency curves from the same HV scan but for disk 6 in both endcaps are presented in Figure 4.19. As expected, the efficiency is lower for middle ($\eta_{\text{index}} = 1$) and inner ($\eta_{\text{index}} = 2$) rings due to the higher fluences observed

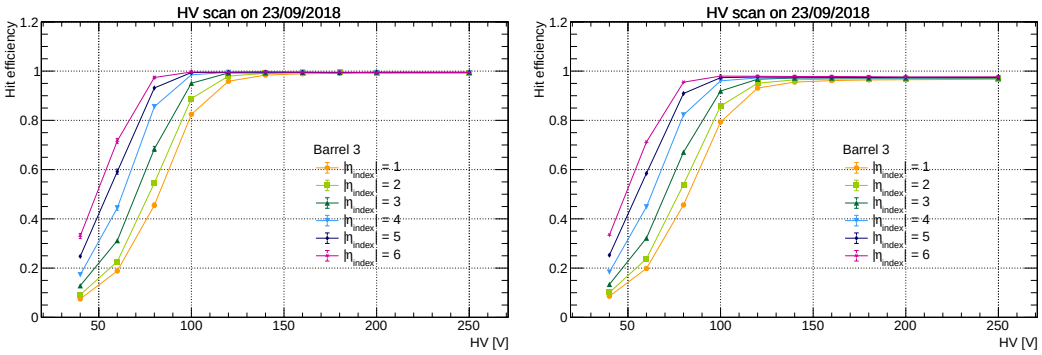

(a) First bunch crossing (b) All bunches

Figure 4.17: Hit efficiency as a function of HV for barrel 3 modules with different absolute values of η-indices represented by different colours and points. The efficiencies are measured using data collected in the HV scan performed during pp collisions at $\sqrt{s} = 13$ TeV in September 2018. The values are obtained for configurations denoted in the sub-figure captions and are averaged over both sides of the layer. Only statistical uncertainties are included in the error bars. Modules with crystal orientation $< 100 >$ are excluded from the efficiency calculation.

for the η region covered by these rings. When comparing results between the endcaps it is visible that the efficiency is lower in endcap C. The efficiency drop is observed at around 100 V.

By comparing the results of HV scans performed at different times during Run 2 over the same SCT layers, one can observe a shift of the efficiency curves towards higher values of HV and therefore the evolution of the full depletion voltage with increasing radiation damage. Figure 4.20 presents a comparison of efficiency curves for barrel 3 with distinction to different η_{index} for HV scans performed in April and September 2018. A shift of the efficiency curves is clearly visible, which indicates a change of the depletion voltage by around 30 V over 5 months of operation.

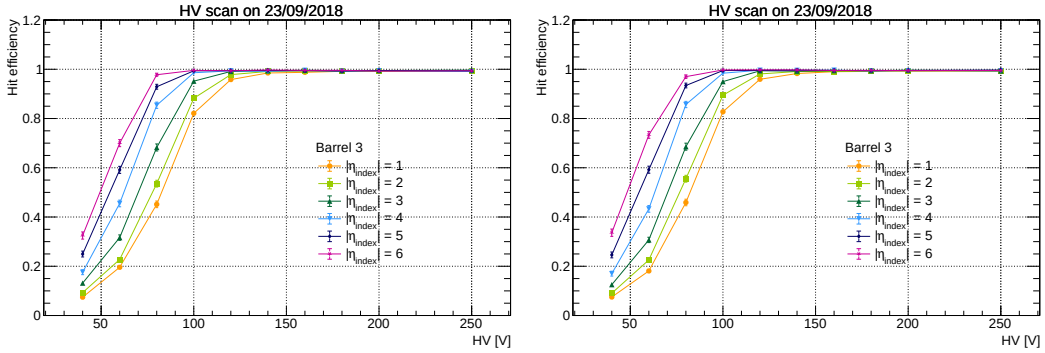

(a) Side-0 (b) Side-1

Figure 4.18: Hit efficiency as a function of HV for barrel 3 modules with different absolute values of η-indices represented by different colours and points. The efficiencies are measured using data collected in the HV scan performed during pp collisions at $\sqrt{s} = 13$ TeV in September 2018. The values are obtained separately for the two sides denoted in the sub-figure captions. Only statistical uncertainties are included in the error bars. Modules with crystal orientation $< 100 >$ are excluded from the efficiency calculation.

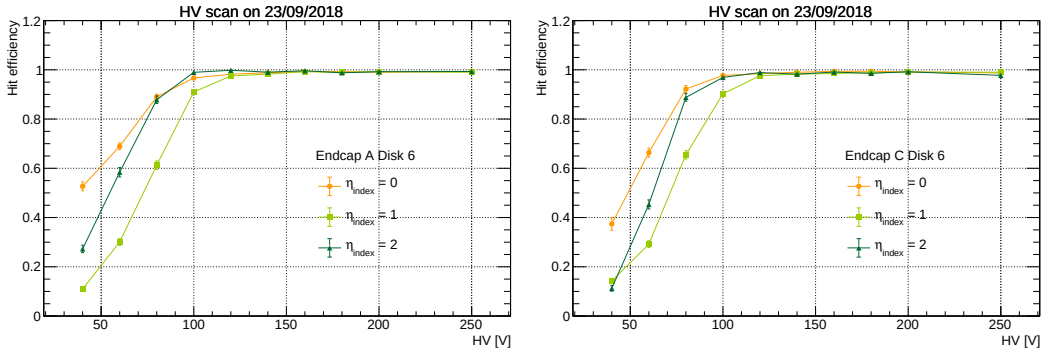

(a) Endcap A (b) Endcap C

Figure 4.19: Hit efficiency as a function of HV for disk 6 in both endcaps denoted in the sub-figure captions. Modules with different absolute values of η-indices are represented by different colours and points. The efficiencies are measured using data collected in the HV scan performed during pp collisions at $\sqrt{s} = 13$ TeV in September 2018. The values are averaged over both sides of the layer. Only statistical uncertainties are included in the error bars.

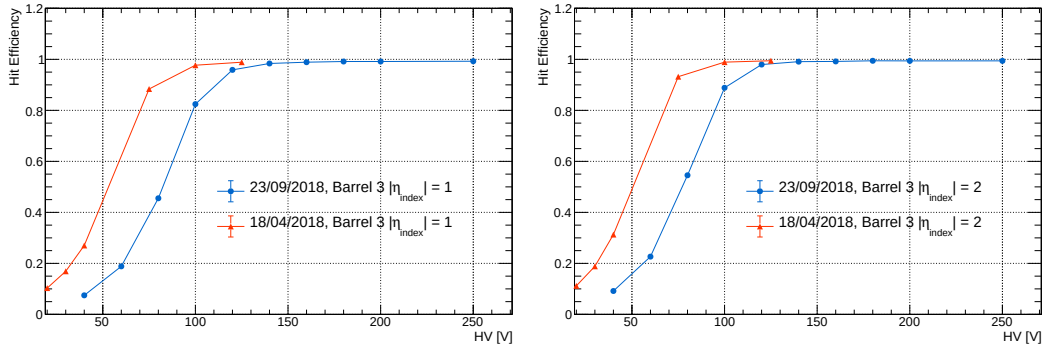

(a) $\eta_{\text{index}} = 1$

(b) $\eta_{\text{index}} = 2$

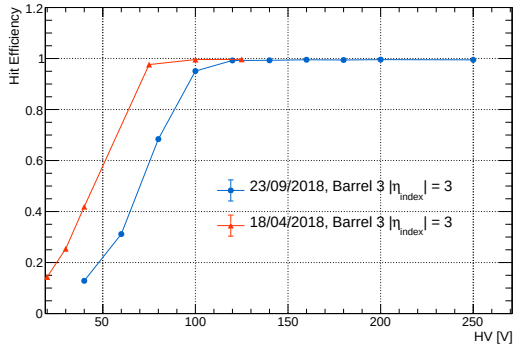

(c) $\eta_{\text{index}} = 3$

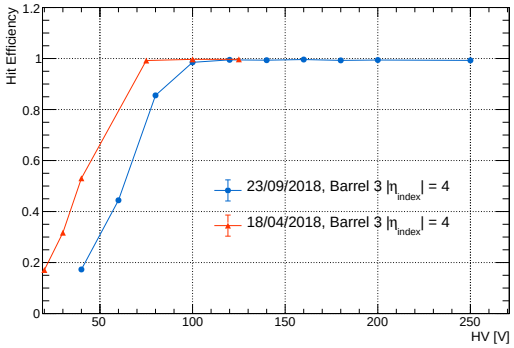

(d) $\eta_{\text{index}} = 4$

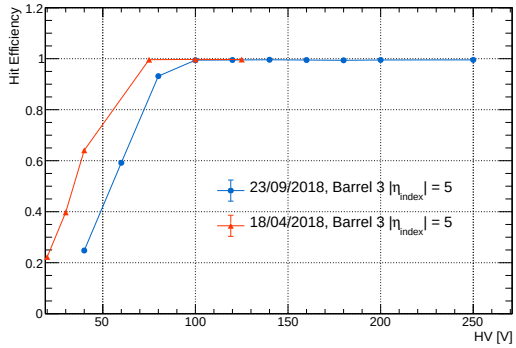

(e) $\eta_{\text{index}} = 5$

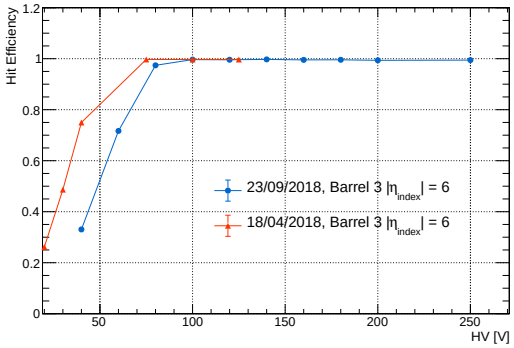

(f) $\eta_{\text{index}} = 6$

Figure 4.20: Hit efficiency as a function of HV for barrel 3 modules with η-indices indicated in the sub-figure captions. Orange triangles represent the HV scan data collected on 18/04/2018, corresponding to an irradiation of 2.7×10^{13} 1-MeV n-eq /cm^2. Blue circles represent the HV scan data collected on 23/09/2018, corresponding to an irradiation of 4.0×10^{13} 1-MeV n-eq /cm^2. The values are averaged over both sides of the layer. Only statistical uncertainties are included in the error bars. Modules with crystal orientation $< 100 >$ are excluded from the efficiency calculation.

4.6 Conclusions

Monitoring and correct modelling of the radiation-induced changes in the silicon sensors is crucial to maintain good performance of the detector.

The leakage current simulations presented in this chapter show a very good agreement with the data for both models used. This gives confidence that both models can be used to predict the leakage current evolution until the end of Run 3 assuming certain conditions like operation temperatures and fluences.

Also presented is the estimation of full depletion voltage from hit efficiency curves. The obtained value of 120 V for barrel 3 corresponding to September 2018 is far greater than the predicted V_{FD} from the Hamburg model shown in Figure 4.21. Other methods of V_{FD} estimation show similar values, which is still to be understood. It is interesting to note that, as presented in Figure 4.21, all barrel layers are now type-inverted. The V_{FD} will keep increasing with occasional drops corresponding to technical stops when the detector is kept at room temperature. The increasing depletion voltage has to be taken into account and the bias voltage applied to modules will have to be raised to fully deplete the sensors to recover their efficiency.

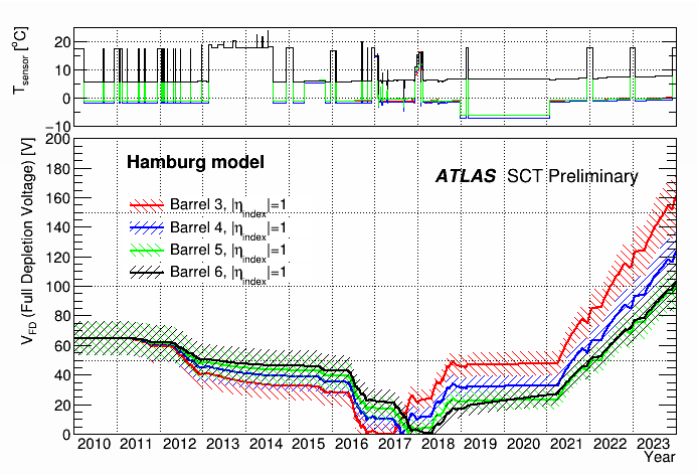

Figure 4.21: Hamburg model prediction for the full depletion voltage until the end of 2023 (previously anticipated end of Run 3 data-taking period) [64].

Chapter 5

Modelling of physics processes

Monte Carlo (MC) simulation of a process of interest and its backgrounds constitutes a vital part of any physics analysis. In the searches presented in this thesis, MC simulation is used to define selection and categorisation, and to find models describing signal and constraining backgrounds. Generation of pp collision events at the LHC is performed in a series of steps:

1. Hard-scatter process.
2. Initial state radiation (ISR) and final state radiation parton shower.
3. Hadronisation.
4. Underlying event generation.
5. Decays of unstable particles.

Each of these steps is presented graphically for the example of Higgs boson production associated with a $t\bar{t}$ pair in Figure 5.1. A more detailed description of the listed generation steps as well as a description of the modelling of additional proton-proton interactions and simulation of the detector response to different particles is provided in the following sections.

5.1 Hard-scatter process

The cross-section of a hard-scatter process $a + b \to n$ in pp collisions can be written using the factorisation theorem [66] as:

$$\sigma = \sum_{a,b} \int_0^1 dx_a dx_b \int f_a^{h1}(x_a, \mu_F) f_b^{h2}(x_b, \mu_F) d\sigma_{a+b\to n}(\mu_F, \mu_R). \tag{5.1}$$

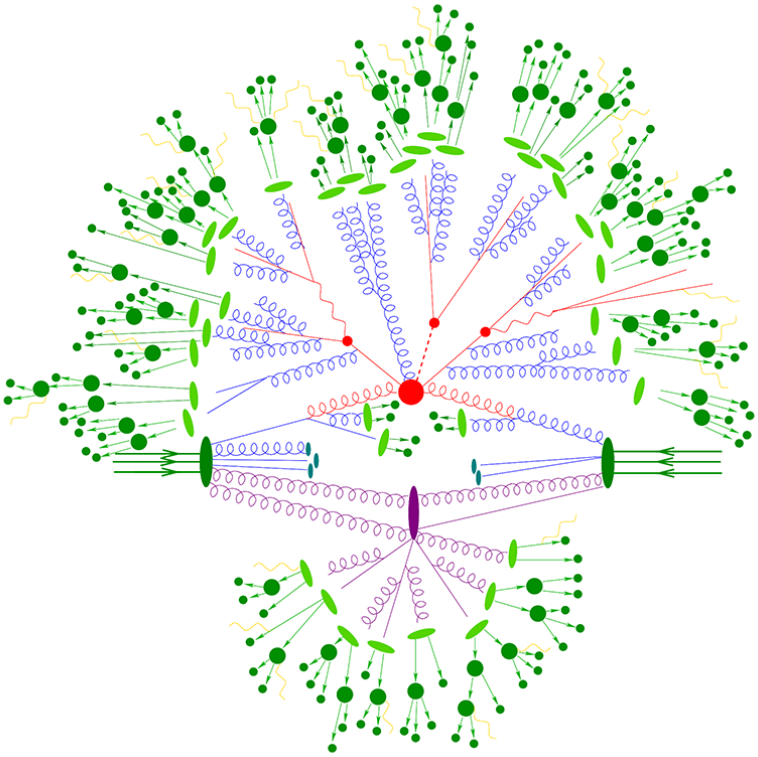

Figure 5.1: A graphical representation of Higgs boson production associated with a $t\bar{t}$ pair as produced by an event generator [65]. The big red blob in the middle represents the hard-scatter process. The three smaller red blobs represent the two top quarks with a Higgs boson in between. The purple blob represents an additional interaction (underlying event). The light and dark green elements show the hadronisation and decays of the formed hadrons, respectively. The yellow lines represent photon radiation, which can take place at any stage of the event generation.

The cross-section therefore depends on two main components. The function f_i^j is a parton distribution function and describes the probability of finding a parton of type i within a hadron j, carrying a momentum fraction x_i of the hadron. The momentum fraction is the so-called Bjorken x. The PDFs are independent of the hard-scatter process, but have to be determined from experimental data. The currently available PDFs are obtained from fits to the deep inelastic scattering data from HERA, fixed target experiments, Tevatron and LHC data. The PDF evolution with the factorisation scale μ_F is described by the DGLAP equations [67–69]. There are various sets of PDFs, which

differ in the choice of input data and treatment of: underlying perturbative QCD calculations; heavy quarks; correlations with parameters such as strong coupling constant α_S; and experimental and theoretical uncertainties.

The quantity $d\sigma_{a+b\to n}$ is dependent on the hard process of interest. It is the parton-level cross-section on the process of creating n from the initial-state partons a and b which can be calculated using perturbative QCD (short distance/high energy interaction). It depends on both μ_F and the renormalisation scale μ_R to avoid divergences in the calculations. The parton-level cross-section can be written as the product of the parton flux $1/(2\hat{s})$ and the corresponding squared matrix element (ME) $\mathcal{M}^2$ averaged over initial-state spin and colour degrees of freedom:

$$\begin{aligned} d\sigma_{a+b\to n} &= \tfrac{1}{2\hat{s}} \left|\mathcal{M}_{a+b\to n}\right|^2 (\Phi_n; \mu_F, \mu_R) \\ &= \tfrac{1}{2x_a x_b s} \left|\mathcal{M}_{a+b\to n}\right|^2 (\Phi_n; \mu_F, \mu_R)\,, \end{aligned} \tag{5.2}$$

The ME is a sum over all possible Feynman diagrams to the order of the calculations and depends on the momenta given by the final-state phase space Φ_n and factorisation and renormalisation scales, s denotes the hadronic centre-of-mass energy squared.

The dominant contribution to the overall cross-section comes from a LO Feynman diagram, which has the lowest possible number of interaction vertices. The higher-order corrections to this value are related to additional quark or gluon emissions, or loops and they are added to the cross-section in the form of a perturbation expansion in terms of powers of the strong interaction coupling α_S.

5.2 Parton shower

Partons involved in the hard-scatter interaction can radiate gluons which carry colour charge and therefore themselves can lead to further radiation. The step of the event generation which determines the behaviour of the incoming and outgoing partons is called parton showering. A FSR parton shower is a

sequential process which describes the evolution of the hard-scatter process downwards to lower momentum scale until the perturbation theory breaks down (at the order of 1 GeV). Simulation of the ISR is similar to FSR, except that in the case of ISR there are kinematic constraints determined by the hard-scatter process. The parton showering describes radiation at the collinear limit (the opening angle between the direction of a quark and a gluon radiated from the quark goes to zero or π) and the soft limit (the fraction of momentum carried by a radiated gluon goes to zero). It describes well the structure of a jet. However, it cannot simulate the production of high-p_{T} and well-separated jets for which fixed-order MEs perform better. As MEs do not describe the structure of a jet thus merging of MEs and parton showering is required.

The QED parton shower is modelled similarly to the QCD one. It is mostly relevant for photon radiation from light charged leptons.

5.3 Hadronisation

As mentioned in Section 2.1, partons cannot be observed freely due to their confinement within colour-neutral hadrons and therefore are not observed in final state. Instead, quarks and gluons which remain after the parton shower hadronise. As perturbative theory breaks down at the end of the parton shower it cannot be applied there. The confinement of quarks and gluons within hadrons is simulated with hadronisation models, which form the next step of event generation. There are two main phenomenological models used in MC generators to simulate hadronisation, the string model [70] and the cluster model [71], which were developed in the last few decades. The created hadrons may decay into further hadrons, giving rise to the hadronic jets observed in the detector.

5.4 Underlying event generation

Due to the large overlap between the colliding hadrons, the partons not involved in the hard-scatter process can interact with each other giving rise to

an underlying event. As a result, many soft hadrons can be produced. The underlying event is described using phenomenological models.

5.5 Decays of unstable particles

The final states of proton-proton collisions typically consists of neutral and charged pions and kaons, leptons and photons, which are the result of decays of unstable hadrons. Tables with life times and branching ratios for different decay channels are used to model these secondary decays using measurements from previous experiments. These are often taken from lower energy e^+e^- collider experiments.

5.6 Simulation of pile-up events

As discussed in Section 3.1, the high instantaneous luminosity of the LHC leads to multiple pp collisions in one bunch crossing. A special sample of minimum bias events is needed to simulate the effect of these additional proton-proton interactions. The minimum bias events are typical results of pp collisions dominated by low-p_{T} hadrons. The number of these additional interactions is matched to the observed average pile-up in the data.

5.7 Detector response simulation

To mimic the detector response to different particles, generated events are interfaced to a special software where a detailed detector geometry is defined. Simulation of the passage of these particles through the active and passive detector material is most commonly achieved using the GEANT4 [72] toolkit. After the detector simulation, the energy deposits are digitised to provide the simulation outputs in a format similar to that obtained from the real detector and then the events are reconstructed using the same algorithms as the ones used for data. It is also possible to skip the step of full detector simulation, as this is the most time consuming part of the event generation and instead use a set of derived parameterisations to obtain a fast simulation of the detector response. This approach is presented in more detail in Section 7.5.

Chapter 6

Object reconstruction

6.1 Electrons and photons

Electron reconstruction starts by first looking for energy deposits in the electromagnetic calorimeter and then matching them to a track reconstructed in the Inner Detector. A photon, as particle not carrying an electromagnetic charge, is characterised by energy deposits in the EM calorimeter not matching any of the tracks in the ID. However, a photon often converts into an electron-positron pair inside the detector volume, leading to two tracks from charged particles originating from the same vertex consistent with an electron-positron signature. These tracks allow the reconstruction of such photon. An electron may lose significant fraction of its energy via photon radiation as a result of the interaction with the detector (Bremsstrahlung). These photons are highly collimated with the electron track leading to more energy deposits in the adjacent cells of the EM calorimeter. The photons can convert then into electron-positron pair leading to additional tracks associated with the initial electron. An example electron trajectory through the ATLAS detector components is presented in Figure 6.1.

Electrons and photons are reconstructed in the ATLAS detector in the $|\eta| < 2.47$ range typically excluding the crack region corresponding to $1.37 < |\eta| < 1.52$, where the services and cooling for ID are placed. The reconstruction starts with selecting so-called topo-clusters, clusters with energy deposits in topologically connected cells in EM calorimeters. The interesting cells are found basing on the signal-to-noise ratio. A more detailed description of the

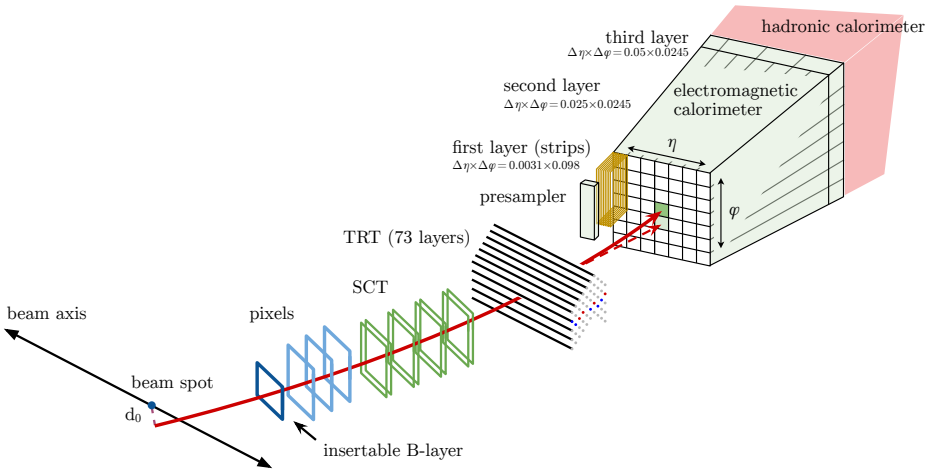

Figure 6.1: A view of the electron passing through layers of the Pixel and SCT detectors, TRT straws and EM calorimeter module. The electron path is marked in solid red line. The dashed red line represents path of a photon radiated by the electron as a result of interaction with the detector matter [73].

topo-clusters is provided in Section 6.4. Next, the trajectories found in the ID that loosely match the energy deposits in the calorimeter are refitted in order to take into account the possible energy loss due to Bremsstrahlung. In the case of converted photons, the conversion vertices are built. The vertices or the refitted tracks are then matched to the clusters. Then, the previously found topo-clusters are tested as seed candidates, which form the basis of the super-clusters. This is done by scanning the clusters one-by-one and testing them in decreasing-E_{T} order. A topo-cluster can become a seed if the reconstructed E_{T} is above 1 GeV (1.5 GeV) for electrons (photons) and matches a track with at least 4 hits in either the Pixel or SCT detector (it does not have to match any of the tracks in the silicon detectors or any conversion vertex). If a seed cluster is found, then the algorithm searches for satellite clusters, clusters in vicinity of the seed cluster with energy deposits due to photon radiation or topo-cluster splitting. A connected set of seed cluster and its satellite clusters is called a supercluster. The energy and position corrections are then applied to each supercluster and they are again matched to tracks or to conversion vertices. An ambiguity-resolving algorithm needs to be applied in order to decide whether a given supercluster comes from a photon or electron. Energy of

the object needs to be recalibrated in order to account for the track refit. The whole procedure is presented diagrammatically in Figure 6.2 and described extensively in Ref. [74]. After all the steps are finished, the built object can be used in the physics analysis.

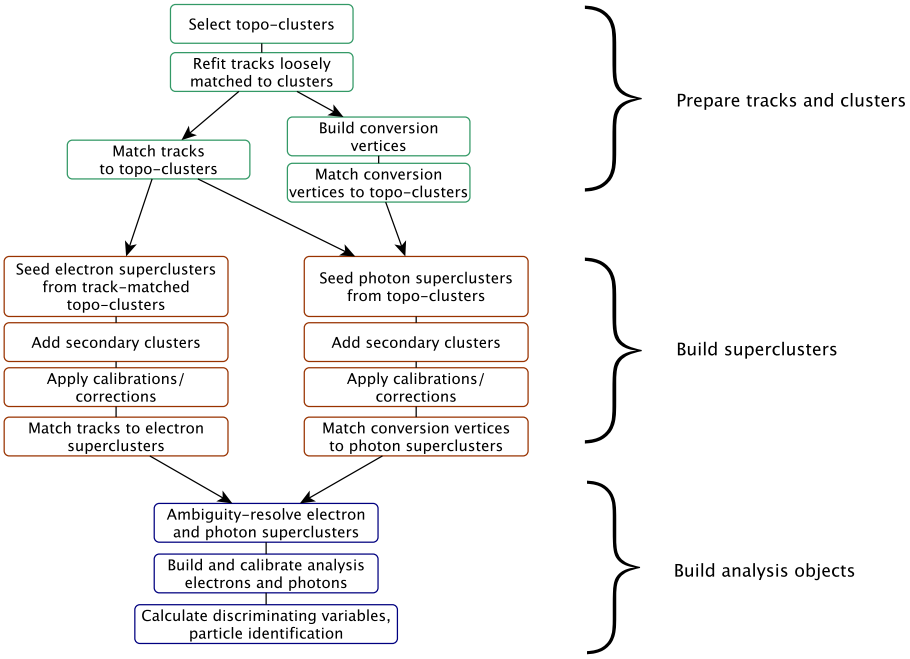

Figure 6.2: The electron and photon reconstruction algorithm [74].

Electron identification working points (WPs) are defined in order to select prompt electrons and reject electrons coming from photon conversions, non-prompt electrons coming from the decays of hadrons with heavy flavour or hadronic jets leaving energy deposits in the EM calorimeter. The identification uses a likelihood (LH) method with the discriminant based on a likelihood for a given electron to come from signal (L_S) or background (L_B). The likelihood is defined as

$$L_{S(B)}(x) = \prod_{i=1}^{n} P_{S(B),i}(x_i), \tag{6.1}$$

where $P_{S,i}$ and $P_{B,i}$ are the values of the probability density functions for the signal and background, respectively, for a given quantity x_i. The quantities

x_i describe the information from the Inner Detector, EM calorimeter and the combined information from the two. The signal here refers to prompt electrons. The background is composed of jets with a signature similar to that of prompt electrons, electrons from photon conversions and decays of heavy-flavour hadrons. For each reconstructed electron, a value of the likelihood discriminant d_L is calculated as the natural logarithm of the ratio of L_S to L_B. The identification working points are defined based on this discriminant and some additional quantities related to the reconstructed energy and trajectory. In order of decreasing efficiency and increasing background rejection factor, these WPs are: Loose, Medium and Tight. Figure 6.3 presents the efficiency as a function of electron E_{T} corresponding to different identification WPs.

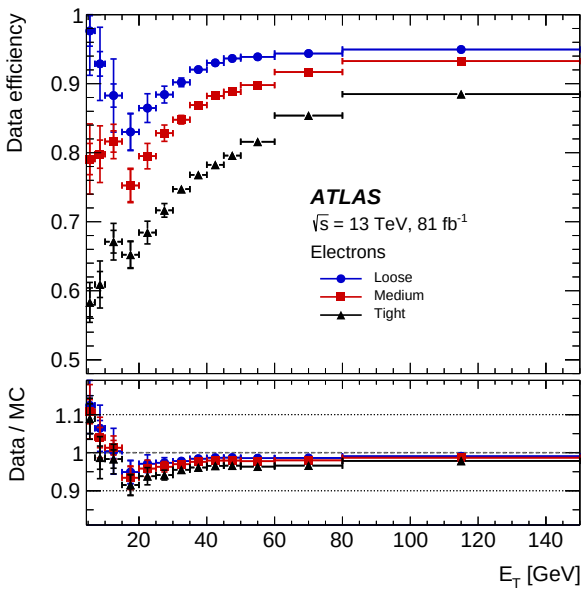

Figure 6.3: The upper panel shows the electron identification efficiency as a function of electron E_{T} as derived using data collected in 2015-2017 with the ATLAS detector with the $Z \to ee$ selection imposed. Different colours and data points correspond to different identification WPs: Loose (blue circles), Medium (red squares) and Tight (black triangles). The lower panel presents the data-to-simulation ratios for the different WPs [74].

Two WPs are provided for photon identification in the offline analysis: Loose and Tight. The WPs are defined with a cut-based method using variables

describing the electromagnetic shower shape. The Loose WP is characterised by high efficiency, however it provides poor fake photon rejection. The Tight WP is in general recommended for physics analysis due to its relatively high efficiency and very good fake photon rejection.

Electron isolation cuts can be imposed on already identified electron in order to further improve their purity. By requiring the object to be isolated, one selects objects with no activity in the vicinity of their trajectory or cluster direction. The track isolation is provided using the $p_{\mathrm{T}}^{\mathrm{coneXX}}$ variable (where $\Delta R = \mathrm{XX}/100$) which is the sum of the p_{T} of the tracks within a certain cone around the electron or converted photon but excluding the track of the object itself. In the case of electrons coming from heavy particles with high-p_{T}, the other decay products are highly collimated with them leading to the requirement of a variable cone size in order to optimise the application of the isolation criteria. This is provided using $p_{\mathrm{T}}^{\mathrm{varconeXX}}$ variable, for which the ΔR of the cone gets smaller for higher transverse momentum of the electron and the relation can be written as:

$$\Delta R = \min\left(\frac{10}{p_{\mathrm{T}}[\mathrm{GeV}]}, \Delta R_{\mathrm{max}}\right), \tag{6.2}$$

where typically $\Delta R_{\mathrm{max}} = 0.2$. The calorimeter isolation variable $E_{\mathrm{T}}^{\mathrm{coneXX}}$ is the sum of transverse energy of the clusters around the electron or photon cluster excluding the cluster energy and any possible energy leakage from the central cluster or pile-up contribution. The cone considered for the calorimeter isolation is typically 0.2 for electrons and 0.2 or 0.4 for photons. There are four isolation working points for electrons which can be imposed on calorimeter energy deposits or tracks reconstructed in the ID: Gradient, HighPtCaloOnly, Loose and Tight. The Gradient WP has a fixed efficiency (90% for $p_{\mathrm{T}} =$ 25 GeV, 99% for $p_{\mathrm{T}} = 60$ GeV, uniform in η) and the other three have fixed cuts on $E_{\mathrm{T}}^{\mathrm{coneXX}}$ and $p_{\mathrm{T}}^{\mathrm{varconeXX}}$ isolation variables. The three isolation working points for photons: Loose, Tight and TightCaloOnly are also defined using the isolation variables.

Electron calibration uses a multivariate method to reconstruct the electron energy from the energies of the associated clusters. The energy scale and resolution are controlled by the position and width of the $Z \to ee$ peak. Figure 6.4 presents the dielectron mass distribution of the $Z \to ee$ candidates for data after the energy scale correction and for the MC simulation after the resolution correction.

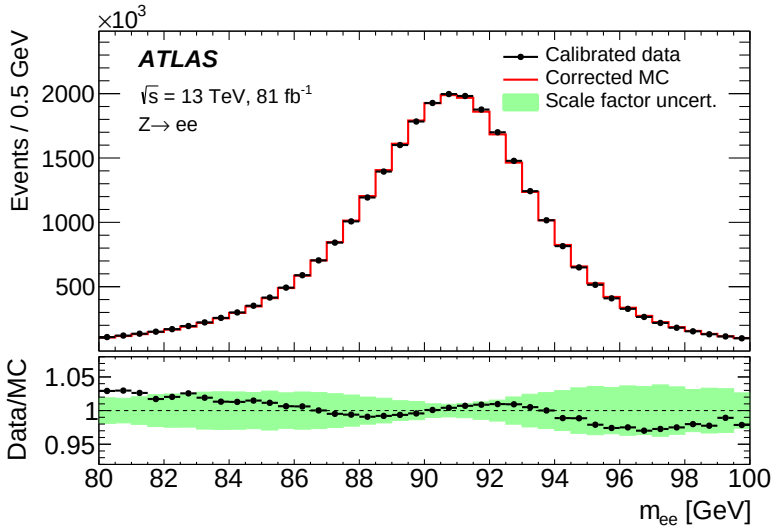

Figure 6.4: The upper panel presents the dielectron invariant mass distribution for the calibrated data (black points) and for the MC simulation (red histogram) of the $Z \to ee$ process after the resolution correction. The lower panel presents the data to MC simulation ratio. The green shaded area represents the scale factor uncertainty band [74].

6.2 Muons

Muons are reconstructed using information from different subdetectors. As charged particles they leave a set of hits along their trajectory in the Inner Detector. As highly penetrating particles they leave hits in the Muon Spectrometers located in the outermost region of the ATLAS detector. Also, they deposit a small amount of their energy upstream of the muon spectrometer, in the calorimeters.

The reconstruction of the muon trajectory is done separately within the ID volume and the muon spectrometer. A more detailed discussion of the muon reconstruction within the MS is provided in Ref. [75].

Depending on the amount of information available from each subdetector, there are four types of muons used in physics analysis:

- Combined muons (CB) - the final track is obtained by performing a global refit using hits from independently found tracks in the ID and MS. To improve the track fit quality, some hits within a certain distance may be added and some discarded in the final fit. The pattern recognition algorithm first takes the hits from MS volume and reconstructs a track, which is then extrapolated into the ID volume and matched to the hits there. The equivalent approach, starting from ID hits, is used as complementary.
- Segment-Tagged muons (ST) - the track is reconstructed using hits in the ID and when extrapolated into the MS volume, is consistent with one segment there. The Segment-Tagged muons are usually characterised by low p_{T} or they are passing the MS in a region with low acceptance.
- Calorimeter-Tagged muons (CT) - the track is reconstructed using hits in the ID, which is extrapolated into the calorimeter volume where it is matched to an energy deposit consistent with that of a minimum-ionising particle. CT muons are reconstructed in the range of $|\eta| < 0.1$, where the MS has a limited acceptance.
- Standalone muons (SA) - reconstructed using hits in the MS only. SA muons are reconstructed in the range $2.5 < |\eta| < 2.7$ not covered by the Inner Detector.

To provide a good selection efficiency for prompt muons as well as good background suppression, a few muon identification WPs are provided: Loose, Medium, Tight, Low-p_{T} and High-p_{T}. The medium WP is characterised by high efficiency for muons with p_{T} down to around 5 GeV. It is provided for muons

in the range $0.1 < |\eta| < 2.7$. The hadron misidentification rate is a few per mill and the associated systematic uncertainties are small. The Loose working point is characterised by high efficiency for muons with p_{T} above 3 GeV and makes use of all types of muons (unlike the Medium WP, it includes also ST and CT muons). The systematic uncertainties and misidentification rates are two times higher than for the Medium WP. The Tight WP provides a lower efficiency (5-10% lower than Medium WP) with lower misidentification rate but at the price of higher systematic uncertainties. The Low-p_{T} WP is characterised by similar efficiencies and size of systematic uncertainties as in the case of Medium muons but with a high efficiency for muons with $p_{\mathrm{T}} > 3$ GeV. The High-p_{T} WP provides the best p_{T}-resolution, thanks to additional criteria imposed at the track reconstruction stage. The efficiency as a function of the muon η for the Medium and Loose WPs in the range $|\eta| < 0.1$ is presented in Figure 6.5.

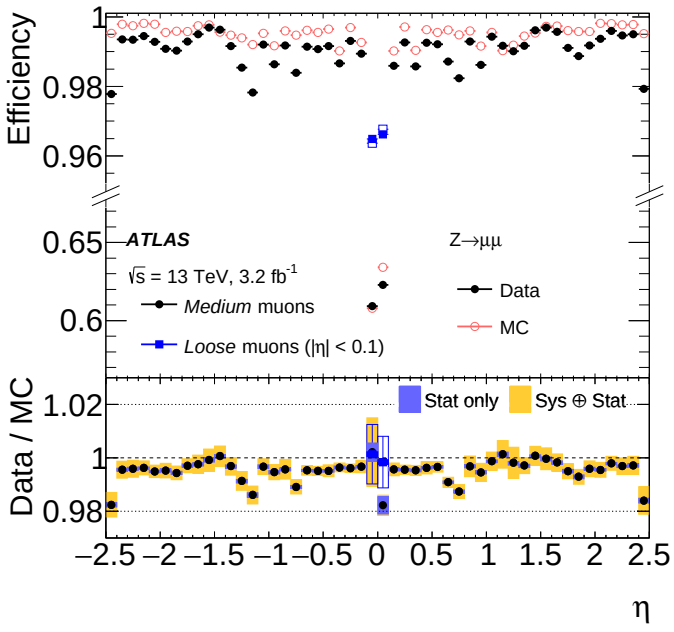

Figure 6.5: The efficiency as a function of muon η for the Medium identification WP (circles) and Loose identification WP (squares) in the region $|\eta| < 0.1$, where Medium muons are not reconstructed. The efficiencies are presented for the data corresponding to 3.2 fb^{-1} (filled points) and MC simulation (empty points) passing a $Z \to \mu\mu$ selection [75].

Further background suppression can be provided by requiring muon isolation. There are a few isolation WPs provided for muons. They are characterised by a set of requirements on isolation variables defined for calorimeters, tracks and for the particle flow objects (particle flow algorithm is discussed in Section 6.4). The $E_{\mathrm{T,raw}}^{\mathrm{isol}}$ variable is the sum of all positive topological clusters in the calorimeters with barycentre within a cone centred around the muon track. The track isolation is described by the $p_{\mathrm{T}}^{\mathrm{coneXX}}$ and $p_{\mathrm{T}}^{\mathrm{varconeXX}}$ variables as defined in Section 6.1. Additionally, in the case of the particle flow isolation, an additional variable is calculated using the calorimeter energy of the neutral flow objects as input.

Muon momentum is estimated from the track curvature and the magnetic field. The scale and resolutions are controlled using the $J/\psi \to \mu\mu$ and $Z \to \mu\mu$ processes. The effect of the muon momentum corrections is presented in Figure 6.6.

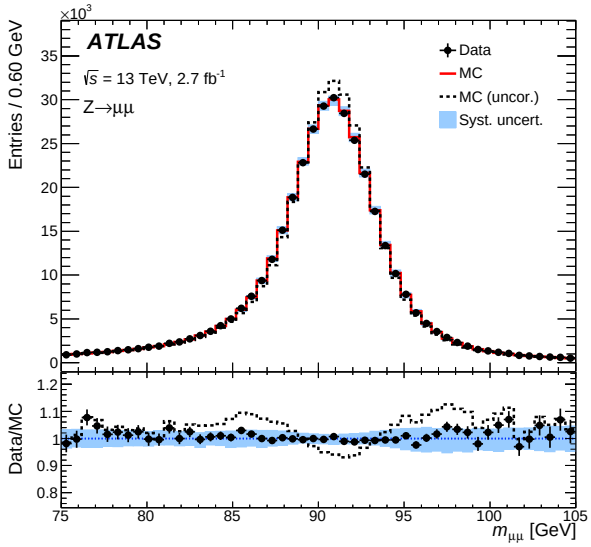

Figure 6.6: The upper panel presents the dimuon mass distribution reconstructed with $Z \to \mu\mu$ candidates for data (black points) and corrected (red histogram) and uncorrected (dashed black histogram) MC simulation of the process [75]. The lower panel presents the data-to-MC simulation ratio. The blue shaded area represents the systematic error band.

6.3 Final State Radiation Photons

Muons can lose a significant fraction of their energy by QED FSR. This is an important effect in the $H \to \mu\mu$ analysis, where the signal extraction improves with the dimuon mass resolution. Including the FSR photons in the invariant mass calculation can improve the resolution. The FSR photons are found with a method similar to that described in Ref. [76]. Two types of photons are reconstructed:

- collinear (also called "near") - obtained from two different objects
  - 3×5 clusters[1] seeded by topo-clusters with $\Delta R(\mu, \gamma) < 0.08$, $E_{\mathrm{T}} < 3.5$ GeV, $f_1 > 0.2$ (where f_1 is the energy fraction of the cluster in the first layer of the EM calorimeter)
  - standard photons and electrons (reconstructed using algorithms described in Section 6.1) satisfying $\Delta R(\mu, \gamma) < 0.2, E_{\mathrm{T}} > 3.5$ GeV, $f_1 > 0.1$

- far - standard photons satisfying the following criteria: $\Delta R(\mu, \gamma) > 0.2, E_{\mathrm{T}} > 10$ GeV, Tight identification WP and FixedCutLoose isolation WP.

The basic selection as detailed above was optimised for the $H \to 4\ell$ analysis. To increase the efficiency and purity of FSR recovery for the $H \to \mu\mu$ analysis, it was optimised further and the details of this optimisation are presented in Section 8.3. The most important result is a $\Delta R(\gamma, \mu)$-dependent increase of the E_{T} threshold on near FSR photon candidates.

6.4 Jets

Instead of observing quarks and gluons in the final states, the experimentally observed objects are collimated sprays of hadrons called jets. In the searches for the $H \to ee$ or $H \to \mu\mu$ decays, jets are particularly important to distinguish

[1] This refers to an area in $\Delta\eta \times \Delta\phi$ space in the units of 0.025×0.025.

between different Higgs boson production modes. Two main methods are used to reconstruct jets for ATLAS physics analysis and these are described below.

Topo-cluster jets

Topo-cluster jets are reconstructed from topological clusters of energy depositions in the calorimeters called topo-clusters [77]. The topo-cluster reconstruction is based on a variable controlling the cluster formation, the cell signal significance $\varsigma_{\text{cell}}^{\text{EM}}$. It is defined as the ratio of the cell signal to the average expected noise for this cell. The reconstruction starts with an identification of cells with an energy deposit four times higher than the noise level. Such cells are referred to as seeds. Then, the neighbouring cells with an energy deposit two times above the threshold are added to the cluster and the last layer is formed using the adjacent cells with non-zero energy deposit. Since these thresholds are applied to the absolute value of the energy deposit, there may be a case where a negative signal forms a seed. These negative signals are usually induced due to pile-up or electronic noise and the clusters with such negative energy depositions are not used in the jet reconstruction.

Particle flow jets

The particle flow algorithm uses combined information from the tracking detector and calorimeter, and the resulting signal ideally represent a single particle. Well measured tracks in the ID that originate from the primary vertex are selected and matched to a single topo-cluster in the calorimeter. The energy expected in the calorimeter for the particle matched to the track and the topo-cluster is calculated based on the information about the topo-cluster position and the transverse momentum of the trajectory. It is possible that the energy deposits corresponding to one particle are split into several topo-clusters, hence, a decision whether more clusters should be added is taken at the next stage and the expected energy in the calorimeter is recomputed if necessary. This energy is then subtracted cell-by-cell from the set of matched topo-clusters. If any remaining energy is consistent with the shower fluctuations coming from a single particle, the topo-cluster remnants are removed.

The final result is a list of tracks, and modified and unmodified topo-clusters. The algorithm is presented diagrammatically in Figure 6.7. The particle flow method is expected to perform better than the simpler method using just calorimeter information. It provides a better pile-up jet rejection thanks to the ability of choosing tracks associated with a specific vertex as well as improved momentum resolution for the charged low-p_{T} tracks due to its more precise measurement in the ID.

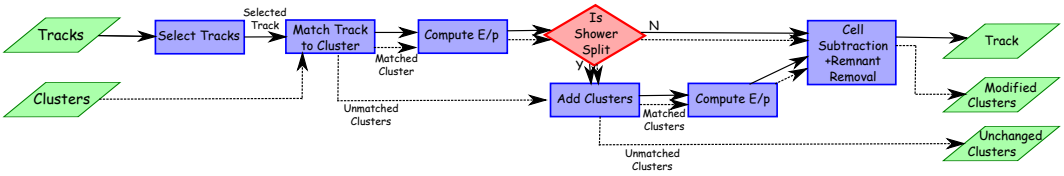

Figure 6.7: A flow chart representing the steps of the particle flow method to reconstruct jets [78].

The topo-clusters or particle flow objects are input to the anti-k_t jet-reconstruction algorithm [79]. This is a sequential recombination algorithm with the parameter R controlling the extension of a jet. The algorithm combines pairs of particles basing on the minimisation of the distance between them:

$$d_{ij} = \min\left(k_{ti}^{2p}, k_{tj}^{2p}\right)\frac{\Delta_{ij}^2}{R^2} \tag{6.3}$$

$$d_{iB} = k_{ti}^{2p} \tag{6.4}$$

where $\Delta_{ij}^2 = (y_i - y_j)^2 + (\phi_i - \phi_j)^2$ and k_{ti}, y_i and ϕ_i are the transverse momentum, rapidity defined as $\frac{1}{2}\ln\left(\frac{E_i+k_{zi}}{E_i-k_{zi}}\right)$, and azimuthal angle of the particle i, respectively. d_{iB} is the distance between the particle i and the beam. The parameter p governs the relative power of the energy versus geometrical scales and in the case of the anti-k_t algorithm, $p = -1$. The algorithm loops over entities and finds the two with smallest distance. If this distance is smaller than d_{iB} the two entities are recombined. However, if they are equal, i is called a jet and removed from the list of entities. The combination of particles takes place until there are no entities left. The anti-k_t algorithm is collinear and

infrared safe, meaning that the objects reconstructed with this algorithm can be safely compared to theoretical simulations and computations. For the analyses presented here, the distance parameter $R = 0.4$ is used. Jets produced by this procedure are referred to as the Antikt4TopoEM or Antikt4Pflow jets.

A jet energy calibration is performed in order to recover the jet energy scale of the truth-level jets[2] from the reconstructed objects. A more detailed description is provided in Ref. [80]. This process is done in several stages, presented diagrammatically in Figure 6.8. In the first step, an adjustment of the jet four-momentum is performed so that it points to the hard scatter interaction vertex rather than interaction point. Here, the jet η resolution is improved while not changing its energy. Next, the pile-up contributions are subtracted from the jet p_{T} using the area-based method [81]. A pile-up can contribute to the p_{T} if it creates clusters above the calorimeter thresholds or when the pile-up clusters overlap with clusters coming from the hard-scatter. To estimate the pile-up contribution in the calorimeter, a median p_{T} density ρ is calculated for the jets reconstructed with the k_t algorithm (within $|\eta| < 2$), which is more sensitive to the soft radiation. The density is defined as a ratio of the p_{T} of the jet to its area A. The area A is determined using ghost association [82], where ghosts are particles with infinitesimally small p_{T} and distributed in the whole calorimeter. A ghost is associated with the jet if it is classified to it using the jet reconstruction algorithm. The estimated pile-up contribution is then subtracted from the jet momentum, not changing its η and ϕ coordinates. Since the correction is derived using jets in the central region of the calorimeter, it does not correctly describe the pile-up contribution in the forward region, leading to pile-up dependence of the jet p_{T}. This is mitigated by a residual pile-up correction. The residual p_{T} dependence is defined as a difference in p_{T} between the reconstructed and truth-level jets. The reconstructed jet is required to match the truth-level jet by imposing

[2] Truth-level jets are formed using simulated stable particles as input to the anti-k_t algorithm.

$\Delta R < 0.3$ and have $p_{\mathrm{T}} > 10$ GeV. The correction removes the dependence on the number of primary vertices and average number of interactions per bunch crossing. Further correction brings the energy scale to the particle-level energy scale while removing any biases in the jet η reconstruction, which are a result of the transition between the calorimeter technologies or different granularity. This correction is derived using simulated events after adjustment of the jet η and pile-up corrections. Only isolated jets matching the truth-level jets ($\Delta R < 0.3$) are used here. The average energy response is defined as the mean of a Gaussian function fitted to $E^{\mathrm{reco}}/E^{\mathrm{truth}}$ distributions in different E^{truth} and η_{det} (jet η pointing towards the centre of the detector) bins. To perform the η calibration, a second correction is derived as the difference between η^{reco} and η^{truth} as well in E^{truth} and η_{det} bins. In the next step a global sequential calibration procedure is performed. Here, the energy response dependence on longitudinal and transverse features of the jet is removed using five variables describing the shower. The five variables are:

- the fraction of energy measured in the first layer of the hadronic Tile calorimeter,
- the fraction of energy measured in the third layer of the EM LAr calorimeter,
- the number of tracks with $p_{\mathrm{T}} > 1$ GeV ghost-associated with the jet,
- the average p_{T}-weighted transverse distance in the $\eta - \phi$ plane between the jet axis and all tracks with $p_{\mathrm{T}} > 1$ GeV ghost-associated with the jet,
- the number of muon track segments ghost-associated with the jet.

For each of the variables, a correction is derived for different $p_{\mathrm{T}}^{\mathrm{truth}}$ and $|\eta_{\mathrm{det}}|$ regions and applied independently and sequentially. The corrections are derived and applied in such a way that the jet energy scale remains unchanged. As a result, the dependence on the above-mentioned observables is reduced to at most 2%. The final stage consists of in situ corrections applied only to data. These corrections aim to reduce the residual discrepancy between the data

and the MC simulation due to imperfect description of the detector response and material in the simulation or imperfect simulation of the hard-scatter, underlying eventsor the pile-up. The differences between data and simulation are evaluated by balancing jet p_{T} against other well-measured objects (central jets constitute reference for the forward jets, Z bosons, photons and multijet systems constitute reference objects for central jets corresponding to different p_{T} intervals). For each in situ calibration a response $\mathcal{R}_{\text{in situ}}$ is obtained as the average ratio between the jet and reference object p_{T} for different p_{T} regions of the reference object. A correction factor is defined as:

$$c = \frac{\mathcal{R}^{\mathrm{Data}}_{\text{in situ}}}{\mathcal{R}^{\mathrm{MC}}_{\text{in situ}}} \tag{6.5}$$

and is evaluated in different jet p_{T} and η regions.

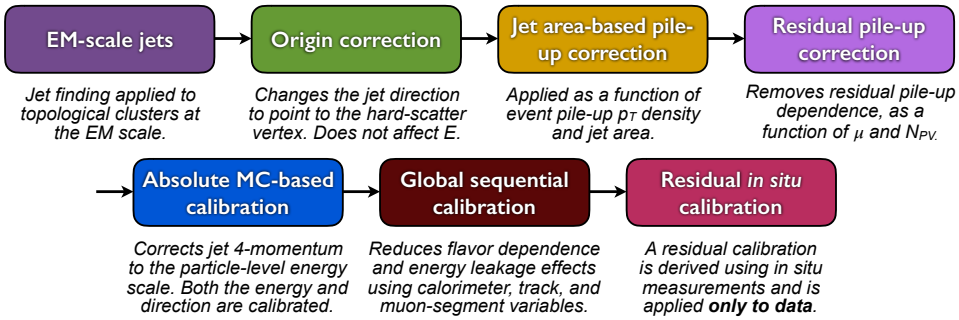

Figure 6.8: The stages of the jet energy calibration [80].

In the central region, tracks geometrically matching jets can be used for pile-up suppression and the identification of jets originating from bottom quarks. Pile-up suppression for jets is achieved using a 2D likelihood algorithm called the Jet Vertex Tagger (JVT) [83]. The two variables used in the JVT are: the jet p_{T} and the ratio of the scalar p_{T} sum of tracks within a jet that originate from the primary vertex, to the scalar p_{T} sum of all tracks.

Jets can be identified as originating from bottom (charm or light-flavour) quarks using the algorithm referred to as flavour-tagging. The decay of b-hadrons in a jet is characterised by a presence of at least one secondary vertex and tracks with large impact parameters (defined in Figure 6.9). There are

two main types of the b-tagging algorithms, the low-level and high-level algorithms. The low-level algorithms use the signed transverse and longitudinal impact parameter significance of the tracks, reconstruct the displaced vertex in a jet and try to reconstruct the full b-hadron decay chain using topological information on weak b-hadron decays. The high-level algorithms combine the outputs of the low-level algorithms as well as kinematic information like p_{T} and $|\eta|$ of the jet into one discriminant using multivariate methods. The high-level algorithm used in the two presented analyses is the MV2 algorithm using Boosted Decision Tree (BDT) multivariate method. Specifically, the MV2c10 tagger [84] is employed, which is trained with the signal sample being composed of events with b-jets and the background composed of events with 7% and 93% c- and light-jets, respectively. The operating point corresponding to specific efficiency and c- or light-jet rejection is chosen by a requirement on MV2c10 variable. In both analyses presented in this document a 60% efficiency WP of the MV2c10 tagger is chosen, which is characterised by c-jet, τ-jet and light-flavour-jet rejection of 23, 140 and 1200, respectively.

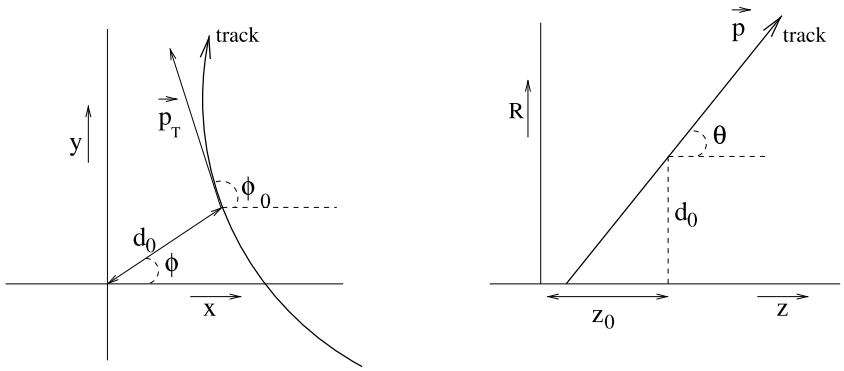

Figure 6.9: Definitions of the transverse (d_0) and longitudinal (z_0) impact parameters [85].

6.5 Missing transverse momentum

In pp collisions there is generally no information about the longitudinal momentum balance in a reaction, as only parts of the proton interact. However,

in the initial state there is no momentum in the transverse plane and momentum conservation dictates, that the same is true in the final state. Thus, if all final state particles are successfully reconstructed any missing transverse momentum, $E_{\mathrm{T}}^{\mathrm{miss}}$, can ideally be attributed to non-interacting particles such as neutrinos. The $E_{\mathrm{T}}^{\mathrm{miss}}$ is defined as a negative vectorial sum of the transverse momenta of the hard objects (reconstructed and calibrated muons, electrons, photons and jets) as well as soft term, (signals not associated with any of the reconstructed objects) [86]. The vector of missing transverse momentum is defined as:

$$E_{x(y)}^{\mathrm{miss}} = E_{x(y)}^{\mathrm{miss},\mu} + E_{x(y)}^{\mathrm{miss},e} + E_{x(y)}^{\mathrm{miss},\gamma} + E_{x(y)}^{\mathrm{miss},jets} + E_{x(y)}^{\mathrm{miss},soft}. \tag{6.6}$$

The order of objects used in the calculation is important as it prevents the double-counting and corresponds to the order of the terms in Equation 6.6. The amount of missing transverse momentum is given by the magnitude of the $E_{\mathrm{T}}^{\mathrm{miss}}$ vector and the direction in the transverse plane is given by the azimuthal angle ϕ^{miss}. In the $H \to ee$ and $H \to \mu\mu$ decays, where no undetected particles are expected, a non-zero value of the missing transverse momentum is a result of either object momentum mis-measurement, mis-calibration, particles going through un-instrumented regions of the detector or pile-up. Nevertheless, it is an important object, as it can be used to discriminate against the $t\bar{t}$ background, where neutrinos are expected from the leptonic W boson decays.

In the search for the $H \to ee$ decay, discrimination against the $t\bar{t}$ background is provided by applying a requirement on $E_{\mathrm{T}}^{\mathrm{miss}}$ significance. This quantity takes into account the resolution of the transverse momentum measurement and is expected to detect a significant $E_{\mathrm{T}}^{\mathrm{miss}}$ more reliably. It is defined as:

$$E_{\mathrm{T}}^{\mathrm{miss}} \text{ significance} = E_{\mathrm{T}}^{\mathrm{miss}} / \sqrt{H_{\mathrm{T}}}, \tag{6.7}$$

where H_{T} is a sum of the p_{T} of all leptons and jets in an event.

Chapter 7

Search for the Higgs boson decay to dielectrons

The branching ratio for the $H \to ee$ decay predicted by the SM is given by $\mathcal{B}(H \to ee) = G_F m_H m_e^2/(4\sqrt{2}\pi\Gamma_H) \approx 5 \cdot 10^{-9}$ [87], where m_H and Γ_H are the Higgs boson mass and width, respectively. Its very low value is far below the sensitivity of any currently operating experiment [88]. However, searching for this rare decay is an important test of the Standard Model. If observed, it could indicate that the Higgs mechanism does not work as expected.

The analysis presented in this chapter is the first search for the $H \to ee$ decay performed using data from the ATLAS experiment. Previously, only the CMS Collaboration has presented results of such a search using 8 TeV data from Run 1 corresponding to an integrated luminosity of 19.7 fb^{-1} [89]. The presented analysis closely follows the strategy of the published $H \to \mu\mu$ search using ATLAS data collected in 2015 and 2016 during Run 2 and corresponding to an integrated luminosity of 36 fb^{-1} [90].

In the course of the analysis, simulations of the properties of Higgs boson production and decay are made using SM predictions. The only exception is the branching ratio, which is to be determined, and which is initially normalised to an arbitrary reference number of 0.1%. The search is performed in several stages. Events passing a basic selection are divided into seven exclus-

ive categories to improve the sensitivity to the $H \to ee$ signal by exploiting differences with respect to the background. The categorisation is based on the similarity to a VBF signature, the dielectron transverse momentum and electron pseudorapidity. A signal+background ($S+B$) fit is performed to the dielectron mass distribution in data for each analysis category to extract the signal, expected to be a narrow peak at around 125 GeV on top of a falling background.

7.1 Data and simulated event samples

The search is performed using 13 TeV data corresponding to an integrated luminosity of 139 fb^{-1} recorded by the ATLAS detector in Run 2. MC simulation of the signal and background processes is used to optimise object and event selection, define the categorisation, and to select analytical functions to describe signal and background components in the fits to dielectron mass distributions.

The simulated signal samples used in the analysis correspond to the main Higgs production processes: ggF, VBF and associated VH production, and are generated for the Higgs boson mass of $m_H = 125$ GeV. The ggF signal sample is generated with the Powheg-Box v2 program using the NNLOPS prescription [91–98] with the PDF4LHC15 set [99] of PDFs. The Higgs boson rapidity is reweighted to achieve NNLO accuracy in QCD [100]. MC simulation of the VBF production process is performed with Powheg-Box v2 [91–93] at next-to-leading-order (NLO) accuracy in QCD with the NNPDF3.0 PDF set [101]. The VH associated production process is generated with Powheg [91–93] at the NLO in QCD. The ZH associated production includes both quark and gluon initial states scaled to their corresponding cross-sections.

All signal samples are interfaced to Pythia8 [54] with the AZNLO tune parameters [102] for parton showering, hadronisation and underlying event generation, and all are processed through the full simulation of the detector in Geant4 [72].

The Z/γ^* background sample is produced using POWHEG-BOX v1 [91–93] with the CT10 PDF set [103] at NLO accuracy in QCD. The events are interfaced to PYTHIA8 [54] with the AZNLO tune parameters [102] for parton showering, hadronisation and underlying event generation and to Photos++ [104] for simulation of the final state radiation. The CTEQ6L1 PDF set [105] is used for the parton shower. The detector simulation is performed in GEANT4 [72].

The effects of pile-up are added using minimum bias samples generated with PYTHIA8 [54] using NNPDF2.3LO PDF set [106] and the A3 tune [56]. Events are reweighted so that the average number of pile-up events in the simulation matches the number in the data.

Furthermore, a fast simulation chain is developed to generate a large-statistics Drell-Yan (DY) background (Z/γ^*) sample in order to evaluate the possible bias introduced by the choice of a particular background fitting model. The produced sample corresponds to an integrated luminosity of 5.6 ab^{-1} and is 40 times higher than the luminosity of the full Run-2 dataset. The Drell-Yan events are generated using two particle generators; $Z/\gamma^* + 0, 1$ jet events are generated inclusively at NLO accuracy using POWHEG [107] with the CT10 PDF set [103]; $Z/\gamma^* + 2$ jet events are generated using ALPGEN [108] with the CTEQ6L PDF set [105] at the LO accuracy. The QED FSR is simulated with Photos++ [104]. Special parameterisations are implemented to mimic the detector response to final-state objects. A more detailed description of this fast simulation chain is provided in Section 7.5.

7.2 Object and event selection

7.2.1 Electrons

The final state of the $H \to ee$ decay is a pair of oppositely charged electrons. They are reconstructed with the algorithms described in Section 6.1 in the region $|\eta| < 2.47$, excluding the $1.37 < |\eta| < 1.52$ range with limited calorimeter coverage. Only electrons with p_{T} above 15 GeV are considered. Since

the $H \to ee$ search suffers from a large irreducible background (Drell-Yan) it is important to ensure as high efficiency of the signal selection as possible. Taking this into account, the Loose identification WP is used (the corresponding efficiency as a function of the electron E_{T} is presented in Figure 6.3), which is expected to provide on average efficiency of 95% for signal electrons. In order to reduce the number of background electrons coming from hadron decays or induced by pile-up, electrons are required to be isolated. This is provided by selection of the Loose isolation WP, characterised by an efficiency of around 99%. Furthermore, any electrons reconstructed from the clusters with at least one dead cell in the first or second layer of the calorimeter are considered as bad ("BADCLUSELECTRON") and rejected. Further background coming from non-prompt electrons is suppressed by adding requirements on transverse and longitudinal impact parameters. The electron selection criteria are summarised in Table 7.1.

Identification	Loose Likelihood WP
p_{T}	> 15 GeV
$\lvert\eta\rvert$	< 2.47 excluding $1.37 < \lvert\eta\rvert < 1.52$
Quality	Not "BADCLUSELECTRON"
Isolation	Loose WP
Impact parameters	$\lvert d_0^{\mathrm{BL}}$ significance$\rvert < 5$ $\lvert z_0^{\mathrm{PV}} \cdot \sin\theta\rvert < 0.5$ mm

Table 7.1: The electron selection criteria.

7.2.2 Jets

Jets are particularly important in the categorisation of events to select these coming from the VBF production process. The jets used in this analysis are reconstructed from topo-clusters passed on to the anti-k_t algorithm with the radius parameter $R = 0.4$. Only jets within $|\eta| < 4.5$ are considered and

they are required to have p_{T} above 30 GeV. To reduce the pile-up-induced background, jets with $p_{\mathrm{T}} < 60$ GeV and reconstructed in the range $|\eta| < 2.4$ are required to have the value of JVT discriminant larger than 0.59 corresponding to the Medium WP. The MV2c10 tagger at the 60% efficiency WP is employed to identify jets within $|\eta| < 2.5$ that originate from bottom quarks. The jet selection criteria are summarised in Table 7.2.

Algorithm	AntiktTopo4EM
p_{T}	> 30 GeV
$\|\eta\|$	< 4.5
JVT	> 0.59 for $p_{\mathrm{T}} < 60$ GeV and $\|\eta\| < 2.4$
b-jet	MV2c10 60% WP for jets with $\|\eta\| < 2.5$

Table 7.2: The jet selection criteria.

7.2.3 Missing transverse momentum

The $E_{\mathrm{T}}^{\mathrm{miss}}$ is reconstructed as described in Section 6.5. In the $H \to ee$ search, it is an important quantity to discriminate against the $t\bar{t}$ background. Better background rejection can be achieved by imposing a requirement on the $E_{\mathrm{T}}^{\mathrm{miss}}$ significance (defined in Equation 6.7) as it takes into account the event-by-event differences in $E_{\mathrm{T}}^{\mathrm{miss}}$ resolution and is expected to detect real $E_{\mathrm{T}}^{\mathrm{miss}}$ more reliably. The requirement on the value of the $E_{\mathrm{T}}^{\mathrm{miss}}$ significance is imposed at the level of event selection and is discussed later.

7.2.4 Muons

Although no muons are present in the final state of the presented search, they are used in the overlap removal procedure described in the next section. Muons are required to have p_{T} larger than 15 GeV and to be reconstructed within the η range covered by the Inner Detector. They are required to be isolated based on the FCLoose_FixedRad WP. The selection of prompt muons is ensured by applying requirements on the transverse and longitudinal impact parameters. The muon selection criteria are summarised in Table 7.3.

Identification	Loose WP
p_{T}	15 GeV
$\lvert\eta\rvert$	2.5
Isolation	FCLoose_FixedRad WP
Impact parameters	$\lvert d_0^{\mathrm{BL}}$ significance$\rvert < 3$ $\lvert z_0^{\mathrm{PV}} \cdot \sin\theta\rvert < 0.5$ mm

Table 7.3: The muon selection criteria.

7.2.5 Overlap removal

It is possible for one object to be reconstructed by two different algorithms producing different classes of object. For example, the same calorimeter energy deposit may be used in the construction of a jet or an electron. The overlap removal procedure is applied in order to avoid such duplication and choose the best object assignment. Any electrons sharing an ID track with a muon candidate are discarded. Jets within a distance of $\Delta R < 0.2$ of a selected electron or with less than three associated tracks and within $\Delta R < 0.2$ of a selected muon are rejected. Finally, electrons falling into a range within $0.2 < \Delta R < 0.4$ of selected jets may be coming from an EM shower in these jets and are therefore rejected.

7.2.6 Event selection

All data events must pass the Good Runs List (GRL) selection to ensure that they are good for physics analysis. The GRL consists of luminosity blocks (time periods of around 1 minute), for which all detector sub-systems are working properly. There may be also single corrupted or incomplete events due to hardware problems with liquid argon, tile or SCT detectors, which are also rejected. All other requirements are applied to both data and simulated events. Each event is required to have a reconstructed primary vertex with at least two tracks with $p_{\mathrm{T}} > 400$ MeV and $|\eta| < 2.5$ originating from it. A set of

single-electron triggers is used in order to choose the interesting events. The trigger selection changed over the years during Run-2 data-taking, and different p_{T} thresholds, and identification and isolation working points are used. For the 2015 data-taking the electron candidates are required to have p_{T} above 24 or 60 GeV and be identified as Medium LH electrons or have p_{T} larger than 120 GeV and pass the Loose LH identification WP. For the data-taking from 2016 to the end of Run 2, electrons are required to have p_{T} larger than 26, 60 or 140 GeV, with identification WPs Tight, Medium and Loose LH, respectively. There is also additional trigger selection choosing high-p_{T} electrons (with p_{T} above 300 GeV) with no explicit identification requirement. The triggers with lower p_{T} threshold are characterised by worse efficiency in the case of high-p_{T} electrons. This efficiency is recovered by imposing looser identification and isolation selection in triggers with high-p_{T} requirement, which explains the specific choice of a few single-electron triggers combined with a logic OR. The trigger selection is presented in Table 7.4. Events are required to have exactly two opposite-sign electrons with the p_{T} of the leading electron above 27 GeV to ensure high trigger efficiency. Any events with jets identified as fake using a jet cleaning algorithm [109] are rejected as this affects the calculation of the missing transverse momentum. In order to reduce the $t\bar{t}$ background contribution, any event with a jet identified as a b-jet with the 60% efficiency WP of the MV2c10 tagger is discarded. Further reduction of events with semi-leptonic top-quark decays is achieved by requiring the $E_{\mathrm{T}}^{\mathrm{miss}}$ significance to be less than 3.5 $\mathrm{GeV}^{1/2}$.

The agreement of kinematic distributions of the selected events between the MC simulation and the data was validated and found to be good and similar to that of the $H \to \mu\mu$ search, which is presented in details in Section 8.2.

Dataset	p_{T} threshold [GeV]	HLT selection
2015	24	Medium LH identification WP
	60	Medium LH identification WP
	120	Loose LH identification WP
2016–2018	26	Tight LH identification WP $p_{\mathrm{T}}^{\mathrm{varcone20}}/E_{\mathrm{T}} < 0.1$
	60	Medium LH identification WP
	140	Loose LH identification WP
	300	-

Table 7.4: The single electron triggers used in the $H \to ee$ search. Apart from the HLT selection explicitly mentioned in the third column, objects with p_{T} reconstructed at L1 below 50 GeV have to satisfy additional requirements on hadronic and EM activity around the electron at the hardware-level trigger (except for the trigger with p_{T} threshold at 24 GeV during data-taking in 2015, where only requirements on hadronic activity are applied) [110].

7.3 Categorisation

To exploit differences between the $H \to ee$ signal and the background, it is beneficial to separate the selected events into categories with different expected signal-to-background ratio. Seven categories are defined, targeting the two production processes with the highest cross-sections, gluon-gluon fusion and vector boson fusion. The categories are described in more detail in the following sections.

7.3.1 VBF category

The VBF production process is characterised by two high-p_{T} jets produced in opposite forward directions with a large rapidity gap between them. This information is exploited by applying a set of requirements in order to assign events into a single VBF-enriched category:

- two jets with $p_{\mathrm{T}} > 30$ GeV
- $\eta_{j_1} \cdot \eta_{j_2} < 0$
- $\Delta\eta_{jj} > 3$
- $m_{jj} > 500$ GeV.

7.3.2 ggF categories

The events which do not fall into the VBF category are classified as coming from the ggF production process and are split further into six categories. First, the events are classified according to the dielectron system p_{T} into three categories: High-, Medium- and Low-p_{T}^{ee}. Signal events are characterised by higher p_{T}^{ee} values compared to the Drell-Yan dominated background, due to the higher QCD ISR. Thus, the High- and Medium-p_{T}^{ee} categories are expected to have higher signal-to-background ratio than Low-p_{T}^{ee}. Next, each p_{T}^{ee} category is further split into two categories, Central and Forward, depending on the pseudorapidity of the electrons. The distinction in the electron centrality is motivated by the fact that the p_{T} measurement is more precise for the central electrons leading to better dielectron mass resolution and therefore better signal sensitivity. The selection criteria used in the ggF categorisation are summarised in Table 7.5.

Category	Criteria
Central High-p_{T}^{ee}	$p_{\mathrm{T}}^{ee} > 50$ GeV and ($\lvert\eta_{e_1}\rvert < 1$ and $\lvert\eta_{e_2}\rvert < 1$)
Forward High-p_{T}^{ee}	$p_{\mathrm{T}}^{ee} > 50$ GeV and ($\lvert\eta_{e_1}\rvert > 1$ or $\lvert\eta_{e_2}\rvert > 1$)
Central Medium-p_{T}^{ee}	15 GeV $< p_{\mathrm{T}}^{ee} < 50$ GeV and ($\lvert\eta_{e_1}\rvert < 1$ and $\lvert\eta_{e_2}\rvert < 1$)
Forward Medium-p_{T}^{ee}	15 GeV $< p_{\mathrm{T}}^{ee} < 50$ GeV and ($\lvert\eta_{e_1}\rvert > 1$ or $\lvert\eta_{e_2}\rvert > 1$)
Central Low-p_{T}^{ee}	$p_{\mathrm{T}}^{ee} < 15$ GeV and ($\lvert\eta_{e_1}\rvert < 1$ and $\lvert\eta_{e_2}\rvert < 1$)
Forward Low-p_{T}^{ee}	$p_{\mathrm{T}}^{ee} < 15$ GeV and ($\lvert\eta_{e_1}\rvert > 1$ or $\lvert\eta_{e_2}\rvert > 1$)

Table 7.5: Definitions of the six categories targeting the ggF production process.

7.4 Signal and background modelling

The $H \to ee$ search is based on a signal+background fit to the dielectron invariant mass distribution in the range of 110–160 GeV. The signal is expected

to be a narrow peak at around 125 GeV on top of a falling background. The models describing the signal and background contribution are described in the following sections.

7.4.1 Signal modelling

The Higgs boson decay width is predicted by the SM to be around 4 MeV, however, the width of the signal peak is completely dominated by the electron momentum resolution. To account for this and the slightly non-symmetric shape of the signal due to the final state radiation, the signal is modelled as a sum of Crystal Ball (CB) [111] and Gaussian (G) functions:

$$P_{\text{sig}}(m_{ee}; f, \alpha, n, \mu_{\text{CB}}, \sigma_{\text{CB}}, \mu_{\text{G}}, \sigma_{\text{G}}) = (1-f) \cdot CB(m_{ee}; \alpha, n, \mu_{\text{CB}}, \sigma_{\text{CB}}) + f \cdot G(m_{ee}; \mu_{\text{G}}, \sigma_{\text{G}}). \tag{7.1}$$

The parameters α and n describe the power-law tail of the Crystal Ball function and μ_{CB} and σ_{CB} describe its mean and width. The μ_{G} and σ_{G} are the mean and width of the Gaussian function, respectively, and f is the normalisation parameter, describing the fraction of events fitted with the Gaussian function. A signal fit is performed in each analysis category separately to a mass distribution that is a sum of simulated events coming from different Higgs boson production processes. The signal model obtained from the fit to signal MC simulation is later fixed in the combined $S+B$ fit to the data.

7.4.2 Background modelling

Drell-Yan dielectron production is the dominant background process. Smaller contributions come from the $t\bar{t}$ and diboson processes. The background model is inspired by the Z/γ^* line-shape and extended to include more flexibility to fit the data including the additional background processes. The following analytic formula is used as the background model:

$$P_{\text{bkg}}(m_{ee}; m_{BW}, \Gamma_{BW}, \sigma_G, f, b) = f \cdot (BW(m_{BW}, \Gamma_{BW}) * G(\sigma_G))(m_{ee}) + (1-f) \cdot (e^{b \cdot m_{ee}})/m_{ee}^3. \tag{7.2}$$

The BW is the non-relativistic Breit-Wigner function describing the Z/γ^* peak and is defined as:

$$BW(m_{ee}; m_{BW}, \Gamma_{BW}) = \frac{1}{(m_{ee} - m_{BW})^2 + \left(\frac{\Gamma_{BW}}{2}\right)^2}, \tag{7.3}$$

where the mass m_{BW} and width Γ_{BW} parameters are fixed to the Particle Data Group (PDG) values of 91.2 GeV and 2.48 GeV [2], respectively. The Breit-Wigner function is convolved with a Gaussian function to account for resolution effects. The σ_G parameter of the Gaussian function is obtained from a Gaussian fit to the difference in mass between the reconstructed and truth-level final-state electrons using DY MC simulation. The σ_G values are presented in Table 7.6. The last term, which is an exponential function divided by a cubic function is needed to model the $t\bar{t}$ and diboson backgrounds. The parameter b varies between -1 and 1 and the fraction f varies between 0 and 1. The values of b and f parameters in different categories obtained from background-only fits to data are presented in Table 7.7.

Category	σ_G [GeV]
Central High-p_{T}^{ee}	1.82
Forward High-p_{T}^{ee}	2.80
Central Medium-p_{T}^{ee}	1.92
Forward Medium-p_{T}^{ee}	2.88
Central Low-p_{T}^{ee}	1.87
Forward Low-p_{T}^{ee}	2.89
VBF	2.49

Table 7.6: Average m_{ee} resolution as derived from the signal MC simulation and used in the background model as σ_G parameter of the Gaussian function.

Category	b	f
Central High-p_{T}^{ee}	-0.002$\pm$0.002	0.40$\pm$0.03
Forward High-p_{T}^{ee}	0.002$\pm$0.001	0.44$\pm$0.02
Central Medium-p_{T}^{ee}	-0.012$\pm$0.002	0.27$\pm$0.02
Forward Medium-p_{T}^{ee}	-0.008$\pm$0.001	0.35$\pm$0.01
Central Low-p_{T}^{ee}	-0.025$\pm$0.001	0.21$\pm$0.03
Forward Low-p_{T}^{ee}	-0.016$\pm$0.001	0.26$\pm$0.01
VBF	0.003$\pm$0.004	0.40$\pm$0.06

Table 7.7: The fitted values of the background function parameters: the power function exponent b and the fraction parameter f obtained from the background-only fits to data.

7.5 Fast Drell-Yan generator and estimation of background modelling systematic uncertainty

The choice of the background model in the final $S+B$ fit to data is crucial. An incorrect model may lead to bias and introduce a "spurious signal". In order to ensure that the chosen functional form limits this bias, it is necessary to perform a dedicated study using a large-statistics background MC sample. The number of spurious signal events can be extracted through a signal+background fit to mass distributions of signal-free simulated data. These are later assigned as a systematic uncertainty on the final result. As the full simulation of the Drell-Yan process is highly CPU-consuming and takes too much time, a special dedicated fast simulation chain is developed (full simulation of ATLAS detector, digitisation and reconstruction of a single $Z \to ee$ event takes of around 1000 s, whereas the fast generator is quicker by a factor of 10^6). The fast Drell-Yan generator employs two particle generators: POWHEG to generate events inclusively with up to one jet at NLO accuracy and ALPGEN to generate events with exactly two jets with LO accuracy. This particular

choice of the MC generators is supported by the fact that they are very fast (10^3 events per second on one CPU core for POWHEG and 10–20 events per second on one CPU core for ALPGEN) and they have a small fraction of negative weights. The event generation is usually done in the following steps: matrix element calculation, parton shower, underlying event and hadronisation. As leptons are not significantly affected by the QCD showering, this part is skipped in order to improve the speed of the event generation and the following procedure is employed:

1. Matrix element event listings stored in Les Houches Event (LHE) files are read in one-by-one and stored into the HepMC format. The HepMC structure holds the event record separating entries into particles and vertices characterised by a few parameters.

2. The events stored in the HepMC format are passed on to Photos++ to simulate the QED final state radiation.

3. The p_{T}^{ee} spectrum is reweighted to include the effect of parton showering.

4. The detector response to the final-state objects is parameterised using a set of functions derived from fully simulated ATLAS MC samples.

Both POWHEG and ALPGEN samples are produced in two parts corresponding to different m_{ee} ranges to improve the generation efficiency while avoiding bias in the m_{ee} spectrum. For the study presented in the following sections 10^9 and $0.5 \cdot 10^9$ events are generated with POWHEG in the mass ranges $m_{ee} >$ 95 GeV and $60 < m_{ee} < 95$ GeV, respectively. In addition, 10^8 events with $m_{ee} > 95$ GeV and $2.5 \cdot 10^8$ events with $60 < m_{ee} < 95$ GeV are generated with ALPGEN. The POWHEG and ALPGEN samples are combined by scaling them to their corresponding cross-sections (the cross-section for the $Z/\gamma^* + 2$ jet process corresponds to around 10% of the NLO $Z/\gamma^* + 0,1$ jet process cross-section). In total, 5.6 ab^{-1} of data are produced with the fast DY MC generator for the spurious signal study.

7.5.1 Implementation and validation of detector response parameterisations

Since the full GEANT4 simulation of the detector response is the slowest part of the full-chain simulation, it is replaced in the fast DY generator by a set of parameterisations describing the detector response to electrons. There is no explicit energy smearing implemented for the jets used to categorise events into the VBF category. The electron parameterisations are described below.

The electron momentum resolution in the sampling calorimeters depends on a few η-dependent terms and can be parameterised as [112]:

$$\frac{\sigma^2}{E^2} = \frac{A^2}{E} + \frac{B^2 + PU^2}{E^2} + C^2. \tag{7.4}$$

The E is the energy of the incoming particle in GeV. The A term is a stochastic term which describes the fluctuations in the number of electrons and photons produced in an electromagnetic shower. The term B represents the noise from readout electronics, which is more significant in the detection of low-p_{T} electrons. The noise term typically includes also the noise related to pile-up, however, in this case, it is derived using samples with no pile-up contribution. The pile-up term PU is therefore parameterised separately with the following formula:

$$PU = \sqrt{\mu} \cdot \left[60 + 40 \cdot \log\left(E_{\mathrm{T}}/10000\right)/\log\left(5\right)\right], \tag{7.5}$$

where μ is a mean pile-up. E_{T} is fixed to 5000 MeV for $E_{\mathrm{T}} < 5000$ MeV and to 50000 MeV for $E_{\mathrm{T}} > 50000$ MeV. The constant term C usually dominates in case of high-p_{T} electrons and consists of two terms: C_{MC} due to imperfections in the corrections used to estimate electron energies and $C_{Data/MC}$ due to data imperfections in calibration or uniformity of the detector. The above-mentioned terms derived for the electrons in the ATLAS EM calorimeter are presented in Figure 7.1.

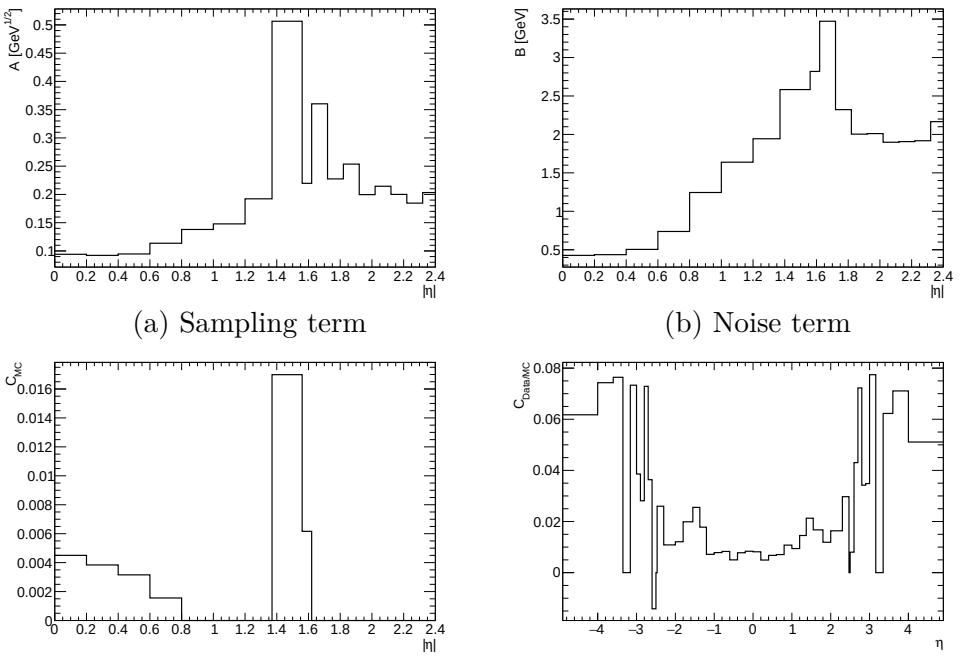

(a) Sampling term (b) Noise term

(c) MC constant term (d) Data-to-MC constant term

Figure 7.1: The parameters affecting the resolution of the electron energy measured in the ATLAS electromagnetic calorimeter [113]. The terms are denoted in the sub-figure captions.

In addition to the energy resolution, it is also important to correctly parameterise the electron object selection efficiencies. For this purpose, 2D efficiency maps are used which describe the efficiency in different electron p_{T} and η bins. The maps are derived separately for the reconstruction, trigger, identification and isolation of the electron objects using the tag-and-probe method. The measurements are performed by the central ATLAS electron identification subgroup and their results are presented in Figure 7.2. Either of the electrons can fire the trigger, hence the final trigger efficiency is calculated as:

$$\epsilon_{\mathrm{trigg}} = 1 - (1 - \epsilon_{\mathrm{trigg},e_1})(1 - \epsilon_{\mathrm{trigg},e_2}) \tag{7.6}$$

where $\epsilon_{\mathrm{trigg},e_1}$ and $\epsilon_{\mathrm{trigg},e_2}$ are the values taken from the efficiency maps for the leading and sub-leading electron, respectively. The electron identification efficiencies presented in Figures 7.2c and 7.2d are derived for Medium LH electrons. However, in the course of the analysis, it was decided to use Loose LH electrons instead to maximise the signal acceptance. This inconsistency is

mitigated by reweighting the mass distribution to data sidebands as described later in Section 7.5.2. The identification efficiency maps are presented separately for the low- and high-p_{T} electrons as they are derived separately using ATLAS data with two different selections. $J/\psi \to ee$ process events are used to derive the identification efficiency for low-p_{T} electrons and $Z/\gamma^* \to ee$ events are used to derive the efficiency for high-p_{T} electrons.

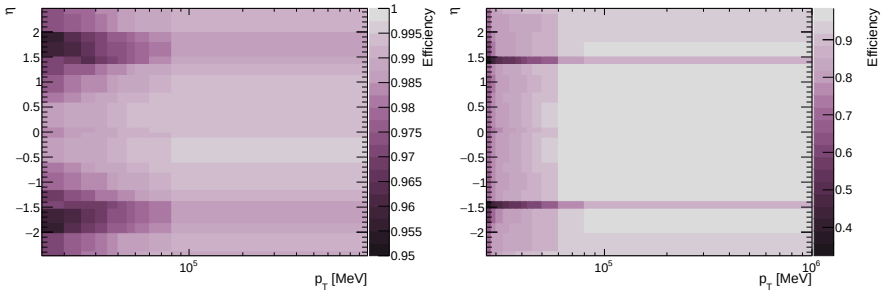

(a) Reconstruction

(b) Trigger

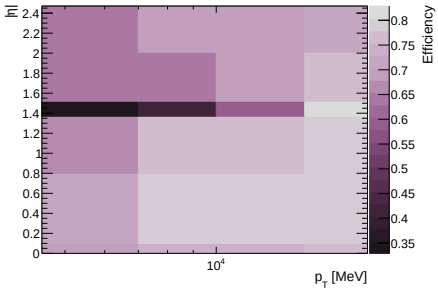

(c) Identification for low-p_{T} e

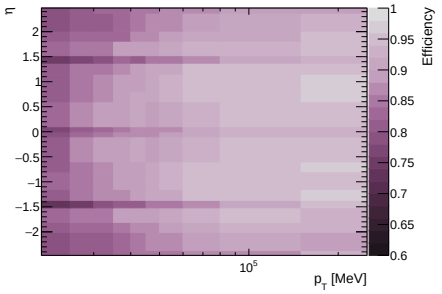

(d) Identification for high-p_{T} e

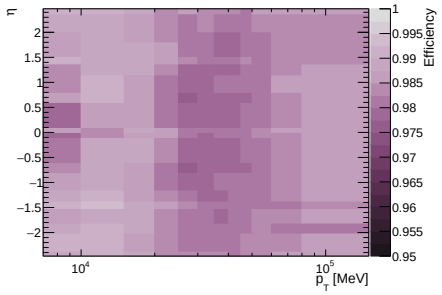

(e) Isolation

Figure 7.2: The electron efficiency in different electron p_{T} and η bins [113]. The efficiencies for different levels of electron detection are denoted in the sub-figure captions.

To mimic the response of the detector to electrons and their final state radiation, the energy of the generated electrons is changed in a procedure called dressing to include the energy of the radiated photons in a cone of a certain

radius around their directions. The dress cone size and the dressing fraction are chosen following a study of their effect on the dielectron mass resolution. Figure 7.3 presents the dielectron mass distributions in the Central High-p_{T}^{ee} category for full and fast simulation of the Z/γ^* process with different electron dressing configurations. It can be observed that increasing the cone size improves the resolution while decreasing the dressing fraction worsens it. It is therefore decided that the most optimal resolution is achieved with the dressing fraction of 1 and the dressing cone size of $\Delta R = 0.02$. Table 7.8 presents a comparison of the means of the dielectron mass in ggF analysis categories for the fully simulated background sample and sample generated with the fast DY generator with the chosen electron dressing configuration. It can be appreciated that the ratios of the two means are very close to unity.

The detector response parameterisations are validated by comparing the distributions of relevant variables, like the ones used for the categorisation or the invariant mass, between the fully simulated sample and the one generated with the fast DY MC generator. Figure 7.4a presents this comparison for the p_{T} of the dielectron system and Figure 7.4b presents the summed distributions of η_{e_1} and η_{e_2} (although η_{e_1} and η_{e_2} are used separately in the categorisation). The p_{T}^{ee} distribution shows a reasonable agreement. For values up to 100 GeV the ratio between full and fast simulation lies between 5 and 10%. The η distributions present good agreement although in the forward region the fast simulation is typically above the distribution from the fully simulated sample and their ratio reaches below 0.9 for highest $|\eta|$ values. Figure 7.5 shows a comparison of the dielectron invariant mass distributions in the ggF categories. The distributions show that the resolution in fast DY MC generator roughly matches the one in the full simulation of the ATLAS detector. In the region where the fitting range starts, the ratio between full and fast simulation is close to unity with a small slope visible. Although the agreement between the two samples is not perfect, it is sufficiently good, and the fast DY MC can be used as pseudo-data for the estimation of the spurious signal systematic uncertainty.

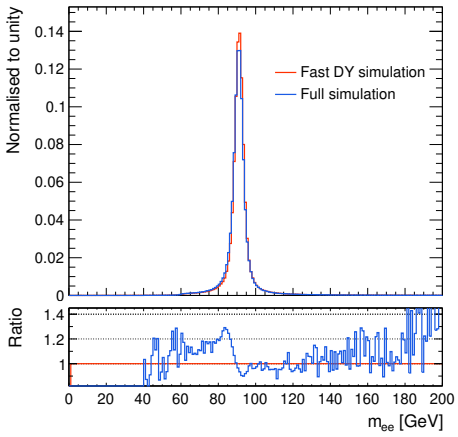

(a) Fraction: 1, cone size: 0.1

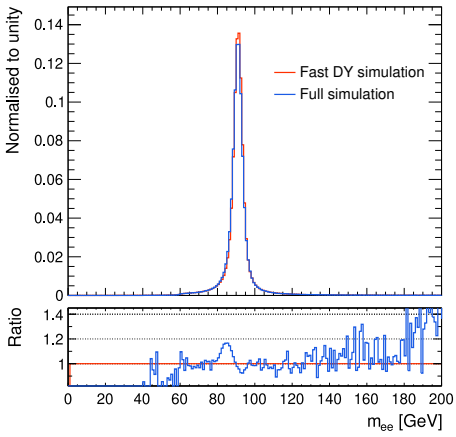

(b) Fraction: 1, cone size: 0.05

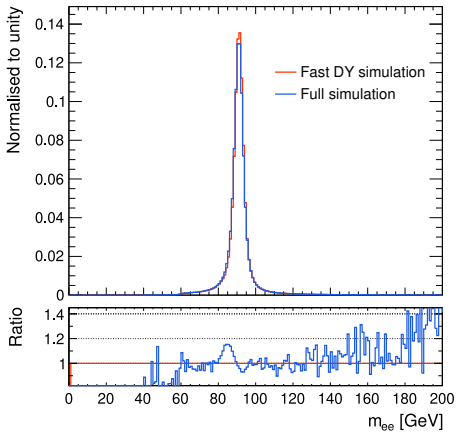

(c) Fraction: 1, cone size: 0.02

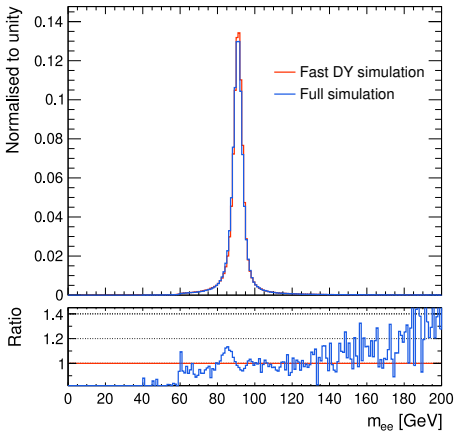

(d) Fraction: 0.75, cone size: 0.1

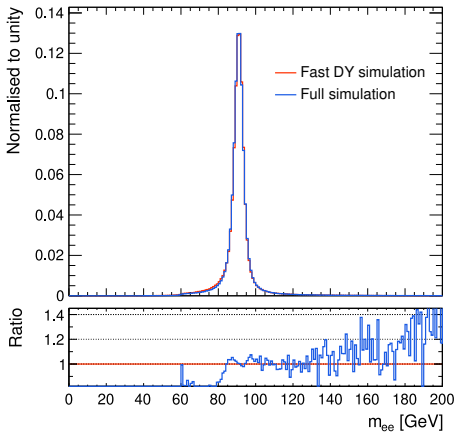

(e) Fraction: 0.5, cone size: 0.1

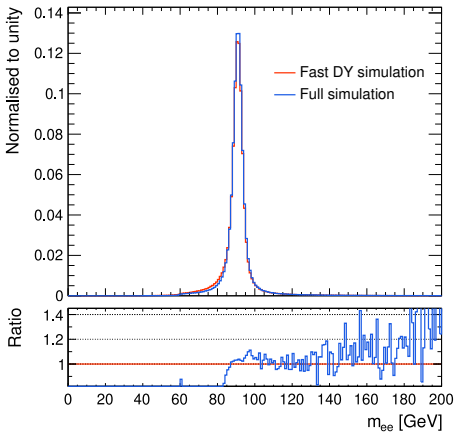

(f) Fraction: 0.25, cone size: 0.1

Figure 7.3: The upper panels present the dielectron mass distribution in the Central High-p_{T}^{ee} category generated with Fast DY generator (orange histograms) with different electron dressing configurations indicated in the sub-figure captions and full simulation (blue histogram) of the Z/γ^* background. The lower panels present the ratio of the fast to full simulation.

Category	$\mu_{\text{Full-sim}}$ [GeV]	$\mu_{\text{Fast-DY}}$ [GeV]	$\frac{\mu_{\text{Full-sim}}}{\mu_{\text{Fast-DY}}}$
Central High-p_{T}^{ee}	90.693	90.848	0.998
Forward High-p_{T}^{ee}	90.517	90.928	0.995
Central Medium-p_{T}^{ee}	90.537	90.667	0.999
Forward Medium-p_{T}^{ee}	90.308	90.750	0.995
Central Low-p_{T}^{ee}	90.483	90.626	0.998
Forward Low-p_{T}^{ee}	90.264	90.704	0.995

Table 7.8: Means and mean-ratios of the dielectron mass distributions for the full simulation background MC sample and the sample generated with the fast DY generator with the dressing fraction of 1 and dressing cone size of 0.02 for electrons. The values are provided for the ggF analysis categories.

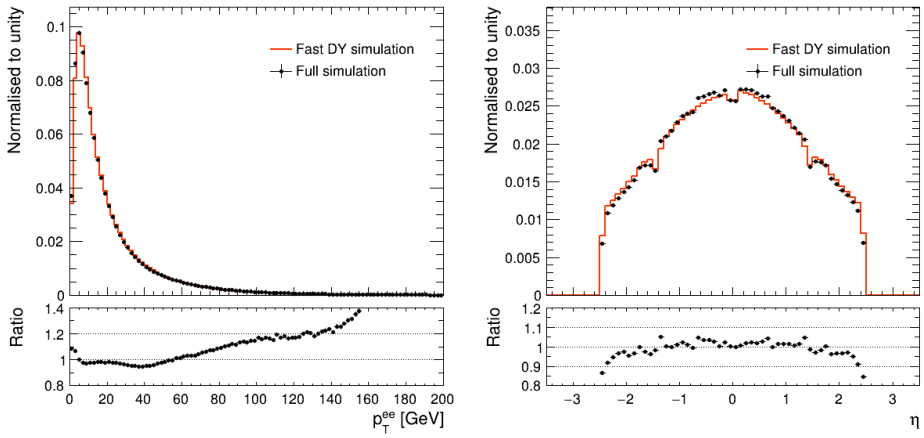

(a) p_{T} of the dielectron system (b) Summed η_{e_1} & η_{e_2} distributions

Figure 7.4: The upper panels present the distributions indicated in the sub-figure captions for the fast Drell-Yan MC simulation (orange histogram) and fully simulated ATLAS MC sample (black points) of the Z/γ^* background process. The distributions are provided only for the part of the fast simulation generated with POWHEG for the consistency with fully simulated sample produced with the same generator. The distributions are normalised to unity to allow for shape comparison. The lower panels show the ratio of the full to the fast simulation.

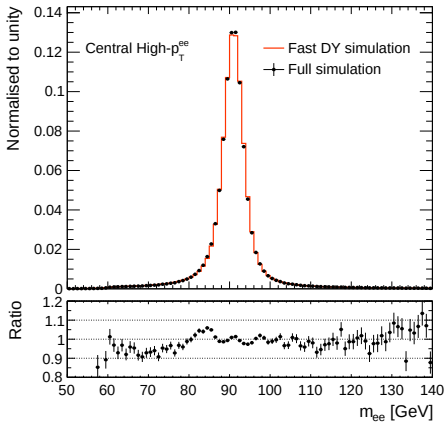

(a) Central High-p_{T}^{ee}

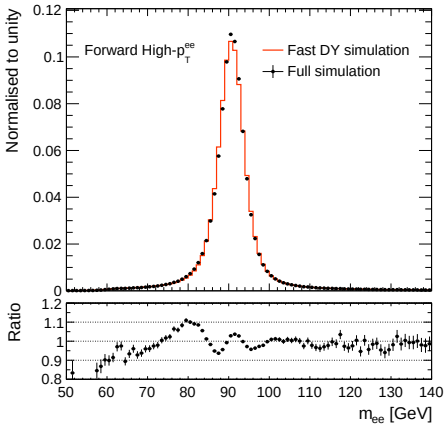

(b) Forward High-p_{T}^{ee}

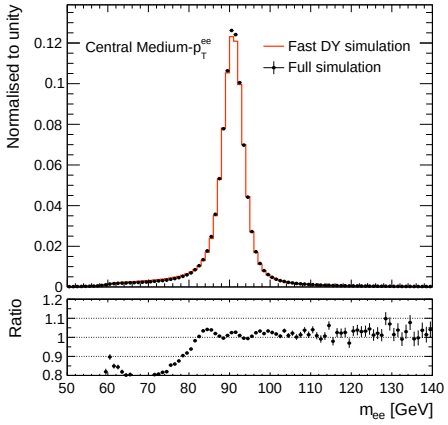

(c) Central Medium-p_{T}^{ee}

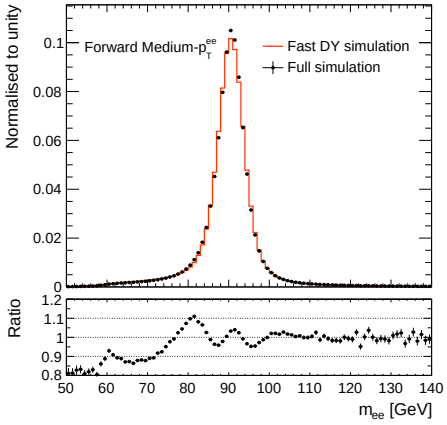

(d) Forward Medium-p_{T}^{ee}

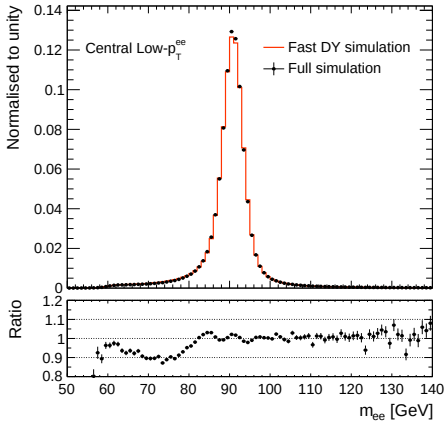

(e) Central Low-p_{T}^{ee}

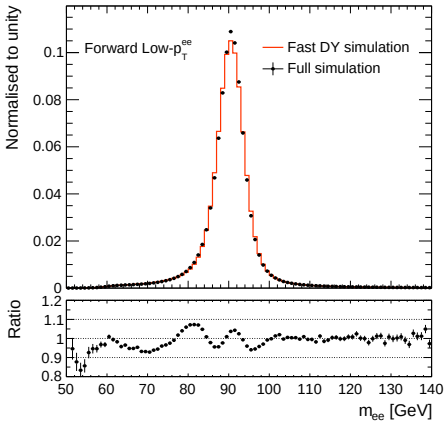

(f) Forward Low-p_{T}^{ee}

Figure 7.5: The upper panels present the dielectron mass distributions in the ggF analysis categories indicated in the sub-figure captions for the fast Drell-Yan MC simulation (orange histogram) and full simulation (black points) of the Z/γ^* process. The distributions are provided only for the part of the fast simulation generated with POWHEG for the consistency with fully simulated sample produced with the same generator. The distributions are normalised to unity to allow for shape comparison. The lower panels show the ratio of the full to the fast simulation.

7.5.2 Reweighting of the fast DY simulation to data sidebands

As presented in Figure 7.5 the mass distributions generated with the fast DY generator show good but not perfect agreement with the fully simulated ATLAS MC sample. To account for any differences between the fast and full simulation as well as differences between the simulation and the data sidebands (mass region between 110 and 160 GeV with blinded (120, 130) GeV range as most of the $H \to ee$ signal is expected there), the following procedure is employed:

1. The ratio of the mass distributions in the data sidebands to the fast DY generator is calculated in the fitting range for each analysis category.
2. A linear fit is performed to the ratio in each category.
3. The number of events in each bin of the DY template is multiplied by the value of the fitted function at the bin centre.

This procedure is similar to the one first introduced in the measurement of the Higgs boson production with diphoton final state using 7 and 8 TeV ATLAS data from Run 1 [114]. Figure 7.6 presents the invariant mass distributions in the fitting range in categories for the fast DY MC simulation and the data in the sidebands along with their ratio, and a linear fit to this ratio. The spurious signal is estimated from the fits to the fast simulation before and after reweighting. However, the estimates without reweighting are used only as a cross-check to ensure the chosen function is able to fit the distribution with the changed slope, without significantly changing the number of spurious signal events. This is discussed later.

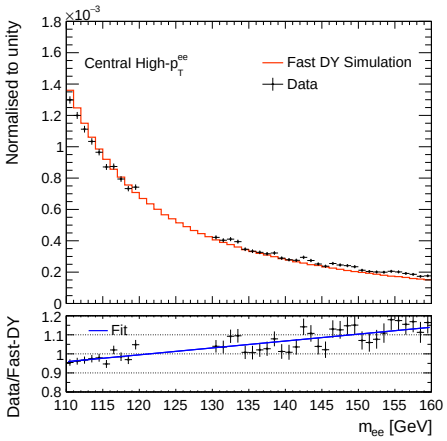

(a) Central High-p_{T}^{ee}

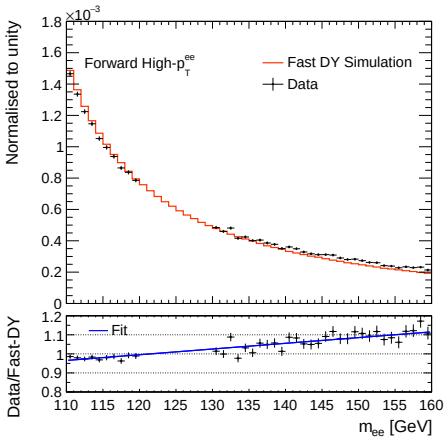

(b) Forward High-p_{T}^{ee}

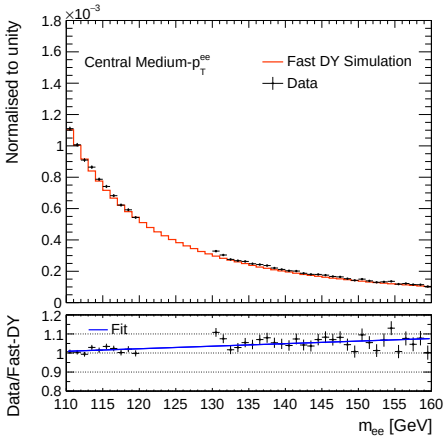

(c) Central Medium-p_{T}^{ee}

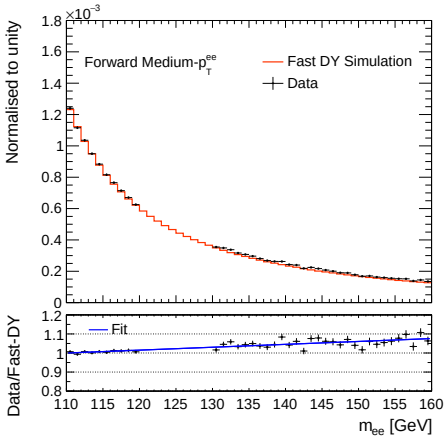

(d) Forward Medium-p_{T}^{ee}

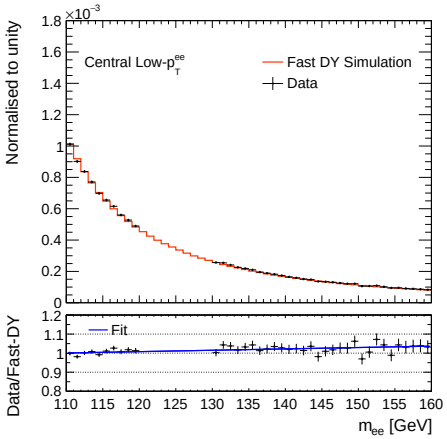

(e) Central Low-p_{T}^{ee}

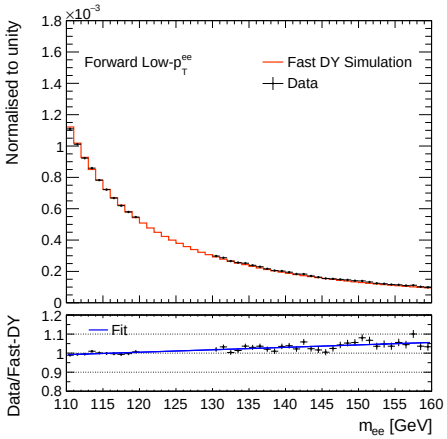

(f) Forward Low-p_{T}^{ee}

Figure 7.6

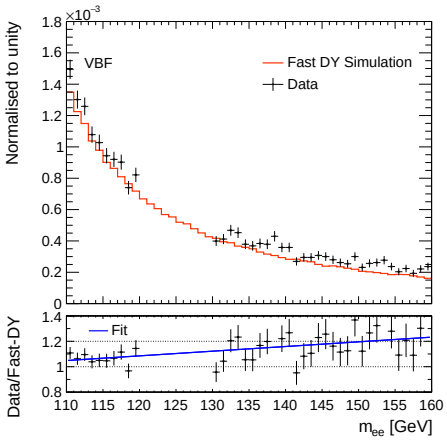

(g) VBF

Figure 7.6: The upper panels present the dielectron mass distributions for the fast DY MC simulation (orange histogram) and full Run-2 ATLAS dataset (black points) in the analysis categories indicated in the sub-figure captions. The distributions are normalised to unity to allow for shape comparison. The black points in the lower panel represent the ratio of the fast DY MC simulation to the data, and the blue line is the 1^{st}-order polynomial fit.

7.5.3 Spurious signal fits and mass scan

The spurious signal systematic uncertainty is estimated by performing a $S+B$ fit to the signal-free pseudo-data generated with the fast DY MC generator. The number of signal events from such fit is spurious and taken as the uncertainty due to the background modelling in a given analysis category.

Example fits to the reweighted fast simulation are presented in Figure 7.7. The signal shape in these fits is obtained from a fit to signal MC simulation with Higgs boson mass generated at 125 GeV and has no free parameters. The combined $S+B$ model generally fits well the mass distributions with only slight mis-modelling visible, mostly at the beginning of the fitting range where the distribution is very steep. In some categories the fitted spurious signal is negative, hence, the signal peak is not visible there. In general, the number of spurious signal events in all categories is small so to make it visible it is multiplied by a factor of 100. Table 7.9 presents the fitted spurious signal strength in the categories and the results are again presented

graphically in Figure 7.8, where the error bars represent the 1σ statistical uncertainty. All values are consistent with zero within one or two times the statistical uncertainty even though the used sample corresponds to a 40 times higher luminosity than the luminosity of the full Run-2 dataset.

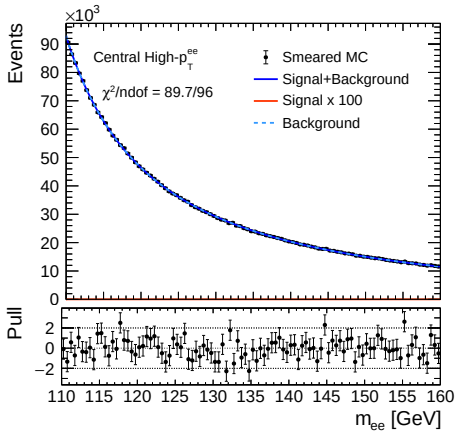

(a) Central High-p_{T}^{ee}

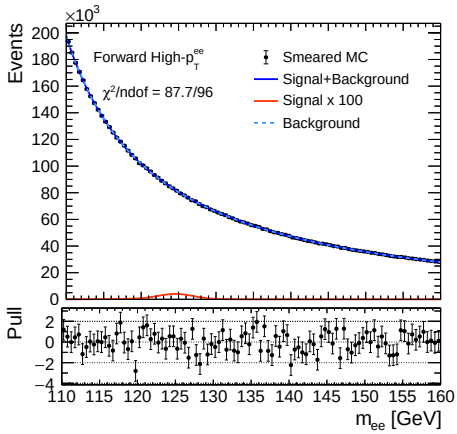

(b) Forward High-p_{T}^{ee}

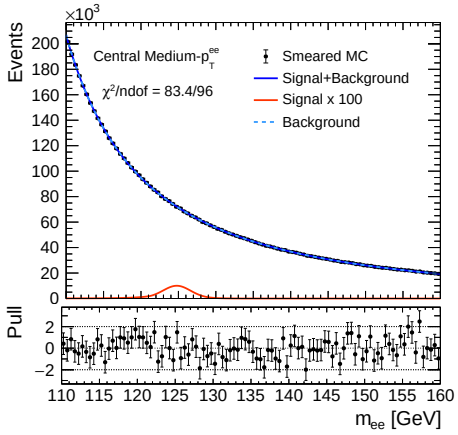

(c) Central Medium-p_{T}^{ee}

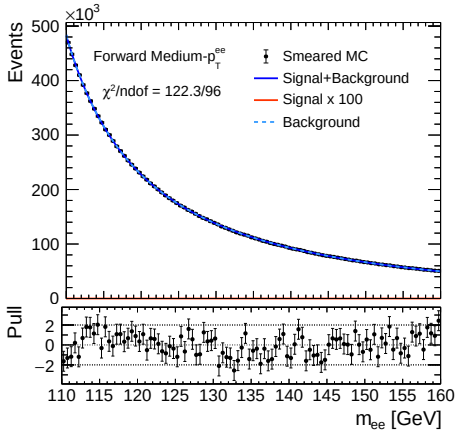

(d) Forward Medium-p_{T}^{ee}

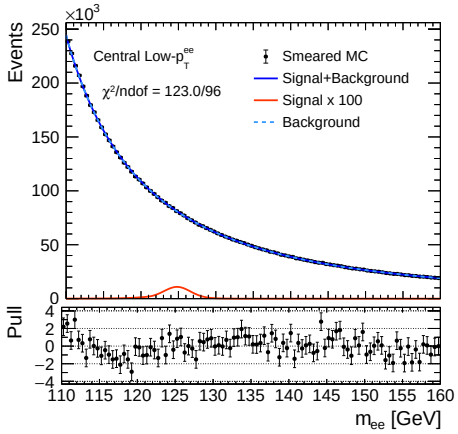

(e) Central Low-p_{T}^{ee}

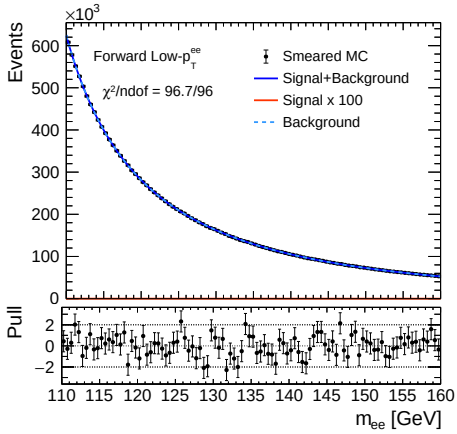

(f) Forward Low-p_{T}^{ee}

Figure 7.7

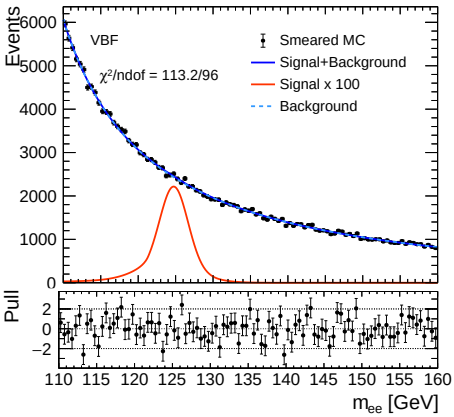

(g) VBF

Figure 7.7: Likelihood $S+B$ fits to dielectron invariant mass in the categories indicated in the sub-figure captions. The signal shape used here is obtained from a fit to signal MC simulation with Higgs boson mass generated at 125 GeV and has no free parameters. Black points in the upper panels represent the reweighted fast DY MC to the data sidebands. The solid blue line is the combined signal+background model, the dashed light-blue line is the background model and the solid orange line is the fitted spurious signal peak multiplied by 100 to make it visible. The lower panels show the pull distributions, where pull value is the difference between the data point and the fitted function value divided by the uncertainty of the point.

Category	μ_{SS}
Central High-p_{T}^{ee}	-0.011$\pm$0.057
Forward High-p_{T}^{ee}	0.057$\pm$0.067
Central Medium-p_{T}^{ee}	0.057$\pm$0.074
Forward Medium-p_{T}^{ee}	-0.099$\pm$0.083
Central Low-p_{T}^{ee}	0.11$\pm$0.15
Forward Low-p_{T}^{ee}	-0.23$\pm$0.17
VBF	0.046$\pm$0.050

Table 7.9: The spurious signal strength μ_{SS} and its statistical uncertainty in the analysis categories, obtained from the likelihood $S+B$ fits to the fast DY MC simulation reweighted to data sidebands. The signal shape used in these fits is obtained from a fit to signal MC simulation with Higgs boson mass generated at 125 GeV and has no free parameters. The μ_{SS} correspond to a reference branching ratio of $\mathcal{B}(H \to ee) = 0.1\%$.

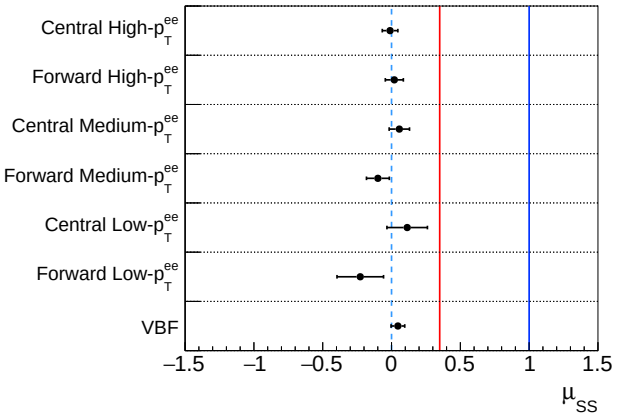

Figure 7.8: The spurious signal strength μ_{SS} in analysis categories obtained from the likelihood S+B fits to the fast DY MC simulation reweighted to data sidebands. The signal shape used here is obtained from a fit to signal MC simulation with Higgs boson mass generated at 125 GeV and has no free parameters. The error bars show the 1σ statistical uncertainty. The solid blue line corresponding to $\mu = 1$ indicates the reference point of $\mathcal{B}(H \to ee) = 0.1\%$. The solid red line represents the expected exclusion of $\mathcal{B}(H \to ee) < 0.035\%$.

It is important that the chosen background model does not introduce any spurious signal events not only near the mass point at 125 GeV, but also in a certain range around it. The quality of the background modelling in the signal region is checked by performing a series of $S+B$ fits in all categories with shifted values of the parameters describing the mean of the signal peak, μ_{CB} and μ_{G}, that are modified by offsets of $\Delta m = -5, \cdots, 5$ GeV. The number of spurious signal events at each point for different categories obtained from the fits to the reweighted fast DY MC sample is presented in Figure 7.9. The full procedure is repeated using the fast simulation before the reweighting to the data sidebands and the results are presented in Figure 7.10. In all cases the chosen functional form is able to fit the distributions successfully. The distributions of the number of spurious signal events are roughly similar before and after the reweighting. They usually show the same trends, except for the Forward Low-p_{T}^{ee} category, where the number of spurious signal events after reweighting stays roughly constant for $m_H > 122$ GeV, whereas it increases slightly with increasing hypothetical Higgs boson mass before reweighting of the fast simulation. The final numbers of spurious signal events in each categories as well as their uncertainties are summarised in Table 7.10. The final uncertainty is obtained from the maximum number of spurious signal events obtained from the mass scan performed on the reweighted fast simulation. The difference to the values obtained at $m_H = 125$ GeV before the reweighting of the fast simulation is generally smaller than this final uncertainty.

Furthermore, taking into account the similar trend of the results of the mass scan, the effect of correlating the spurious signal systematic uncertainties across all categories except for the Central Low-p_{T}^{ee}, which shows the opposite trend (increasing spurious signal for higher m_H) is tested. The effect is small and the value of the expected exclusion limit on $\mathcal{B}(H \to ee)$ is changing from $3.5 \cdot 10^{-4}$ to $3.6 \cdot 10^{-4}$. In the end, however, the uncorrelated scenario is used, as the number of spurious signal events obtained from fits for $m_H = 125$ GeV is not statistically significant.

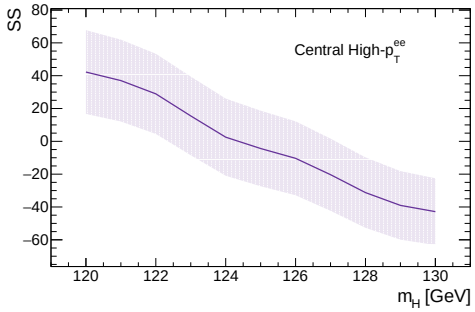

(a) Central High-p_{T}^{ee}

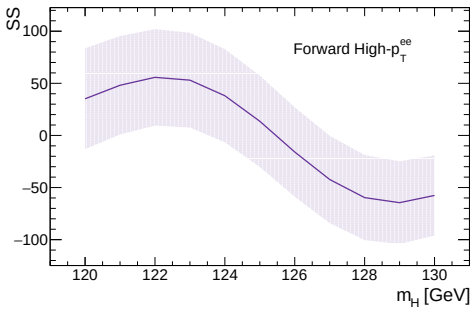

(b) Forward High-p_{T}^{ee}

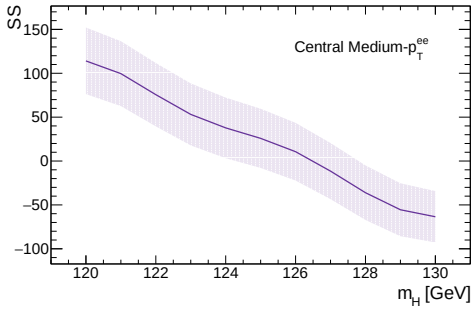

(c) Central Medium-p_{T}^{ee}

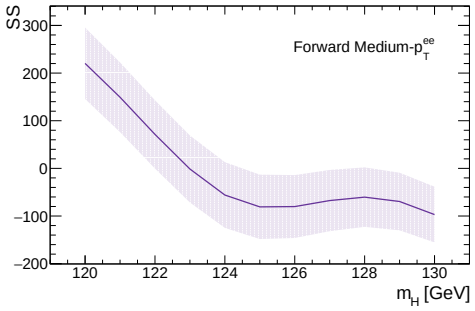

(d) Forward Medium-p_{T}^{ee}

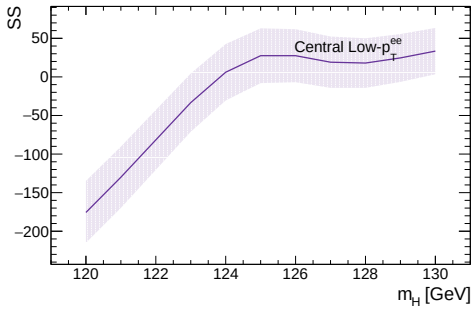

(e) Central Low-p_{T}^{ee}

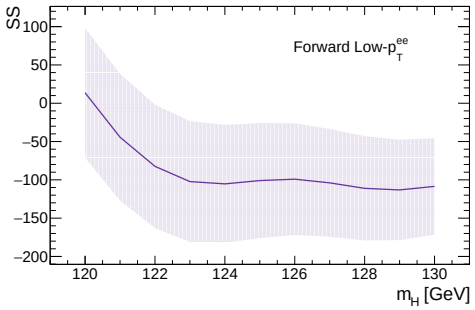

(f) Forward Low-p_{T}^{ee}

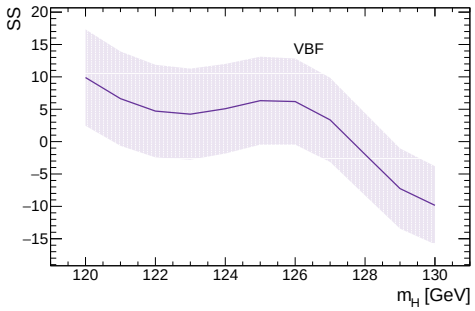

(g) VBF

Figure 7.9: The number of spurious signal events obtained by performing a likelihood $S+B$ fit to the mass distributions in the analysis categories indicated in the sub-figure captions to reweighted fast DY MC to data sidebands. The fits are performed for varying $H \to ee$ signal peak position between 120 and 130 GeV with a step size of 1 GeV.

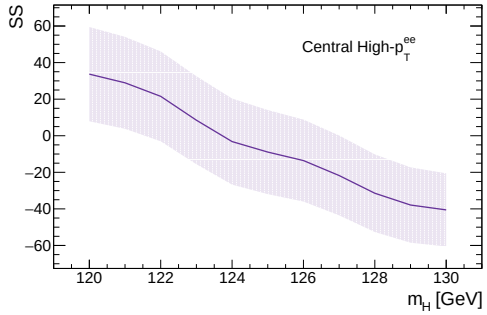

(a) Central High-p_{T}^{ee}

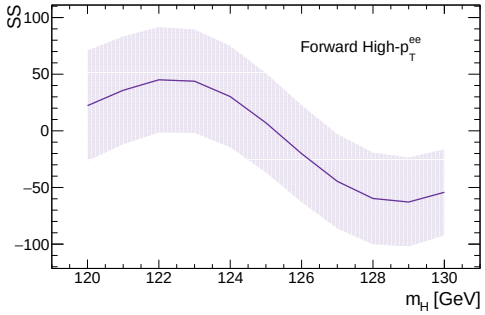

(b) Forward High-p_{T}^{ee}

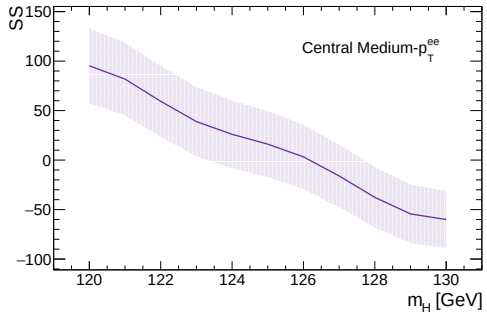

(c) Central Medium-p_{T}^{ee}

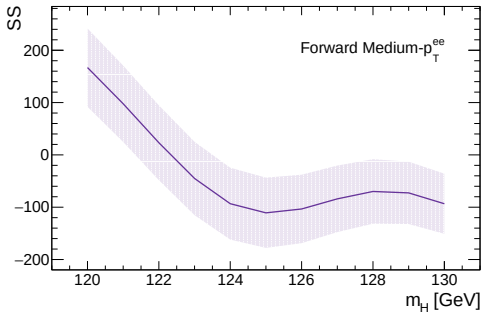

(d) Forward Medium-p_{T}^{ee}

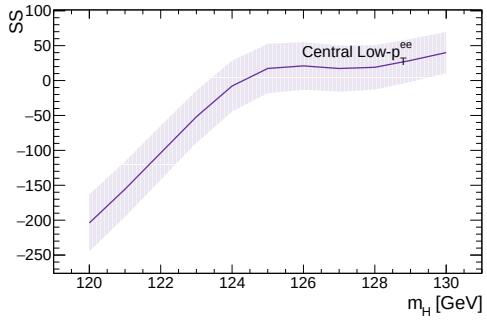

(e) Central Low-p_{T}^{ee}

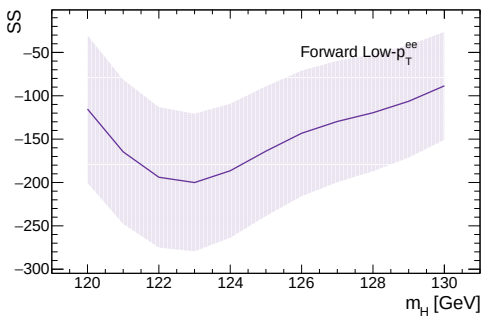

(f) Forward Low-p_{T}^{ee}

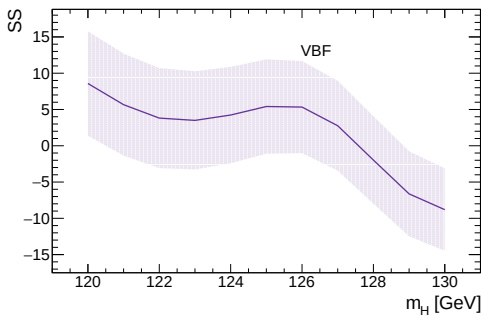

(g) VBF

Figure 7.10: The number of spurious signal events obtained by performing a likelihood $S+B$ fit to the mass distributions in the analysis categories indicated in the sub-figure captions to fast DY MC before reweighting to data sidebands. The fits are performed for varying $H \to ee$ signal peak position between 120 and 130 GeV with a step size of 1 GeV.

Category	N_{SS} before rw	N_{SS} after rw	max $\lvert N_{SS}\rvert$
Central High-p_{T}^{ee}	-9$\pm$23	-4$\pm$23	43
Forward High-p_{T}^{ee}	7$\pm$44	14$\pm$44	65
Central Medium-p_{T}^{ee}	16$\pm$33	26$\pm$34	114
Forward Medium-p_{T}^{ee}	-110$\pm$67	-81$\pm$68	220
Central Low-p_{T}^{ee}	17$\pm$35	28$\pm$36	176
Forward Low-p_{T}^{ee}	-164$\pm$75	-101$\pm$75	113
VBF	5.4$\pm$6.5	6.3$\pm$6.8	9.9

Table 7.10: The number of spurious signal events obtained from $S+B$ fits to fast DY MC simulation. The second and third column correspond to unreweighted and reweighted fast simulation to data sidebands with signal shape obtained from a fit to signal MC simulation with Higgs boson mass generated at 125 GeV. The presented uncertainties are statistical. The fourth column presents the maximum absolute number of spurious signal events in $S+B$ fits to reweighted fast simulation of the Drell-Yan background when varying the signal peak position between 120 and 130 GeV. The values presented in the last column are assigned as the final background modelling systematic uncertainty for a given category.

7.6 Signal systematic uncertainties

The impact of the systematic uncertainties on the measured value of the signal strength is presented in Figure 7.11. The naming convention for the uncertainties presented there is explained in Table 7.11. The spurious signal is the leading systematic uncertainty in this search. The other systematic uncertainties can be divided into two types, theoretical and experimental. The theoretical systematic uncertainties comprise the uncertainties due to QCD scale, parton distribution functions, underlying event tune and parton showering, and are evaluated using truth-level MC simulation. The experimental uncertainties are derived for each object used in the search by a dedicated performance group within the ATLAS Collaboration and they are presented in Table 7.12. Among the experimental systematic uncertainties, the one affecting the measurement

the most is the electron energy scale and resolution, which affects the shape and normalisation of the m_{ee} distribution.

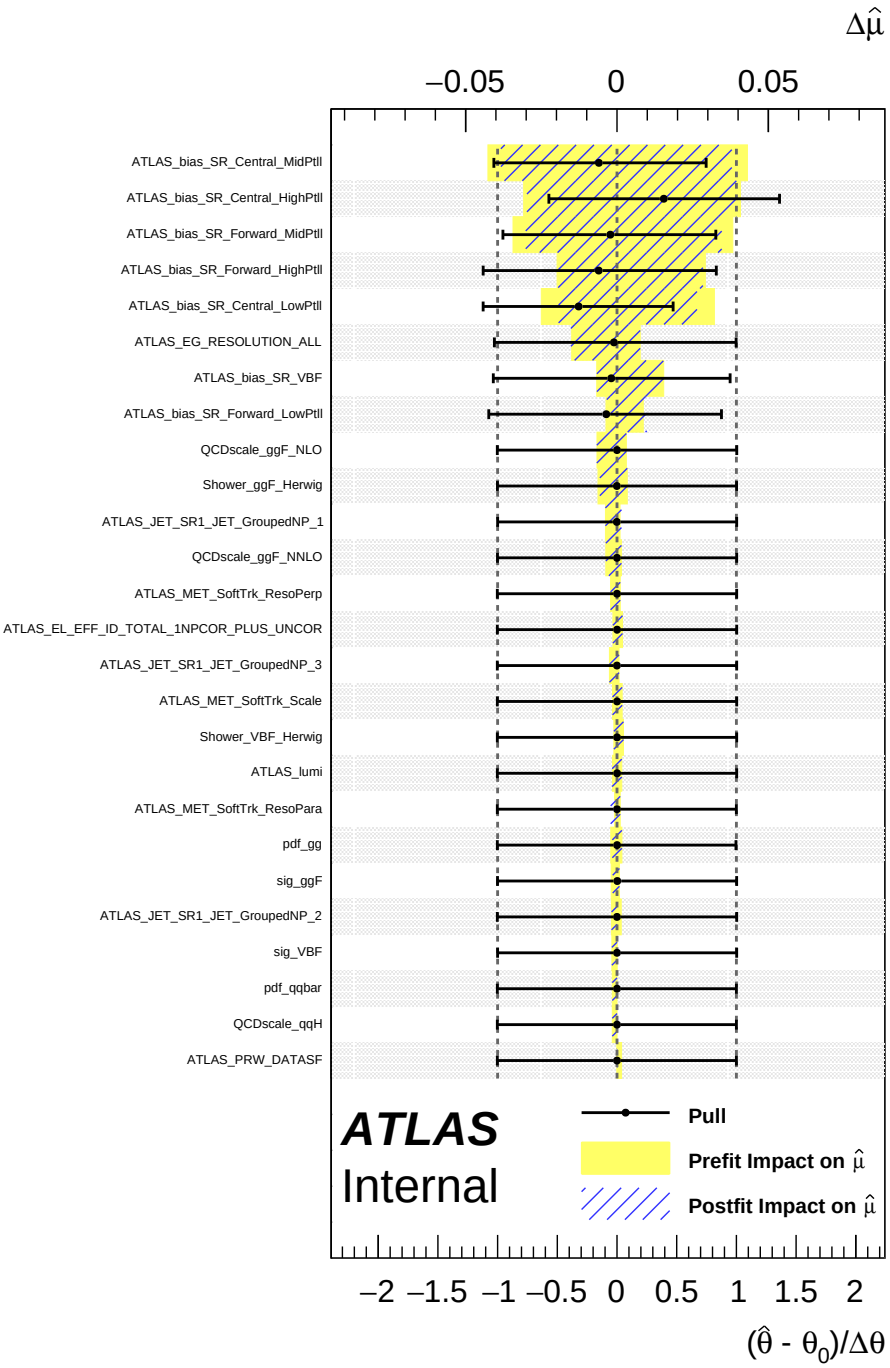

Figure 7.11: Impact of the systematic uncertainties on the observed signal strength μ [115]. The naming convention of uncertainties presented here is explained in Table 7.11.

Type	Name	Description
Theoretical	QCDscale_ggF_<order> and QCDscale_qqH	Highest variations in QCD scale for ggF and VBF processes
	Shower_<process>_Herwig	Parton shower modelling uncertainty estimated by comparing Herwig to Pythia for the given process
	pdf_gg and pdf_qqbar	Uncertainties due to PDF choice for ggF and VBF samples
	sig_<process>	Uncertainty on the production cross-section for the given process
Experimental	ATLAS_bias_SR_<category-name>	Background modelling uncertainty (spurious signal)
	ATLAS_EG_RESOLUTION_ALL	Electron momentum scale and resolution uncertainty
	ATLAS_EL_EFF_ID_TOTAL_1NPCOR_PLUS_UNCOR	Electron identification efficiency uncertainty
	ATLAS_JET_SR1_JET_GroupedNP_<N>	Jet energy scale and resolution uncertainties
	ATLAS_MET_SoftTrk_<X>	Track soft-term scale and resolution uncertainty
	ATLAS_Lumi	Uncertainty of the luminosity measurement
	ATLAS_PRW_DATASF	Pile-up reweighting uncertainty

Table 7.11: The naming convention for the systematic uncertainties presented in Figure 7.11.

Object	Uncertainty type
Luminosity	Combined 2015-2018 integrated luminosity uncertainty
Electron	Trigger, isolation, identification and reconstruction efficiency Energy scale and resolution
$E_{\mathrm{T}}^{\mathrm{miss}}$	Track soft-term scale and resolution
Jet	Energy scale and resolution, JVT efficiency, b-tagging efficiency

Table 7.12: The experimental uncertainties affecting the measurement of the $H \to ee$ signal strength.

7.7 Results

The results presented in this section come from Ref. [116]. The background-only likelihood fits to the dielectron mass distribution in the analysis categories are presented in Figure 7.12. The signal presented there is the SM prediction scaled to the branching ratio of $\mathcal{B}(H \to ee) = 2\%$ to make it visible. The expected signal and background yields along with their ratio and the number of observed events in the Run-2 data in the signal region for $120 < m_{ee} < 130$ GeV are presented in Table 7.13. As expected, the signal-to-background ratios are better in central categories and improve with increasing p_{T}^{ee}. The highest S/B is for the VBF category. The results using full Run-2 data show no evidence for the $H \to ee$ decay. The best fit value of the branching ratio is

$$\mathcal{B}\,(H \to ee) = (0.0 \pm 1.7(\text{stat.}) \pm 0.6(\text{syst.})) \cdot 10^{-4}. \tag{7.7}$$

The uncertainty is dominated by data statistics. The systematic uncertainty is dominated by the background modelling component. The observed (expected) limit on the branching ratio at the 95 % confidence level is set at $3.6 \cdot 10^{-4}$ ($3.5 \cdot 10^{-4}$). The observed result represents a significant improvement with respect to the result of $1.9 \cdot 10^{-3}$ presented by the CMS Collaboration using Run-1 dataset [89].

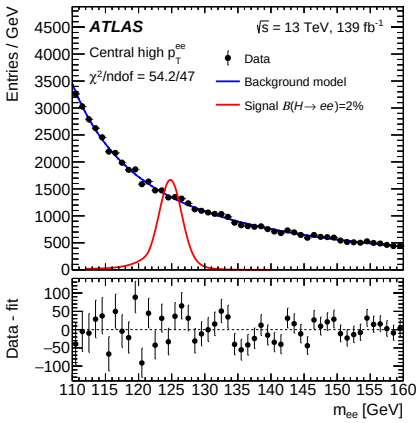

(a) Central High-p_{T}^{ee}

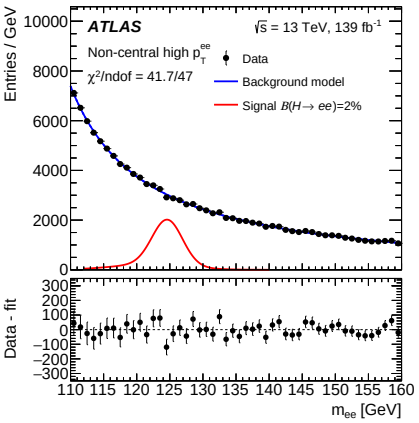

(b) Forward High-p_{T}^{ee}

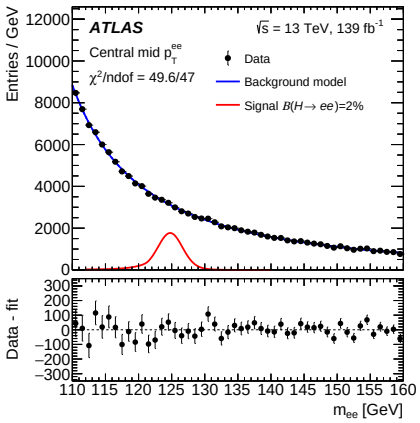

(c) Central Medium-p_{T}^{ee}

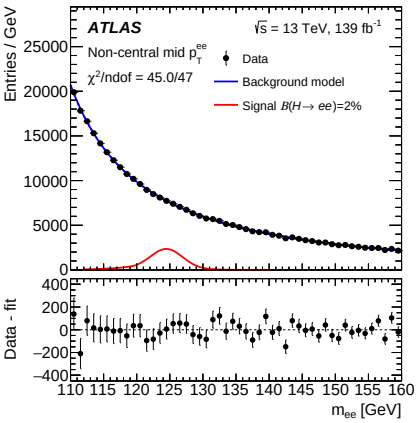

(d) Forward Medium-p_{T}^{ee}

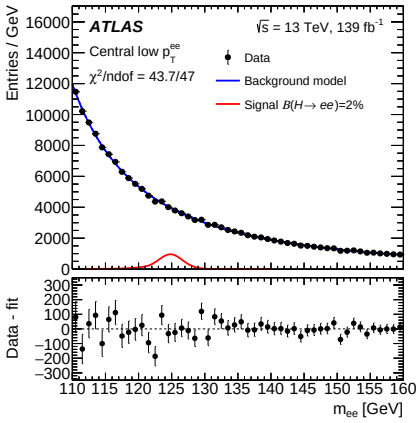

(e) Central Low-p_{T}^{ee}

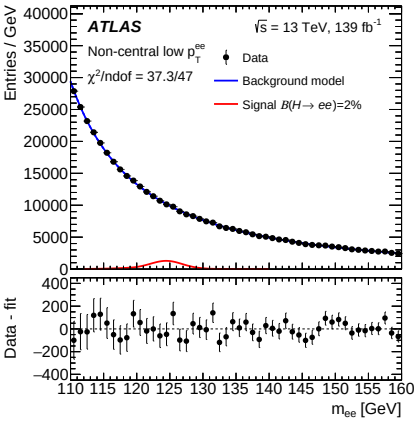

(f) Forward Low-p_{T}^{ee}

Figure 7.12

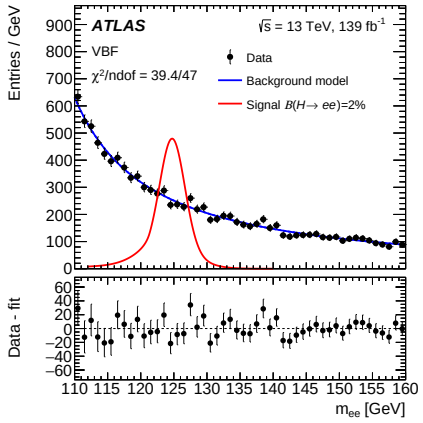

(g) VBF

Figure 7.12: Likelihood background-only fits to the dielectron mass distributions in the analysis categories indicated in the sub-figure captions [116]. The black points represent the ATLAS Run-2 data, the blue line is the background model and the orange line shows the predicted signal distribution for the arbitrary branching fraction of $\mathcal{B}(H \to ee) = 2\%$ for visibility. The lower panel presents the difference between the data and the fit.

Category	S	B	S/B	Data
Central High-p_{T}^{ee}	380	13400	0.028	13625
Forward High-p_{T}^{ee}	590	29900	0.020	30164
Central Medium-p_{T}^{ee}	420	30700	0.014	31182
Forward Medium-p_{T}^{ee}	710	74900	0.0095	76477
Central Low-p_{T}^{ee}	230	39200	0.0057	39872
Forward Low-p_{T}^{ee}	390	98500	0.0039	100844
VBF	120	2530	0.049	2561

Table 7.13: The expected signal (S) and background (B) yield, their ratio (S/B) and the number of observed data events in the signal region corresponding to $120 < m_{ee} < 130$ GeV, presented for each analysis category [116]. The number of signal events is presented for $\mathcal{B}(H \to ee) = 0.1\%$, whereas the background yield is obtained from a background-only fit to data.

Chapter 8

Search for the Higgs boson decay to dimuons

Identification of the $H \to \mu\mu$ decay would allow measurement of the yet unobserved Higgs boson coupling to second-generation fermions. Its very low SM branching ratio of $\mathcal{B}(H \to \mu\mu) = 2.17 \cdot 10^{-4}$ [15] leaves room for a potential new physics contribution [30].

Searches for this decay have been performed several times in ATLAS: using data from Run 1 with an integrated luminosity of 24.8 fb^{-1} corresponding to the centre of mass energy of $\sqrt{s} = 7$ and 8 TeV [117], and with $\sqrt{s} = 13$ TeV data from Run 2 corresponding to an integrated luminosity of 36.1 fb^{-1} [28], 79.8 fb^{-1} [118] and 139 fb^{-1} [31] (preliminary result with full Run-2 dataset). The CMS Collaboration also performed this search with the dataset collected in Run 1 corresponding to an integrated luminosity of 5.0 fb^{-1} at 7 TeV and 19.7 fb^{-1} at 8 TeV [89] and using data from Run 2 with $\sqrt{s} = 13$ TeV, and an integrated luminosity of 35.9 fb^{-1} [29].

The analysis strategy is similar to that used in the search for the Higgs boson decay to dielectrons. A loose muon selection is applied to maximise the signal acceptance. Up to one FSR photon candidate is added in the mass calculation to improve the dimuon mass resolution. Events are divided into twenty mutually exclusive categories defined using multivariate techniques and targeting the ggF, VBF and the Higgs boson production associated with a vector boson or $t\bar{t}$ pair. A signal+background fit is performed to invariant mass distribution

in each category using analytic functions to describe the signal and background shapes. The signal strength μ is extracted from the fit. The full analysis is developed excluding the data in the invariant mass region of 120–130 GeV to avoid unconscious biases, so-called "blinding". The analysis uses a few mass regions: the Z control region with the invariant mass between 76 and 106 GeV, the sideband region with $m_{\mu\mu(\gamma)} \in (110, 120) \cup (130, 160)$ GeV and the fit region with the $m_{\mu\mu(\gamma)}$ in the range 110–160 GeV.

8.1 Data and simulated event samples

The search presented here is performed using data collected by the ATLAS detector in pp collisions at the centre of mass energy of 13 TeV during Run 2 and corresponding to an integrated luminosity of 139 fb^{-1}.

A signal and background MC simulation is used to optimise the selection, categorisation and to study the signal and background modelling, as well as, the recovery of FSR photons.

The signal MC simulation is prepared with the same setup as for the $H \to ee$ signal presented in Section 7.1 with the only exception being that the Higgs boson decays to $\mu\mu$ instead of ee.

The MC simulation of the Z/γ^* background for the study of the background modelling is generated with Sherpa 2.2.1 [119] using the NNPDF3.0NNLO [101] PDF set. Events with up to two jets are generated with NLO matrix elements and with three or four jets with LO matrix elements calculated with the Comix [120] and OpenLoops [121, 122] libraries. The sample is normalised to an NNLO prediction [123]. An additional sample with electroweak Z boson production with up to two additional jets is generated with the same setup but using LO matrix elements. The Z/γ^* sample for the study of FSR recovery efficiency is generated with the same setup as the Z/γ^* sample described in Section 7.1, but with the Z/γ^* decaying to a pair of oppositely-charged muons.

Simulation of the $t\bar{t}$ and single-top backgrounds is performed with POWHEG-BOX v2 [91–93, 124] generator at NLO accuracy with the NNPDF3.0NLO [101] PDF set. Parton showering, hadronisation and the underlying event are modelled by interfacing events to PYTHIA8 [54] with the A14 [125] set of tune parameters and the NNPDF2.3LO [101] PDF set. The mass of the top quark is set to 172.5 GeV.

The diboson background MC simulation with semi-leptonic decays is generated with SHERPA v2.2.1 [119] and fully-leptonic decays are generated with SHERPA v2.2.2 [119]. In both cases, the NNPDF3.0 [101] PDF set is used. Events with up to one additional parton are generated using NLO matrix elements and with two or three additional partons with LO matrix elements. The loop-induced process $gg \to VV$ is generated using LO matrix elements.

A large-statistics MC simulation of the main background, Drell-Yan, is required to estimate the background modelling systematic uncertainty. Two fast simulation chains are developed for this purpose, with dedicated smearing functions implemented on top of the truth-level objects. The main fast simulation sample with up to three jets is generated with SHERPA v.2.2.4 [126] at leading order accuracy. Events are interfaced to PYTHIA8 for parton showering, hadronisation, QCD ISR and QED FSR. The results obtained with this SHERPA sample are cross-checked using an improved version of the POWHEG +ALPGEN setup described in Section 7.5. The improvements include an implementation of an ISR and FSR parton shower algorithm. The same parameterisations describing the detector response to muons, jets, FSR photons as well as missing transverse energy and inclusion of pile-up jets are implemented in both fast simulation chains.

8.2 Object and event selection

The analysis uses several types of objects to reconstruct the Higgs boson candidates and to categorise events. Muons are the most important objects as the constituents of the $H \to \mu\mu$ final state. Additional jets are required in order to

target events where the Higgs boson is produced in the VBF or $t\bar{t}H$ processes and to aid discrimination against non-Higgs background processes. Furthermore, electrons are used in the selection of events in categories targeting VH or $t\bar{t}H$ production processes or to remove overlaps with jets. Calibrated photons with a loose pre-selection are used to recover the FSR photons added to the invariant mass calculation. Missing transverse energy, $E_{\mathrm{T}}^{\mathrm{miss}}$, is reconstructed in order to apply a selection reducing the background coming from top and diboson processes in ggF and VBF categories as well as in the event categorisation in the VH and $t\bar{t}H$ enriched categories.

8.2.1 Muons

The loose identification WP is chosen for muons in order to maximise the signal acceptance. This WP includes all four types of muons (described in detail in Section 6.2) reconstructed in the $|\eta| < 2.7$ range. Muons coming from Higgs decay are well isolated, hence an isolation selection is applied to reduce the background from non-prompt and fake muons. For this purpose a FixedCutPFlowLoose isolation WP is required, which is characterised by good performance in high pile-up conditions and provides high heavy-flavour jet rejection. Each muon is required to have $p_{\mathrm{T}} > 6$ GeV. Cosmic muons are discarded by implementing cuts on impact parameters: $|d_0^{BL}$ significance$| < 3$ and $|z_0^{PV} \cdot \sin\theta| < 0.5$ mm. All muon selection criteria are summarised in Table 8.1.

8.2.2 Jets

In the search for the $H \to \mu\mu$ decay, jets are useful to target categories sensitive to VBF and $t\bar{t}H$ production. In the presented analysis, jets are reconstructed using particle flow objects passed to the anti-k_t algorithm with the radius parameter $R = 0.4$.

Type	CB, CT, ST, SA
Identification	Loose WP
Isolation	FixedCutPflowLoose WP
p_{T}	$p_{\mathrm{T}} > 6$ GeV
η	$\lvert\eta\rvert < 2.7$
Impact parameters	$\lvert d_0^{BL}$ significance$\rvert < 3$ $\lvert z_0^{PV} \cdot \sin\theta\rvert < 0.5$ mm

Table 8.1: The muon selection criteria.

Jets are required to be within $|\eta| < 4.5$ with p_{T} above 25 GeV in the central region ($|\eta| < 2.4$) and above 30 GeV otherwise. The pile-up contribution in the central region is reduced using the JVT discriminant.

Jets with $|\eta| < 2.5$ can be identified as originating from bottom quarks through the reconstruction of secondary vertices and tracks with large impact parameter from the decay of b-hadrons. For this purpose, a multivariate discriminant MV2c10 is used. Different WPs are chosen to identify b-jets in categories targeting different production processes: the 60% efficiency WP is used in the ggF or VBF categories and the 85% efficiency WP is used in the categories enriched with VH or $t\bar{t}H$ events, where identifying a b-jet with higher efficiency is more important. The jet selection criteria are summarised in Table 8.2.

8.2.3 Missing transverse momentum

Missing transverse momentum is an important quantity to discriminate against the $t\bar{t}$ background in events with at least 2 jets, therefore, it is used as one of the variables in the multivariate event categorisation targeting the ggF and VBF production processes. It is also one of the training variables of the classifier used to categorise events into the VH-enriched category targeting production associated with W boson and is used in the calculation of training variables used to define the $t\bar{t}H$ category.

Algorithm	Particle flow
η	$\lvert\eta\rvert < 4.5$
p_{T}	$p_{\mathrm{T}} > 25$ GeV for $\lvert\eta\rvert < 2.4$ $p_{\mathrm{T}} > 30$ GeV for $2.4 < \lvert\eta\rvert < 4.5$
JVT	JVT> 0.2 for $\lvert\eta\rvert < 2.4$ and 20 GeV $< p_{\mathrm{T}} <$ 60 GeV
b-jet	MV2c10 60% WP in ggF/VBF cat. and 85% WP in $VH/t\bar{t}H$ cat. for jets with $\lvert\eta\rvert < 2.5$

Table 8.2: The jet selection criteria.

8.2.4 Electrons

Electrons in the search for the $H \to \mu\mu$ decays are used in the electron–jet overlap removal and as additional leptons in the categories targeting the VH or $t\bar{t}H$ production processes.

Electrons are required to have p_{T} above 6 GeV and to be reconstructed within the range $|\eta| < 2.47$, excluding the calorimeter transition region (between the barrel and the endcaps), where they are measured with large uncertainties. To ensure the selection of prompt electrons, the Medium LH identification WP is chosen. Additional isolation selection reduces the number of electrons coming from pile-up or decays of hadrons. For this purpose, the FCLoose isolation WP is used. Non-prompt electrons are suppressed by requirements on transverse and longitudinal impact parameters. Furthermore, any electron reconstructed from a cluster with a faulty cell is rejected. The electron selection criteria are summarised in Table 8.3.

8.2.5 Overlap removal

An overlap removal procedure is employed in order to resolve ambiguities in the case when one object is reconstructed by several algorithms. The criteria used to remove objects in this procedure are presented in Table 8.4.

Identification	Medium LH WP
Isolation	FCLoose WP
p_{T}	$p_{\mathrm{T}} > 6$ GeV
η	$\lvert\eta\rvert < 2.47$ excluding crack region ($1.37 < \lvert\eta\rvert < 1.52$)
Quality	Not "BADCLUSELECTRON"
Impact Parameters	$\lvert d_0^{BL}$ significance$\rvert < 5$ $\lvert z_0^{PV} \cdot \sin\theta\rvert < 0.5$ mm

Table 8.3: The electron selection criteria.

8.2.6 Event selection

Common selection

All data events must pass the GRL selection in order to reject periods of unstable beam or detector conditions. Events with jets reconstructed from calorimeter noise or beam halo background are vetoed based on discriminating variables calculated using calorimeter clusters, such as LAr signal shape or total energy of cells with negative energy.

Data and simulated events are selected by triggers requiring the presence of at least one high-p_{T} muon. For the 2015 data-taking period, muons are required to have p_{T} above 20 GeV and to be isolated by imposing a requirement on the isolation variable $p_{\mathrm{T}}^{\mathrm{cone20}}/p_{\mathrm{T}} < 0.12$. For the data-taking period between 2016 and 2018, muons are required to have p_{T} larger than 26 GeV and to satisfy the requirement of $p_{\mathrm{T}}^{\mathrm{varcone30}}/p_{\mathrm{T}} < 0.07$. To improve the trigger efficiency for high-p_{T} muons affected by the isolation selection, an additional trigger with p_{T} threshold at 50 GeV is defined, without any criteria on muon isolation. The single-muon triggers employed in the analysis are summarised in Table 8.5.

Events are split into twenty categories targeting different Higgs production processes; ggF and VBF-enriched categories share the event selection criteria,

	Removed object	Reference object	Removal criteria
1.	Electron	Electron	Sharing track and lower p_{T}
2.	Muon	Electron	Sharing ID track and calo-tagged muon
3.	Electron	Muon	Sharing ID track
4.	Jet	Electron	$\Delta R(\mathrm{jet}, e) < 0.2$
5.	Electron	Jet	$0.2 < \Delta R(\mathrm{jet}, e) < 0.4$
6.	Jet	Muon	$\Delta R(\mathrm{jet}, \mu) < 0.2$ and $[N_{\mathrm{tracks}}(\mathrm{jet}) < 3$ or $(p_{\mathrm{T}}^{\mathrm{jet}}/p_{\mathrm{T}}^{\mu} < 2$ and $p_{\mathrm{T}}^{\mu}/\Sigma_{\mathrm{tracks}} p_{\mathrm{T}} > 0.7)]$
7.	Muon	Jet	$0.2 < \Delta R(\mathrm{jet}, \mu) < 0.4$ or $\Delta R(\mathrm{jet}, \mu) < 0.2$ when muon cannot remove jet

Table 8.4: Overlap removal criteria for objects used in the $H \to \mu\mu$ search.

Dataset	p_{T} threshold [GeV]	Isolation
2015	20	$p_{\mathrm{T}}^{\mathrm{cone20}}/p_{\mathrm{T}} < 0.12$
	50	-
2016–2018	26	$p_{\mathrm{T}}^{\mathrm{varcone30}}/p_{\mathrm{T}} < 0.07$
	50	-

Table 8.5: Single-muon triggers used in the $H \to \mu\mu$ search.

whereas requirements for events falling into VH or $t\bar{t}H$ categories are different. The categories are defined so that they are orthogonal to each other. The details of the event selection for categories targeting different Higgs production processes are described below.

Event selection in the $t\bar{t}H$ category

To target $t\bar{t}H$ associated production events are required to have an oppositely-charged muon pair that constitutes the $H \to \mu\mu$ signal, at least one b-tagged jet, and at least one additional lepton (either electron or muon). The p_{T} of the leading, subleading and additional lepton is required to be above 27, 15 and 15 GeV, respectively.

Event selection in the *VH* categories

The selection targeting the *VH* signal production process is defined separately for the 3-lepton and 4-lepton channels to reconstruct the $H \to \mu\mu$ decay and the leptonic $W \to \ell\nu$ or $Z \to \ell\ell$ decays. Exactly three leptons are required in the 3-lepton channel. The subleading muon used to reconstruct the Higgs candidate is required to have p_{T} larger than 10 GeV and the additional (third) lepton can be either a muon with p_{T} larger than 10 GeV or an electron with p_{T} above 15 GeV. Events with Z candidates (oppositely-charged dilepton pairs with $m_{\ell\ell} \in (80, 105)$ GeV) are rejected in this channel. The 4-lepton channel is required to have at least another oppositely-charged lepton pair to reconstruct the Z boson, with either muons or electrons with p_{T} of the leading and subleading lepton larger than 8 and 6 GeV, respectively. Only events with less than two Z candidates are considered. At least one $\mu^+\mu^-$ pair is required in both channels, where the leading muon has p_{T} larger than 27 GeV. To suppress the top background, any event with a jet identified as a b-jet, using the 85% efficiency WP of the MV2c10 tagger, is removed. The selection criteria for the *VH* categories are summarised in Table 8.6.

N-lepton Channel	3-lepton	4-lepton
N_{leptons}	3	≥ 4
$N_{\mu\mu\,\text{pairs}}$	≥ 1	≥ 1
Additional leptons	Electron or muon	e^+e^- or $\mu^+\mu^-$ pair
$N_{b-\text{jets}}$ (MV2c10 85% WP)	0	0
$N_{Z\,\text{candidates}}$	0	< 2
Lepton p_{T}	27, 10, 10 (15) GeV for μ (e)	27, 15, 8, 6 GeV

Table 8.6: The event selection applied to target *VH* production process.

Event selection in the ggF and VBF categories

Only events with exactly two opposite-sign muons are considered in categories targeting the ggF and VBF production processes. The leading muon is required to have p_{T} larger than 27 GeV to select a region of high trigger efficiency and

the subleading muon is required to have p_{T} above 15 GeV. The top background is suppressed by removing all events with at least one jet originating from a b-hadron, by requiring the 60% efficiency WP of the MV2c10 tagger.

8.2.7 Validation plots

The following section describes the data-to-MC comparison for the muon and jet variables in two analysis regions: the Z control region and the sideband region. Only events passing the selection defined for the ggF or VBF categories are considered here.

Figure 8.1 presents the p_{T} and η distributions for leading and subleading muon for events falling into the Z control region. The mismodelling of the muon p_{T} visible in the ratio plots is a known issue of the Sherpa samples that is also observed in other ATLAS analyses [127]. The p_{T} and η distributions of the leading and subleading jets in events with at least two jets and dimuon mass within the Z control region are presented in Figure 8.2. The MC and data show reasonable agreement in the p_{T} distribution. The larger discrepancies visible in the η distribution mostly in the forward region are related to pile-up mismodelling. The distribution of the jet multiplicity for events with invariant mass around the Z peak is presented in Figure 8.3. In general, good agreement is observed between the MC and the data for $N_{\mathrm{jets}} \geq 5$ with up to 15% discrepancy visible for higher jet multiplicities.

The same set of distributions but for events with mass falling into the sideband region is presented in Figures 8.4–8.6. The distributions show in general very good agreement between the MC and the data. The muon p_{T} mismodelling is not visible here, probably due to higher contribution of the top background events produced with Powheg-Box, where there is no p_{T} mismodelling like it is observed in the samples generated with Sherpa. The jet p_{T} and η distributions also show a good data–MC agreement. The difference is usually at the level of 5% and does not exceed 10%. The larger discrepancies in the N_{jets} modelling are visible only for very high jet multiplicities.

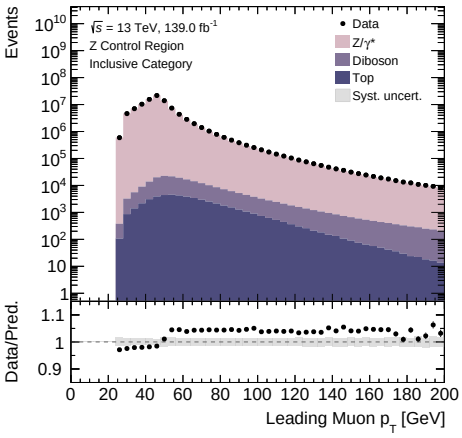

(a) Leading muon p_{T}

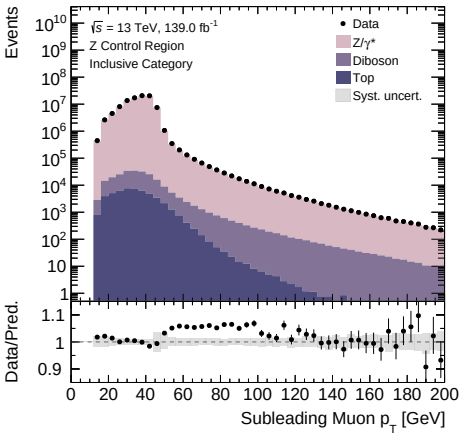

(b) Subleading muon p_{T}

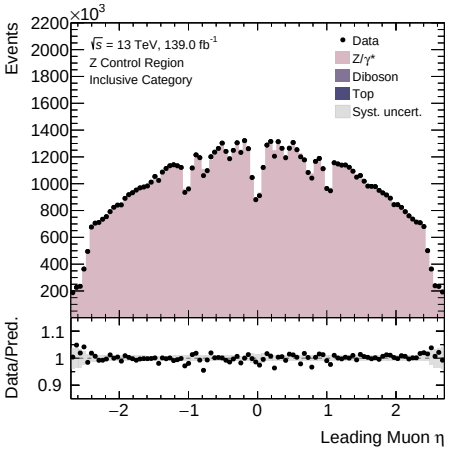

(c) Leading muon η

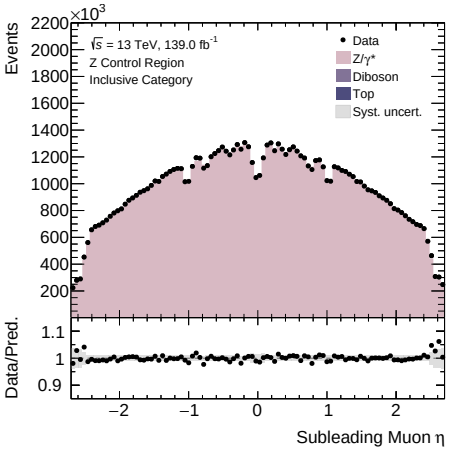

(d) Subleading muon η

Figure 8.1: The upper panels show the distributions of the muon kinematic variables indicated in the sub-figure captions for events with $76 < m_{\mu\mu(\gamma)} < 106$ GeV in the summed ggF and VBF categories. The black points represent the data. The filled histograms present the MC simulation of the background processes: Drell-Yan, diboson and top production, and are normalised to the luminosity of the data. The lower panels show the ratio of the data to the SM prediction. The grey shaded area represents the statistical and systematic uncertainty band with only experimental systematic uncertainties included (muon momentum scale and resolution and muon trigger and reconstruction efficiencies).

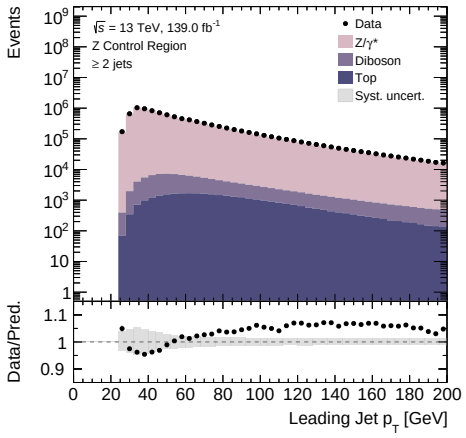

(a) Leading jet p_{T}

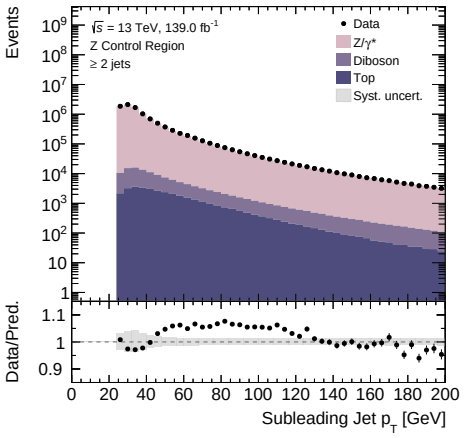

(b) Subleading jet p_{T}

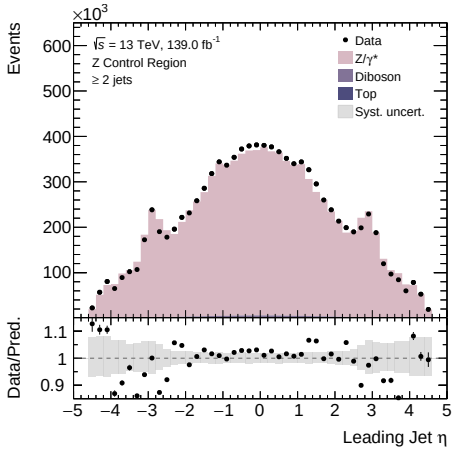

(c) Leading jet η

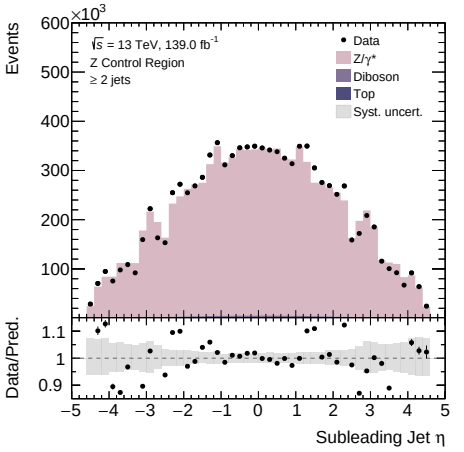

(d) Subleading jet η

Figure 8.2: The upper panels show the distributions of the jet kinematic variables indicated in the sub-figure captions for events with $76 < m_{\mu\mu(\gamma)} < 106$ GeV in the inclusive 2-jet category. The black points represent the data. The filled histograms present the MC simulation of the background processes: Drell-Yan, diboson and top production, and are normalised to the luminosity of the data. The lower panels show the ratio of the data to the SM prediction. The grey shaded area represents the statistical and systematic uncertainty band with only experimental systematic uncertainties included (muon momentum scale and resolution and muon trigger and reconstruction efficiencies).

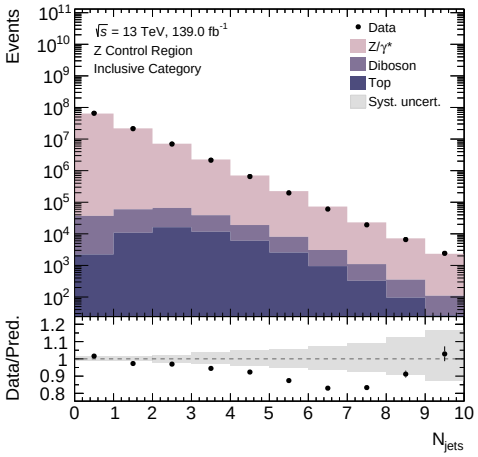

Figure 8.3: The upper panel shows the distribution of the jet multiplicity for events with $76 < m_{\mu\mu(\gamma)} < 106$ GeV in the summed ggF and VBF categories. The black points represent the data. The filled histograms present the MC simulation of the background processes: Drell-Yan, diboson and top production, and are normalised to the luminosity of the data. The lower panel shows the ratio of the data to the SM prediction. The grey shaded area represents the statistical and systematic uncertainty band with only experimental systematic uncertainties included (muon momentum scale and resolution and muon trigger and reconstruction efficiencies).

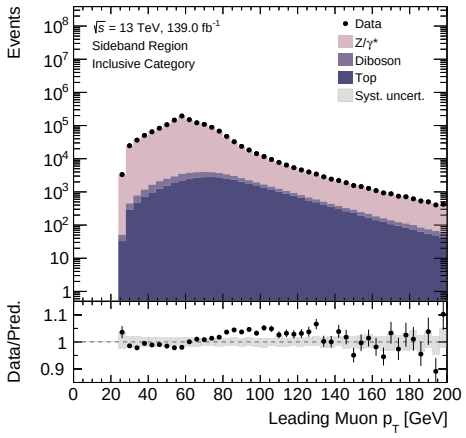

(a) Leading muon p_{T}

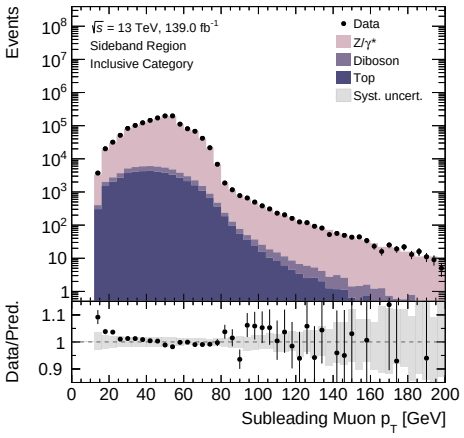

(b) Subleading muon p_{T}

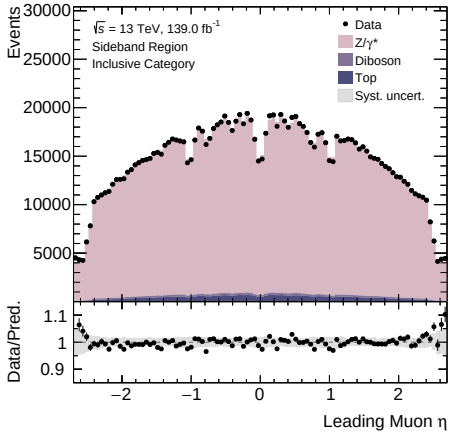

(c) Leading muon η

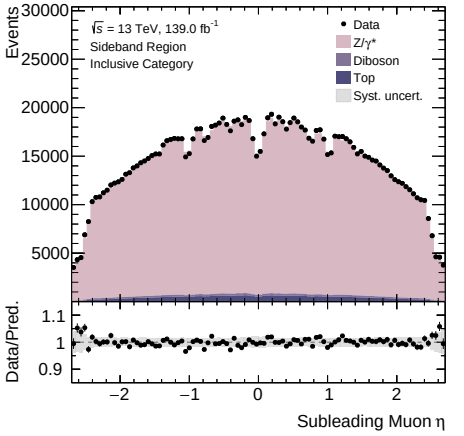

(d) Subleading muon η

Figure 8.4: The upper panels show the distributions of the muon kinematic variables indicated in the sub-figure captions for events with $m_{\mu\mu(\gamma)} \in (110, 120) \cup (130, 160)$ GeV in the summed ggF and VBF categories. The black points represent the data. The filled histograms present the MC simulation of the background processes: Drell-Yan, diboson and top production, and are normalised to the luminosity of the data. The lower panel shows the ratio of the data to the SM prediction. The grey shaded area represents the statistical and systematic uncertainty band with only experimental systematic uncertainties included (muon momentum scale and resolution and muon trigger and reconstruction efficiencies).

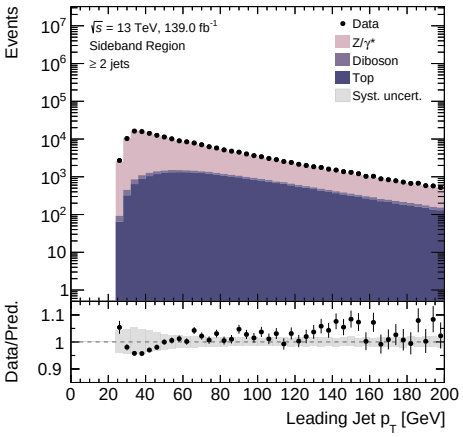

(a) Leading jet p_{T}

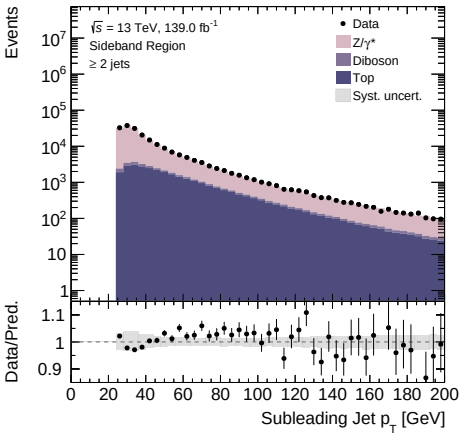

(b) Subleading jet p_{T}

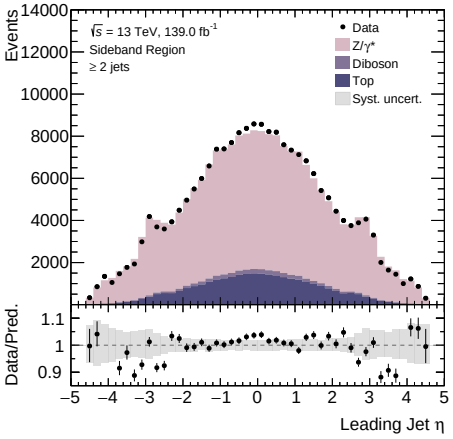

(c) Leading jet η

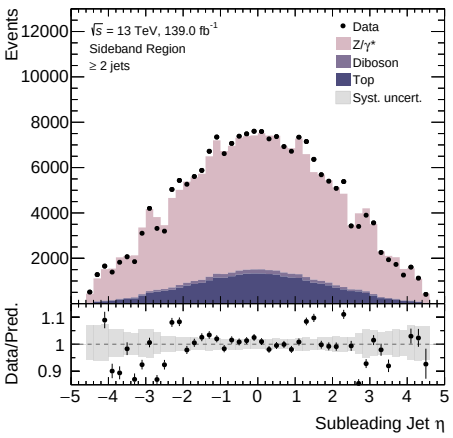

(d) Subleading jet η

Figure 8.5: The upper panels show the distributions of the jet kinematic variables indicated in the sub-figure captions for events with $m_{\mu\mu(\gamma)} \in (110, 120) \cup (130, 160)$ GeV in the inclusive 2-jet category. The black points represent the data. The filled histograms present the MC simulation of the background processes: Drell-Yan, diboson and top production, and are normalised to the luminosity of the data. The lower panel shows the ratio of the data to the SM prediction. The grey shaded area represents the statistical and systematic uncertainty band with only experimental systematic uncertainties included (muon momentum scale and resolution and muon trigger and reconstruction efficiencies).

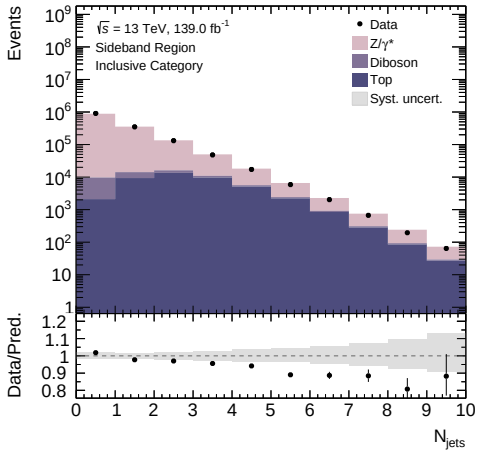

Figure 8.6: The upper panel shows the distribution of the jet multiplicity for events with $m_{\mu\mu(\gamma)} \in (110, 120) \cup (130, 160)$ GeV in the summed ggF and VBF categories. The black points represent the data. The filled histograms present the MC simulation of the background processes: Drell-Yan, diboson and top production, and are normalised to the luminosity of the data. The lower panel shows the ratio of the data to the SM prediction. The grey shaded area represents the statistical and systematic uncertainty band with only experimental systematic uncertainties included (muon momentum scale and resolution and muon trigger and reconstruction efficiencies).

8.3 Final State Radiation photon recovery

Muons from the $H \to \mu\mu$ decay can lose a significant fraction of their energy by QED FSR. This process (a corresponding Feynman diagram is presented in Figure 8.7) significantly affects the shape of the dimuon mass peak, migrates events to lower mass and worsens the dimuon mass resolution, which is a critical quantity for the extraction of the $H \to \mu\mu$ signal. Including the FSR photons in the invariant mass calculation can improve the resolution. The reconstruction of FSR photon candidates is performed with a procedure similar to that described in Ref. [76] and [21]. Two types of FSR photons are reconstructed, collinear and far, differing mainly in the $\Delta R(\mu, \gamma)$ range, < 0.2 for collinear photons and > 0.2 for far photons. Selection criteria corresponding to both types of FSR photons are described in more detail in Section 6.3. The FSR recovery is applied only to events falling into categories targeting VBF or ggF production processes, as the effect in the VH or $t\bar{t}H$ categories would be negligible.

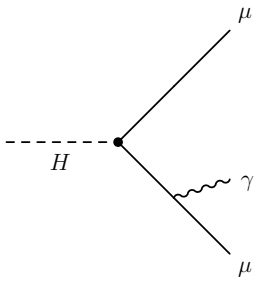

Figure 8.7: Feynman diagram presenting the emission of final state radiation photon by one of the muons from the $H \to \mu\mu$ decay.

8.3.1 Illustrative study

The effect of the FSR recovery performed at the truth level is presented in Figure 8.8. Only events with at least one truth-level photon with E_{T} above 10 GeV are considered here. Figure 8.8a presents the invariant mass distribution before the FSR recovery. It can be observed that the distribution is very wide and has a distinct tail on the left, as well as a peak shifted towards values far below the simulated Higgs boson mass of 125 GeV. Figure 8.8b presents the

invariant mass distribution $m_{\mu\mu\gamma}$ after adding the leading-E_{T} photon to the mass calculation, i.e. calculating the invariant mass of the four-vector sum of the muons and the photon. The mass distribution improves significantly after performing the FSR recovery. The peak becomes very sharp after recovering all FSR photons as presented in Figure 8.8c. Therefore, it can be concluded that the FSR recovery works as expected at the truth level. Moreover, reconstructing the leading-E_{T} photon should be sufficient to recover the majority of the radiation effect. Figure 8.9 presents a 2D histogram of the truth FSR photon E_{T} versus the angular distance between the photon and the closest muon. Most of the truth FSR photons have very low E_{T} and, therefore, are impossible to reconstruct. However, the effect of adding them to the mass calculation would be very small.

A similar check is performed at the reconstruction level, where also only events with the truth-level photon E_{T} above 10 GeV are selected. This requirement ensures higher reconstruction probability of a given photon. The results are shown in Figure 8.10. Figure 8.10a presents the invariant mass distribution after adding to its calculation the leading-E_{T} FSR photon, which happens in two-thirds of the selected events. Figure 8.10b shows the $m_{\mu\mu}$ distribution for remaining one-third of events, where the truth-level photon is not reconstructed. This leads to a much wider distribution with a peak much below the expected 125 GeV. The histogram presented in Figure 8.10c is the sum of the two distributions, hence it represents the best possible reconstructed mass available by adding information about the FSR photon candidate when it is available, and combining it with the dimuon mass for events where there is no reconstructed photon. The histogram is therefore presenting the distribution of $m_{\mu\mu(\gamma)}$, where two separate peaks coming from events with and without recovered FSR photon are clearly visible.

It is found that adding the leading-E_{T} FSR photon of any type (collinear or far) or the leading-E_{T} collinear photon to the mass calculation leads to similar results. In an event, in which more than one FSR photon is reconstructed,

only the one with highest E_{T} is added to the mass calculation giving priority to collinear photons. This is the same strategy as that used in the search for the four-lepton decay of the Higgs boson. The far FSR photon recovery is eventually dropped completely, which is discussed later in this section.

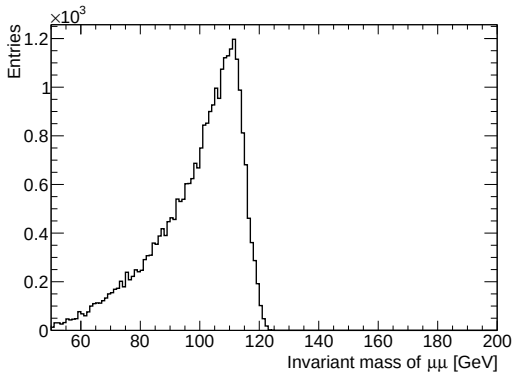

(a) Before recovery

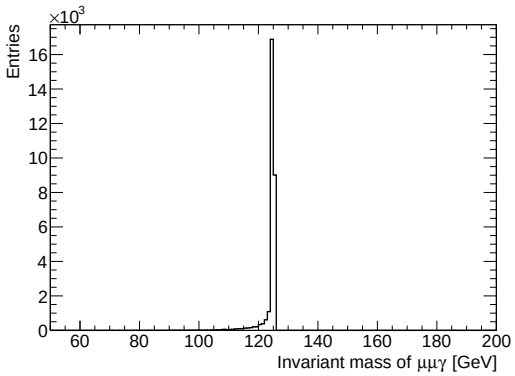

(b) After recovery of leading-E_{T} γ

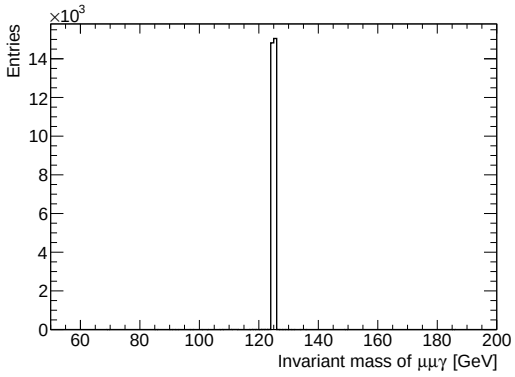

(c) After recovery of all FSR photons

Figure 8.8: Truth-level invariant mass distributions for the $H \to \mu\mu$ signal events with at least one true photon with $E_{\mathrm{T}} > 10$ GeV corresponding to the FSR recovery scenarios indicated in the sub-figure captions. The histograms are not normalised, hence the y axis presents the number of entries in each bin.

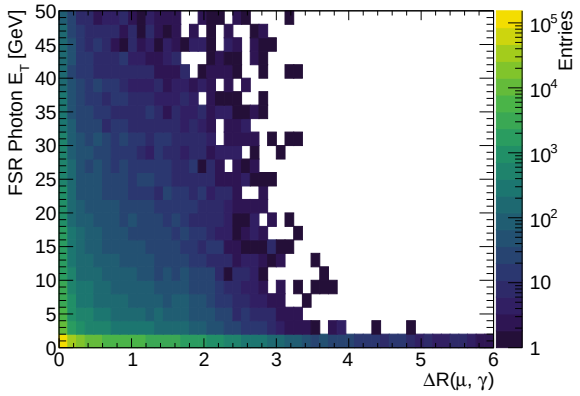

Figure 8.9: 2D distribution of the truth-level FSR photon E_{T} versus $\Delta R(\mu, \gamma)$. The histogram is not normalised, hence the z axis presents the number of entries in the 2D bins.

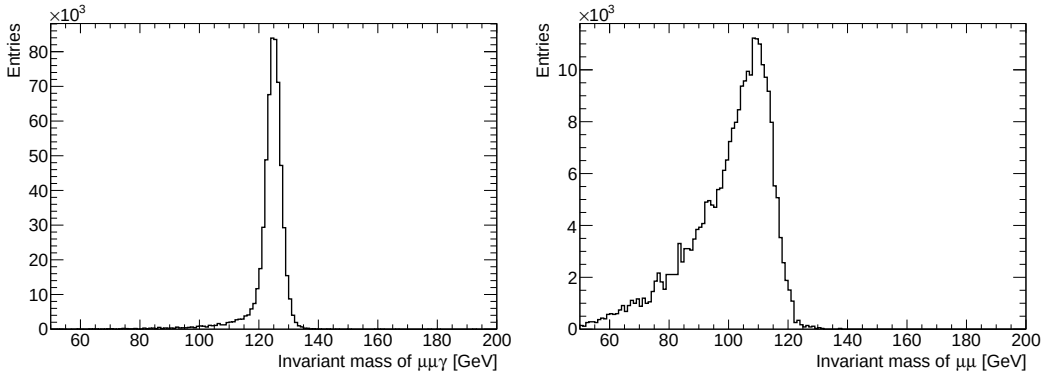

(a) After recovery of leading-E_{T} γ (b) Events with no reconstructed photon

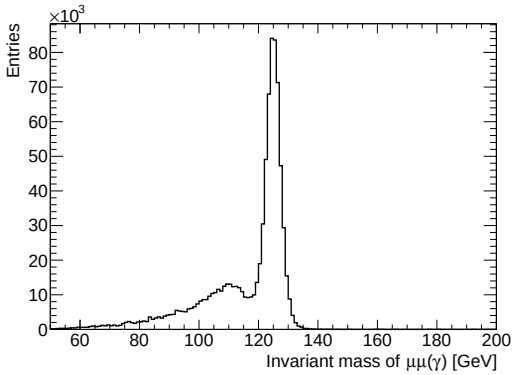

(c) Sum of the two distributions

Figure 8.10: Reconstruction-level invariant mass distributions for the $H \to \mu\mu$ signal events with at least one true photon with $E_{\mathrm{T}} > 10$ GeV corresponding to the FSR recovery scenarios indicated in the sub-figure captions. The histograms are not normalised, hence the y axis presents the number of entries in each bin.

8.3.2 Reduction of fake FSR recoveries

The default E_{T} selection for the FSR photons (discussed in Section 6.3) is optimised in order to reduce the number of fake FSR recoveries, i.e. incorrectly assigned FSR photons due to pile-up. The study is performed using truth information available in the signal MC simulation. A fake FSR photon is defined as a reconstructed FSR photon that fails the requirement of $\Delta R(\gamma^{\mathrm{reco}}, \gamma^{\mathrm{truth}}) < 0.2$. Based on this information, the fake FSR photon rate is defined as:

$$\text{Fake FSR } \gamma \text{ rate} = \frac{\text{Events with fake FSR candidate reconstructed}}{\text{All events with FSR candidate reconstructed}}. \quad (8.1)$$

Figure 8.11 presents the fake FSR photon rate as a function of $\Delta R(\mu, \gamma)$ and photon E_{T}. It can be observed that the fake FSR photons dominate the low-E_{T} and low-ΔR region. The E_{T} threshold is scanned to reduce the fake FSR photon rate while maximising the significance ($S/\sqrt{B}$). Two forms of an E_{T} threshold dependent on $\Delta R(\mu, \gamma)$ are considered:

- $E_{\mathrm{T}}^{\mathrm{thres}}\,[\mathrm{GeV}] = 25 \cdot \Delta R(\mu, \gamma) + A_{\mathrm{near}}$ for near FSR photon, where A_{near} is scanned from 2 to 6 GeV with a step size of 1 GeV,
- $E_{\mathrm{T}}^{\mathrm{thres}}\,[\mathrm{GeV}] = \frac{B_{\mathrm{far}}}{0.8} \cdot (\Delta R(\mu, \gamma) - 0.2) + 10$ for far FSR photon, where B_{far} is scanned between 0 and 16 with a step size of 1.

This particular choice of functions is motivated by the dependence of the E_{T} threshold on $\Delta R(\mu, \gamma)$ seen in Figure 8.11. It is clear that the E_{T} threshold should be raised for higher angular distances between muon and the FSR photon candidate. The results of the threshold scan show the best significance for $A_{\mathrm{near}} = 3$ (an improvement of 2% with respect to the default requirement) and no significant change for any of the scanned values of B_{far}, therefore, the default requirement at 10 GeV remains unchanged for the far FSR photons.

8.3.3 The effect of the FSR recovery on the background contribution in the $H \to \mu\mu$ signal region

The $H \to Z\gamma \to \mu\mu\gamma$ process has the same final state as the $H \to \mu\mu$ channel with an additional FSR photon. This makes the $H \to Z\gamma \to \mu\mu\gamma$ process

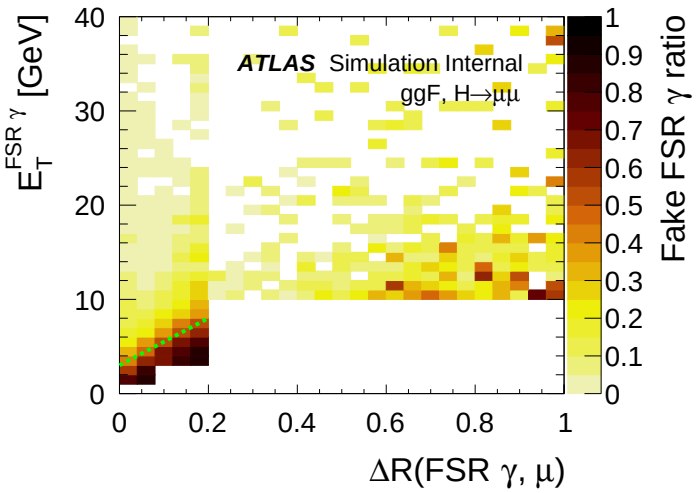

Figure 8.11: Fake FSR photon rate defined in Equation 8.1 as a function of the angular difference between the FSR photon and the closest muon, and the FSR photon E_{T} [128]. The dashed green line represents the ΔR-dependent requirement imposed on the E_{T} of the collinear FSR photon in order to reduce the fake FSR recovery rate.

an important background to consider when performing the FSR recovery as it can lead to a peak in the signal region and constitute a part of the extracted $H \to \mu\mu$ signal [129]. Figure 8.12 shows the overlaid mass distributions for the $H \to \mu\mu$ signal and $H \to Z\gamma$ background produced in the ggF process before and after performing the FSR recovery with the selections discussed in Subsection 8.3.2. It can be observed that before the FSR recovery there is almost no overlap between the two Higgs decay channels in the region between 120 and 130 GeV and the $H \to Z\gamma$ yield in this region is around 0.3 events. After the FSR recovery a peak of the $H \to Z\gamma$ events is clearly visible in the signal region and the yield increases significantly to 33.5 events, which is around 5% of the expected $H \to \mu\mu$ signal.

Moreover, performing the FSR recovery changes the number of Drell-Yan background events in the signal region by pulling events from the Z/γ^* peak towards higher masses. In this case, however, the added background is smoother and does not form an additional peak as opposed to the $H \to Z\gamma$ process.

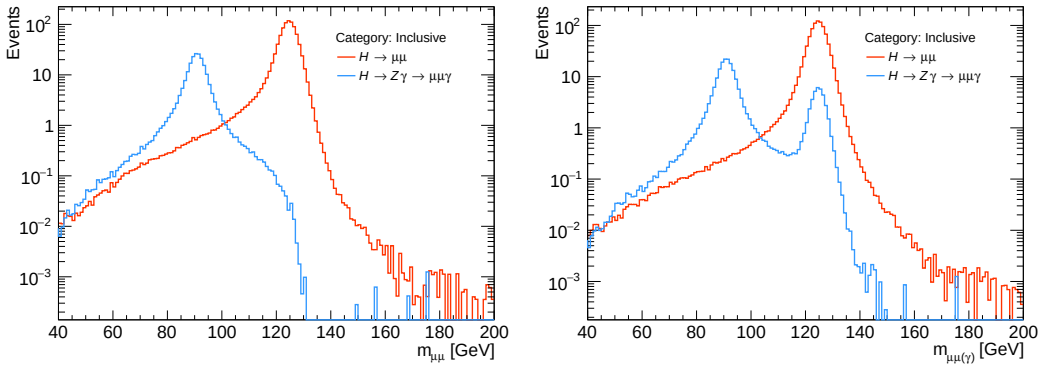

(a) Before FSR recovery

(b) After FSR recovery

Figure 8.12: Invariant mass distributions of the $H \to Z\gamma$ (blue histogram) and $H \to \mu\mu$ signal (orange histogram) events, passing the selection discussed in Subsection 8.3.2, before and after performing the FSR recovery. For both Higgs boson decay channels only MC simulation of the ggF production process is used. The distributions are normalised to the luminosity of the Run-2 data corresponding to 139 fb^{-1}.

Different modifications to the FSR recovery procedure are studied in order to minimise the $H \to Z\gamma$ contribution in the analysis and to avoid pulling the Z/γ^* events towards the $H \to \mu\mu$ signal region. Figure 8.13 presents the distributions of the FSR photon E_{T} versus $\Delta R(\mu, \gamma)$ for the $H \to \mu\mu$ signal and the $H \to Z\gamma \to \mu\mu\gamma$ background, where the Higgs boson is produced in the ggF production process. The Run-2 data events with a requirement of $m_{\mu\mu(\gamma)} \in (110, 120) \cup (130, 160)$ GeV range due to the blinding procedure are also presented. Most FSR photon candidates for the signal are expected at low $\Delta R(\mu, \gamma)$ and small E_{T}, corresponding to collinear and soft photons. In the case of the $H \to Z\gamma$ process, a high fraction of these collinear photons exists as well, but there is a second significant population of photons from the Higgs decay observed at $\Delta R(\mu, \gamma) > 0.2$ and $E_{\mathrm{T}} > 20$ GeV.

Given the observations, a potential strategy to minimise the $H \to Z\gamma$ contribution can be to only use the near FSR photon candidates and reject those with $\Delta R(\mu, \gamma) > 0.2$ (far photons). In order to avoid moving Drell-Yan events into the signal region it could be beneficial to apply the FSR recovery to events

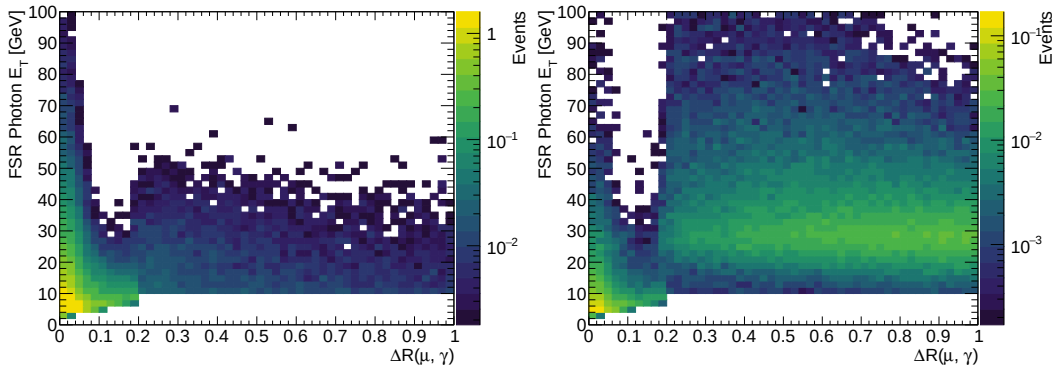

(a) $ggH \to \mu\mu$ (b) $ggH \to Z\gamma \to \mu\mu\gamma$

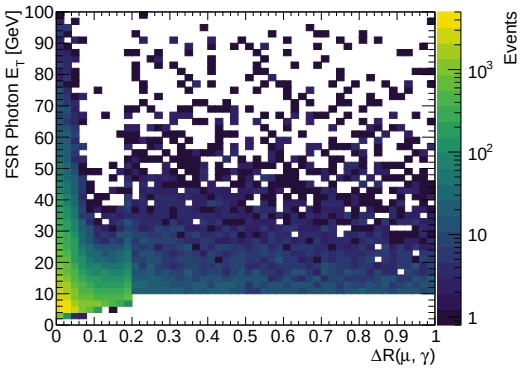

(c) Run-2 data events with
$m_{\mu\mu(\gamma)} \in (110, 120) \cup (130, 160)$ GeV

Figure 8.13: Distributions of the FSR photon candidate E_{T} versus $\Delta R(\mu, \gamma)$ for different samples indicated in the sub-figure captions.

only with dimuon mass above the central value expected for the Z/γ^* peak. A study checking the $H \to Z\gamma$ yield and evaluating the signal and background yields after employing different modifications to the FSR recovery is performed and the investigated scenarios are summarised in Table 8.7.

The overlaid invariant mass distributions of the $H \to Z\gamma$ and $H \to \mu\mu$ processes corresponding to near-and-far recovery with $m_{\mu\mu}$ thresholds are presented in Figure 8.14. Similar distributions but for the near-only recovery case are presented in Figure 8.15. It can be observed that the additional peak in the $H \to \mu\mu$ signal region for the near-and-far FSR recovery scenario is minimal only for the high $m_{\mu\mu}$ threshold. As expected, dropping recovery of the far FSR photon candidates reduces the $H \to Z\gamma$ contamination significantly.

The $H \to Z\gamma$ yields in the signal region for different cases are presented in Table 8.8 and confirm the conclusions from the distribution comparison. To reduce the number of $H \to Z\gamma$ events in the signal region to below one event for the near-and-far recovery scenario, the $m_{\mu\mu}$ threshold would have to be set at around 105 GeV, which is very close to the lower bound of the fitting range. This, however, could lead to potential problems with modelling of the background distribution in the part of the mass spectrum that is already difficult to model due to its steepness, by introducing a threshold effect. In the near-only recovery scenario, the $H \to Z\gamma$ yield is already below one event without any mass threshold.

The $H \to \mu\mu$ signal yield before FSR recovery and the percentage increase of the signal in the mass region between 120 and 130 GeV after recovering a photon candidate are presented in Table 8.9. As expected, the signal increase becomes lower when adding a mass threshold for the application of the FSR recovery. The average difference in categories between the signal increase for the near-and-far recovery case without $m_{\mu\mu}$ threshold and the threshold at 105 GeV is around 1.3%. Recovering only a collinear photon candidate instead of collinear or far and without any mass threshold leads to a lower signal increase of only 0.6%.

Scenario	FSR photons considered		$m_{\mu\mu}$ threshold [GeV]
	Collinear	Far	
1	✓	✓	None
2	✓	✓	95
3	✓	✓	100
4	✓	✓	105
5	✓	×	None
6	✓	×	95
7	✓	×	100
8	✓	×	105

Table 8.7: Modifications to the FSR recovery procedure under consideration.

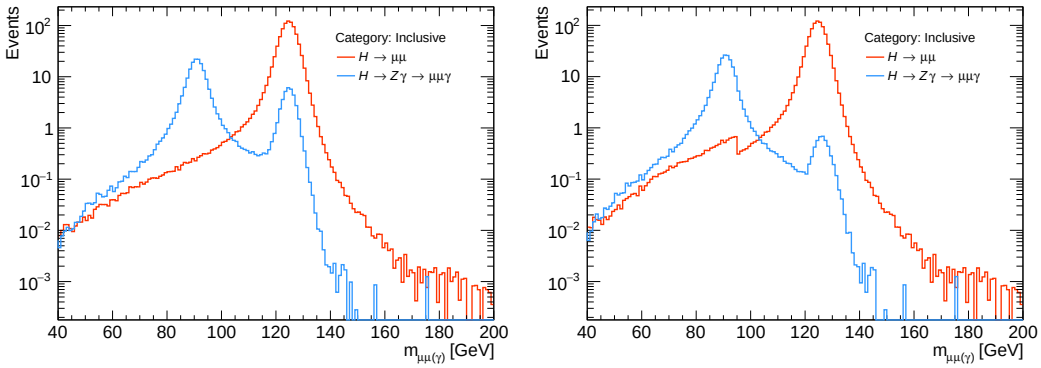

(a) $m_{\mu\mu} > 0$ GeV

(b) $m_{\mu\mu} > 95$ GeV

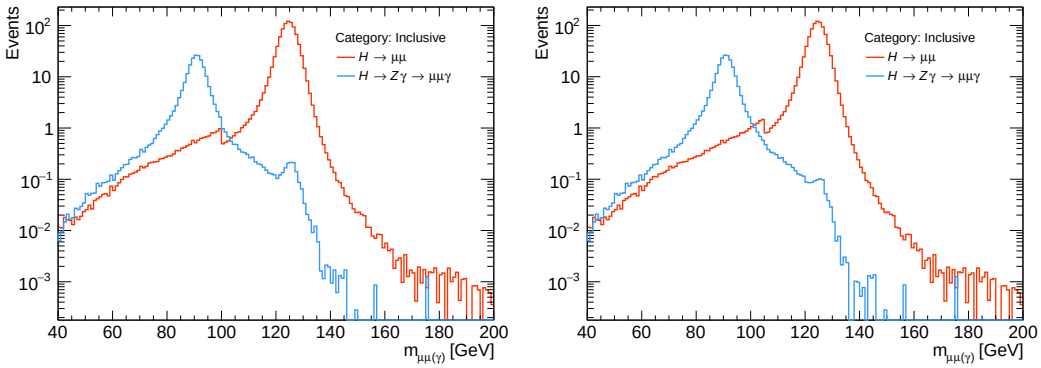

(c) $m_{\mu\mu} > 100$ GeV

(d) $m_{\mu\mu} > 105$ GeV

Figure 8.14: Invariant mass distributions after the recovery of collinear and far FSR photon candidates applied to events with $m_{\mu\mu}$ mass above thresholds indicated in the sub-figure captions. The blue histograms represent the $H \to Z\gamma$ events passing the $H \to \mu\mu$ selection and the orange histograms represent the $H \to \mu\mu$ signal. In both cases only the ggF production process is considered. The distributions are normalised to the luminosity of the Run-2 data. The overlaid distributions presented in Figure 8.14a are the same as those presented in Figure 8.12b and are added here for easier comparison with other scenarios for collinear-and-far FSR recovery.

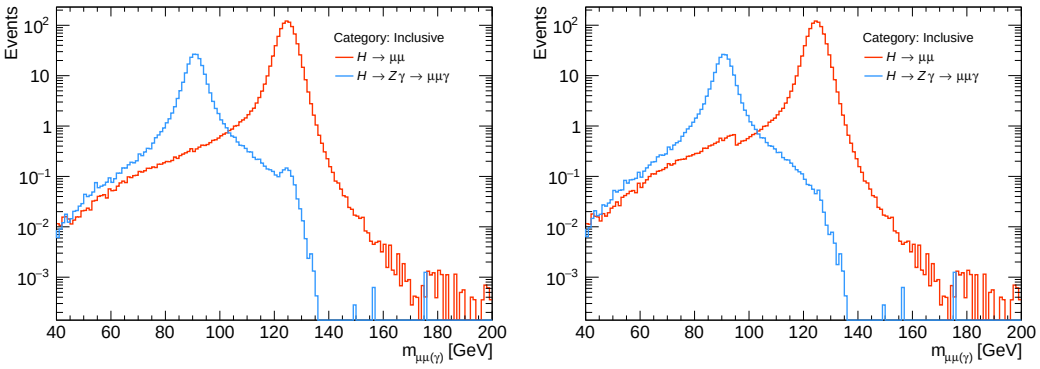

(a) $m_{\mu\mu} > 0$ GeV

(b) $m_{\mu\mu} > 95$ GeV

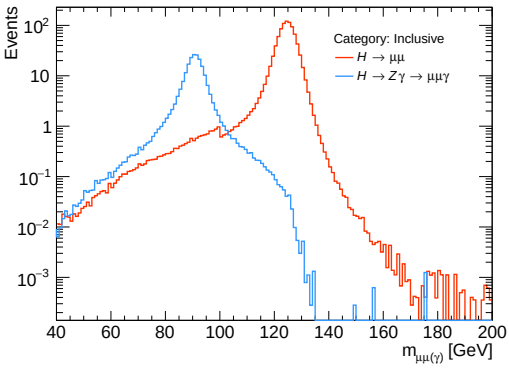

(c) $m_{\mu\mu} > 100$ GeV

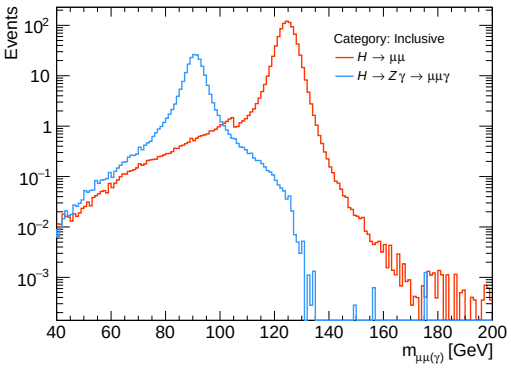

(d) $m_{\mu\mu} > 105$ GeV

Figure 8.15: Invariant mass distributions after the recovery of collinear-only FSR photon candidates applied to events with $m_{\mu\mu}$ mass above thresholds indicated in the sub-figure captions. The blue histograms represent the $H \to Z\gamma$ events passing the $H \to \mu\mu$ selection and the orange histograms represent the $H \to \mu\mu$ signal. In both cases only the ggF production process is considered. The distributions are normalised to the luminosity of the Run-2 data.

Category	No recovery	Near+Far FSR recovery				Near-only FSR recovery			
		$m_{\mu\mu} > 0$	$m_{\mu\mu} > 95$	$m_{\mu\mu} > 100$	$m_{\mu\mu} > 105$	$m_{\mu\mu} > 0$	$m_{\mu\mu} > 95$	$m_{\mu\mu} > 100$	$m_{\mu\mu} > 105$
VBF Very High	0.00	0.01	0.00	0.00	0.00	0.00	0.00	0.00	0.00
VBF High	0.00	0.04	0.01	0.00	0.00	0.00	0.00	0.00	0.00
VBF Medium	0.00	0.06	0.01	0.01	0.00	0.00	0.00	0.00	0.00
VBF Low	0.00	0.16	0.02	0.01	0.00	0.01	0.00	0.00	0.00
2-jet Very High	0.01	0.93	0.15	0.06	0.03	0.05	0.02	0.02	0.02
2-jet High	0.02	2.36	0.32	0.11	0.06	0.06	0.03	0.03	0.03
2-jet Medium	0.01	3.89	0.44	0.12	0.05	0.05	0.02	0.02	0.02
2-jet Low	0.01	2.90	0.26	0.05	0.02	0.02	0.01	0.01	0.01
1-jet Very High	0.01	0.53	0.07	0.03	0.01	0.04	0.01	0.01	0.01
1-jet High	0.03	1.79	0.26	0.12	0.06	0.08	0.04	0.04	0.03
1-jet Medium	0.03	3.53	0.47	0.15	0.09	0.11	0.05	0.04	0.04
1-jet Low	0.02	4.54	0.50	0.16	0.07	0.06	0.03	0.03	0.03
0-jet Very High	0.01	2.22	0.19	0.04	0.02	0.03	0.01	0.01	0.01
0-jet High	0.03	4.09	0.52	0.15	0.07	0.09	0.04	0.03	0.03
0-jet Medium	0.05	4.07	0.56	0.22	0.11	0.15	0.08	0.06	0.06
0-jet Low	0.07	2.38	0.45	0.23	0.17	0.23	0.11	0.10	0.10
Inclusive	0.29	33.49	4.23	1.45	0.77	0.98	0.45	0.40	0.38

Table 8.8: Expected yields of $H \to Z\gamma \to \mu\mu\gamma$ events in the signal region ($m_{\mu\mu(\gamma)} \in (120, 130)$ GeV) corresponding to different FSR recovery scenarios and presented in ggF and VBF analysis categories. The yields are normalised to the luminosity of the Run-2 data of 139 fb^{-1}. Only events produced in the ggF process are considered.

Category	No recovery	Near+Far FSR recovery (% increase)				Near-only FSR recovery (% increase)			
		$m_{\mu\mu} > 0$	$m_{\mu\mu} > 95$	$m_{\mu\mu} > 100$	$m_{\mu\mu} > 105$	$m_{\mu\mu} > 0$	$m_{\mu\mu} > 95$	$m_{\mu\mu} > 100$	$m_{\mu\mu} > 105$
VBF Very High	2.697	4.15	3.63	3.37	2.97	3.82	3.37	3.11	2.74
VBF High	3.322	4.18	3.61	3.34	2.98	3.67	3.22	2.98	2.68
VBF Medium	4.605	4.13	3.58	3.34	2.95	3.54	3.13	2.95	2.65
VBF Low	7.212	3.92	3.31	3.05	2.70	3.36	2.93	2.75	2.45
2-jet Very High	16.322	4.53	3.82	3.58	3.14	4.09	3.46	3.25	2.87
2-jet High	45.424	4.04	3.37	3.13	2.74	3.44	2.97	2.80	2.54
2-jet Medium	69.161	4.02	3.21	2.95	2.57	3.24	2.79	2.62	2.33
2-jet Low	51.722	4.00	2.91	2.61	2.20	2.86	2.46	2.29	2.00
1-jet Very High	15.682	4.11	3.53	3.30	2.85	3.63	3.18	2.98	2.60
1-jet High	43.671	3.74	3.12	2.85	2.49	3.27	2.82	2.61	2.32
1-jet Medium	83.695	3.65	3.05	2.80	2.44	3.12	2.72	2.54	2.27
1-jet Low	115.084	3.46	2.83	2.57	2.20	2.81	2.47	2.29	2.03
0-jet Very High	54.59	4.01	3.03	2.73	2.34	3.15	2.72	2.52	2.21
0-jet High	94.613	3.84	3.19	2.88	2.47	3.21	2.79	2.58	2.27
0-jet Medium	113.657	3.15	2.72	2.50	2.15	2.80	2.46	2.30	2.02
0-jet Low	76.068	2.83	2.49	2.29	1.99	2.64	2.34	2.16	1.89
Inclusive	797.522	3.64	2.99	2.74	2.37	3.06	2.66	2.48	2.19

Table 8.9: Expected $H \to \mu\mu$ signal yields before the FSR recovery and the percentage $H \to \mu\mu$ signal increase in the signal region ($m_{\mu\mu(\gamma)} \in (120, 130)$ GeV) after FSR recovery with different scenarios, presented in ggF and VBF analysis categories. The yields are normalised to the luminosity of the Run-2 data of 139 fb^{-1}. The numbers are obtained as the sum of events falling into the signal region, when considering the ggF and VBF production processes.

The mass shapes of the summed ggF and VBF categories for the Run-2 data with blinded signal region corresponding to different FSR recovery scenarios are presented in Figures 8.16 and 8.17. As expected, adding a mass threshold changes the slope of the distribution in the left sideband range. The background yield before, and an increase of the background in the signal region after performing FSR recovery with different considered modifications to the procedure, are shown in Table 8.10. The presented background yields are estimated using Run-2 data events with $m_{\mu\mu(\gamma)} \in (115, 120) \cup (130, 135)$ GeV to approximate the background contamination in the signal region. The presented statistical uncertainties are calculated assuming that the FSR recovery only moves additional events into the signal region. The near-and-far recovery scenario leads to a significant increase of the background of 3.7% which reduces the effect of adding 3.6% more of the signal events. When moving from the near-and-far recovery scenario with no threshold to the threshold at 105 GeV the difference in the average background increase in categories is around 3.6%. When dropping recovery of far FSR photon candidates the difference is 1.7%. In this case the 2.2% increase of the background corresponds to a 3% increase of the signal. Even though performing near-only FSR recovery scenario provides two time worse background reduction than adding a mass threshold at high $m_{\mu\mu}$ value, it does not introduce any threshold effect in the mass spectrum.

The significance defined as $S/\sqrt{B}$ is estimated for each ggF and VBF category with various modifications to the FSR recovery procedure and is presented in Table 8.11. Taking into account contributions from various backgrounds it is decided that performing a near-only FSR recovery without any dimuon mass threshold is the optimal choice. It provides a significant reduction of the $H \to Z\gamma$ yield in the $H \to \mu\mu$ signal region to less than one event, improves the number-counting significance in high-statistics categories and does not create a step in the invariant mass distribution leading to a changed slope.

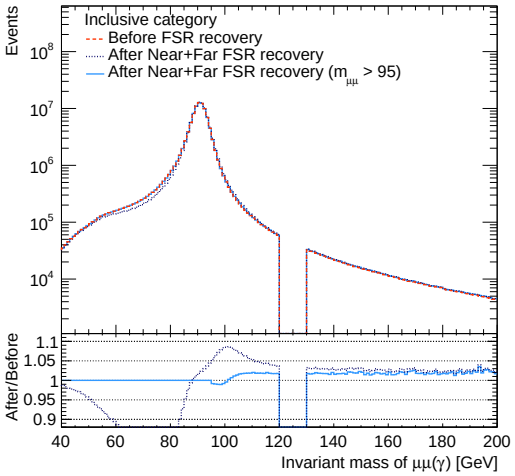

(a) $m_{\mu\mu} > 95$ GeV

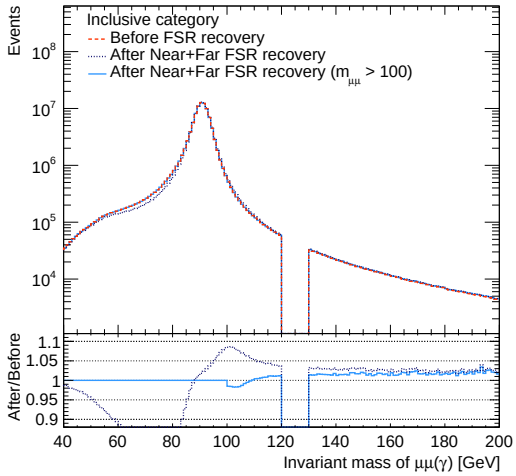

(b) $m_{\mu\mu} > 100$ GeV

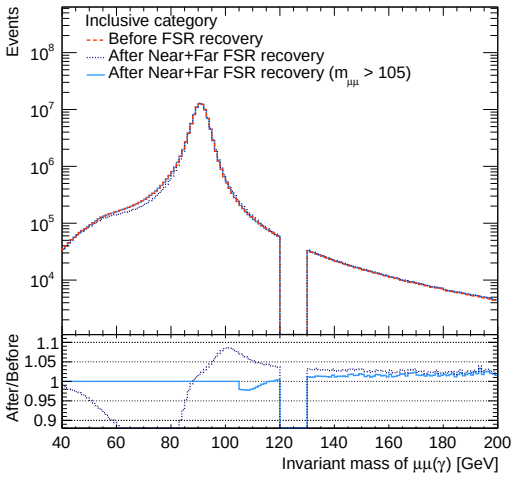

(c) $m_{\mu\mu} > 105$ GeV

Figure 8.16: The upper panels show the invariant mass distributions before and after the recovery of collinear and far FSR photon candidates for events with $m_{\mu\mu}$ above thresholds indicated in the sub-figure captions. The histograms represent the Run-2 data with a blinded signal region. The dashed orange histogram presents the mass before FSR recovery. The dotted blue line and solid light blue line represent the mass distributions after FSR recovery applied to all events and events with $m_{\mu\mu}$ above threshold, respectively. The lower panels present a ratio of the histograms after the FSR recovery to before FSR recovery.

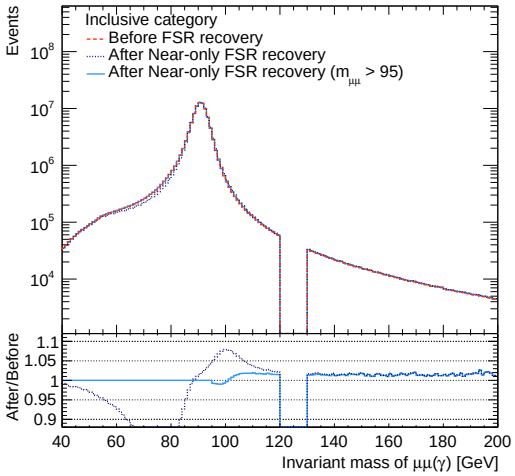

(a) $m_{\mu\mu} > 95$ GeV

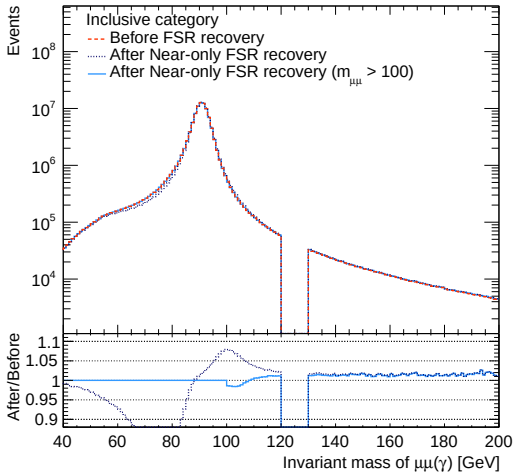

(b) $m_{\mu\mu} > 100$ GeV

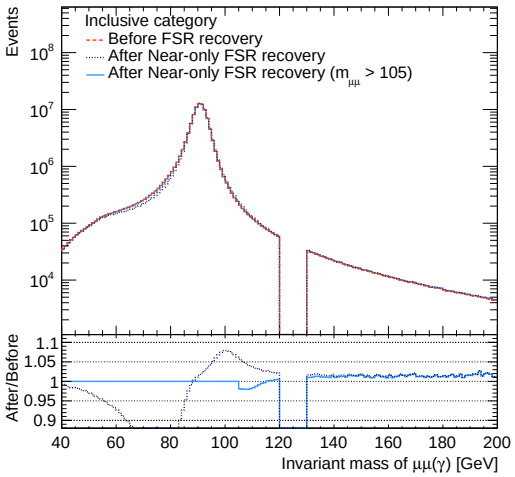

(c) $m_{\mu\mu} > 105$ GeV

Figure 8.17: The upper panels show the invariant mass distributions before and after the recovery of collinear FSR photon candidates for events with $m_{\mu\mu}$ above thresholds indicated in the sub-figure captions. The histograms represent the Run-2 data with a blinded signal region. The dashed orange histogram presents the mass before FSR recovery. The dotted blue line and solid light blue line represent the mass distributions after FSR recovery applied to all events and events with $m_{\mu\mu}$ above threshold, respectively. The lower panels present a ratio of the histograms after the FSR recovery to before FSR recovery.

Category	No recovery	Near+Far FSR recovery (% increase)				Near-only FSR recovery (% increase)			
		$m_{\mu\mu} > 0$	$m_{\mu\mu} > 95$	$m_{\mu\mu} > 100$	$m_{\mu\mu} > 105$	$m_{\mu\mu} > 0$	$m_{\mu\mu} > 95$	$m_{\mu\mu} > 100$	$m_{\mu\mu} > 105$
VBF Very High	11	9 ± 9	9 ± 9	0 ± 9	0 ± 9	9 ± 9	9 ± 9	0 ± 9	0 ± 9
VBF High	35	0 ± 3	0 ± 3	0 ± 3	0 ± 3	3 ± 3	3 ± 3	3 ± 3	3 ± 3
VBF Medium	88	7 ± 3	5 ± 2	5 ± 2	3 ± 2	5 ± 2	3 ± 2	3 ± 2	2 ± 2
VBF Low	288	4.2 ± 1.2	2.8 ± 1.0	2.4 ± 0.9	1.4 ± 0.7	3.8 ± 1.2	3.1 ± 1.1	2.8 ± 1.0	1.7 ± 0.8
2-jet Very High	1093	2.2 ± 0.5	0.8 ± 0.3	0.5 ± 0.2	-0.2 ± 0.1	1.5 ± 0.4	1.0 ± 0.3	0.7 ± 0.3	0.2 ± 0.1
2-jet High	5785	3.4 ± 0.2	1.8 ± 0.2	1.3 ± 0.2	0.6 ± 0.1	2.2 ± 0.2	1.6 ± 0.2	1.3 ± 0.1	0.7 ± 0.1
2-jet Medium	19769	3.62 ± 0.14	1.42 ± 0.09	0.76 ± 0.06	-0.08 ± 0.02	1.85 ± 0.10	1.16 ± 0.08	0.74 ± 0.06	0.06 ± 0.02
2-jet Low	39233	4.59 ± 0.11	1.79 ± 0.07	1.06 ± 0.05	0.24 ± 0.03	2.25 ± 0.08	1.55 ± 0.06	1.20 ± 0.06	0.56 ± 0.04
1-jet Very High	1146	2.7 ± 0.5	1.3 ± 0.3	0.9 ± 0.3	0.0 ± 0.1	1.7 ± 0.4	1.2 ± 0.3	0.9 ± 0.3	0.2 ± 0.1
1-jet High	6756	3.1 ± 0.2	1.3 ± 0.1	0.8 ± 0.1	-0.1 ± 0.1	2.0 ± 0.2	1.3 ± 0.1	0.9 ± 0.1	0.1 ± 0.1
1-jet Medium	26349	4.13 ± 0.13	1.98 ± 0.09	1.40 ± 0.07	0.52 ± 0.04	2.45 ± 0.10	1.70 ± 0.08	1.32 ± 0.07	0.63 ± 0.05
1-jet Low	81266	4.11 ± 0.07	1.75 ± 0.05	1.15 ± 0.04	0.36 ± 0.02	2.17 ± 0.05	1.53 ± 0.04	1.16 ± 0.04	0.52 ± 0.03
0-jet Very High	17586	6.91 ± 0.21	2.16 ± 0.11	1.19 ± 0.08	0.13 ± 0.03	3.00 ± 0.13	2.00 ± 0.11	1.51 ± 0.09	0.64 ± 0.06
0-jet High	50447	5.31 ± 0.11	2.49 ± 0.07	1.71 ± 0.06	0.75 ± 0.04	2.94 ± 0.08	2.11 ± 0.07	1.69 ± 0.06	0.92 ± 0.04
0-jet Medium	100466	3.62 ± 0.06	2.01 ± 0.05	1.43 ± 0.04	0.59 ± 0.02	2.33 ± 0.05	1.67 ± 0.04	1.31 ± 0.04	0.63 ± 0.03
0-jet Low	135258	2.32 ± 0.04	1.48 ± 0.03	1.08 ± 0.03	0.46 ± 0.02	1.75 ± 0.04	1.28 ± 0.03	1.00 ± 0.03	0.47 ± 0.02
Inclusive	485576	3.73 ± 0.03	1.82 ± 0.02	1.23 ± 0.02	0.45 ± 0.01	2.20 ± 0.02	1.56 ± 0.02	1.21 ± 0.02	0.56 ± 0.01

Table 8.10: Background yields before the FSR recovery and the percentage background increase in the signal region along with the statistical uncertainty after the FSR recovery with different scenarios, presented in ggF and VBF analysis categories. The yields are obtained from Run-2 data as the sum of events in the range $m_{\mu\mu(\gamma)} \in (115, 120) \cup (130, 135)$ GeV due to the blinding procedure.

Category	No recovery	Near+Far FSR recovery				Near-only FSR recovery			
		$m_{\mu\mu} > 0$	$m_{\mu\mu} > 95$	$m_{\mu\mu} > 100$	$m_{\mu\mu} > 105$	$m_{\mu\mu} > 0$	$m_{\mu\mu} > 95$	$m_{\mu\mu} > 100$	$m_{\mu\mu} > 105$
VBF Very High	0.813	0.811	0.807	0.841	0.837	0.808	0.805	0.839	0.836
VBF High	0.562	0.585	0.582	0.580	0.578	0.574	0.571	0.570	0.569
VBF Medium	0.491	0.495	0.497	0.496	0.497	0.497	0.498	0.497	0.498
VBF Low	0.425	0.433	0.433	0.433	0.433	0.431	0.431	0.431	0.432
2-jet Very High	0.494	0.511	0.510	0.510	0.510	0.510	0.508	0.508	0.507
2-jet High	0.597	0.611	0.612	0.612	0.612	0.611	0.610	0.610	0.610
2-jet Medium	0.492	0.503	0.504	0.504	0.505	0.504	0.503	0.503	0.503
2-jet Low	0.261	0.266	0.266	0.267	0.267	0.266	0.266	0.266	0.266
1-jet Very High	0.463	0.476	0.476	0.476	0.476	0.476	0.475	0.475	0.475
1-jet High	0.531	0.543	0.544	0.544	0.545	0.543	0.543	0.543	0.543
1-jet Medium	0.516	0.524	0.526	0.526	0.527	0.525	0.525	0.525	0.526
1-jet Low	0.408	0.409	0.412	0.412	0.412	0.411	0.411	0.411	0.411
0-jet Very High	0.412	0.414	0.420	0.420	0.421	0.418	0.419	0.419	0.419
0-jet High	0.421	0.426	0.429	0.430	0.430	0.429	0.428	0.429	0.429
0-jet Medium	0.359	0.363	0.365	0.365	0.365	0.364	0.364	0.364	0.365
0-jet Low	0.207	0.210	0.210	0.210	0.210	0.210	0.210	0.210	0.210
Combined	1.937	1.970	1.973	1.986	1.985	1.969	1.965	1.979	1.978

Table 8.11: Expected number-counting significance ($S/\sqrt{B}$) corresponding to different FSR recovery scenarios presented in ggF and VBF analysis categories. The combined significance is obtained as the square root of the sum of squared significances in all categories. The signal yield (S) is obtained as the sum of events falling into the signal region ($m_{\mu\mu(\gamma)} \in (120, 130)$ GeV), when considering the ggF and VBF production processes. The background yield (B) is obtained from the Run-2 data in range $m_{\mu\mu(\gamma)} \in (115, 120) \cup (130, 135)$ GeV due to the blinding procedure.

8.3.4 Improvement from the FSR recovery

The FSR recovery is applied when a collinear FSR candidate with $E_{\mathrm{T}} > 25 \cdot \Delta R(\mu, \gamma) + 3$ GeV is found. The kinematic distributions for selected FSR photon candidates in the $H \to \mu\mu$ signal events are presented in Figure 8.18. The invariant mass distribution before and after the FSR recovery for events from the ggF signal production process is presented in Figure 8.19. The width of the distribution calculated in the 110 – 135 GeV range decreases by almost 6%. A collinear FSR photon candidate is reconstructed in 4.7% of all signal events passing the basic dimuon selection. The mass distribution before and after FSR recovery for these events, as well as the mass distribution for the remaining events without a photon found at the reconstruction level but passing the dimuon selection, are presented in Figure 8.20. A significant improvement in the mass resolution can be observed for the 4.7% of events with a recovered photon.

The invariant mass distributions before and after FSR recovery for background MC simulation overlaid with Run-2 data with blinded signal region are presented in Figure 8.21. An improvement in the mass resolution can be observed in the Z/γ^* peak. Figure 8.22 presents the overlaid mass distributions from the background MC simulation and the Run-2 data before and after FSR recovery. Only events with a reconstructed collinear photon candidate are considered. The result of the photon recovery is clearly visible. The background MC simulation agrees well with the data, which gives confidence that the FSR recovery procedure should work well for the $H \to \mu\mu$ signal.

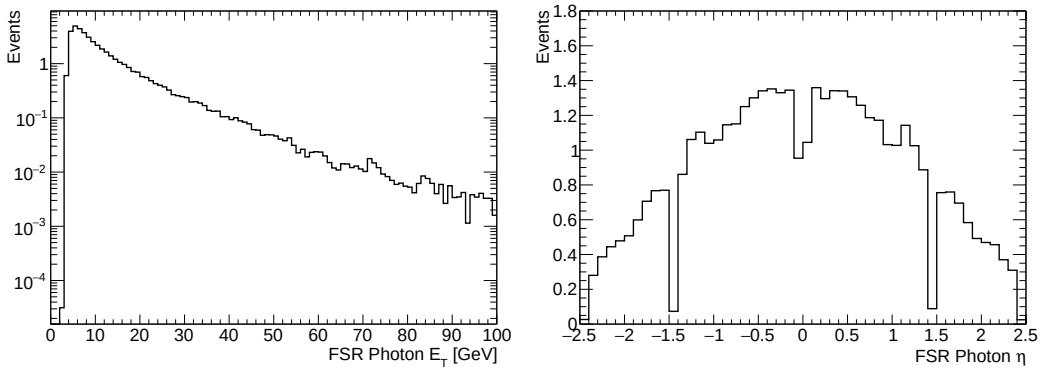

(a) Transverse energy

(b) Pseudorapidity

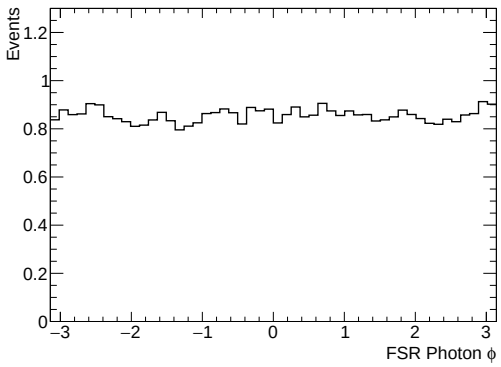

(c) Azimuthal angle

Figure 8.18: Kinematic properties of the selected FSR photon.

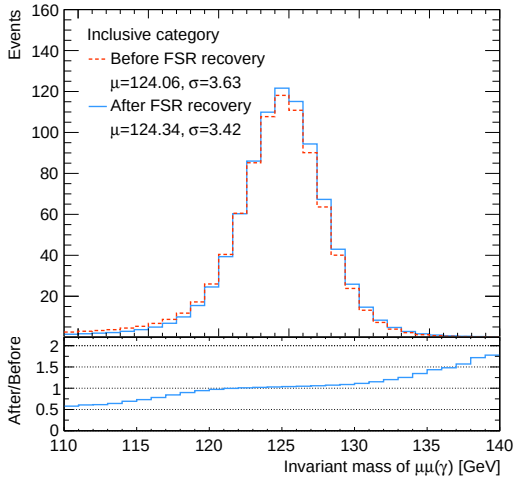

Figure 8.19: Invariant mass distribution of the $H \to \mu\mu$ signal events before and after the FSR recovery. Only the ggF Higgs production process is considered. The distributions are normalised to the luminosity of the Run-2 data. The mean and the width of the distributions before and after the FSR recovery are estimated in the 110 – 135 GeV range and are presented in units of GeV.

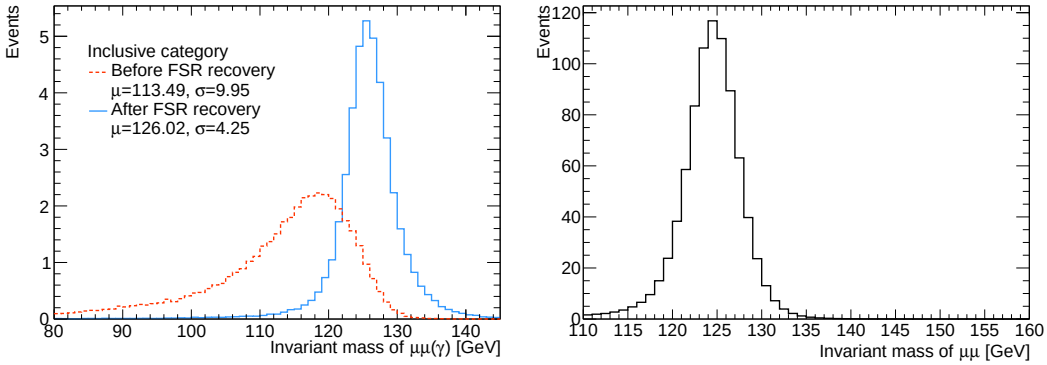

(a) Only events with a FSR photon (b) Only events without FSR photon

Figure 8.20: Invariant mass distributions for $H \to \mu\mu$ signal events indicated in the sub-figure captions. Only ggF Higgs production process is considered. The distributions are normalised to the luminosity of the Run-2 data. The mean and the width of the distribution before and after FSR recovery are estimated in range 90 – 135 GeV and 110 – 145 GeV, respectively, and their values are presented in units of GeV.

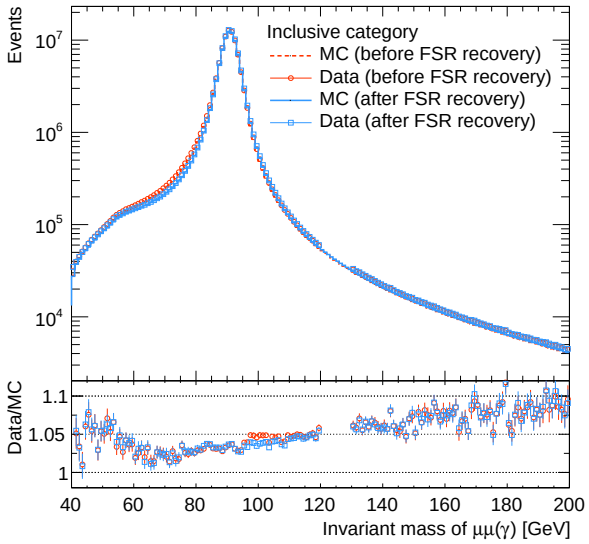

Figure 8.21: The upper panel presents the invariant mass distribution before and after FSR recovery for all events passing the selection. The dashed orange line and blue solid line represent MC simulation of the background processes (Drell-Yan, top and diboson) before and after FSR recovery, respectively. The background simulation is normalised to the luminosity of the Run-2 data. The orange circles and blue squares represent the Run-2 data before and after FSR recovery, respectively. The lower panel presents the ratio of data to MC simulation for the case before and after FSR recovery with orange circles and blue squares, respectively. The data points are removed in region 120–130 GeV due to the blinding procedure.

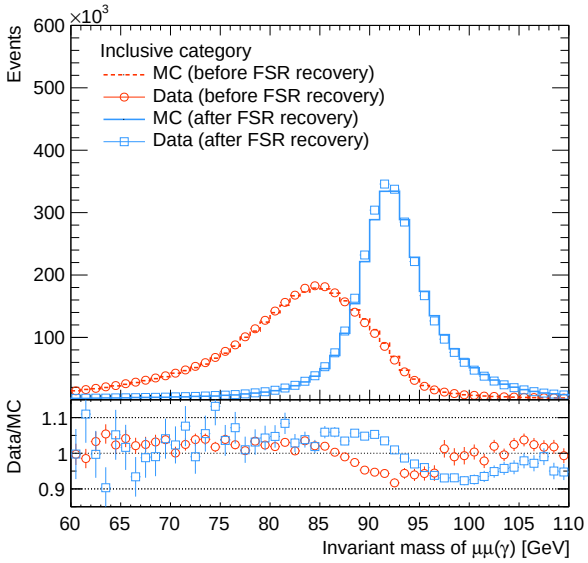

Figure 8.22: The upper panel presents invariant mass distribution around the Z boson peak before and after the FSR recovery only for events with an FSR photon found at the reconstruction level. The dashed orange line and blue solid line represent MC simulation of the background processes (Drell-Yan, top and diboson) before and after the FSR recovery, respectively. The background simulation is normalised to the luminosity of the Run-2 data. The orange circles and blue squares represent the Run-2 data before and after the FSR recovery, respectively. The lower panel presents the ratio of data to MC simulation for the case before and after FSR recovery with orange circles and blue squares, respectively.

8.3.5 FSR recovery efficiency

As in the search for the $H \to ee$ decay, it is necessary to estimate the possible bias coming from a particular choice of the background model. The spurious signal systematic uncertainty is estimated in the $H \to \mu\mu$ analysis using the two fast simulation setup chains discussed briefly in Section 8.1. In the case of the $H \to \mu\mu$ decay, FSR recovery is performed explicitly and therefore it is important to correctly implement the FSR recovery efficiency in the fast simulation.

The efficiency maps are derived using fully simulated ATLAS MC simulation of the Z/γ^* process. The FSR recovery efficiency is defined as the ratio of the number of events with an FSR photon found at the reconstruction level and matching the truth-level photon, to the number of events with an FSR photon found at the truth level. A reconstruction-level photon matches the truth-level photon if the angular distance between these objects is less than 0.1. This requirement is satisfied for vast majority of events with reconstruction-level FSR photon, as can be seen in Figure 8.23. The obtained 2D FSR efficiency map as a function of $\Delta R(\mu, \gamma^{\text{truth}})$ and truth-level FSR photon E_{T} is presented in Figure 8.24 separately for the η regions below and above the calorimeter transition region.

To reduce the effect of statistical fluctuations in the 2D efficiency map, a 1D FSR efficiency histogram is used instead. The histogram is derived as a projection of the 2D map in the ΔR range corresponding to collinear photons onto the y axis and is therefore presented as a function of FSR photon E_{T}. The resulting 1D efficiency histograms for the two η regions are presented in Figure 8.25. The region corresponding to $E_{\text{T}} < 5$ GeV is characterised by worse efficiency, however, the majority of reconstructed photons falling into this range are rejected as a result of the imposed E_{T} cuts. As expected, the efficiency is high in the higher-E_{T} region and remains in the range 80–90%. In order to avoid propagating statistical fluctuations, the distributions are smoothed

by performing a linear fit to the distribution in the E_{T} range between 20 and 100 GeV. The derived efficiency maps are implemented in both fast simulation chains used for the spurious signal estimation.

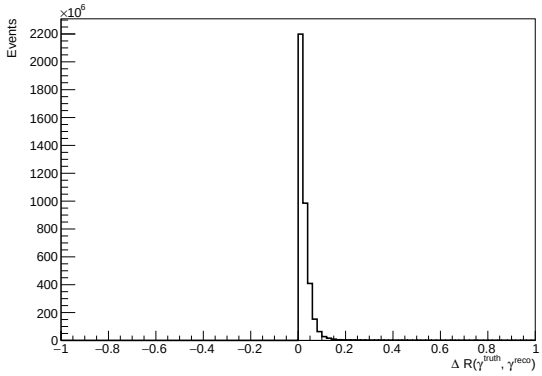

Figure 8.23: Histogram of $\Delta R(\gamma^{\mathrm{truth}}, \gamma^{\mathrm{reco}})$ used to define the matching between the truth- and reconstruction-level FSR photon.

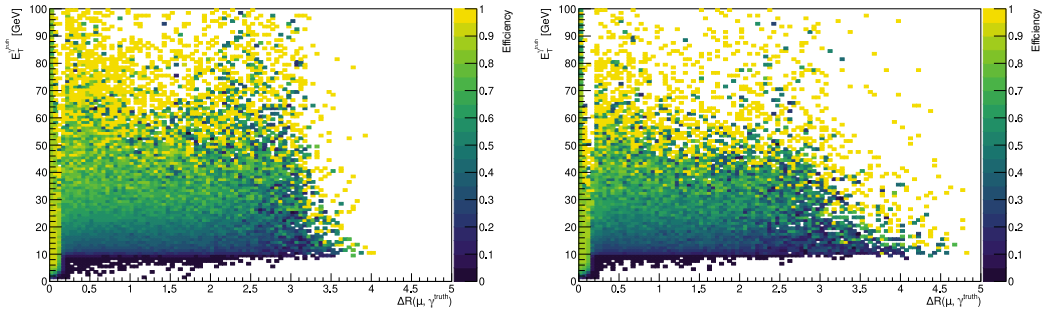

(a) $|\eta| < 1.37$ (b) $1.52 < |\eta| < 2.47$

Figure 8.24: 2D FSR efficiency maps corresponding to different η regions indicated in the sub-figure captions and presented as functions of the $\Delta R(\mu, \gamma^{\mathrm{truth}})$ and truth-level FSR photon E_{T}. The efficiencies are derived using fully simulated ATLAS MC simulation of the Z/γ^* process.

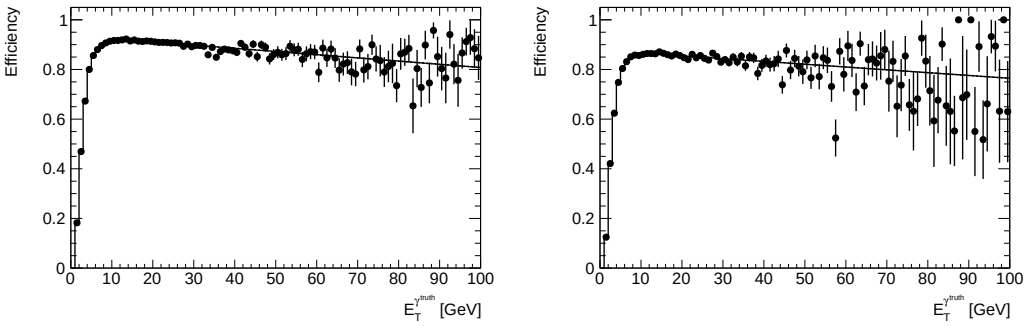

(a) $|\eta| < 1.37$ (b) $1.52 < |\eta| < 2.47$

Figure 8.25: FSR recovery efficiency as a function of the FSR photon E_{T} corresponding to different η regions indicated in the sub-figure captions. The black line represents a linear fit to the points in range between 20 and 100 GeV.

8.4 Categorisation

To improve the sensitivity of the search, events are divided into 20 mutually exclusive categories. There are 16 categories targeting the ggF and VBF signal production processes and three and one category targeting the VH and $t\bar{t}H$ associated production, respectively. In all cases, the categorisation is performed using multivariate methods and employs BDT algorithm from the XGBoost package [130]. The classifiers are trained using a k-fold method to avoid overtraining related to classifier learning fluctuations in the dataset. In this method training data are divided into different folds. The classifier is then trained, validated and tested in different folds in k iterations. The BDT outputs in different folds are transformed in a way that the signal has a uniform BDT output distribution. After the transformation, the test sets of all folds are combined and used in the final evaluation of the specific classifier. The categorisation is performed in the following order: first, events are categorised into the single $t\bar{t}H$ category, then to the VH categories (VH3LH, VH3LM and VH4L) and lastly to the VBF (VBF very high, high, medium and low) and ggF-enriched categories (N-jet very high, high, medium and low). The details of the BDT training and categorisation optimisation are discussed below.

8.4.1 $t\bar{t}H$ category

Events passing the $t\bar{t}H$ selection are categorised using a dedicated BDT classifier into the single $t\bar{t}H$-enriched category. The training is performed using $t\bar{t}H$, $H \to \mu\mu$ simulation as signal and all considered background process as background, with the additional requirement that $m_{\mu\mu} \in (100, 200)$ GeV in both cases. Twelve variables are used to separate the $t\bar{t}H$ events from backgrounds and they are summarised in Table 8.12. The $m_{t\,\mathrm{lep}}$ is calculated as a transverse mass of the third lepton, missing transverse momentum and a b-tagged jet. In the case where there is more than one b-jet in an event, the one that leads to the calculated mass being closest to 173 GeV (approximate mass of the top quark) is used. The quantity $m_{t\,\mathrm{had}}$ is calculated from three jets with exactly one of them being b-tagged. The transverse mass of a leptonically decaying W boson is calculated as $\sqrt{2 \cdot p_{\mathrm{T}}^{\ell_3} \cdot E_{\mathrm{T}}^{\mathrm{miss}} \cdot (1 - \cos\Delta\phi)}$, with $\Delta\phi$ being the azimuthal difference between the $E_{\mathrm{T}}^{\mathrm{miss}}$ and the third lepton. The mass variables used in the training, $m_{\ell_3\ell_4}$, $m_{t\,\mathrm{lep}}$, $m_{t\,\mathrm{had}}$, $m_{W\,\mathrm{lep}}$, $m_{\mu_3\mu_n}$ are set to non-physical values if there is no required information available. The cosine of the decay angle is calculated in the Collins-Soper [131] frame with the following formula:

$$\cos\theta^* = \frac{(E_{\mu^-} + p_{z,\mu^-})\,(E_{\mu^+} - p_{z,\mu^+}) - (E_{\mu^-} - p_{z,\mu^-})\,(E_{\mu^+} + p_{z,\mu^+})}{m_{\mu\mu} \cdot \sqrt{m_{\mu\mu}^2 + (p_{\mathrm{T}}^{\mu\mu})^2}}. \quad (8.2)$$

The BDT output requirement to categorise events into the $t\bar{t}H$ category is defined to maximise the signal sensitivity while ensuring enough events to constrain the background (coming mostly from $t\bar{t}Z$ events). Events selected to the $t\bar{t}H$ category are required to have the the BDT output $\mathcal{O}_{t\bar{t}H} > 0.35$.

8.4.2 VH categories

Events failing the $t\bar{t}H$ category are considered for the three VH-enriched categories. Higgs boson production associated with a W boson (3-lepton channel) is targeted with two dedicated categories and Higgs boson production with a Z boson (4-lepton channel) is targeted with a single category. In events with more

Variable	Description
N_{jets}	Multiplicity of central jets ($\|\eta\| < 2.5$)
$N_{b-\text{jets}}$	Multiplicity of b-tagged jets
$p_{\text{T}}^{\mu\mu}$	Dimuon system p_{T}
$p_{\text{T}}^{\ell_3}$	p_{T} of the third lepton
$p_{\text{T}}^{\ell_4}$	p_{T} of the fourth lepton
$\cos\theta^*$	Cosine of the decay angle
H_{T}	Scalar sum of jet transverse momenta
$m_{\ell_3\ell_4}$	Invariant mass of the third and fourth lepton
$m_{t\,\text{lep}}$	Mass of leptonically decaying top quark candidate
$m_{t\,\text{had}}$	Mass of hadronically decaying top quark candidate
$m_{W\,\text{lep}}$	Mass of leptonically decaying W boson candidate
$m_{\mu_3\mu_N},\ N = 1, 2$	Mass of third μ and opposite-charge μ from H candidate

Table 8.12: BDT variables used to categorise events into $t\bar{t}H$-enriched category.

than two leptons, the assignment of a muon to a particular decay ($H \to \mu\mu$ and either $Z \to \mu\mu$ or $W \to \mu\nu$) is based on the minimisation of a chi-squared function. The chi-squared value is defined using the Higgs candidate mass and the transverse mass of the W boson candidate in the 3-lepton channel or the dimuon mass of the Z candidate in the 4-lepton channel. The BDTs are trained separately for each N-lepton channel and use the corresponding signal MC simulation as signal and the MC simulation of all considered background processes as background. The list of variables used in the BDT training is presented in Table 8.13 for the 3-lepton channel and in Table 8.14 for the 4-lepton channel. Events are required to have the WH output $\mathcal{O}_{WH} \geq 0.7$ for the VH3LH category and $0.1 \leq \mathcal{O}_{WH} < 0.7$ for the VH3LM category. In the 4-lepton channel the single VH4L category events are required to have the BDT score $\mathcal{O}_{ZH} > 0.12$. Similarly to the $t\bar{t}H$ category the BDT boundaries are defined to maximise the signal sensitivity while ensuring enough events.

Variable	Description
N_{jets}	Jet multiplicity
$E_{\text{T}}^{\text{miss}}$	Missing transverse momentum
$p_{\text{T}}^{\ell_3}$	p_{T} of the third lepton
$p_{\text{T}}^{j_1}$	p_{T} of the leading jet (if present)
m_W	Transverse mass of the W candidate
$\Delta\phi_{E_{\text{T}}^{\text{miss}},\,H}$	Azimuthal difference between $E_{\text{T}}^{\text{miss}}$ and H candidate
$\Delta\phi_{\ell_3,\,H}$	Azimuthal difference between third lepton and H candidate
$\Delta\eta_{\ell_3,\,H}$	Pseudorapidity difference between third lepton and H candidate

Table 8.13: BDT variables used to target Higgs boson production in association with a W boson.

Variable	Description
N_{jets}	Jet multiplicity
$p_{\text{T}}^{j_1}$	p_{T} of leading jet (if present)
$p_{\text{T}}^{j_2}$	p_{T} of subleading jet (if present)
m_Z	Z candidate mass
$\Delta\phi_{\ell_3,\,\ell_4}$	Azimuthal difference between third and fourth lepton
$\Delta\phi_{Z,\,H}$	Azimuthal difference between Z and H boson candidates
$\Delta\eta_{Z,\,H}$	Pseudorapidity difference between Z and H boson candidates

Table 8.14: BDT variables used to target Higgs boson production in association with a Z boson.

8.4.3 ggF and VBF categories

Dimuon events passing the selection defined for ggF and VBF categories and failing the $t\bar{t}H$ or VH selection are first divided according to jet multiplicity into different N-jet channels: 0-jet, 1-jet and 2-jet, with the latter including events with two or more jets. To fully exploit the difference between the $H \to \mu\mu$ signal and its backgrounds, the BDTs are trained in each N-jet channel separately. As the 2-jet channel is expected to contain the majority of the VBF events, there is an additional dedicated VBF classifier with output denoted by $\mathcal{O}_{\text{VBF}}$. This classifier is trained with only the VBF MC simulation as signal and uses 17 variables in the training. In each N-jet channel, there is a ggF classifier with output denoted by $\mathcal{O}_{\text{ggF}}^{(N)}$, where N equals 0, 1 or 2, depending on the channel. The classifier is trained using simulations of all Higgs boson production process as signal and uses 17, 7 or 3 variables for the training in the 2-, 1- and 0-jet channels, respectively. Simulated background events for all backgrounds, Drell-Yan, top and diboson, with the invariant mass falling into the $H \to \mu\mu$ signal region, are used as background in the classifier training.

A list of all variables used in the training in the different N-jet channels along with their description is presented in Table 8.15. Figure 8.26 presents example distributions of the three variables used in the BDT training in the 2-jet channel. A good separation between the $H \to \mu\mu$ signal and the backgrounds is visible. The signal events are characterised by a harder dimuon p_{T} spectrum and are more central. The difference between the signal and background in the distribution of the decay angle θ^* is related to a spin. Higgs boson as spin-0 particle is characterised by a flat $\cos\theta^*$ distribution, which affected by the selection leads to lower acceptance in the region near $|\cos\theta^*| = 1$. The dominating background DY has an asymmetric shape in $\cos\theta^*$ as a result of the forward/backward asymmetry related to interference effects between the Z and γ^*.

The categorisation in each N-jet channel is done according to the outputs of the dedicated classifiers. First, events in the 2-jet channel are categorised into four categories, very high, high, medium and low, basing on the output of the VBF classifier. Then, the 2-jet channel events that fail the VBF categories ($\mathcal{O}_{\text{VBF}} < 0.62$), are categorised according to the output of the ggF classifier. In the 1- and 0-jet channels events are categorised only according to the ggF classifier. Four categories are defined for each N-jet channel using the ggF classifier score: very high, high, medium and low. The BDT score boundaries are optimised to provide the best total significance, defined as the square root of the significance in categories added in quadrature. The definitions of the 16 categories targeting the VBF and ggF production processes are presented in Table 8.16. Data-to-MC simulation plots showing the distribution of the four classifiers are presented in Figure 8.27 and Figure 8.28 for the Z control region and for the sideband region, respectively. There is a slope visible in the ratio panels especially in the 0- and 1-jet categories, however, this is expected to have only a small impact on the classification performance. As the background is determined separately in each category, it has no effect on the background estimate.

The invariant mass distribution (including the collinear FSR photon candidates) for the summed VBF and ggF category is presented in Figure 8.29. The mass range presented covers both the Z control and the sideband regions. It can be observed that the agreement between the data and the MC simulation is very good. The systematic band shape near the Z peak is an effect of the muon momentum systematic variation. Similar distributions for each of the VBF and ggF categories are presented in Figures 8.30–8.33. Again, a good data-to-MC agreement can be observed. It is worth noting that the expected strong dependence of the signal-to-background ratio on the analysis category is clearly visible.

Channel	Variable	Description
Common	$p_{\mathrm{T}}^{\mu\mu}$	Dimuon system p_{T}
	$y_{\mu\mu}$	Dimuon system rapidity
	$\cos\theta^*$	Cosine of the decay angle in Collins-Soper frame
1-jet & 2-jet	$p_{\mathrm{T}}^{j_1}$	Leading jet p_{T}
	η_{j_1}	Leading jet η
	$\Delta\phi_{\mu\mu,j_1}$	Azimuthal difference between dimuon system and j_1
	$N_{\mathrm{tracks}}^{j_1}$	Multiplicity of ID tracks associated with j_1
2-jet	$p_{\mathrm{T}}^{j_2}$	Subleading jet p_{T}
	η_{j_2}	Subleading jet η
	$\Delta\phi_{\mu\mu,j_2}$	Azimuthal difference between dimuon system and j_2
	$N_{\mathrm{tracks}}^{j_2}$	Multiplicity of ID tracks associated with j_2
	p_{T}^{jj}	Dijet system p_{T}
	m_{jj}	Dijet system mass
	y_{jj}	Dijet system rapidity
	$\Delta\phi_{\mu\mu,jj}$	Azimuthal difference between dimuon and dijet systems
	H_{T}	Scalar sum of jet transverse momenta
	$E_{\mathrm{T}}^{\mathrm{miss}}$	Missing transverse momentum

Table 8.15: A list of variables used in the VBF and ggF classifier training.

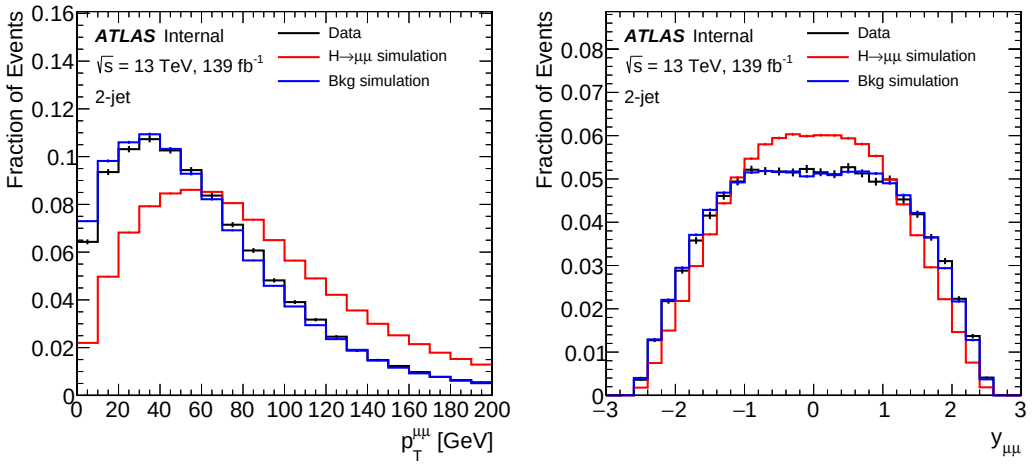

(a) Dimuon system p_{T} (b) Dimuon system rapidity

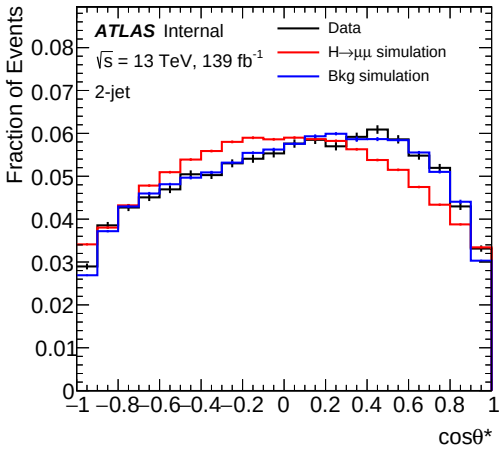

(c) Cosine of the decay angle

Figure 8.26: Example distributions of the training variables in the 2-jet channel [132].

Category	0-jet	1-jet	2-jet VBF	2-jet ggF $\mathcal{O}_{\mathrm{VBF}} < 0.62$
High	$\mathcal{O}^{(0)}_{\mathrm{ggF}} \geq 0.81$	$\mathcal{O}^{(1)}_{\mathrm{ggF}} \geq 0.88$	$\mathcal{O}_{\mathrm{VBF}} \geq 0.93$	$\mathcal{O}^{(2)}_{\mathrm{ggF}} \geq 0.65$
Medium	$0.53 \leq \mathcal{O}^{(0)}_{\mathrm{ggF}} < 0.81$	$0.67 \leq \mathcal{O}^{(1)}_{\mathrm{ggF}} < 0.88$	$0.85 \leq \mathcal{O}_{\mathrm{VBF}} < 0.93$	$0.42 \leq \mathcal{O}^{(2)}_{\mathrm{ggF}} < 0.65$
Low	$0.21 \leq \mathcal{O}^{(0)}_{\mathrm{ggF}} < 0.53$	$0.36 \leq \mathcal{O}^{(1)}_{\mathrm{ggF}} < 0.67$	$0.75 \leq \mathcal{O}_{\mathrm{VBF}} < 0.85$	$0.16 \leq \mathcal{O}^{(2)}_{\mathrm{ggF}} < 0.42$
VeryLow	$\mathcal{O}^{(0)}_{\mathrm{ggF}} < 0.21$	$\mathcal{O}^{(1)}_{\mathrm{ggF}} < 0.36$	$0.62 \leq \mathcal{O}_{\mathrm{VBF}} < 0.75$	$\mathcal{O}^{(2)}_{\mathrm{ggF}} < 0.16$

Table 8.16: Definitions of the 16 categories targeting the VBF and ggF production processes.

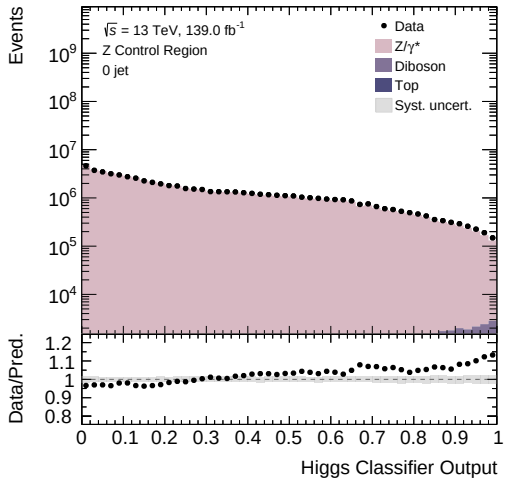

(a) Higgs classifier in 0-jet channel

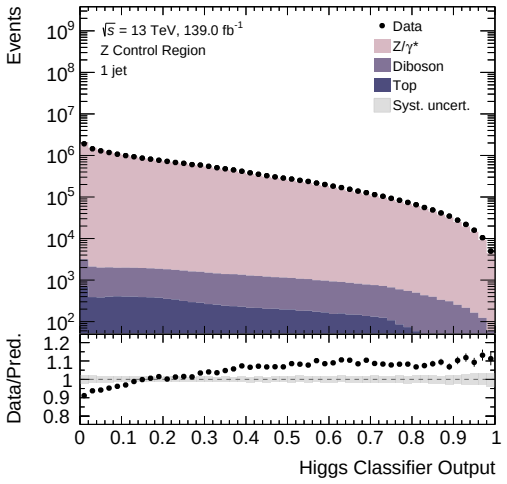

(b) Higgs classifier in 1-jet channel

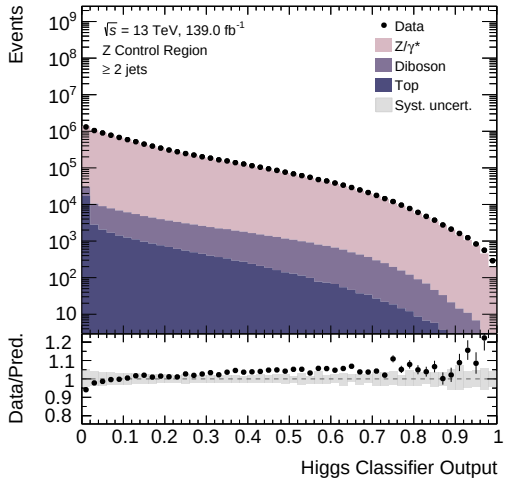

(c) Higgs classifier in 2-jet channel

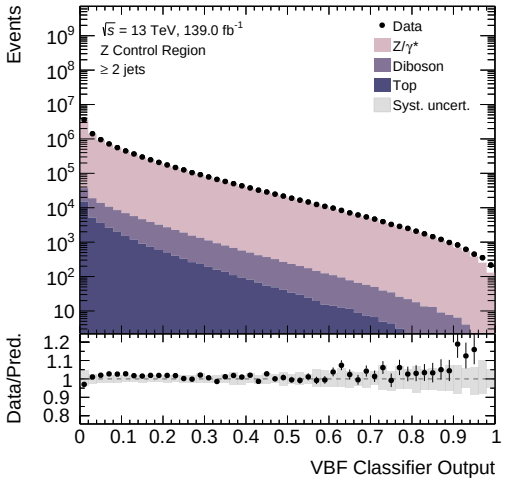

(d) VBF classifier in 2-jet channel

Figure 8.27: The upper panels show the distributions of the BDT classifier outputs indicated in the sub-figure captions for events with $76 < m_{\mu\mu(\gamma)} < 106$ GeV. Black points represent the data. The filled histograms present the MC simulation of different background processes: Drell-Yan, diboson and top, and are normalised to the luminosity of the data. The lower panels show the ratios of the data to the SM prediction. The grey shaded areas represent the statistical and systematic uncertainty band with only experimental systematic uncertainties included (muon momentum scale and resolution and muon trigger and reconstruction efficiencies).

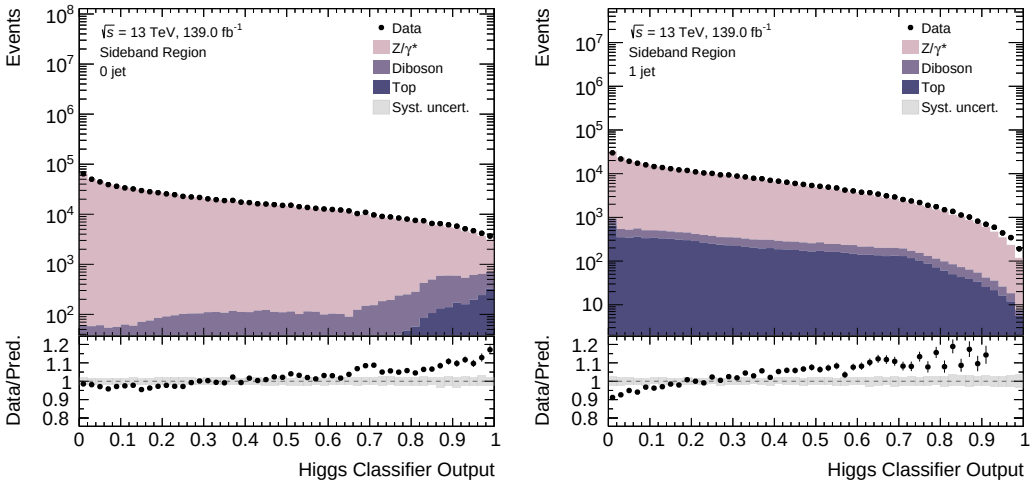

(a) Higgs classifier in 0-jet channel

(b) Higgs classifier in 1-jet channel

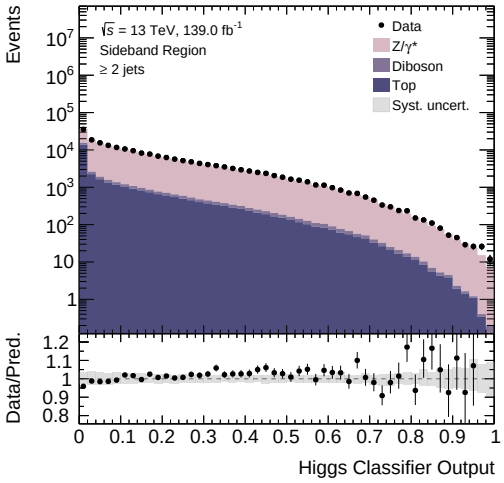

(c) Higgs classifier in 2-jet channel

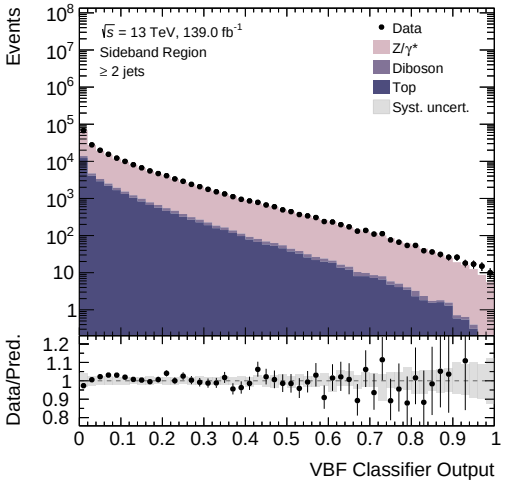

(d) VBF classifier in 2-jet channel

Figure 8.28: The upper panels show the distributions of the BDT classifier outputs indicated in the sub-figure captions for events with $m_{\mu\mu(\gamma)} \in (110, 120) \cup (130, 160)$ GeV. Black points represent the data. The filled histograms present the MC simulation of different background processes: Drell-Yan, diboson and top, and are normalised to the luminosity of the data. The lower panels show the ratios of the data to the SM prediction. The grey shaded areas represent the statistical and systematic uncertainty band with only experimental systematic uncertainties included (muon momentum scale and resolution and muon trigger and reconstruction efficiencies).

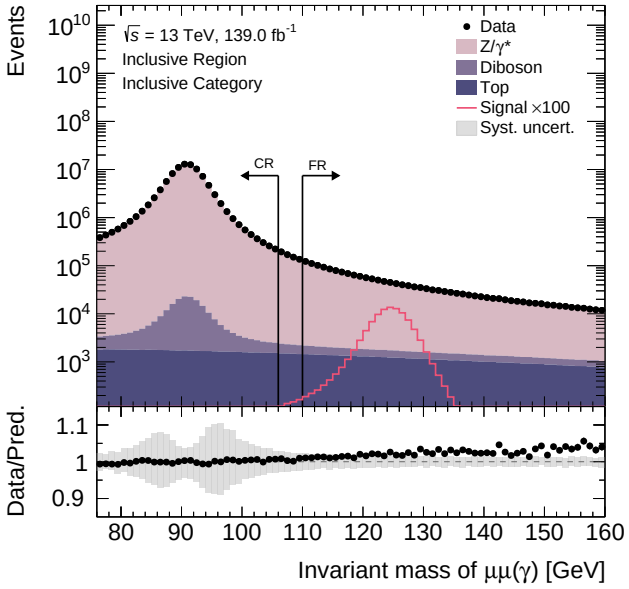

Figure 8.29: The upper panel shows the invariant mass distribution in the summed ggF and VBF categories in the mass range between 76 and 160 GeV. Black points represent the data. The filled histograms present the MC simulation of different background processes: Drell-Yan, diboson and top, and are normalised to the luminosity of the data. The pink line presents the expected $H \to \mu\mu$ signal peak, with all Higgs boson production processes included, and is multiplied by a factor of 100 to make it visible. The black markers indicate the range of the invariant mass distribution corresponding to the Z control region (CR) and to the fitting range (FR). The lower panel shows a ratio of the data to the SM prediction. The grey shaded area represents the statistical and systematic uncertainty band with only experimental systematic uncertainties included (muon momentum scale and resolution and muon trigger and reconstruction efficiencies).

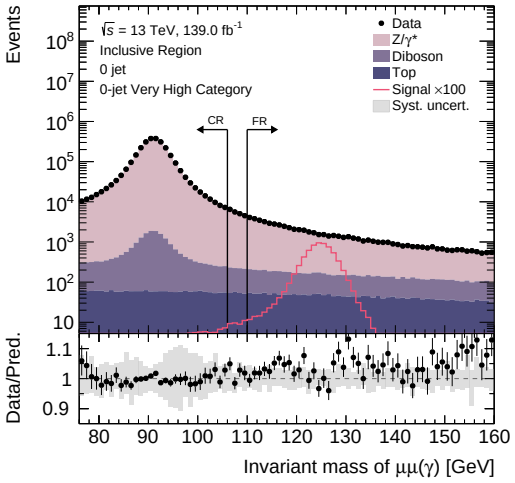

(a) 0-jet Very High

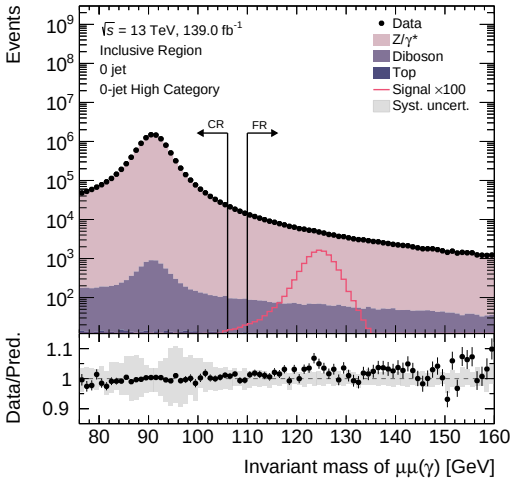

(b) 0-jet High

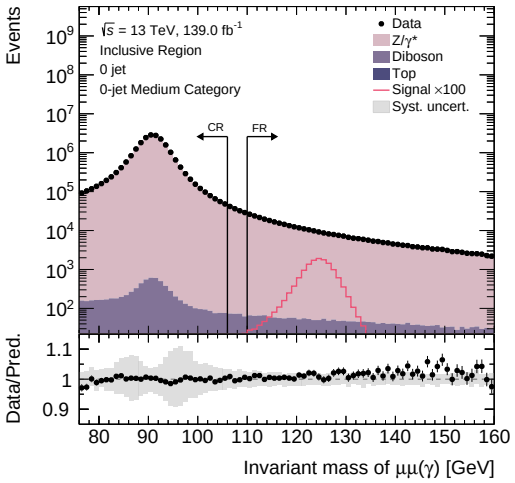

(c) 0-jet Medium

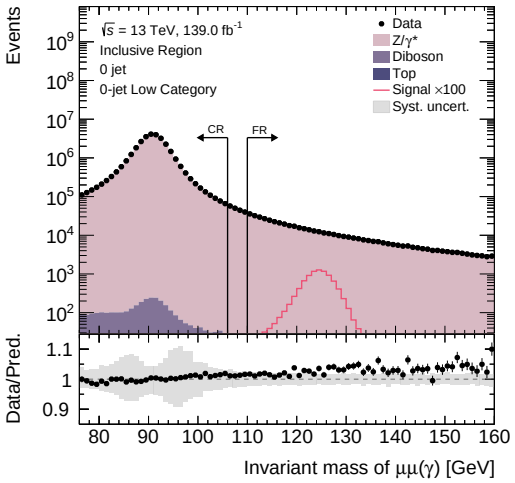

(d) 0-jet Low

Figure 8.30: The upper panels show the invariant mass distributions in the 0-jet categories in the mass range between 76 and 160 GeV. Black points represent the data. The filled histograms present the MC simulation of different background processes: Drell-Yan, diboson and top, and are normalised to the luminosity of the data. The pink line presents the expected $H \to \mu\mu$ signal peak, with all Higgs boson production processes included, and is multiplied by a factor of 100 to make it visible. The black markers indicate the range of the invariant mass distribution corresponding to the Z control region (CR) and to the fitting range (FR). The lower panels show the ratio of the data to the SM prediction. The grey shaded areas represent the statistical and systematic uncertainty band with only experimental systematic uncertainties included (muon momentum scale and resolution and muon trigger and reconstruction efficiencies).

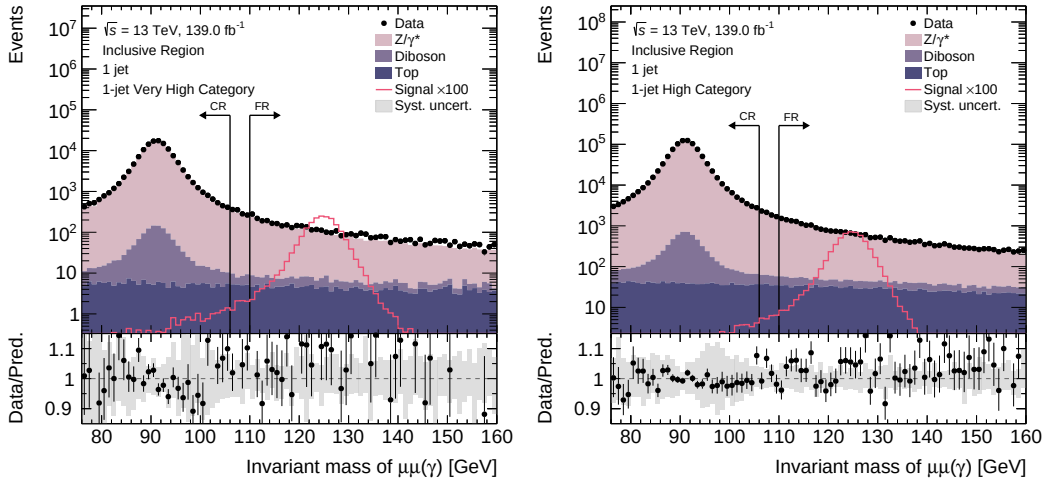

(a) 1-jet Very High (b) 1-jet High

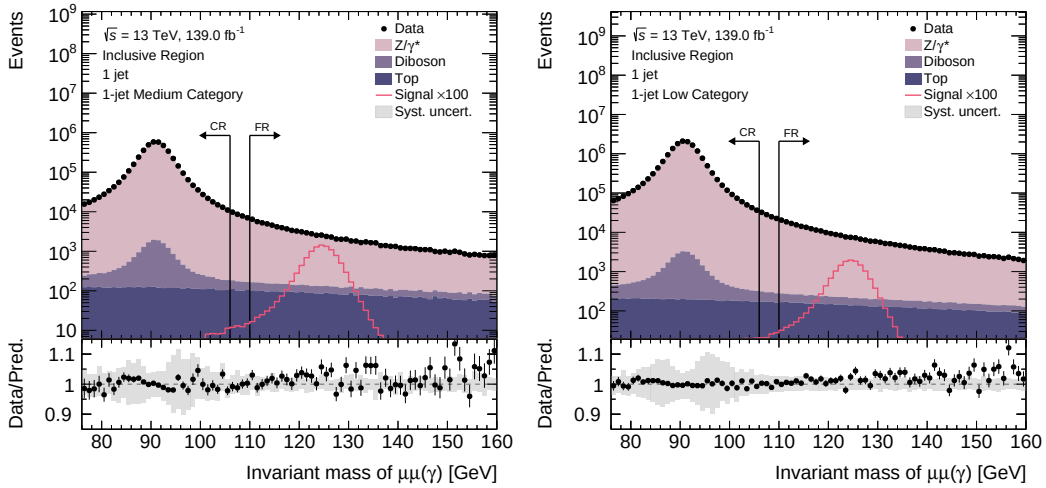

(c) 1-jet Medium (d) 1-jet Low

Figure 8.31: The upper panels show the invariant mass distributions in the 1-jet categories in the mass range between 76 and 160 GeV. Black points represent the data. The filled histograms present the MC simulation of different background processes: Drell-Yan, diboson and top, and are normalised to the luminosity of the data. The pink line presents the expected $H \to \mu\mu$ signal peak, with all Higgs boson production processes included, and is multiplied by a factor of 100 to make it visible. The black markers indicate the range of the invariant mass distribution corresponding to the Z control region (CR) and to the fitting range (FR). The lower panels show the ratio of the data to the SM prediction. The grey shaded areas represent the statistical and systematic uncertainty band with only experimental systematic uncertainties included (muon momentum scale and resolution and muon trigger and reconstruction efficiencies).

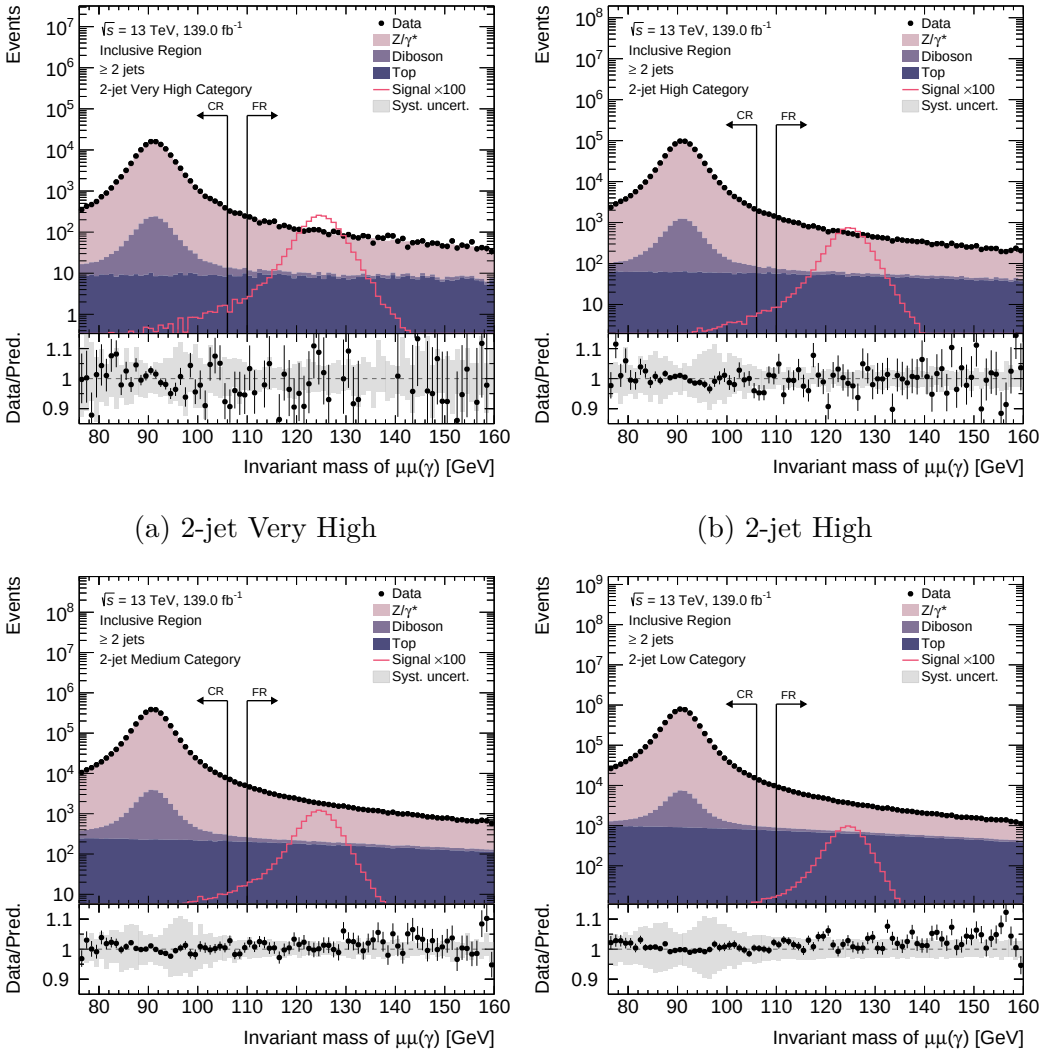

(a) 2-jet Very High

(b) 2-jet High

(c) 2-jet Medium

(d) 2-jet Low

Figure 8.32: The upper panels show the invariant mass distributions in the 2-jet ggF categories in the mass range between 76 and 160 GeV. Black points represent the data. The filled histograms present the MC simulation of different background processes: Drell-Yan, diboson and top, and are normalised to the luminosity of the data. The pink line presents the expected $H \to \mu\mu$ signal peak, with all Higgs boson production processes included, and is multiplied by a factor of 100 to make it visible. The black markers indicate the range of the invariant mass distribution corresponding to the Z control region (CR) and to the fitting range (FR). The lower panels show the ratio of the data to the SM prediction. The grey shaded areas represent the statistical and systematic uncertainty band with only experimental systematic uncertainties included (muon momentum scale and resolution and muon trigger and reconstruction efficiencies).

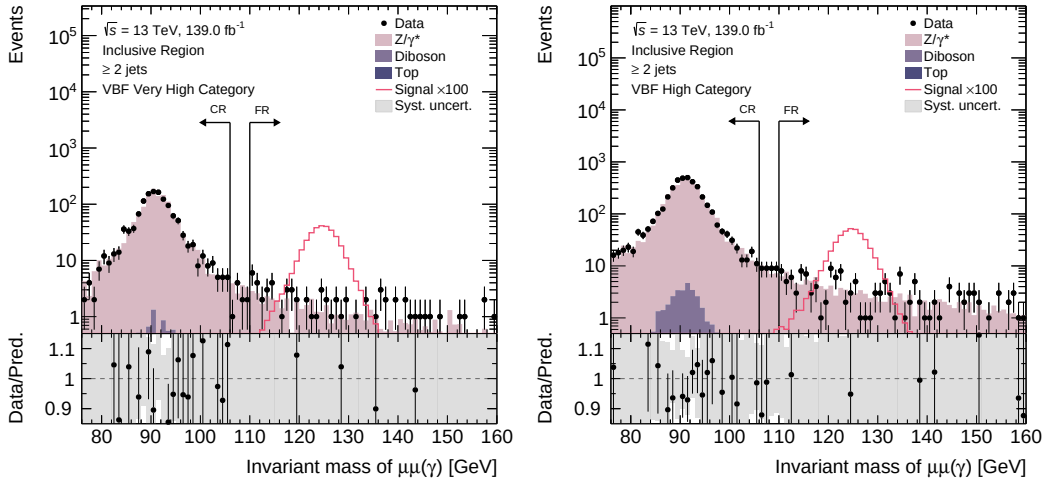

(a) VBF Very High

(b) VBF High

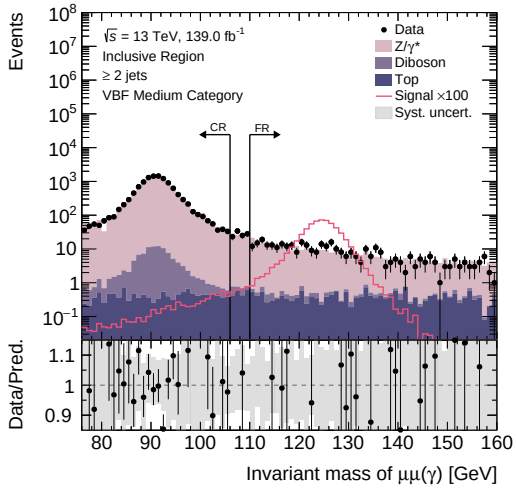

(c) VBF Medium

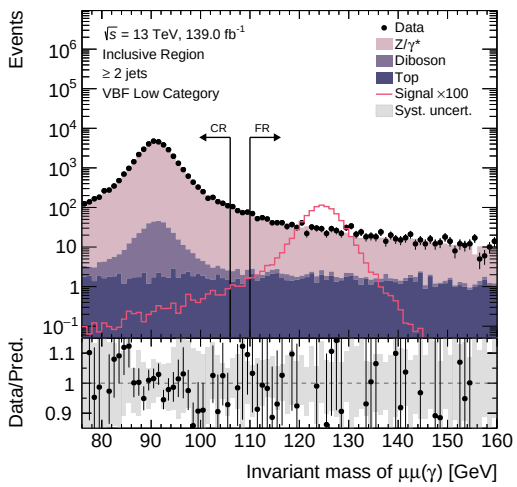

(d) VBF Low

Figure 8.33: The upper panels show the invariant mass distributions in the 2-jet VBF categories in the mass range between 76 and 160 GeV. Black points represent the data. The filled histograms present the MC simulation of different background processes: Drell-Yan, diboson and top, and are normalised to the luminosity of the data. The pink line presents the expected $H \to \mu\mu$ signal peak, with all Higgs boson production processes included, and is multiplied by a factor of 100 to make it visible. The black markers indicate the range of the invariant mass distribution corresponding to the Z control region (CR) and to the fitting range (FR). The lower panels show the ratio of the data to the SM prediction. The grey shaded areas represent the statistical and systematic uncertainty band with only experimental systematic uncertainties included (muon momentum scale and resolution and muon trigger and reconstruction efficiencies).

8.5 Signal and background modelling

8.5.1 Signal modelling

The $H \to \mu\mu$ signal is fitted with a double-sided Crystal Ball function, with the central part described by a Gaussian function and power-law tails on both sides. The function depends on several parameters. The parameters μ_{CB} and σ_{CB}, are the mean and width of the Crystal Ball function. The parameters α_L and n_L describe the power-law tail in the low-mass region and α_H and n_H describe the power-law tail in the high-mass region. The signal model parameters are obtained from a fit to the summed mass distribution of all Higgs production processes and are fixed in the $S+B$ fits.

8.5.2 Background modelling

As already mentioned, modelling of the $H \to \mu\mu$ background is highly non-trivial due to the steepness of the $m_{\mu\mu}$ spectrum in the low-mass region. In order to constrain the background at the per mill level, the background model is defined as the product of two components: a core function and an empirical function.

The core function is a physics-inspired model based on the LO DY line-shape [133]. This function describes the difficult to model part of the mass spectrum. To account for resolution effects, the DY line-shape is convolved with a Gaussian function. The core function has no free parameters and it is common to all categories.

To model backgrounds other than DY and to take into account mass distortions induced by the event selection and categorisation, the core component is multiplied by an empirical function. The empirical function is chosen from the two function families power law functions and exponential functions of polynomials, as presented in Table 8.17. The choice of a particular function with a particular number of degrees of freedom is based on the following criteria:

1. The tested background model must fit the background distribution in data sidebands, fully simulated background MC (top, diboson and in the case of ggF and VBF categories also DY) and fast simulation of the DY background (only in ggF and VBF categories), with a χ^2 probability above 1%,
2. The spurious signal uncertainty associated with a particular model must be lower than 20% of the statistical uncertainty,
3. If more than one function passes criteria 1. and 2., the one with the lowest number of degrees of freedom and then with lowest spurious signal is selected.

Function	Expression
PowerN	$m_{\mu\mu}^{\left(a_0+a_1 m_{\mu\mu}+a_2 m_{\mu\mu}^2+\cdots+a_N m_{\mu\mu}^N\right)}$
EpolyN	$\exp\left(a_0+a_1 m_{\mu\mu}+a_2 m_{\mu\mu}^2+\cdots+a_N m_{\mu\mu}^N\right)$

Table 8.17: Two families of empirical functions used in the background modelling.

8.6 Systematic uncertainties

The systematic uncertainties are estimated in the same way as in the $H \to ee$ search presented in Section 7.6. The theory systematic uncertainties vary in categories from a few per mill up to 15% for the ggF production, up to 7% for the VBF production and up to 18% for the $t\bar{t}H$ and VH production processes.

The systematic uncertainties related to the reconstruction of the different objects used in the analysis are also taken into account. The leading uncertainties come from the jet energy scale and resolution which affect the signal yields up to 10% in some of the 2-jet categories, and the muon momentum resolution which affects the signal yields ranging from 1 to 6% depending on the category.

The background modelling uncertainty is estimated with a spurious signal procedure similar to the one described in Section 7.5 for the $H \to ee$ analysis. The

systematic uncertainty varies from a few percent up to 20% in the VBF/ggF categories and to 30% in the $t\bar{t}H$ and VH-enriched categories.

Also considered is the systematic uncertainty related to the luminosity measurement of 1.7%.

8.7 Results

Figure 8.34 presents the signal plus background fits shown in the inclusive category for unweighted and weighted data. The number of data events, expected number of signal events and signal and background yields in the mass region $m_{\mu\mu} \in (120, 130)$ GeV obtained form the $S+B$ fits to data, as well as significance ($S/\sqrt{B}$) and signal-to-background ratio in analysis categories are presented in Table 8.18. The observed background yields are consistent with the expected values within the uncertainties. The signal-to-background ratio decreases when going from very high to low category. As expected, the best S/B is observed for the two VBF categories, very high and high. The significance is roughly constant for the ggF and VBF categories as designed, with slightly lower values observed in the 0-jet ggF categories.

The best fit values of the signal strength in the five major categories: VH $+t\bar{t}H$, ggF 0-, 1- and 2-jet and VBF, along with the combined μ, are presented in Figure 8.35. As expected, the best constraints on the μ are in the VBF categories. The combined signal strength, defined as the ratio of the observed to the expected number of signal events, is:

$$\mu = 1.2 \pm 0.6 \text{ (stat.)} \, ^{+0.2}_{-0.1} \text{ (syst.)}, \tag{8.3}$$

corresponding to an observed (expected) significance of 2.0σ (1.7σ) assuming no $H \to \mu\mu$ signal. The result is dominated by the data statistics. The largest contribution to the overall systematic uncertainty comes from the signal theory uncertainties ($^{+0.13}_{-0.08}$). Smaller contribution comes from the signal experimental uncertainties ($^{+0.07}_{-0.03}$) and background modelling (± 0.10). The observed upper limit on the signal strength at 95% confidence level is 2.2, whereas the expected

limit is 1.1 and 2.0 for the background-only and SM hypotheses, respectively. The upper limit on the $H \to \mu\mu$ branching ratio at 95% confidence level is $\mathcal{B}(H \to \mu\mu) < 4.7 \cdot 10^{-4}$.

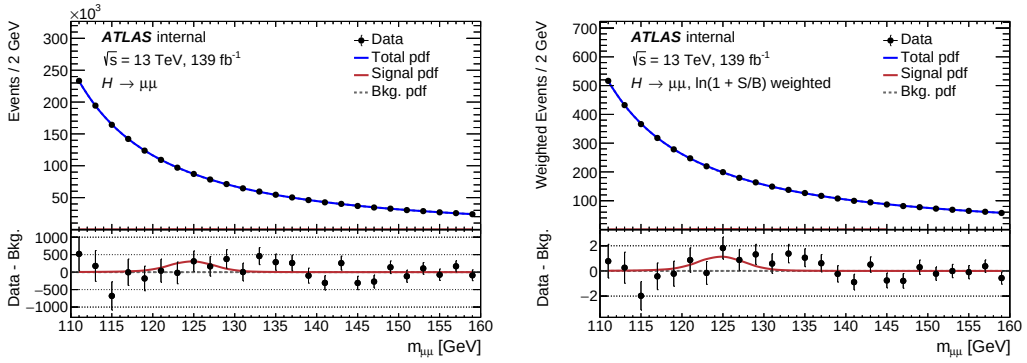

(a) Unweighted (b) Weighted

Figure 8.34: The upper panels present the signal plus background fits to dimuon mass distributions presented in the inclusive category for unweighted and weighted data indicated in the sub-figure captions [132]. The weighted data are scaled by $\ln(1 + S/B)$, where S and B are the signal and background yields in mass region $m_{\mu\mu} \in (120, 130)$ GeV, respectively, obtained from the S+B fits to data. Black points represent the Run-2 data. The solid blue line is the total S+B model, whereas the signal and background components are represented by solid red and dashed black line, respectively. The lower panels show the difference between the data points and the background fit.

Category	Data	S_{SM}	S	B	$S/\sqrt{B}$	S/B [%]
VBF Very High	15	2.81 ± 0.27	3.3 ± 1.7	14.5 ± 2.1	0.86	22.6
VBF High	39	3.46 ± 0.36	4.0 ± 2.1	32.5 ± 2.9	0.71	12.4
VBF Medium	112	4.8 ± 0.5	5.6 ± 2.8	85 ± 4	0.61	6.6
VBF Low	284	7.5 ± 0.9	9 ± 4	273 ± 8	0.53	3.2
2-jet Very High	1030	17.6 ± 3.3	21 ± 10	1024 ± 22	0.63	2.0
2-jet High	5433	50 ± 8	58 ± 30	5440 ± 50	0.77	1.0
2-jet Medium	18311	79 ± 15	90 ± 50	18320 ± 90	0.66	0.5
2-jet Low	36409	63 ± 17	70 ± 40	36340 ± 140	0.37	0.2
1-jet Very High	1097	16.5 ± 2.4	19 ± 10	1071 ± 22	0.59	1.8
1-jet High	6413	46 ± 7	54 ± 28	6320 ± 50	0.69	0.9
1-jet Medium	24576	90 ± 11	100 ± 50	24290 ± 100	0.67	0.4
1-jet Low	73459	125 ± 17	150 ± 70	73480 ± 190	0.53	0.2
0-jet Very High	15986	59 ± 11	70 ± 40	16090 ± 90	0.55	0.4
0-jet High	46523	99 ± 13	120 ± 60	46190 ± 150	0.54	0.3
0-jet Medium	91392	119 ± 14	140 ± 70	91310 ± 210	0.46	0.2
0-jet Low	121354	79 ± 10	90 ± 50	121310 ± 280	0.26	0.1
VH4L	34	0.53 ± 0.05	0.6 ± 0.3	24 ± 4	0.13	2.6
VH3LH	41	1.45 ± 0.14	1.7 ± 0.9	41 ± 5	0.27	4.2
VH3LM	358	2.76 ± 0.24	3.2 ± 1.6	347 ± 15	0.17	0.9
$t\bar{t}H$	17	1.19 ± 0.13	1.4 ± 0.7	15.1 ± 2.2	0.36	9.2

Table 8.18: Number of data events, expected signal yield and the observed signal and background yields in mass region $m_{\mu\mu} \in (120, 130)$ GeV along with the significance $S/\sqrt{B}$ and signal-to-background ratio in analysis categories [132]. The observed yields are obtained from the $S+B$ fit to data assuming the signal strength $\mu = 1.2$.

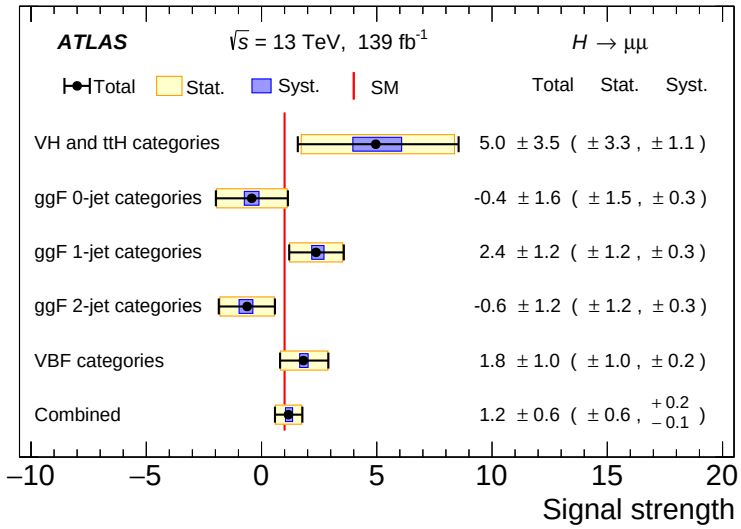

Figure 8.35: The best fit values of the signal strength in the summed categories targeting different production channels: VH $+t\bar{t}H$, ggF 0-, 1- and 2-jet, and VBF, along with a combined signal strength [132]. The yellow and blue rectangles show the statistical and systematic uncertainties, respectively, and the error bars represent their combination. The vertical red line represents the signal strength corresponding to SM hypothesis.

Chapter 9

Conclusions

This thesis presents searches for Higgs boson decays to dielectrons and to dimuons, performed using the ATLAS detector data from proton-proton collisions in Run 2 corresponding to an integrated luminosity of 139 fb^{-1}.

The search for the $H \to ee$ decay is performed for the first time within the ATLAS experiment. The analysis is done in several stages. Events passing selection are split into seven categories to improve the overall signal sensitivity. The categorisation is defined to target the two Higgs boson production channels with the highest cross-sections, ggF and VBF. An $S+B$ fit is performed to the dielectron mass distributions in each category, using analytical functions to describe the signal and the background. The obtained best fit value of the branching ratio is:

$$\mathcal{B}(H \to ee) = (0.0 \pm 1.7(\text{stat.}) \pm 0.6(\text{syst.})) \cdot 10^{-4}. \tag{9.1}$$

The result is dominated by the data statistics with the leading systematic uncertainty coming from the choice of a particular background model. This result, presented in Ref. [116], represents a factor of 5 improvement on the result presented by the CMS Collaboration using data from Run 1.

The $H \to \mu\mu$ analysis strategy is similar. Events are selected with loose requirements to maximise the signal acceptance. Up to one FSR photon candidate is added to the dimuon mass calculation to improve the resolution in the categories targeting the ggF and VBF Higgs production processes. The event categorisation is defined using the outputs of the BDT classifiers into 20

categories targeting ggF, VBF and Higgs production associated with a vector boson or $t\bar{t}$ pair. An $S+B$ fit is performed in each analysis category to extract the signal peak from a falling background. The background model is constructed from two components, a core function shared across all categories, and an empirical function, selected for each category based on a number of criteria. The extracted combined signal strength is:

$$\mu = 1.2 \pm 0.6 \text{ (stat.)} \, ^{+0.2}_{-0.1} \text{ (syst.)} \tag{9.2}$$

which is consistent with both the SM and the background-only hypothesis within the uncertainties. The observed (expected) significance is 2.0σ (1.7σ) assuming no SM signal. The analysis is presented in Ref. [132]. The obtained result represents a significant improvement with respect to the previous published ATLAS result. The improvement is achieved not only due to the nearly 4 times larger dataset, but also thanks to significant improvements implemented in the analysis. These include employing BDTs to define categories, dividing data into more categories, additionally targeting the VH and $t\bar{t}H$ production processes, excellent background modelling and FSR recovery.

A combination of results from the ATLAS and CMS Collaborations could lead to the first evidence for the Higgs decay to dimuons using data from Run 2. If the $H \to \mu\mu$ branching ratio is as expected in the SM, the decay could be observed with close to 4σ significance by combining ATLAS and CMS results using data from Run 2 and Run 3. The dataset expected to be collected at the High-Luminosity LHC corresponding to around 3000 fb^{-1} could decrease the uncertainty of the ATLAS result to the level of 13% [134] (or further if the dataset increases to 4000 fb^{-1}).

This thesis also presents a study of the effects of radiation damage in the ATLAS SCT detector sensors. The evolution of the leakage current is predicted using two phenomenological models, the Hamburg model and the Sheffield model. When comparing the predictions to data, both models agree well, with the deviations not beyond the 1σ systematic uncertainty. This gives confidence

that the leakage current increase can be predicted well until the end of SCT operation at the end of Run 3, assuming certain operation conditions. It can also be used to verify the running conditions in Run 3, such as effects of lowering the operation temperature. Another important result of the radiation damage is the evolution of the full depletion voltage. An estimate of V_{FD} is evaluated by looking at the hit efficiency curves obtained using data from HV scans performed during collisions. The results show a large discrepancy between the estimated V_{FD} and the Hamburg model prediction. The cause of this discrepancy is still to be understood. It may be related to low electric field in the depletion zone affecting the charge collection.

Bibliography

[1] Y. Fukuda et al., *Evidence for oscillation of atmosferic neutrinos*, Phys. Rev. Lett. **81** (1998) 1562 (cit. on p. 16).

[2] M. Tanabashi et al., *Review of Particle Physics*, Phys. Rev. **D98** (2018) 030001 (cit. on pp. 17, 18, 113).

[3] F. Englert and R. Brout, *Broken Symmetry and the Mass of Gauge Vector Mesons*, Phys. Rev. Lett. **13** (1964) 321 (cit. on p. 18).

[4] P. W. Higgs, *Broken Symmetries and the Masses of Gauge Bosons*, Phys. Rev. Lett. **13** (1964) 508 (cit. on p. 18).

[5] S. L. Glashow, *Partial Symmetries of Weak Interactions*, Nucl. Phys. **22** (1961) 579 (cit. on p. 20).

[6] S. Weinberg, *A Model of Leptons*, Phys. Rev. Lett. **19** (1967) 1264 (cit. on p. 20).

[7] A. Salam, *Weak and Electromagnetic Interactions*, Conf. Proc. **C680519** (1968) 367 (cit. on p. 20).

[8] G. Arnison et al., *Experimental Observation of Isolated Large Transverse Energy Electrons with Associated Missing Energy at $\sqrt{s} = 540$ GeV*, Phys. Lett. **122B** (1983) 103 (cit. on p. 20).

[9] M. Banner et al., *Observation of Single Isolated Electrons of High Transverse Momentum in Events with Missing Transverse Energy at the CERN $\bar{p}p$ Collider*, Phys. Lett. **122B** (1983) 476 (cit. on p. 20).

[10] G. Arnison et al., *Experimental Observation of Lepton Pairs of Invariant Mass Around 95 GeV/c^2 at the CERN SPS Collider*, Phys. Lett. **126B** (1983) 398 (cit. on p. 20).

[11] P. Bagnaia et al., *Evidence for $Z^0 \to e^+e^-$ at the CERN $\bar{p}p$ Collider*, Phys. Lett. **B129** (1983) 130 (cit. on p. 20).

[12] ATLAS Collaboration, *Observation of a new particle in the search for the Standard Model Higgs boson with the ATLAS detector at the LHC*, Phys. Lett. B **716** (2012) 1, arXiv: 1207.7214 [hep-ex] (cit. on pp. 20, 24).

[13] CMS Collaboration, *Observation of a new boson at a mass of 125 GeV with the CMS experiment at the LHC*, Phys. Lett. B **716** (2012) 30, arXiv: 1207.7235 [hep-ex] (cit. on pp. 20, 24).

[14] L. Álvarez-Gaumé and J. Ellis, *Eyes on a prize particle*, Nature Physics **7** (2011) 2 (cit. on p. 21).

[15] D. de Florian et al., *Handbook of LHC Higgs Cross Sections: 4. Deciphering the Nature of the Higgs Sector*, (2016), arXiv: 1610.07922 [hep-ph] (cit. on pp. 21, 23, 24, 26, 138).

[16] ATLAS and CMS Collaborations, *Measurements of the Higgs boson production and decay rates and constraints on its couplings from a combined ATLAS and CMS analysis of the LHC pp collision data at $\sqrt{s} = 7$ and 8 TeV*, JHEP **08** (2016) 045, arXiv: 1606.02266 [hep-ex] (cit. on pp. 22, 23).

[17] ATLAS Collaboration, *Observation of $H \to b\bar{b}$ decays and VH production with the ATLAS detector*, Phys. Lett. B **786** (2018) 59, arXiv: 1808.08238 [hep-ex] (cit. on p. 23).

[18] CMS Collaboration, *Observation of Higgs Boson Decay to Bottom Quarks*, Phys. Rev. Lett. **121** (2018) 121801, arXiv: 1808.08242 [hep-ex] (cit. on p. 23).

[19] ATLAS Collaboration, *Observation and measurement of Higgs boson decays to WW^* with the ATLAS detector*, Phys. Rev. D **92** (2015) 012006, arXiv: 1412.2641 [hep-ex] (cit. on p. 23).

[20] ATLAS Collaboration, *Measurements of gluon-gluon fusion and vector-boson fusion Higgs boson production cross-sections in the $H \to WW^* \to e\nu\mu\nu$ decay channel in pp collisions at $\sqrt{s} = 13$ TeV with the ATLAS detector*, Phys. Lett. B **789** (2019) 508, arXiv: 1808.09054 [hep-ex] (cit. on p. 23).

[21] ATLAS Collaboration, *Measurements of Higgs boson production and couplings in the four-lepton channel in pp collisions at center-of-mass energies of 7 and 8 TeV with the ATLAS detector*, Phys. Rev. D **91** (2015) 012006, arXiv: 1408.5191 [hep-ex] (cit. on pp. 24, 154).

[22] ATLAS Collaboration, *Higgs boson production cross-section measurements and their EFT interpretation in the 4ℓ decay channel at $\sqrt{s} = 13$ TeV with the ATLAS detector*, (2020), arXiv: 2004.03447 [hep-ex] (cit. on p. 24).

[23] ATLAS Collaboration, *Measurements of fiducial and differential cross sections for Higgs boson production in the diphoton decay channel at $\sqrt{s} = 8$ TeV with ATLAS*, JHEP **09** (2014) 112, arXiv: 1407.4222 [hep-ex] (cit. on p. 24).

[24] ATLAS Collaboration, *Evidence for the Higgs-boson Yukawa coupling to tau leptons with the ATLAS detector*, JHEP **04** (2015) 117, arXiv: 1501.04943 [hep-ex] (cit. on p. 24).

[25] ATLAS Collaboration, *Cross-section measurements of the Higgs boson decaying into a pair of τ-leptons in proton–proton collisions at $\sqrt{s} = 13$ TeV with the ATLAS detector*, Phys. Rev. D **99** (2019) 072001, arXiv: 1811.08856 [hep-ex] (cit. on p. 24).

[26] ATLAS Collaboration, *Combined measurements of Higgs boson production and decay using up to $80\,fb^{-1}$ of proton–proton collision data at $\sqrt{s} = 13$ TeV collected with the ATLAS experiment*, Phys. Rev. D **101** (2020) 012002, arXiv: 1909.02845 [hep-ex] (cit. on p. 25).

[27] ATLAS Collaboration, *Search for the Decay of the Higgs Boson to Charm Quarks with the ATLAS Experiment*, Phys. Rev. Lett. **120** (2018) 211802, arXiv: 1802.04329 [hep-ex] (cit. on p. 25).

[28] ATLAS Collaboration, *Search for the Dimuon Decay of the Higgs Boson in pp Collisions at $\sqrt{s} = 13$ TeV with the ATLAS Detector*, Phys. Rev. Lett. **119** (2017) 051802, arXiv: 1705.04582 [hep-ex] (cit. on pp. 26, 138).

[29] CMS Collaboration, *Search for the Higgs Boson Decaying to Two Muons in Proton–Proton Collisions at $\sqrt{s} = 13$ TeV*, Phys. Rev. Lett. **122** (2019) 021801, arXiv: 1807.06325 [hep-ex] (cit. on pp. 26, 138).

[30] A. Dery, A. Efrati, Y. Hochberg and Y. Nir, *What if $BR(h \to \mu\mu)$ $BR(h \to \tau\tau) \neq m_\mu^2/m_\tau^2$?*, JHEP **05** (2013) 039, arXiv: 1302.3229 [hep-ph] (cit. on pp. 26, 138).

[31] ATLAS Collaboration, *A search for the dimuon decay of the Standard Model Higgs boson in pp collisions at $\sqrt{s} = 13$ TeV with the ATLAS Detector*, ATLAS-CONF-2019-028, 2019, URL: https://cds.cern.ch/record/2682155 (cit. on pp. 26, 138).

[32] ATLAS Collaboration, *Summary plots from the ATLAS Higgs physics group*, URL: https://atlas.web.cern.ch/Atlas/GROUPS/PHYSICS/CombinedSummaryPlots/HIGGS/ (cit. on p. 27).

[33] L. Evans and P. Bryant, *LHC Machine*, JINST **3** (2008) S08001 (cit. on pp. 28, 30).

[34] E. Mobs, *The CERN accelerator complex - August 2018. Complexe des accélérateurs du CERN - Août 2018*, (2018), General Photo, URL: https://cds.cern.ch/record/2636343 (cit. on p. 29).

[35] ATLAS Collaboration, *Luminosity Public Results*, URL: https://twiki.cern.ch/twiki/bin/view/AtlasPublic/LuminosityPublicResultsRun2 (cit. on pp. 31, 32).

[36] S. van der Meer, *Calibration of the effective beam height in the ISR*, tech. rep. CERN-ISR-PO-68-31. ISR-PO-68-31, CERN, 1968, URL: https://cds.cern.ch/record/296752 (cit. on p. 32).

[37] ATLAS Collaboration, *Luminosity determination in pp collisions at $\sqrt{s} = 13$ TeV using the ATLAS detector at the LHC*, ATLAS-CONF-2019-021, 2019, URL: https://cds.cern.ch/record/2677054 (cit. on p. 32).

[38] ATLAS Collaboration, *The ATLAS Experiment at the CERN Large Hadron Collider*, JINST **3** (2008) S08003 (cit. on pp. 33, 34, 37, 40–42, 44).

[39] ATLAS Collaboration, *Operation and performance of the ATLAS semiconductor tracker*, JINST **9** (2014) P08009, arXiv: 1404.7473 [hep-ex] (cit. on p. 36).

[40] D. Attree et al., *The evaporative cooling system for the ATLAS inner detector*, JINST **3** (2008) P07003 (cit. on p. 36).

[41] M. Battistin et al., *The Thermosiphon Cooling System of the ATLAS Experiment at the CERN Large Hadron Collider*, Int. J. Chem. React. Eng. **13** (2015) 511, URL: https://cds.cern.ch/record/2062241 (cit. on p. 38).

[42] G. Avoni et al., *The new LUCID-2 detector for luminosity measurement and monitoring in ATLAS*, JINST **13** (2018) P07017 (cit. on p. 45).

[43] S. Monzani, *The ZDC Detector in ATLAS*, Nuovo Cim. C **036** (2013) 310 (cit. on p. 45).

[44] L. Adamczyk et al., *Technical Design Report for the ATLAS Forward Proton Detector*, tech. rep. CERN-LHCC-2015-009. ATLAS-TDR-024, 2015, URL: https://cds.cern.ch/record/2017378 (cit. on p. 45).

[45] Abdel K. S. et al., *The ALFA Roman Pot Detectors of ATLAS*, JINST **11** (2016) P11013, arXiv: 1609.00249 [physics.ins-det] (cit. on p. 45).

[46] ATLAS Collaboration, *ATLAS Photos*, 2018, URL: https://cds.cern.ch/record/2627582 (cit. on p. 46).

[47] ATLAS Collaboration, *Performance of the ATLAS trigger system in 2015*, Eur. Phys. J. C **77** (2017) 317, arXiv: 1611.09661 [hep-ex] (cit. on p. 46).

[48] ATLAS Collaboration, *ATLAS Public Results Page*, URL: https://twiki.cern.ch/twiki/bin/view/AtlasPublic/ApprovedPlotsDAQ (cit. on p. 47).

[49] Encyclopædia Britannica, *Electrical conductor*, accessed 24 Jun 2020, URL: https://www.britannica.com/science/electrical-conductor#/media/1/182829/139 (cit. on p. 49).

[50] S. Sadeghi, *Nitrogen-Doped Carbon Nanotube/Polymer Nanocomposites Towards Thermoelectric Applications*, Thermoelectrics for Power Generation - A Look at Trends in the Technology (2016) 325 (cit. on p. 49).

[51] *Adapted from image published in Wikimedia Commons on a CC BY 3.0 license*, accessed 24 Jun 2020, URL: https://commons.wikimedia.org/wiki/File:Pn-junction-equilibrium-graph.svg (cit. on p. 53).

[52] A. Ahmad et al., *The Silicon microstrip sensors of the ATLAS semiconductor tracker*, Nucl. Instrum. Meth. A **578** (2007) 98 (cit. on p. 57).

[53] R. Wunstorf et al., *Damage-induced surface effects in silicon detectors*, Nuclear Instruments and Methods in Physics Research Section A: Accelerators, Spectrometers, Detectors and Associated Equipment **377** (1996) 290, Proceedings of the Seventh European Symposium on Semiconductor, ISSN: 0168-9002, URL: http://www.sciencedirect.com/science/article/pii/0168900296002185 (cit. on p. 58).

[54] T. Sjostrand et al., *An introduction to PYTHIA 8.2*, Comput. Phys. Commun. **191** (2015) 159, arXiv: 1410.3012 [hep-ph] (cit. on pp. 59, 104, 105, 140).

[55] A. D. Martin, W. J. Stirling, R. S. Thorne and G. Watt, *Parton distributions for the LHC*, Eur. Phys. J. C **63** (2009) 189, arXiv: 0901.0002 [hep-ph] (cit. on p. 59).

[56] ATLAS Collaboration, *The Pythia 8 A3 tune description of ATLAS minimum bias and inelastic measurements incorporating the Donnachie–Landshoff diffractive model*, ATL-PHYS-PUB-2016-017, 2016, URL: https://cds.cern.ch/record/2206965 (cit. on pp. 59, 105).

[57] G. Battistoni et al., *The FLUKA code: Description and benchmarking*, AIP Conf. Proc. **896** (2007) 31, ed. by M. Albrow and R. Raja (cit. on p. 59).

[58] A. Ferrari, P. R. Sala, A. Fassò and J. Ranft, *FLUKA: A multi-particle transport code (program version 2005)*, CERN Yellow Reports: Monographs, CERN, 2005, URL: https://cds.cern.ch/record/898301 (cit. on p. 59).

[59] ATLAS Collaboration, *Radiation Background Simulations For Run 2 Using A3 Tune*, Internal Material, URL: https://twiki.cern.ch/twiki/bin/view/Atlas/RadiationBackgroundSimulationsRun2UsingA3Tune (cit. on p. 59).

[60] R. S. Harper, *Radiation damage studies of silicon detectors and searching for an intermediate mass Higgs boson in ATLAS*, Thesis, University of Sheffield, 2001 (cit. on pp. 61, 62).

[61] M. Moll, *Radiation damage in silicon particle detectors: Microscopic defects and macroscopic properties*, Thesis, DESY-THESIS-1999-040, University of Hamburg, 1999, URL: https://cds.cern.ch/record/425274 (cit. on p. 61).

[62] A. Chilingarov et al., *Radiation studies and operational projections for silicon in the ATLAS inner detector*, Nuclear Instruments and Methods in Physics Research Section A: Accelerators, Spectrometers, Detectors and Associated Equipment **360** (1995) 432, Proceedings of the Sixth Pisa Meeting on Advanced Detectors, ISSN: 0168-9002, URL: http://

www.sciencedirect.com/science/article/pii/0168900295001107 (cit. on pp. 62, 63).

[63] A. Chilingarov, *Temperature dependence of the current generated in Si bulk*, Journal of Instrumentation **8** (2013) P10003, URL: https://doi.org/10.1088%2F1748-0221%2F8%2F10%2Fp10003 (cit. on pp. 62, 64).

[64] ATLAS Collaboration, *SCT radiation damage plots, prepared for Radiation damage workshop*, URL: https://atlas.web.cern.ch/Atlas/GROUPS/PHYSICS/PLOTS/SCT-2019-001/ (cit. on p. 80).

[65] S. Hoeche, 'Introduction to parton-shower event generators', *Theoretical Advanced Study Institute in Elementary Particle Physics: Journeys Through the Precision Frontier: Amplitudes for Colliders*, 2015 235, arXiv: 1411.4085 [hep-ph] (cit. on p. 82).

[66] J. C. Collins, D. E. Soper and G. F. Sterman, 'Factorization of Hard Processes in QCD', vol. 5, 1989 1, arXiv: hep-ph/0409313 (cit. on p. 81).

[67] V. N. Gribov and L. N. Lipatov, *Deep inelastic e p scattering in perturbation theory*, Sov. J. Nucl. Phys. **15** (1972) 438, [Yad. Fiz.15,781(1972)] (cit. on p. 82).

[68] Y. L. Dokshitzer, *Calculation of the Structure Functions for Deep Inelastic Scattering and e+ e- Annihilation by Perturbation Theory in Quantum Chromodynamics.*, Sov. Phys. JETP **46** (1977) 641 (cit. on p. 82).

[69] G. Altarelli and G. Parisi, *Asymptotic Freedom in Parton Language*, Nucl. Phys. **B126** (1977) 298 (cit. on p. 82).

[70] B. Andersson, G. Gustafson, G. Ingelman and T. Sjostrand, *Parton Fragmentation and String Dynamics*, Phys. Rept. **97** (1983) 31 (cit. on p. 84).

[71] T. D. Gottschalk, *A Simple Phenomenological Model for Hadron Production From Low Mass Clusters*, Nucl. Phys. B **239** (1984) 325 (cit. on p. 84).

[72] S. Agostinelli et al., GEANT4 – *a simulation toolkit*, Nucl. Instrum. Meth. A **506** (2003) 250 (cit. on pp. 85, 104, 105).

[73] ATLAS Collaboration, *Electron reconstruction and identification in the ATLAS experiment using the 2015 and 2016 LHC proton–proton collision data at* $\sqrt{s} = 13$ *TeV*, Eur. Phys. J. C **79** (2019) 639, arXiv: 1902.04655 [hep-ex] (cit. on p. 87).

[74] ATLAS Collaboration, *Electron and photon performance measurements with the ATLAS detector using the 2015–2017 LHC proton-proton collision data*, JINST **14** (2019) P12006, arXiv: 1908.00005 [hep-ex] (cit. on pp. 88, 89, 91).

[75] ATLAS Collaboration, *Muon reconstruction performance of the ATLAS detector in proton–proton collision data at* $\sqrt{s} = 13$ *TeV*, Eur. Phys. J. C **76** (2016) 292, arXiv: 1603.05598 [hep-ex] (cit. on pp. 92–94).

[76] ATLAS Collaboration, *Reconstruction of collinear final-state-radiation photons in Z decays to muons in* $\sqrt{s} = 7$ *TeV proton–proton collisions*, ATLAS-CONF-2012-143, 2012, URL: https://cds.cern.ch/record/1491697 (cit. on pp. 95, 154).

[77] ATLAS Collaboration, *Topological cell clustering in the ATLAS calorimeters and its performance in LHC Run 1*, Eur. Phys. J. C **77** (2017) 490, arXiv: 1603.02934 [hep-ex] (cit. on p. 96).

[78] ATLAS Collaboration, *Jet reconstruction and performance using particle flow with the ATLAS Detector*, Eur. Phys. J. C **77** (2017) 466, arXiv: 1703.10485 [hep-ex] (cit. on p. 97).

[79] M. Cacciari, G. P. Salam and G. Soyez, *The anti-*k_t *jet clustering algorithm*, JHEP **04** (2008) 063, arXiv: 0802.1189 [hep-ph] (cit. on p. 97).

[80] ATLAS Collaboration, *Jet energy scale measurements and their systematic uncertainties in proton–proton collisions at $\sqrt{s} = 13$ TeV with the ATLAS detector*, Phys. Rev. D **96** (2017) 072002, arXiv: 1703.09665 [hep-ex] (cit. on pp. 98, 100).

[81] M. Cacciari and G. P. Salam, *Pileup subtraction using jet areas*, Phys. Lett. B **659** (2008) 119, arXiv: 0707.1378 [hep-ph] (cit. on p. 98).

[82] M. Cacciari, G. P. Salam and G. Soyez, *The Catchment Area of Jets*, JHEP **04** (2008) 005, arXiv: 0802.1188 [hep-ph] (cit. on p. 98).

[83] ATLAS Collaboration, *Tagging and suppression of pileup jets with the ATLAS detector*, ATLAS-CONF-2014-018, 2014, URL: https://cds.cern.ch/record/1700870 (cit. on p. 100).

[84] ATLAS Collaboration, *Optimisation of the ATLAS b-tagging performance for the 2016 LHC Run*, ATL-PHYS-PUB-2016-012, 2016, URL: https://cds.cern.ch/record/2160731 (cit. on p. 101).

[85] M Limper, *Track and vertex reconstruction in the ATLAS inner detector*, Thesis, CERN-THESIS-2009-061, NIKHEF, 2009, URL: https://cds.cern.ch/record/1202457 (cit. on p. 101).

[86] ATLAS Collaboration, *E_T^{miss} performance in the ATLAS detector using 2015–2016 LHC pp collisions*, ATLAS-CONF-2018-023, 2018, URL: https://cds.cern.ch/record/2625233 (cit. on p. 102).

[87] A. Djouadi, *Decays of the Higgs Bosons*, (1997) 26 p, URL: https://cds.cern.ch/record/340786 (cit. on p. 103).

[88] W. Altmannshofer, J. Brod and M. Schmaltz, *Experimental constraints on the coupling of the Higgs boson to electrons*, JHEP **05** (2015) 125, arXiv: 1503.04830 [hep-ph] (cit. on p. 103).

[89] CMS Collaboration, *Search for a standard model-like Higgs boson in the $\mu^+\mu^-$ and e^+e^- decay channels at the LHC*, Phys. Lett. B **744** (2015) 184, arXiv: 1410.6679 [hep-ex] (cit. on pp. 103, 135, 138).

[90] ATLAS Collaboration, *Search for the dimuon decay of the Higgs boson in pp collisions at $\sqrt{s}$ = 13 TeV with the ATLAS detector*, Phys. Rev. Lett. **119** (2017) 051802, arXiv: 1705.04582 [hep-ex] (cit. on p. 103).

[91] P. Nason, *A new method for combining NLO QCD with shower Monte Carlo algorithms*, JHEP **11** (2004) 040, arXiv: hep-ph/0409146 (cit. on pp. 104, 105, 140).

[92] S. Frixione, P. Nason and C. Oleari, *Matching NLO QCD computations with Parton Shower simulations: the POWHEG method*, JHEP **11** (2007) 070, arXiv: 0709.2092 [hep-ph] (cit. on pp. 104, 105, 140).

[93] S. Alioli, P. Nason, C. Oleari and E. Re, *A general framework for implementing NLO calculations in shower Monte Carlo programs: the POWHEG BOX*, JHEP **06** (2010) 043, arXiv: 1002.2581 [hep-ph] (cit. on pp. 104, 105, 140).

[94] J. M. Campbell et al., *NLO Higgs boson production plus one and two jets using the POWHEG BOX, MadGraph4 and MCFM*, Journal of High Energy Physics **2012** (2012), ISSN: 1029-8479, URL: http://dx.doi.org/10.1007/JHEP07(2012)092 (cit. on p. 104).

[95] K. Hamilton, P. Nason and G. Zanderighi, *MINLO: Multi-Scale Improved NLO*, JHEP **10** (2012) 155, arXiv: 1206.3572 [hep-ph] (cit. on p. 104).

[96] K. Hamilton, P. Nason, C. Oleari and G. Zanderighi, *Merging H/W/Z + 0 and 1 jet at NLO with no merging scale: a path to parton shower + NNLO matching*, JHEP **05** (2013) 082, arXiv: 1212.4504 [hep-ph] (cit. on p. 104).

[97] K. Hamilton, P. Nason, E. Re and G. Zanderighi, *NNLOPS simulation of Higgs boson production*, JHEP **10** (2013) 222, arXiv: 1309.0017 [hep-ph] (cit. on p. 104).

[98] K. Hamilton, P. Nason and G. Zanderighi, *Finite quark-mass effects in the NNLOPS POWHEG+MiNLO Higgs generator*, JHEP **05** (2015) 140, arXiv: 1501.04637 [hep-ph] (cit. on p. 104).

[99] J. Butterworth et al., *PDF4LHC recommendations for LHC Run II*, J. Phys. G **43** (2016) 023001, arXiv: 1510.03865 [hep-ph] (cit. on p. 104).

[100] S. Catani and M. Grazzini, *An NNLO subtraction formalism in hadron collisions and its application to Higgs boson production at the LHC*, Phys. Rev. Lett. **98** (2007) 222002, arXiv: hep-ph/0703012 [hep-ph] (cit. on p. 104).

[101] R. D. Ball et al., *Parton distributions for the LHC Run II*, JHEP **04** (2015) 040, arXiv: 1410.8849 [hep-ph] (cit. on pp. 104, 139, 140).

[102] ATLAS Collaboration, *Measurement of the Z/γ^* boson transverse momentum distribution in pp collisions at $\sqrt{s} = 7$ TeV with the ATLAS detector*, JHEP **09** (2014) 145, arXiv: 1406.3660 [hep-ex] (cit. on pp. 104, 105).

[103] H.-L. Lai et al., *New parton distributions for collider physics*, Phys. Rev. D **82** (2010) 074024, arXiv: 1007.2241 [hep-ph] (cit. on p. 105).

[104] P. Golonka and Z. Was, *Next to Leading Logarithms and the PHOTOS Monte Carlo*, Eur. Phys. J. C **50** (2007) 53, arXiv: hep-ph/0604232 (cit. on p. 105).

[105] J. Pumplin et al., *New generation of parton distributions with uncertainties from global QCD analysis*, JHEP **07** (2002) 012, arXiv: hep-ph/0201195 (cit. on p. 105).

[106] R. D. Ball et al., *Parton distributions with LHC data*, Nucl. Phys. B **867** (2013) 244, arXiv: 1207.1303 [hep-ph] (cit. on p. 105).

[107] L. Barze et al., *Neutral current Drell-Yan with combined QCD and electroweak corrections in the POWHEG BOX*, Eur. Phys. J. C **73** (2013) 2474, arXiv: 1302.4606 [hep-ph] (cit. on p. 105).

[108] M. L. Mangano et al., *ALPGEN, a generator for hard multiparton processes in hadronic collisions*, JHEP **07** (2003) 001, arXiv: hep-ph/0206293 (cit. on p. 105).

[109] ATLAS Collaboration, *Selection of jets produced in* 13 *TeV proton–proton collisions with the ATLAS detector*, ATLAS-CONF-2015-029, 2015, URL: https://cds.cern.ch/record/2037702 (cit. on p. 109).

[110] ATLAS Collaboration, *Performance of electron and photon triggers in ATLAS during LHC Run 2*, Eur. Phys. J. C **80** (2020) 47, arXiv: 1909.00761 [hep-ex] (cit. on p. 110).

[111] M. Oreglia, 'A Study of the Reactions $\psi' \to \gamma\gamma\psi$', PhD thesis: SLAC, 1980, URL: http://www-public.slac.stanford.edu/sciDoc/docMeta.aspx?slacPubNumber=slac-r-236.html (cit. on p. 112).

[112] ATLAS Collaboration, *Electron and photon energy calibration with the ATLAS detector using LHC Run 1 data*, Eur. Phys. J. C **74** (2014) 3071, arXiv: 1407.5063 [hep-ex] (cit. on p. 116).

[113] ATLAS Collaboration, *Electron and photon performance measurements with the ATLAS detector using the 2015–2017 LHC proton–proton collision data*, JINST **14** (2019) P12006, arXiv: 1908.00005 [hep-ex] (cit. on pp. 117, 118).

[114] ATLAS Collaboration, *Measurement of Higgs boson production in the diphoton decay channel in pp collisions at center-of-mass energies of* 7 *and* 8 *TeV with the ATLAS detector*, Phys. Rev. D **90** (2014) 112015, arXiv: 1408.7084 [hep-ex] (cit. on p. 123).

[115] A. Mehta et al., *Search for the decays of the Higgs boson $H \to e^+e^-$ and $H \to e^\pm\mu^\mp$ in pp collisions at $\sqrt{s}$ = 13 TeV with the ATLAS detector*, tech. rep. ATL-COM-PHYS-2019-121, CERN, 2019, URL: https://cds.cern.ch/record/2660225 (cit. on p. 133).

[116] ATLAS Collaboration, *Search for the Higgs boson decays $H \to ee$ and $H \to e\mu$ in pp collisions at $\sqrt{s} = 13$ TeV with the ATLAS detector*, Phys. Lett. B **801** (2020) 135148, arXiv: 1909.10235 [hep-ex] (cit. on pp. 135, 137, 200).

[117] ATLAS Collaboration, *Search for the Standard Model Higgs boson decay to $\mu^+\mu^-$ with the ATLAS detector*, Phys. Lett. B **738** (2014) 68, arXiv: 1406.7663 [hep-ex] (cit. on p. 138).

[118] ATLAS Collaboration, *A search for the rare decay of the Standard Model Higgs boson to dimuons in pp collisions at $\sqrt{s} = 13$ TeV with the ATLAS detector*, ATLAS-CONF-2018-026, 2018, URL: https://cds.cern.ch/record/2628763 (cit. on p. 138).

[119] E. Bothmann et al., *Event Generation with Sherpa 2.2*, SciPost Phys. **7** (2019) 034, arXiv: 1905.09127 [hep-ph] (cit. on pp. 139, 140).

[120] T. Gleisberg and S. Hoeche, *Comix, a new matrix element generator*, JHEP **12** (2008) 039, arXiv: 0808.3674 [hep-ph] (cit. on p. 139).

[121] F. Cascioli, P. Maierhofer and S. Pozzorini, *Scattering Amplitudes with Open Loops*, Phys. Rev. Lett. **108** (2012) 111601, arXiv: 1111.5206 [hep-ph] (cit. on p. 139).

[122] A. Denner, S. Dittmaier and L. Hofer, *Collier: a fortran-based Complex One-Loop LIbrary in Extended Regularizations*, Comput. Phys. Commun. **212** (2017) 220, arXiv: 1604.06792 [hep-ph] (cit. on p. 139).

[123] C. Anastasiou, L. J. Dixon, K. Melnikov and F. Petriello, *High precision QCD at hadron colliders: Electroweak gauge boson rapidity distributions at NNLO*, Phys. Rev. D **69** (2004) 094008, arXiv: hep-ph/0312266 (cit. on p. 139).

[124] ATLAS Collaboration, *Studies on top-quark Monte Carlo modelling for Top2016*, ATL-PHYS-PUB-2016-020, 2016, URL: https://cds.cern.ch/record/2216168 (cit. on p. 140).

[125] ATLAS Collaboration, *ATLAS Pythia 8 tunes to 7 TeV data*, ATL-PHYS-PUB-2014-021, 2014, URL: https://cds.cern.ch/record/1966419 (cit. on p. 140).

[126] S. Hoeche, S. Prestel and H. Schulz, *Simulation of Vector Boson Plus Many Jet Final States at the High Luminosity LHC*, Phys. Rev. D **100** (2019) 014024, arXiv: 1905.05120 [hep-ph] (cit. on p. 140).

[127] ATLAS Collaboration, *Measurement of the transverse momentum distribution of Drell-Yan lepton pairs in proton-proton collisions at $\sqrt{s}$ = 13 TeV with the ATLAS detector*, (2019), arXiv: 1912.02844 [hep-ex] (cit. on p. 147).

[128] G. Artoni et al., *Search for the Higgs boson decaying to a pair of muons in pp collisions at $\sqrt{s}$ = 13 TeV with the ATLAS detector: Support note with updates on the EPS 2019 CONF-note analysis.*, tech. rep. ATL-COM-PHYS-2019-1444, CERN, 2019, URL: https://cds.cern.ch/record/2703492 (cit. on p. 159).

[129] Y. Sun, H.-R. Chang and D.-N. Gao, *Higgs decays to gamma l+ l- in the standard model*, JHEP **05** (2013) 061, arXiv: 1303.2230 [hep-ph] (cit. on p. 159).

[130] T. Chen and C. Guestrin, *XGBoost: A Scalable Tree Boosting System*, (2016), arXiv: 1603.02754 [cs.LG] (cit. on p. 179).

[131] John C. Collins and Davison E. Soper, *Angular Distribution of Dileptons in High-Energy Hadron Collisions*, Phys. Rev. D **16** (1977) 2219 (cit. on p. 180).

[132] ATLAS Collaboration, *A search for the dimuon decay of the Standard Model Higgs boson with the ATLAS detector*, (2020), arXiv: 2007.07830 [hep-ex] (cit. on pp. 186, 197–199, 201).

[133] ATLAS Collaboration, *Measurement of the Drell–Yan triple-differential cross section in pp collisions at $\sqrt{s}$ = 8 TeV*, JHEP **12** (2017) 059, arXiv: 1710.05167 [hep-ex] (cit. on p. 194).

[134] ATLAS Collaboration, *Prospects for the measurement of the rare Higgs boson decay $H \to \mu\mu$ with 3000 fb^{-1} of pp collisions collected at $\sqrt{s} =$ 14 TeV by the ATLAS experiment*, ATL-PHYS-PUB-2018-006, 2018, URL: `https://cds.cern.ch/record/2319741` (cit. on p. 201).